

Philipps



Universität
Marburg

**MOVPE Growth Studies on
Dilute Bismide Containing III/Vs
&
Development of an MOVPE In-Situ
Gas Phase Analysis Setup**

Dissertation

zur

Erlangung des Doktorgrades
der Naturwissenschaften
(Dr. rer. nat.)

dem

Fachbereich Physik
der Philipps-Universität Marburg

vorgelegt von

Lukas Klaus Nattermann, M.Sc.

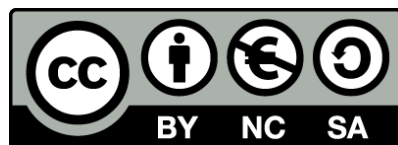
aus

Duisburg

Marburg/Lahn, 2017

Vom Fachbereich Physik der Philipps-Universität Marburg
als Dissertation angenommen am: 29.09.2017
Erstgutachter: Prof. Dr. Kerstin Volz
Zweitgutachter: Prof Dr. Martin Koch
Tag der mündlichen Prüfung: 15.11.2017
Hochschulkennziffer: 1180

Originaldokument gespeichert auf dem Publikationsserver der
Philipps-Universität Marburg
<http://archiv.ub.uni-marburg.de>



Dieses Werk bzw. der Inhalt dieser Arbeit steht unter einer
Creative Common
Namensnennung
Keine kommerzielle Nutzung
Weitergabe unter gleichen Bedingungen
3.0 Deutschland Lizenz.

Die vollständige Lizenz finden Sie unter:
<http://creativecommons.org/licenses/by-nc-sa/3.0/de/>

Zusammenfassung (Summary in German)

Aufgrund des drastischen Anstiegs der optischen Datenübertragung durch kabelgebundenes und mobiles Internet, steigt der damit zusammenhängende Stromverbrauch kontinuierlich und beträgt bereits 3 % Prozent des globalen Strombedarfs¹. Grund für den hohen Stromverbrauch sind vor allem ineffiziente $\text{In}_y\text{Ga}_{1-y}\text{As}_{1-z}\text{P}_z$ (Indiumgalliumarsenidphosphid) Laser (Light amplification by stimulated emission of radiation), deren Effizienz mit eingerechnetem Kühlaufwand lediglich 2 % beträgt². Verantwortlich für die geringe Effizienz sind Verlustprozesse, wie Auger Rekombination³ und Intervallenzband Absorption^{4,5} in den Halbleitern, die hauptsächlich in einer Erwärmung der Bauelemente resultieren. Ebenso wird in weiteren Bereichen der optoelektronischen Bauelemente mit hohem finanziellen Einsatz und Materialaufwand nach effizienten Lösungen gesucht. Genannt seien hier die Forschung an hocheffizienten Solarzellen sowie nach einer Möglichkeit eines Lasers auf Silizium (Si) Basis (on-board communication). Verschiedene Bismut (Bi) haltige III/V Halbleiter werden dabei als vielversprechende Kandidaten diskutiert^{6–13}. Hintergrund ist dabei die Möglichkeit die Bandstruktur des Basismaterials, wie zum Beispiel GaAs (Galliumarsenid), mit nur 10 % Bi auf Arsen (As) Gitterpositionen, derart zu manipulieren, dass die oben genannten Verlustprozesse unterdrückt werden¹⁰. Gleichzeitig entspräche im Fall von $\text{GaAs}_{1-x}\text{Bi}_x$ (Galliumarsenidbismid) die daraus resultierende Bandlücke einer Emissionswellenlänge von $1,55\text{ }\mu\text{m}$, eine der wichtigsten Telekommunikationswellenlängen. Ebenso besteht für III-Bi-V Materialien Anwendungspotential in vielen weiteren optoelektronischen Bereichen^{14–16}. Die Herstellung dieser hoch metastabilen Materialien ist jedoch nicht trivial und Gegenstand der aktuellen Forschung.

In dieser Arbeit wurden verschiedene Bi haltige III/V Materialien untersucht. Beginnend mit dem epitaktischen Wachstum mittels der metallorganischen Gasphasenepitaxie (MOVPE, metalorganic vapour phase epitaxy) wurden $\text{GaAs}_{1-x}\text{Bi}_x$, $\text{GaAs}_{1-x-y}\text{P}_y\text{Bi}_x$ (Galliumarsenidphosphidbismid), $\text{GaAs}_{1-x-y}\text{N}_y\text{Bi}_x$ (Galliumarsenidnitridbismid) und $\text{GaP}_{1-x}\text{Bi}_x$ (Galliumphosphidbismid) abgeschieden und anschließend vielfältig charakterisiert^{17–20}. Dabei bestand die Herausforderung in der Entwicklung von epitaktischen Schichten, die gleichzeitig die benötigte Komposition und eine hohe Materialqualität aufweisen.

Die Herstellung von $\text{GaAs}_{1-x}\text{Bi}_x$ mit mehr als 10 % Bi mittels MOVPE konnte bisher jedoch noch nicht realisiert werden. In dieser Arbeit wurde nach Gründen für das Einbaulimit

von Bi geforscht. Dafür wurden alternative metallorganische Präkursoren verwendet um die Rolle der thermischen Zerlegung dieser Präkursoren und damit zusammenhängende Oberflächenprozesse der Wachstumsoberfläche zu untersuchen. Es konnte gezeigt werden, dass das Einbaulimit nicht unmittelbar von der Art des Präkursors (verschiedene Kohlenwasserstoffgruppen) abhängt. Vielmehr zeigte das Wachstum mit verschiedenen Präkursoren annähernd identische Ergebnisse. Ein Blockieren der Wachstumsoberfläche durch einen speziellen Bi-Präkursor, sowie eine mangelnde thermische Zerlegung der Ausgangsmaterialien kann bei den gegebenen Wachstumstemperaturen als der entscheidende limitierender Faktor also ausgeschlossen werden.

Quaternäre Bi haltige Schichten, namentlich $\text{GaAs}_{1-x-y}\text{P}_y\text{Bi}_x$ und $\text{GaAs}_{1-x-y}\text{N}_y\text{Bi}_x$ auf GaAs, bieten die Möglichkeit eines gitterangepassten Wachstums über einen breiten Bandlückenbereich. Dies wird möglich da die Gitterkonstante und die Bandlücke unabhängig voneinander eingestellt werden können. $\text{GaAs}_{1-x-y}\text{P}_y\text{Bi}_x$ wurde als potentielles Material für 1 eV Zellen in einer Mehrfach-Solarzelle untersucht. Hierbei konnte zum ersten mal PL (Photolumineszenz) an $\text{GaAs}_{1-x-y}\text{P}_y\text{Bi}_x$ nachgewiesen werden, welche das Material für weitere Anwendungen attraktiv macht. Ebenfalls konnte gezeigt werden, dass lokale Verspannung im Halbleiterkristall einen entscheidenden Einfluss auf das Bi Einbaulimit hat. Deshalb wurden im Folgenden $\text{GaAs}_{1-x-y}\text{P}_y\text{Bi}_x$, $\text{GaAs}_{1-x-y}\text{N}_y\text{Bi}_x$ und $\text{GaAs}_{1-x}\text{Bi}_x$ Schichten abgeschieden und verglichen, um die genaue Rolle der Verspannung auf den Bi Einbau zu charakterisieren. Es konnte gezeigt werden, dass eine Kompensation der lokalen Verspannung durch, relativ zu As und Bi gesehen, kleinere Phosphor (P) und Stickstoff (N) Atome zu einem höheren Bi Einbau führen. Die lokale Verspannung hat also einen direkten Einfluss auf den Bi Einbau. Dies spielt bei der Entwicklung neuartiger Bi haltiger III/V Materialien eine wichtige Rolle.

Des Weiteren wurden Untersuchungen an $\text{GaP}_{1-x}\text{Bi}_x$ auf GaP (Galliumphosphid) und GaP auf Si vorgenommen. Ein bisher wenig erforschtes Material, von dem in dieser Arbeit die erste erfolgreiche Abscheidung mittels MOVPE gezeigt werden konnte. Außerdem gelang die Herstellung hoch Bi haltiger Strukturen mit einem Bi Einbau bis zu 8,5 %. Zunächst als Laser Material auf Si angedacht, zeigte sich im Laufe dieser Arbeit, dass die optischen Eigenschaften dieser Verbindung nur bedingt für den Einsatz in der Optoelektronik in Frage kommen. Das Material eignet sich aufgrund eines Zusammenbruchs des Bandkanten Bloch-Charakters und einer weiterhin indirekten Bandlücke, trotz des hohen Bi Anteils und der guten strukturellen Qualität, nicht als aktives Material in optoelektronischen Bauelementen. Aus theoretischer Sicht bietet es jedoch interessante Eigenschaften für das weitere Verständnis der Bandstrukturen Bi haltiger III/V-Verbindungen.

Zuletzt konnte mit den gesammelten Erfahrungen über die Abscheidung Bi haltiger III/V-Materialien eine Verbesserung des zuvor entwickelten $\text{GaAs}_{1-x}\text{Bi}_x$ Lasers erreicht werden. Der neue Laser emittiert bei 1015 nm bei Raumtemperatur.

Über weite Teile dieser Arbeit lief als zweites und paralleles Projekt die Entwicklung eines neuen *in-situ* Massenspektrometer-Aufbaus an einer MOVPE Anlage. Damit sollen

in-situ Gasphasen Untersuchungen während des Wachstums der oben genannten Halbleiterstrukturen zu einem besseren Verständnis der MOVPE Wachstumsprozesse führen. Von besonderem Interesse sind dabei die Zerlegung der Präkursoren, einzeln und in Interaktion, sowie die Analyse der Desorptionsprodukte während des Wachstums. Hierfür wurde in Zusammenarbeit mit der *Carl Zeiss SMT GmbH* ein neu entwickelter Massenspektrometer-Prototyp für den MOVPE Laborbetrieb vorbereitet und anschließend ein Anschluss-System entwickelt, welches die Untersuchung der Prozessgase während des Wachstums erlaubt. Dabei war die Herausforderung den Analyten so unverändert wie möglich ins Massenspektrometer zu leiten, ohne den eigentliche MOVPE Prozess dabei zu sehr zu beeinflussen, so dass tatsächliche *in-situ* Untersuchungen möglich werden. Es gelang die Entwicklung eines solchen Aufbaus und anhand der Zerlegungsuntersuchungen von Tertiärbutylarsine (TBAs) konnte die Eignung, sowie Vorteile des neuen Aufbaus erfolgreich demonstriert werden. Neben der extrem kurzen Messzeit für ein gesamtes Massenspektrum (wenige Sekunden) ist vor allem entscheidend, dass es gelungen ist, Messbedingungen mit dem Massenspektrometer-Prototypen zu finden, bei dem der Analyt unter dem Einfluss der Elektronen-Ionisation kaum zerlegt wird. Dadurch werden Untersuchungen, und vor allem die direkte Interpretation von komplexeren Gasphasen, möglich.

Insgesamt kann gesagt werden, dass aus den in dieser Arbeit durchgeführten Untersuchungen vielfältige neue Erkenntnisse zur Herstellung von Bi haltigen III/V Halbleitern gewonnen wurden. Ebenso bietet die erfolgreiche Entwicklung eines *in-situ* Massenspektrometrie-Aufbaus an einer MOVPE-Anlage die Möglichkeit der Zerlegungs- und Wachstumsuntersuchungen in bisher unerreichtem Detail.

Danksagung (Acknowledgments)

An dieser Stelle möchte ich mich bei allen herzlich bedanken, die mir bei der Erstellung dieser Arbeit geholfen und mich während meiner Promotionszeit begleitet haben. Ganz besonderer Dank gilt dabei ...

... Prof. Dr. Kerstin Volz, für die Möglichkeit diese Arbeit in ihrer Arbeitsgruppe zu schreiben, all die hilfreichen Diskussionen, die Flexibilität bei neuen Ideen und für das Möglichmachen des Aufenthaltes in Madison, sowie die Konferenzbesuche.

... Prof. Dr. Martin Koch für die Übernahme des Zweitgutachtens dieser Arbeit.

... PD Dr. Ralf Tonner und Prof. Dr. Florian Gebhard für hilfreiche Ratschläge und die Teilnahme an meiner Prüfungskommission.

... Prof. Dr. Wolfgang Stolz für die zahlreichen wichtigen Ratschläge und ein offenes Ohr.

... Prof. Dr. Stephen Sweeney und Prof. Dr. Sangam Chatterjee für wichtige Ratschläge und fruchtbare Zusammenarbeit.

... Prof. Dr. Sue Babcock für die Möglichkeit für eine Zeit in Madison zu arbeiten und eine wissenschaftlich wie menschlich wunderbare Zeit.

... der DFG für die Finanzierung meiner Arbeit, innerhalb der Projekte RTG1782 "Functionalization of Semiconductors" und SFB1083 "Structure and Dynamics of Internal Interfaces".

... meiner Arbeitsgruppe für unzählige lustige Momente und die Unterstützung. Dabei sind ganz besonders zu erwähnen Thomas Ochs, Stefan Reinhardt und Celina Becker, sowie Elke Vaupel, Marina Koch und Isabelle Kimmel, die jederzeit mit Rat und Tat zur Seite standen.

... Eddy, für eine unfassbar gute Zeit vom ersten Tag an, für "zwei-Uhr-zwei-Bier" und einfach alles andere.

... Lennart, für die entspannteste WG die ich mir vorstellen kann.

... Ulrike, Antje, Johannes, Peter und Michael für die super Stimmung im Labor und die Hilfsbereitschaft.

... Thilo und Oli für ihre Hilfe und die gute Atmosphäre im Büro.

... Jan Oli, Christian, Peter und Jürgen für ihre Hilfe und Input.

... dem *iTrap Team* von Carl Zeiss SMT GmbH und insbesondere Valerie und Rudi für die Hilfsbereitschaft.

... India, all meinen Freunden und meiner Familie die immer da sind, mir den Rücken frei

halten und einen wieder aufmuntern, wenn es nötig ist. Ohne euch wäre diese Arbeit nicht möglich gewesen.

Contents

1	Introduction	1
2	Theoretical Background and Experimental Methods	5
2.1	Structural Properties of Bi Containing III/Vs	5
2.2	Band Structure of Bi Containing III/Vs	7
2.3	Investigated Materials	8
2.3.1	GaAs _{1-x} Bi _x	9
2.3.2	GaAs _{1-x-y} P _y Bi _x	11
2.3.3	GaAs _{1-x-y} N _y Bi _x	12
2.3.4	GaP _{1-x} Bi _x	13
2.4	Experimental Methods	15
2.4.1	Metalorganic Vapor Phase Epitaxy	16
2.4.2	High Resolution X-Ray Diffraction	18
2.4.3	Atomic Force Microscopy	19
2.4.4	Photoluminescence Spectroscopy	20
2.4.5	Mass Spectrometry	21
3	Dilute Bi Containing III/V Semiconductors	25
3.1	GaAs _{1-x} Bi _x MOVPE with Alternative Bi and Ga Precursors	25
3.2	Quaternary GaAs _{1-x-y} P _y Bi _x for Solar Cell and Laser Applications	27
3.3	The Influence of Strain on the Bi Incorporation Limit	28
3.4	GaP _{1-x} Bi _x on GaP and GaP on Si	29
3.5	Progress on GaAs _{1-x} Bi _x Lasers	31
4	MOVPE In-Situ Gas Phase Analysis	33
4.1	Quadrupole Ion Trap Based Mass Spectrometer Setup on a MOVPE System	33
4.2	Gas Phase Analysis on the Thermal Decomposition of TBAs	35
5	Summary and Outlook	41
6	Author's Contribution	45
6.1	Original Contributions	45

6.2	Publications of this Work	47
6.2.1	MOVPE Gas Phase Analysis Setup - With Newly Designed, Highly Sensitive and Real-Time Quadrupole Ion Trap Mass Spectrometer	47
6.2.2	MOVPE Growth of Ga(PBi) on GaP and GaP on Si With Bi Fractions up to 8%	56
6.2.3	Exploiting Strain to Enhance the Bi Incorporation in GaAs-based III/V Semiconductors Using MOVPE	62
6.2.4	MOVPE Growth and Characterization of Quaternary Ga(PAsBi)/GaAs Alloys for Optoelectronic Applications	68
6.2.5	MOVPE Growth of Ga(AsBi)/GaAs Using Different Metalorganic Precursors	75
6.2.6	Valence Band-Anticrossing in Ga(PBi) Dilute Bismide Alloys: Giant Bowing of the Band Gap and Spin-Orbit Splitting Energy	83
6.2.7	Optical Constants and Critical Points of Dilute Bismide Alloys Studied by Spectroscopic Ellipsometry	91
6.2.8	On The Effects of Column Occupancy and Static Atomic Disorder on the Analysis of Chemical Ordering in Ga(PBi) Compounds	100
6.3	Further Publications	103
	Acronyms	107
	Bibliography	109

CHAPTER 1

Introduction

All applications in which light (electromagnetic radiation) is absorbed by a semiconductor to generate electricity or electricity is used to obtain light from a semiconductor are called optoelectronic applications. Although one will only, if at all, think of solar cells or light emitting diodes (LEDs), optoelectronics are an essential part of many more devices for everyday use, and modern life would be inconceivable without them. The main reason for the assertiveness of optoelectronics is an outstanding combination of compact packaging dimensions, flexibility and low-cost fabrication. Examples of such devices include flat screens, digital camera chips, light amplification by stimulated emission of radiations (lasers), medical applications, all kind of LEDs, as well as solar cells and optical data transmission. The internet is based on optical data transmission between many bigger and smaller data traffic points, spanning the whole world and connecting servers, the industry sector, and households. Lasers translate binary data into optical pulses and inject them into glass fibers, which allow data transmission at the speed of light. Photodetectors at the other end of the fiber retranslate the information carried by the light pulses back into binary electric computer signals. Glass fibers have absorption minima, also referred to as transmission windows, at $1.55\ \mu\text{m}$ and $1.3\ \mu\text{m}$. Therefore, lasers with those emission wavelengths are of interest for optical data transmission. Indium gallium arsenide phosphide ($\text{In}_y\text{Ga}_{1-y}\text{As}_z\text{P}_{1-z}$) electrical injection lasers are currently used. However, they have an efficiency of only about 20 %², since they suffer from heat generating loss mechanisms such as Auger recombination³ and intervalence band absorption (IVBA)^{4,5}, which additionally require further cooling efforts for reliable operation. This is a major issue, since data communication has grown so drastically that the electricity consumption of data-based processes has mushroomed from almost zero to 3 % of the global electricity supply during the last 10 years¹ and is still constantly growing.

Dilute bismide containing gallium arsenide bismide ($\text{GaAs}_{1-x}\text{Bi}_x$) on gallium arsenide (GaAs) is a promising alloy system for highly efficient lasers with $1.55\ \mu\text{m}$ emission wavelength^{10,11}. Auger recombination and IVBA could be suppressed in $\text{GaAs}_{1-x}\text{Bi}_x$ with sufficient Bi fractions.¹⁰ Additionally, it was found that $\text{GaAs}_{1-x}\text{Bi}_x$ has a significantly

lower temperature sensitivity of the emission wavelength compared to currently used $\text{In}_y\text{Ga}_{1-y}\text{As}_z\text{P}_{1-z}$ alloys²¹⁻²⁴. For many other applications as well, such as near infrared (NIR)- and mid infrared (MIR) laser devices⁶⁻¹¹, photodiodes²⁵⁻²⁸, photovoltaics^{12,13}, spintronics^{14,15}, and thermoelectrics¹⁶, bismide containing III/V semiconductors are providing promising properties and have received significant attention recently.

However, the epitaxial growth of those highly metastable bismide containing materials is challenging^{21,22,29,30}. The incorporation of sufficient amounts of Bi using metalorganic vapor phase epitaxy (MOVPE), and, simultaneously realizing the deposition of high quality structures is complex and still an object of ongoing research. The aim of the present work was to gain further insights into the deposition and the properties of various bismide containing III/V semiconductors for optoelectronic applications. Therefore, MOVPE growth studies on $\text{GaAs}_{1-x}\text{Bi}_x$, gallium arsenide phosphide bismide ($\text{GaAs}_{1-y-x}\text{P}_y\text{Bi}_x$), gallium arsenide nitride bismide ($\text{GaAs}_{1-y-x}\text{N}_y\text{Bi}_x$), and gallium phosphide bismide ($\text{GaP}_{1-x}\text{Bi}_x$) were performed. Quaternary bismides such as $\text{GaAs}_{1-y-x}\text{P}_y\text{Bi}_x$ and $\text{GaAs}_{1-y-x}\text{N}_y\text{Bi}_x$ were investigated to unveil the role of local strain on the incorporation limits of Bi into III/Vs. $\text{GaAs}_{1-y-x}\text{P}_y\text{Bi}_x$, a potential candidate for a sub-cell material in a multi-junction solar cell, was extensively characterized, and the first photoluminescence (PL) activity was shown. Additionally, the first MOVPE deposition of $\text{GaP}_{1-x}\text{Bi}_x$ structures on gallium phosphide (GaP) and GaP on Si was demonstrated, and structural as well as optical characterization was performed. Finally, by analyzing the MOVPE growth characteristics of bismide containing III/Vs, the deposition of further enhanced $\text{GaAs}_{1-x}\text{Bi}_x$ laser structures were realized. Room temperature lasing of a SQW laser diode at 1015 nm was demonstrated. Moreover, a deeper understanding of the complex MOVPE growth process of bismide containing materials was of interest. Therefore, a new experimental setup for MOVPE in-situ gas phase investigations was developed, using a highly sensitive mass spectrometer (MS) prototype provided by *Carl Zeiss SMT GmbH*. Thereby, demonstration of detailed decomposition characteristics of tertiarybutylarsine (TBAs) was realized.

This thesis is written in cumulative form and is structured as follows: Chapter 2 contains background information on materials and methods. Instead of a full introduction into the basics of III/V semiconductors, which can be found in textbooks^{31,32}, a detailed discussion of Bi containing materials, the subject of this work, is provided in sections 2.1-2.3. Section 2.4 introduces the most important experimental methods used for this work. Chapter 3 covers the research results of the growth and characterization of bismide containing III/V semiconductors, while chapter 4 deals with the development of the in-situ experiment for MOVPE gas phase investigations. The published research results are briefly presented, since they are discussed in more detail in the published research papers in chapter 6.2. The part of the results not yet published is discussed in more detail. A summary of the results can be found in chapter 5.

List of Publications:

- L. Nattermann, O. Maßmeyer, E. Sterzer, V. Derpmann, H. Y. Chung, W. Stolz, K. Volz, *MOVPE gas-phase analysis setup - with newly designed, highly sensitive and real-time 3D quadrupole ion trap mass spectrometer*, submitted to Scientific Reports (2017)
- L. Nattermann, P. Ludewig, E. Sterzer, K. Volz, *Exploiting strain to enhance the Bi incorporation in GaAs-based III/V semiconductors using MOVPE*, Journal of Crystal Growth **470**, pp. 15-19 (2017)
DOI: 10.1016/j.jcrysgro.2017.04.005
- L. Nattermann, A. Beyer, P. Ludewig, T. Hepp, E. Sterzer, K. Volz, *MOVPE growth of Ga(PBi) on GaP and GaP on Si with Bi fractions up to 8%*, Journal of Crystal Growth **463**, pp. 151-155 (2017)
DOI: 10.1016/j.jcrysgro.2017.02.021
- L. Nattermann, P. Ludewig, N. Knaub, N. W. Rosemann, T. Hepp, E. Sterzer, S. R. Jin, K. Hild, S. Chatterjee, S. J. Sweeney, W. Stolz, K. Volz, *MOVPE growth and characterization of quaternary Ga(PAsBi)/GaAs alloys for optoelectronic applications*, Applied Materials Today **5**, pp. 209-214 (2016)
DOI: 10.1016/j.apmt.2016.09.018
- L. Nattermann, P. Ludewig, L. Meckbach, B. Ringler, D. Keiper, C. von Hänisch, *MOVPE growth of Ga(AsBi)/GaAs hetero structures using different metalorganic precursors*, Journal of Crystal Growth **426**, pp. 54-60 (2015)
DOI: 10.1016/j.jcrysgro.2015.05.015
- J. Belz, A. Beyer, L. Nattermann, K. Volz, *On The Effects of Column Occupancy and Static Atomic Disorder on the Analysis of Chemical Ordering in Ga(PBi) Compounds*, Microscopy and Microanalysis **23 (S1)**, pp. 1474-1475 (2017)
DOI: 10.1017/S1431927617008030
- Z. Bushell, C. Broderick, L. Nattermann, R. Joseph, J. Keddie, J. Rorison, K. Volz, S. Sweeney, *Valence band-anticrossing in Ga(PBi) dilute bismide alloys: giant bowing of the band gap and spin-orbit splitting energy*, submitted to Physical Review Materials (Rapid Communication) (2017)
- Z. Bushell, R. M. Joseph, L. Nattermann, P. Ludewig, K. Volz, J. L. Keddie, S. J. Sweeney *Optical constants and critical points of dilute bismide alloys studied by spectroscopic ellipsometry*, submitted to Journal of Applied Physics (2017)

CHAPTER 2

Theoretical Background and Experimental Methods

This chapter covers the theoretical background, such as important structural and optoelectronic properties of the various investigated materials. Furthermore, an introduction into the most important experimental methods used for this work, in particular MOVPE and MS, will be given.

2.1 Structural Properties of Bi Containing III/Vs

The materials investigated in this work were $\text{GaAs}_{1-x}\text{Bi}_x$, $\text{GaAs}_{1-y-x}\text{P}_y\text{Bi}_x$ as well as $\text{GaAs}_{1-y-x}\text{N}_y\text{Bi}_x$, deposited on GaAs. MOVPE growth of $\text{GaP}_{1-x}\text{Bi}_x$ deposited on GaP and GaP on Si was also developed and structures were characterized. All deposited materials crystallize in the zincblende structure, two face centered cubic (fcc) lattices, shifted by a fourth of the cubical diagonal. One of these two fcc lattices is occupied by group III-, the other one is occupied by group V atoms³². Further information and a more comprehensive introduction into the basics of III/V semiconductor physics can be found in standard works like the books written by Kittel³¹ or Ashcroft and Mermin³³ and will not be covered in this work, which focuses on the deposition by MOVPE and on the characterization of the optoelectronic properties. In order to make an understanding of the MOVPE deposition of Bi containing III/Vs possible, the most important limiting parameters, which are strain, solubility, and the surface kinetics of the growth process, will be discussed.

In order to determine the **strain** ϵ , defined as

$$\epsilon = \frac{a_{sub} - a_L}{a_L}, \quad (2.1)$$

the relaxed lattice constant a_L of the deposited layer needs to be calculated. a_{Sub} is the lattice constant of the substrate. From the binary lattice parameters in table 2.1, the lattice constants of the deposited ternary layer structures $\text{GaE}_{1-x}\text{Bi}_x$, with $E = \text{As}$ and P , can be calculated using Vegard's law³⁴, see equation 2.2:

$$a_{Ga(EBi)} = x \cdot a_{GaE} + (1 - x) \cdot a_{GaB} \quad (2.2)$$

or with equation 2.3

$$a_{Ga(WEBi)} = x \cdot a_{GaW} + y \cdot a_{GaE} + (1 - x - y) \cdot a_{GaBi} \quad (2.3)$$

for the quaternary layers $GaW_{1-y-x}E_yBi_x$, with $E = P$ or As , and $W = P$ or N , and $E \neq W$. The strain refers to the difference between the unstrained lattice constant of the deposited material and the lattice constant of the substrate. An overview of the relevant structural material properties of the binary alloys necessary for combination of ternary and quaternary III/Vs are given in table 2.1.

Properties at 300 K	GaAs	GaP	GaBi	GaN
Lattice Constant a (\AA) ^{35,36}	5.6532	5.4505	6.33	4.5
Elastic Constants C_{11}, C_{12} (GPa) ^{36,37}	1221, 566	1410, 620	73, 32.7	293, 159

Table 2.1: Overview of material properties (at 300 K) of all binaries used to deposit ternary and quaternary III-Bi-V materials.

However, the strain defined in equation 2.1 cannot be measured directly, since it refers to the relaxed lattice constant a_L of the deposited material. In order to determine the strain with equation 2.1, it is necessary to measure the strained vertical lattice constant a_{\perp} of the deposited layer. Furthermore, using a_{\perp} and the elastic constants (material parameter), C_{11} and C_{12} , the relaxed lattice constant a_L of the deposited layer can be calculated³⁸, see equation 2.4.

$$\frac{\Delta a_L}{a_{sub}} = \frac{a_L - a_{sub}}{a_{sub}} = \frac{C_{11}}{C_{11} + 2 \cdot C_{12}} \cdot \left(\frac{\Delta a_{\perp}}{a_{sub}} \right), \quad (2.4)$$

Once the relaxed lattice constant a_L of the deposited material is known, the composition can be determined using Vegard's law equation 2.2. This will be further discussed in section 2.4.2. Nevertheless, it is important that the vertical strained lattice constant a_{\perp} of the deposited material increases with increasing Bi fractions, as for example in ternary $GaAs_{1-x}Bi_x$. Additionally, the strain energy will accumulate with increasing layer thickness. From the point on where the critical layer thickness is reached, the energy of ϵ becomes bigger than the energy barrier of the formation of dislocations. The crystal will relax, $a_{\perp} = a_L$, which means the growth is not pseudomorphic and the equations above are not valid any more. As a rule of thumb the *20 nm per % strain* approach is assumed for most of the conventional III/V semiconductors³⁹. This means that about 20 nm can be deposited with one percent of strain before the crystal forms defects, as the strain energy is too high. However, this rule of thumb is not valid for Bi containing materials, as the

growth temperatures are much lower, which makes it possible to grow thicker layers for one percent of strain.

Furthermore, the **solubility** potentials of different mixtures of the discussed III/V materials are important. In particular, the solubility of Bi in the different III/V host lattices is of interest for this work. Since GaBi is a hypothetical zincblende semi-metallic alloy at room temperature, the solubility of Bi in GaAs and GaP based materials must be calculated. N. Elayech et al. determined the phase equilibria for ternary $\text{GaAs}_{1-x}\text{Bi}_x$ by calculating the thermodynamic descriptions of the constituent binary systems GaAs, GaBi, and AsBi⁴⁰ by using the *CALPHAD* method⁴¹ and thermodynamic parameters from Girard⁴². Their calculations showed an experimentally confirmed decrease of Bi solubility with increasing growth temperature⁴³. As a consequence, low growth temperatures are necessary for deposition of Bi containing $\text{GaAs}_{1-x}\text{Bi}_x$ with significant amounts of Bi, which makes the MOVPE growth challenging, as a certain temperature for thermal decomposition of the precursors used is required. Thermodynamic data for ternary $\text{GaP}_{1-x}\text{Bi}_x$ were published by A. S. Jordan and coworkers⁴⁴. They showed that the solubility of Bi in GaP increases with increasing temperature, although their calculations considered a different temperature range. Calculations for temperatures relevant for MOVPE deposition are not available so far, but a similar trend as observed for $\text{GaAs}_{1-x}\text{Bi}_x$ is expected⁴⁰.

Additionally, **surface kinetics** and **surface chemistry** are crucial points in order to understand MOVPE growth processes of III/V bismides. Beginning with the decomposition of the precursors, followed by the physical and chemical adsorption of the metalorganics (MOs) at the growth surface and finally the movement and mobility of atoms and the surface reconstructions, make MOVPE deposition a highly complex system. Since those processes are strongly connected to MOVPE process parameters, a further discussion of the basics will take place in section 2.4.1. Furthermore, MOVPE kinetics are still a matter of ongoing research and will be discussed in chapter 3 and 4. Supplementary information on MOVPE can be found in *Organometallic Vapor-Phase Epitaxy: Theory and Practice* by G. Stringfellow⁴⁵.

2.2 Band Structure of Bi Containing III/Vs

The band structure^{31,32} parameters of the substrate and binary materials GaAs and GaP, as well as GaN and GaBi, are given in table 2.2. Since the band structure of III-Bi-V semiconductors can not be calculated with the virtual crystal approximation (VCA) model, commonly used for III/V semiconductors, theoretical studies to describe the band structure were performed. The first studies were carried out by Alberi et al.^{46,47}, who showed that the band gap bowing of dilute bismides can be calculated with the valence band anticrossing (VBAC), using a $\mathbf{k} \cdot \mathbf{p}$ formalism, similar to the conduction band anticrossing (CBAC) which was developed for dilute nitrides, e.g. gallium indium arsenide nitride ($\text{Ga}_y\text{In}_{1-y}\text{As}_z\text{N}_{1-z}$)⁴⁸. As those calculations are essential for all investigated materials in

this work, the VBAC basics will be mentioned in the following section. Further details on the standard 6×6 Hamiltonian, describing the four Γ_8 and two Γ_7 valence bands of GaAs, which are modified by the addition of the six localized p-states of the minority Bi atoms, can be found in^{46,47,49}.

Electrical- and Optical Properties of host- and substrate materials				
Properties at 300 K	GaAs	GaP	GaN	GaBi
Band Gap Energy E_g (eV) ^{36,50}	1.424	2.78, 2.26	3.30	0 (-1.45)
Energy Spin-Orbit Splitting ΔSO (eV) ⁴⁹	0.34	0.08	0.017	2.2

Table 2.2: Optoelectronic properties of host- and substrate materials at 300 K. For GaP the direct and indirect band gap are given at L and Γ point.

The VBAC model is only valid for small Bi concentrations, as the electronic states caused by the Bi atoms are considered to be isoelectric impurity states, coupling with the valence band states of the host material. This interaction of the light hole and heavy hole valence band states with the Bi impurity states cause a splitting into energetically higher E_+ and lower E_- bands. However, so far only the E_+ bands could be experimentally confirmed⁵¹. Using a sp^3 s tight-binding model, C. Broderick et al. further developed the model and demonstrated calculations for $\text{GaAs}_{1-x}\text{Bi}_x$ in agreement with experimental data⁴⁹. They also showed that a mixture of VBAC and VCA model leads to exact, experimentally confirmed, values for the band structure of $\text{GaAs}_{1-x}\text{Bi}_x$ and $\text{GaP}_{1-x}\text{Bi}_x$, as the conduction and spin-orbit split-off band edges vary linearly in energy with increasing Bi composition. Band gap calculations for $\text{GaAs}_{1-y-x}\text{N}_y\text{Bi}_x$ and $\text{GaAs}_{1-y-x}\text{P}_y\text{Bi}_x$, which are even more complex, can be found here^{10,11} and here^{18,52}, respectively, and will be further discussed in the next chapter 2.3.

2.3 Investigated Materials

After an illustration of the general structural properties and an introduction of the VBAC model, this section covers the different material systems and their particularities. A short motivation, an overview of important publications, and the material properties of all investigated semiconductors are provided. Before going into the details of the single materials, Figure 2.1 shows an overview of band gaps and lattice constants of Ga-V-Bi alloys. The values for the binary alloys used are marked by red dots. For $\text{GaAs}_{1-x}\text{Bi}_x$ on GaAs (blue) and $\text{GaP}_{1-x}\text{Bi}_x$ on GaP (green), the theoretically achievable lattice constant and band gap is marked up to 12 % Bi and under consideration of the VBAC model^{49,51,53}. For the quaternaries $\text{GaAs}_{1-y-x}\text{P}_y\text{Bi}_x$ and $\text{GaAs}_{1-y-x}\text{N}_y\text{Bi}_x$ on GaAs, the dashed areas illustrate the theoretically feasible alloys. In fact, the possible area of alloys which can be deposited on GaAs is significantly smaller, which is a subject of this work and will be

discussed in chapter 3.2. The strain of the deposited layers on GaAs and GaP are marked by the grey shaded areas up to 2%. Increasing grey means increasing strain.

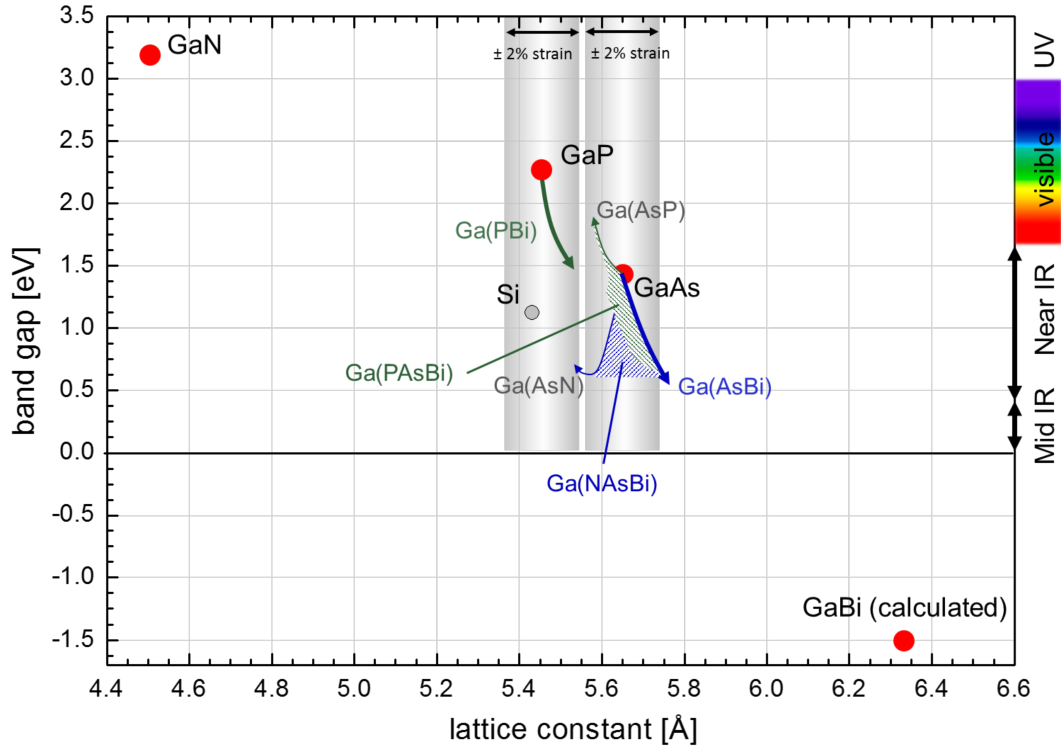


Figure 2.1: Plotted is the band gap against the lattice constant for binary compounds, the ternary compounds $\text{GaAs}_{1-x}\text{Bi}_x$ on GaAs (blue) and $\text{GaP}_{1-x}\text{Bi}_x$ on GaP (green) and for the quaternary alloys $\text{GaAs}_{1-y-x}\text{N}_y\text{Bi}_x$ (shaded blue) and $\text{GaAs}_{1-y-x}\text{P}_y\text{Bi}_x$ (shaded green). The grey shaded area shows the strain up to 2% on GaAs and GaP, respectively.

2.3.1 $\text{GaAs}_{1-x}\text{Bi}_x$

The growth of $\text{GaAs}_{1-x}\text{Bi}_x$ on (001) GaAs has gained significant attention over the last few years^{10,22,29,46,47,54–56}. As the efficiencies of currently used indium phosphide (InP) based 1.3 and 1.55 μm lasers suffer from strong loss mechanisms, namely Auger recombination and IVBA, $\text{GaAs}_{1-x}\text{Bi}_x$ is a promising alternative^{3,57,58}. The incorporation of Bi into the GaAs host material shows a large reduction of the band gap per percent Bi and a strong influence on the spin-orbit splitting. This is predicted to lead to a suppression of the conduction heavy hole spin-orbit heavy hole (CHSH) Auger recombination^{59–61} and IVBA⁴ for Bi fractions above 11.2%¹⁰, as illustrated in Figure 2.2. The band gap decreases with increasing Bi content, while the spin-orbit splitting increases, up to the point at which the band gap is smaller than the spin-orbit splitting. For the sake of completeness, it should be mentioned that the value of 11.2% varies between 9% and 12% Bi between different publications, as it depends on several input parameters⁶².

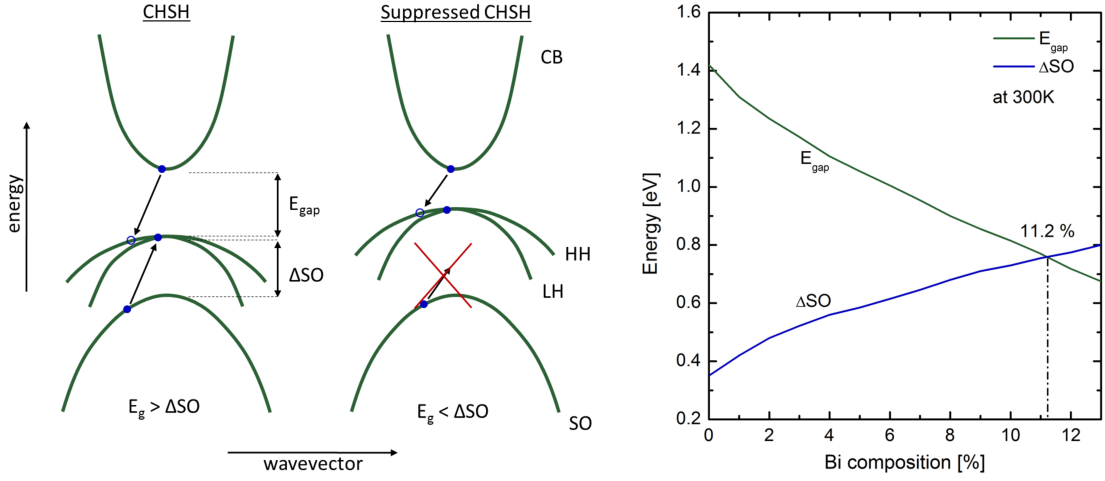


Figure 2.2: Simplified CHSH Auger process and its suppression are depicted on the left-hand side. On the right-hand side, the band gap energy and the distance of valence band to spin-orbit splitoff band vs. Bi content is plotted. Values and parts of the Figures are adopted from⁶¹.

Additionally, $\text{GaAs}_{1-x}\text{Bi}_x$ shows a reduced temperature sensitivity of the band gap, which allows reduction of thermoelectric cooling, so that the efficiency, compared to current devices, is further increased²².

However, MOVPE growth of the highly metastable material $\text{GaAs}_{1-x}\text{Bi}_x$ with more than 7 % of Bi still remains a challenge²⁹ and is the subject of current research. Carefully adjusted growth parameters such as temperature and precursor flow ratios are crucial in order to obtain high quality material. Only slight deviations from suitable growth parameters can lead to Bi or GaBi droplets⁶³ on the surface and to deteriorated optical properties⁶⁴. The MOVPE growth and a growth model is discussed in detail in^{9,29}. Strain, solubility of Bi in GaAs, and growth surface processes as well are responsible for the limitations of Bi incorporation. In particular, the influence of surface chemistry and hydrocarbon residues of different MO precursors on the growth characteristics are debated in^{17,65} and are a topic of this work; see section 3.1.

Deposition of $\text{GaAs}_{1-x}\text{Bi}_x$ laser structures on GaAs by MOVPE was successfully demonstrated with 2.2 % Bi content⁶⁶. Additionally, further $\text{GaAs}_{1-x}\text{Bi}_x$ lasers, grown by molecular beam epitaxy (MBE) and MOVPE, were reported^{67–69}, but electrically pumped room temperature lasing is limited to 3.9 % Bi so far⁸. Further increase of Bi content and decrease of threshold current is the subject of current research and was also tackled in this work, see section 3.5.

2.3.2 $\text{GaAs}_{1-y-x}\text{P}_y\text{Bi}_x$

$\text{GaAs}_{1-y-x}\text{P}_y\text{Bi}_x$ on (001) GaAs, first introduced by Forghani et al.⁵², is a relatively new alloy, and no further theoretical or experimental literature is available. Similar to $\text{GaAs}_{1-x}\text{Bi}_x$ (2.3.1), for $\text{GaAs}_{1-y-x}\text{P}_y\text{Bi}_x$ promising properties, such as the suppression of the CHSH Auger process for suitable Bi and P compositions, were predicted. Furthermore, $\text{GaAs}_{1-y-x}\text{P}_y\text{Bi}_x$ allows independent tuning of band gap and lattice constant over a wide range. Due to the fact that P atoms have a smaller covalent radius than As and Bi atoms, strain, introduced by Bi incorporation into the GaAs host matrix, can be compensated by the incorporation of P. That makes the quaternary alloy interesting for applications in the NIR spectrum, as for example 1 eV subcells for multi-junction solar cells, since it allows the deposition of lattice-matched, Bi containing alloys on GaAs in a certain range. The relation of band gap energy and spin-orbit splitting energy versus Bi content for different P contents is plotted in Figure 2.3 a and illustrates the behavior mentioned above (data adopted from¹⁸). The crossing point of band gap energy and spin-orbit splitting for the different P compositions is marked by black arrows. Figure 2.3 b shows the relation between Bi and P content and strain. The influence of Bi on the lattice constant and band gap is significantly stronger than the one of P.

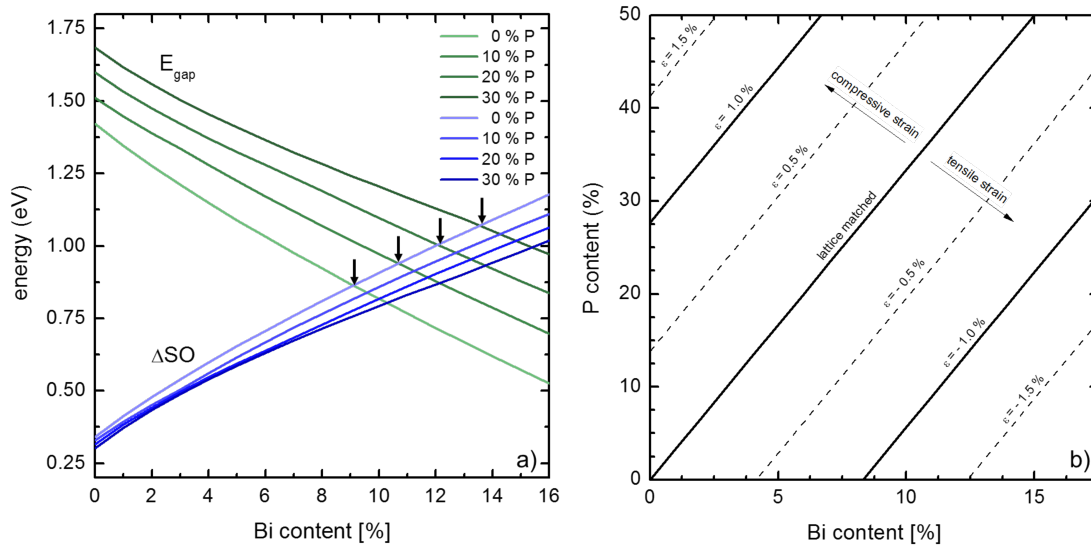


Figure 2.3: Band gap energy and distance of valence band to spin-orbit splitt-off band vs. Bi content is plotted in a). Crossing points of E_g and ΔSO are marked by black arrows. The data are inherited from¹⁸. In Figure b), the Bi content is plotted vs. the P content to illustrate the resulting strain of the deposited $\text{GaAs}_{1-y-x}\text{P}_y\text{Bi}_x$ layer for different material compositions. The data were calculated with equations and material parameters from section 2.2.

The theoretically possible or useful composition range of Ga(PAsBi) reaches from about 0 - 40 % P and up to 16 % Bi, as Ga(PAs) becomes an indirect semiconductor at about 45 % P content⁷⁰. Comprehensive analysis of MOVPE growth characteristics and the possible composition range that can be realized with MOVPE needed to be investigated.

The characterization and validation of theoretically calculated band gap parameters and structural properties will also be discussed in 3.2 and 6.2.4.

2.3.3 $\text{GaAs}_{1-x-y}\text{N}_y\text{Bi}_x$

The first MOVPE growth report on $\text{GaAs}_{1-y-x}\text{N}_y\text{Bi}_x$ was published by Z. Bushell et al. in 2015⁷¹, and many experimental^{11,47,72–75} and theoretical^{23,27,55,76–80} studies were published on this alloy. The strong band gap reduction due to combined VBAC and CBAC leads to a wide application range from NIR up to the MIR spectrum.

In particular, InP based $\text{In}_y\text{Ga}_{1-y}\text{As}_z\text{P}_{1-z}$ telecommunication lasers suffer from poor temperature stability and Auger recombination, which is further exacerbated at higher temperatures by carrier leakage due to electron overflow, caused by small conduction band offsets⁸¹. Indium gallium aluminum arsenide ($\text{In}_{1-x-y}\text{Ga}_y\text{Al}_x\text{As}$) on InP systems allow a reduction of electron overflow due to increased conduction band offset but still show strong losses from Auger recombination¹⁰. Newer dilute nitride GaAs based materials like $\text{Ga}_y\text{In}_{1-y}\text{As}_z\text{N}_{1-z}$ show better performance but suffer from large defect-related recombination and Auger recombination¹⁰. $\text{GaAs}_{1-y-x}\text{N}_y\text{Bi}_x$ would be a promising alternative, as a wide range of band gap energies with reduced strain could be realized by simultaneously achieving larger band offsets and suppressing troubling loss mechanisms¹⁰.

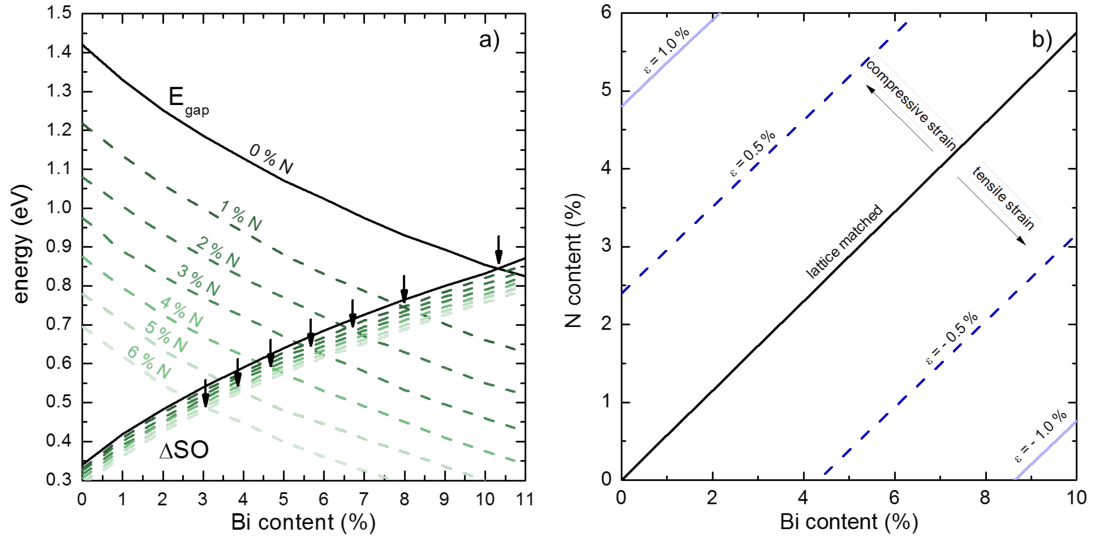


Figure 2.4: Band gap energy and distance of valence band to spin-orbit split-off band vs. Bi content, a). Crossing points of E_g and ΔSO are marked by black arrows. The data are inherited from¹⁰. In Figure b) the Bi content is plotted vs. the N content to illustrate the resulting strain of the deposited $\text{GaAs}_{1-y-x}\text{N}_y\text{Bi}_x$ layer for different material compositions. The data were calculated with equations and material parameters from section 2.2.

$\text{GaAs}_{1-y-x}\text{N}_y\text{Bi}_x$ on GaAs provides similar structural properties as $\text{GaAs}_{1-y-x}\text{P}_y\text{Bi}_x$. Nevertheless, N has an even smaller covalent radius than P, which makes the potential for compensation of compressive strain, introduced by Bi, even more effective. A significant difference from $\text{GaAs}_{1-y-x}\text{P}_y\text{Bi}_x$, however, lies in the behavior of the band structure, as band gap energy and spin-orbit splitting of dilute nitrides must be calculated using the anticrossing model. The disparity of dilute nitrides towards dilute bismides is that the nitride impurity level lies close to the conduction band edge of GaAs, instead of the valence band edge of GaAs, as is the case for Bi. Therefore both the VBAC model and the CBAC model need to be used in order to calculate the band structure of $\text{GaAs}_{1-y-x}\text{N}_y\text{Bi}_x$, which makes the theoretical studies of this alloy complex¹¹. Band gap and spin-orbit calculations for N concentrations up to 6 %, as well as strain calculations on GaAs, are shown in Figure 2.4; the values were adopted from¹⁰. The crossing points of E_{gap} and Δ_{SO} , from which points onwards Auger recombination is suppressed, are marked by black arrows. In this work, $\text{GaAs}_{1-y-x}\text{N}_y\text{Bi}_x$ was mainly investigated in direct comparison to $\text{GaAs}_{1-y-x}\text{P}_y\text{Bi}_x$ for research on the role of strain for the MOVPE growth of bismide containing III/V semiconductors. The results are discussed in detail in chapter 3.3.

2.3.4 $\text{GaP}_{1-x}\text{Bi}_x$

In contrast to the III-Bi-V materials discussed so far, $\text{GaP}_{1-x}\text{Bi}_x$ was deposited on GaP instead of GaAs. The material was considered to have the potential to open up the possibility of depositing laser material on Si, since it was already reported that GaP can be deposited nearly lattice matched on Si⁸²⁻⁹⁰. Similar to N in GaAs and GaP, Bi is an isoelectric impurity in GaP, which results in the formation of localized impurity states in the band structure of the host material⁹¹. Ga(NP) showed an efficient radiative recombination at room temperature and was used for early green light emitting diodes⁹². Therefore, deposition of $\text{GaP}_{1-x}\text{Bi}_x$ on GaP with Bi fractions of several percent of Bi was assumed to give further insights into structural and optoelectronic properties of III/V bismides. T. M. Christian et al. performed photoluminescence and Raman studies on MBE grown Ga(PBi) on GaP samples^{93,94} to investigate the electronic structure and local symmetry at bismuth incorporation sites. However, they incorporated only up to 1 % and 1.1 % Bi, respectively^{93,94}. $\text{GaP}_{1-x}\text{Bi}_x$ with significant concentration of Bi and especially MOVPE grown Ga(PBi) on GaP was not reported so far.

Different theoretical studies on the band structure of Ga(PBi) were published^{49,62,95-100}, and significant reduction of the band gap with increasing Bi incorporation was predicted. The density functional theory (DFT) calculations done by Polak et al. predict -67 meV/% Bi for the band gap and +99 meV/% Bi for the distance of spin-orbit energy to the valence band edge⁹⁵, while Samajdar et al. estimates -206 meV/% Bi for the band gap and +122 meV/% Bi for the distance of spin-orbit energy to the valence band edge using a 12 band $k \cdot p$ method⁹⁶. Also in the framework of the present work, a strong reduction of the band

gap with increasing Bi content was predicted and experimentally confirmed for the first time⁵³. Additionally, Z. Bushell et al. showed that the main features of the band gap of $\text{GaP}_{1-x}\text{Bi}_x$, as well as the evolution with increasing Bi content, is well described by the VBAC interaction between the extended states of the GaP valence band edge and highly localized bound impurity states associated with substitutional Bi impurities. Atomistic supercell calculations were used to analyze the changes to the Bi-induced development of the band edge energies, and to parametrize a suitable VBAC model⁵³. It was found that the primarily Bi-derived band lies energetically within the GaP band gap, approximately 120 meV above the valence band edge. This leads to a giant bowing of the band gap energy

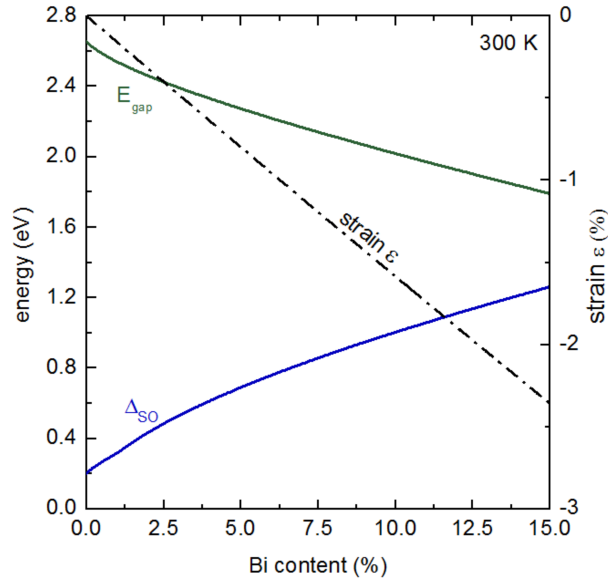


Figure 2.5: Band gap energy (green) and distance of valence band to spin-orbit split-off (blue) band vs. Bi content for Ga(PBi) on GaP at 300K. The dashed line shows the strain (right y axis) vs. Bi content. The data are plotted under consideration of the model described by Z. Bushell et al.⁵³.

and the spin-orbit splitting energy, which is depicted in Figure 2.5. However, a strong composition dependent bowing was observed, resulting in a declining decrease (increase) of the band gap (Δ_{SO}). The exact procedure of the band structure calculations for this new material can be found in⁵³. Further discussion of this material system will take place in chapter 3.4, where structural and optical properties will be explored in the context of the epitaxially grown $\text{GaP}_{1-x}\text{Bi}_x$ layers.

2.4 Experimental Methods

The following chapter will give an overview of the methods used and the workflow applied for **MOVPE deposition of new bismide containing III/V materials** and their characterization. Thereafter, the MS used for the development of an **MOVPE gas phase in-situ setup** will be described. Since the development of a connection between the MS and the MOVPE was a part of this work, (explained in chapter 4), only the MS itself will be discussed in section (2.4.5).

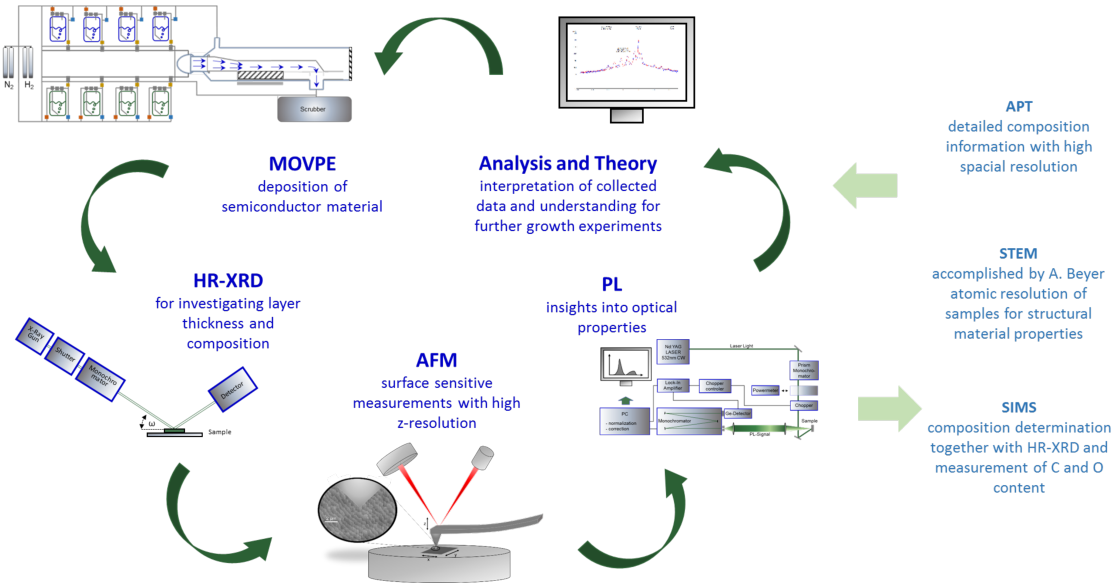


Figure 2.6: Depicted is the interplay of sample synthesis by MOVPE and the different characterization methods. The order and usage of the different methods could vary and was not the same for every sample. Scanning transmission electron microscopy (STEM), secondary ion mass spectrometry (SIMS), and atom probe tomography (APT) experiments are separated, since they were used only in specific cases and STEM as well as SIMS measurements were not directly part of this work.

Figure 2.6 illustrates the interplay of MOVPE growth and III/V semiconductor characterization methods. The order of the different experiments could be different from sample to sample, and not every characterization technique was applied to every deposited layer, depending on specific questions and the purpose of the grown sample. First of all, samples were deposited by MOVPE (2.4.1). The high resolution X-ray diffraction (HR-XRD) (2.4.2) and atomic force microscopy (AFM) measurements (2.4.3) enable first insights on the layer structure, composition, and surface quality of the deposited alloys. Thereafter, PL experiments (2.4.4) allowed insights into the optical properties of fabricated III-Bi-V semiconductors. Furthermore, STEM, SIMS, and APT experiments were used in particular cases. STEM investigations, performed by A. Beyer¹⁹ and J. Belz¹⁰¹, allowed atomic resolution of the bismide containing layers, as well as layer interfaces. SIMS investigations were outsourced to the *RTG Mikroanalyse GmbH* in Berlin. In particular, for the quaternary layers those experiments were essential as a second measurement for composition

determination. Additionally, O and C contents were determined by SIMS measurements. APT was used only for composition investigations and atom distribution determination with an atomic spatial resolution on special quaternary material samples. Discussing the STEM, SIMS, and APT methods would go beyond the scope of this work, but details can be found in ¹⁰²(STEM), ^{103–105}(SIMS) and ^{106,107}(APT). Finally, all collected data together helped to interpret the results of single experiments and allowed the development of MOVPE growth models and application of III/V materials with their properties.

2.4.1 Metalorganic Vapor Phase Epitaxy

MOVPE, or sometimes also referred to as organometallic vapor phase epitaxy (OMVPE), is a process that allows deposition of single crystal films on single crystal substrates from MO precursors on an industrial scale. Due to operation at non-equilibrium conditions, metastable materials such as III-Bi-V semiconductors can be deposited.

While first patents describing chemical vapor deposition processes are already from the 1880s (electric lamp production)¹⁰⁸ and early 1900s (CVD Si deposition)^{109,110}, the first modern MOVPE processes for III/V semiconductor growth (InP and GaAs) started in the 1960s^{111,112}. In our days MOVPE is an essential part of almost all processes for chip- and III/V semiconductor lasers as well as for LED fabrication.

All samples in this work were grown with an Aixtron AIX 200 with gas foil rotation. The system is located in a clean room and a glove box, flooded with N₂, is connected to the system, to prevent contamination during sample exchange. Purified N₂ gas is used to purge the system before sample exchange and maintenance work. The basic concept of MOVPE is that (in this case) H₂ carrier gas (purity of 10N) is used to transport ultra-pure MO precursors into a quartz glass reactor. Here, the MOs decompose, so that the metal part can connect to the surface of the substrate and ideally the hydrocarbon residues desorb fully and flow into the exhaust gas system. For this work, trimethylaluminum (TMAI), triethylgallium (TEGa), tritertiarybutylgallium (TTBGa), trimethylgallium (TMGa), trimethylindium (TMIn), 1,1-dimethylhydrazine (UDMH_y), ditertiarybutylarsanoamine (DTBAA), tertiarybutylphosphine (TBP), TBAs, triisopropylbismuth (TIPBi), tritertiarybutylbismuth (TTBBi), and trimethylbismuth (TMBi) were used. Figure 2.7 shows a simplified sketch of the experimental setup and the decomposition of the MOs, as well as the adsorption to the sample surface and desorption of hydrocarbon rest groups.

The setup consists of three parts. The gas mixing cabinet, the reactor chamber, and the exhaust gas system, passing subsequently into the scrubber. In the gas mixing cabinet, the MOs are stored in a temperature bath in stainless steel containers, called bubblers, to be prepared for the reactor chamber. By using the source MFC (Q_S), the push MFC (Q_P), and one PC (P_{PC}) for every bubbler, the partial pressure P_P of every substance in

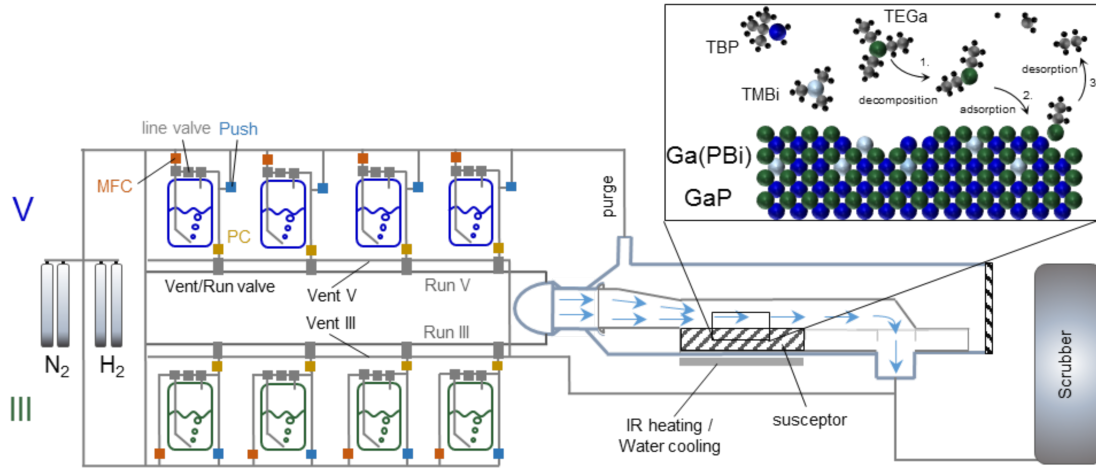


Figure 2.7: Simplified sketch of the setup. From left to right, the gas mixing cabinet with group III and group V MOs, the reactor system, and the scrubber. The system of mass flow controller (MFC)s, pressure controller (PC)s, and valves allows settings for exact partial pressures of all chemical species used. Run and vent lines pass the gas into the reactor or directly into the scrubber system. The sketch in the upper right corner shows a simplified microscopic zoom of the precursor decomposition at the growth surface of the sample.

the reactor can be set exactly, see equation 2.5.

$$P_P = \frac{Q_S}{Q_R} \cdot \frac{P_S}{P_{PC} - P_S} \cdot P_R, \quad (2.5)$$

where Q_R is the total flux through the reactor, P_S is the vapor pressure of the MOs at temperature T and bubbler pressure P_{PC} . P_R represents the reactor pressure. As soon as the line valve is opened, the carrier gas H_2 flows into the liquid phase of the MOs in the bubbler. The MOs saturated H_2 gas is then sucked out of the bubbler, will be further diluted with H_2 by the push MFC, passes the PC, and finally reaches the vent/run valve. The vent/run valve is responsible for deciding whether the MOs go into the reactor chamber or bypass directly into the scrubber. The vent/run system is necessary to allow a preflow of each precursor, without passing the gas into the reactor chamber, as soon as the line valve is opened. A pressure of 50 mbar was always used for deposition. An infrared (IR) heating system makes it possible to set temperatures between room temperature and 1000 °C, so that the MOs will thermally decompose above and at the sample surface. The sample lays on a rotating part of a graphite susceptor. The growth temperature is controlled by a thermocouple inside the susceptor, and the temperature factor between the sample temperature and the inner susceptor temperature was experimentally determined by observing the phase change of an Al-coated Si substrate.

While MBE¹¹³ allows lower growth temperatures favorable for Bi incorporation into III/V material, MOVPE requires certain temperatures for thermal decomposition of the precursors⁴⁵. However, MOVPE allows high quality semiconductor deposition without a supply of expensive ultra-high vacuum (UHV) conditions. This makes upscaling a

straight-forward process on the one hand, which is necessary when it comes to device production. On the other hand, growth under reduced pressure conditions makes the MOVPE growth process highly complex. To get further insights into this processes for the deposition of Bi containing materials at low MOVPE growth temperatures was also an aim of this work and will be discussed in chapters 3 and 4.

2.4.2 High Resolution X-Ray Diffraction

HR-XRD is a non-destructive method that uses X-rays to determine layer thicknesses and composition of crystalline materials on a microscopic scale. The fact that no sample preparation is needed makes this method a fast and important tool for direct feedback after MOVPE growth of semiconductor alloys.

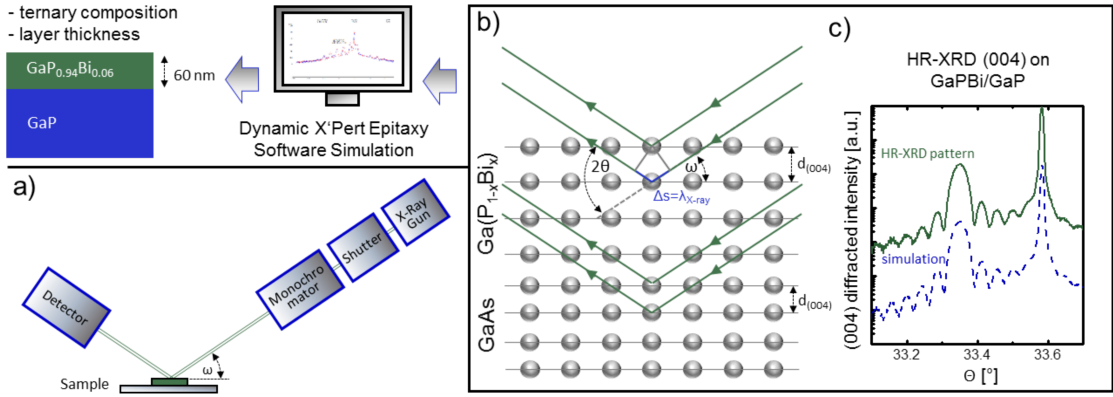


Figure 2.8: Simplified sketch of the HR-XRD setup and the measurement procedure. An HR-XRD pattern is recorded using setup a). The functional principle is depicted in part b), compare to equation 2.6. In part c) are shown a HR-XRD pattern and a fitting simulation, which demonstrate how the interplay of measurement and simulation lead to a determination of layer thickness and composition.

Figure 2.8 depicts the experimental setup and the functional principle of the HR-XRD $\omega/2\theta$ scans. For this work an instrument by PANalytical, type X'Pert Pro, was used. Figure 2.8 a) shows the setup of the X-ray gun ($\text{CuK}\alpha$ -line) with shutter and $4\text{xGe}[220]$ monochromator, which leads to a monochromatic incident X-ray beam with $\lambda = 1.54052 \text{ \AA}$, oriented to the sample at angle ω . The diffracted signal is analyzed by a detector, oriented at angle 2θ to the incident beam, see Figure 2.8 b). Due to the periodic distance between atoms in crystalline semiconductors, high energy monochromatic X-rays, with a wavelength λ in the order of the atom distances, can be used to determine the lattice parameter d_{hkl} , see Figure 2.8 b). Braggs law,

$$2d_{hkl}\sin\theta = n\lambda, \quad (2.6)$$

where $n \in \mathbb{N}$ is the order of diffraction, states constructive interference of the scattered X-rays at the lattice, if equation 2.6 is fulfilled. This means, that in addition to the substrate peak at θ_{Sub} , a second peak for the compressive (or tensile) strained layer occurs with $\theta_{layer} < \theta_{Sub}$ (or $\theta_{layer} > \theta_{Sub}$ for the tensile strained layer). Using equation 2.4 and using the kinematic theory of diffraction, the lattice constant a_L can be calculated:

$$-\Delta\theta \cdot \cot(\theta_{Sub}) = \frac{\Delta a_{\perp}}{a_{sub}} \quad (2.7)$$

where $\Delta\theta = \theta_{layer} - \theta_{Sub}$. This lattice constant leads to the composition of the deposited layer using Vegard's law (2.2). However, a distinct determination of the composition is only possible for ternary materials such as $\text{GaP}_{1-x}\text{Bi}_x$. For quaternary alloys, e.g. $\text{GaAs}_{1-y-x}\text{P}_y\text{Bi}_x$, a second method is necessary for composition determination, as infinite composition pairs lead to the same strain and therefore to the same peak position of θ_{layer} . For this work, SIMS and APT measurements were performed, see also 2.6. The exact procedure for composition determination of the quaternaries developed for this work is described in section 3.2.

Additionally, the layer thickness d_L can be measured, since the deposited layer structure itself can be considered a lattice and therefore also leads to constructive and destructive interferences. Therefore, the so called satellite fringes of the HR-XRD pattern (see Figure 2.8) and their distances $\Delta\theta_{Sat}$ must be analyzed using Bragg's law:

$$d_L = \frac{\lambda}{2\cos(\theta_{Sub})\Delta\theta_{Sat}} \quad (2.8)$$

Figure 2.8 c) shows an HR-XRD pattern and the fitting simulation (*X'Pert Epitaxy* by *PANalytical*) for a $\text{GaAs}_{1-x}\text{Bi}_x$ bulk structure on GaAs.

2.4.3 Atomic Force Microscopy

AFM is a surface sensitive method under atmospheric conditions that uses Van der Waals and Coulomb interactions between a scanning tip and a sample surface to determine topographic information. Thereby, sub nm resolution is obtained for the vertical axes, whereas the size of the sampled area in x and y direction (surface plane) is in the order of μm , due to finite width of the tip. For this work, a *Digital Instruments MultiMode SPM* was used, operating in tapping mode at constant height. Figure 2.9 shows a simplified depiction of the functional principle.

A sharp tip (radius is around 300 nm) oscillating at a cantilever with its eigenfrequency along the z axis, scans the surface of a sample in x and y direction (movement of the stage) using piezo crystals. Figure 2.9 shows the system consisting of a laser, a four zone photo diode, and mirrors. Thereby, the oscillation and even smallest deviations from the eigenfrequency (caused by changes of the Coulomb - and Van der Waals forces between the sample and the tip, due to variation of their distance, when the topography of the

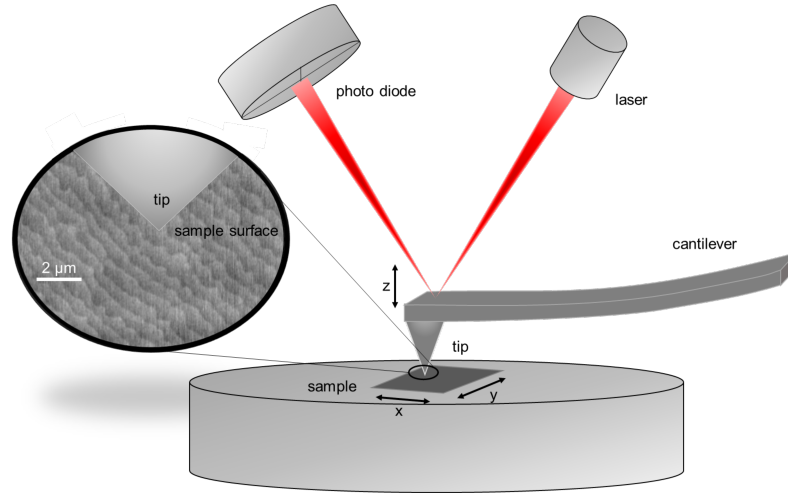


Figure 2.9: Simplified sketch of an AFM setup. A sharp tip oscillating in z direction at a cantilever with its eigenfrequency scans the surface of a sample in x and y direction.

sample changes) are observed. The images were post processed to correct the spherical movement of the piezo crystals using the software packages *Gwyddion* and *NanoScope* (*Digital Instruments*).

2.4.4 Photoluminescence Spectroscopy

PL was used to characterize the samples with respect to their optical properties. PL experiments give information on band gap and defect levels of the deposited layers. Therefore, laser light is used, with an energy higher than the band gap of the investigated material. A photon $h \cdot \nu = E_{laser}$ is used to excite an electron from the valence band into the conduction band so that a hole remains in the valence band, and an electron hole pair is formed. The electron then relaxes to the conduction band edge minimum and recombines with the hole at the valence band edge maximum. Thereby a photon with the energy around the band gap of the semiconductor $h \cdot \nu = E_{gap}$ is emitted, see right hand side of Figure 2.10. By detecting the photons caused by those recombination processes, the band gap can be investigated. Furthermore, the comparison of different PL measurement can give first information on the density of deep level trap states, which can act as non-radiative recombination centers and decrease the optical performance of semiconductor devices.

Figure 2.10 illustrates the setup used for this work. A water cooled, frequency-doubled Nd:YAG laser by *Laser Quantum* was used in CW mode. Several lenses and mirrors guided the beam through a prism monochromator, which selected the 532 nm line, onto the sample. After filtering the reflected laser light with a *RG550*-filter, the generated photons were focused by lenses into a monochromator (*THR 1000*, *Jobin-Yvon*) and were detected by a Ge-Detector by *Applied Detector Corporation (ADC)*, model (*403L*). A lock-in amplifier (*SR510* - *Stanford Research Systems*), connected to a chopper, improved

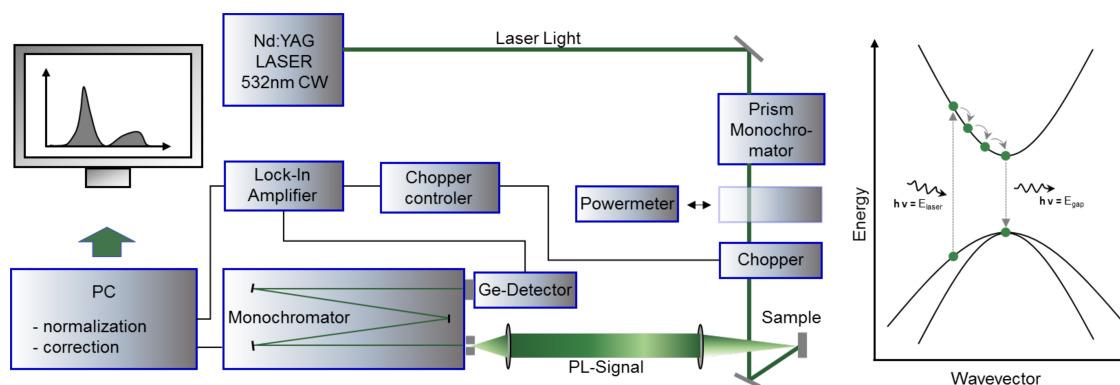


Figure 2.10: Sketch of the experimental setup for PL measurements. A frequency-doubled Nd:YAG laser with 532nm in continuous wave (CW) operation with a prism monochromator are used to excite electrons in the analyzed sample. A monochromator and a Ge-Detector measured the resulting PL signal wavelength dependent. A lock-in amplifier, connected to a chopper, improve the signal-to-noise ratio of the PL signal. A normalized and corrected spectrum of the PL signal against the wavelength is obtained.

the signal-to-noise ratio of the PL emission, before the signal was post processed by a self written software (LabVIEW - National Instruments). Finally, normalized and corrected spectra were obtained using a calibration spectrum.

2.4.5 Mass Spectrometry

Mass spectrometry is a widely used analytical technique to identify and measure the composition of chemical species by ionizing the analyte and separating the ions, regarding their mass to charge ratio. As a result a mass spectrum is plotted, which is a function of the abundance of ions as a function of their mass-to-charge ratio. For this work a newly developed prototype of a 3D ion trap based MS was used. This section will first introduce mass spectrometry in general and then discuss the new prototype in detail.

The beginnings of mass spectrometry started in 1898 with Wilhelm Wien's studies of canal rays, deflecting them with electric and magnetic fields^{114,115}. From the first MSs, built by J. J. Thomson in the early 1900s, until today, a wide field of different MS techniques were developed for many different applications in biology, chemistry, physics, and medicine. The most commonly used MSs are *Sector MSs*, *time-of-flight MSs*, *quadrupole mass analyzers*, and *ion trap based MSs*. All different kinds of MSs consist of an ionization unit, a mechanism to separate the ionized particles, and a detector to determine the abundance of the different separated ions in common. Initially, the analyte needs to be evaporated, if it is not already present in its gaseous state. Thereafter, the gaseous analyte will be ionized. Various techniques are available for ionization, and which ionization technique should be used depends on the type of analyte and purpose of the measurement. The electron ionization (EI) is the most commonly used technique. Here an electron beam with an energy of 70 eV is utilized to split one (or sometimes more) electrons from the

analyte atoms or molecules¹¹⁶. After the analyte was ionized, the ions will be separated according to their mass-to-charge ratio. Many different approaches are available for the process of separation, as well. The most commonly used techniques for mass separation are time-of-flight analyzers, sector mass instruments, linear quadrupole analyzers, orbitrap analyzers, and 3D ion traps¹¹⁷. The disadvantage for most of these techniques is that only the signal of one mass at a time can be analyzed, that means the recording of a mass range is time-consuming and makes measurements of spectra on a short time scale (in the range of seconds) challenging. For the detection itself different detector types, such as a photomultiplier, a micro-channel plate, or a channel electron multiplier, can be used¹¹⁷. The approach for mass separation and detection of the mass spectrometer used for this work is different in the way that separation and detection are performed in one step, which will be described in detail below.

The Fourier-Transform quadrupole ion trap based MS prototype was developed and provided by *Carl Zeiss SMT GmbH*. Originally evolved for the detection of photoresist residues during photolithography processes, this MS enables real-time measurements and a sub-pptV (parts per trillion by volume) detection under optimized conditions. The main part of the new instrument is a quadrupole ion trap (QIT), depicted in Figure 2.11. QITs, also called Paul traps¹¹⁸ (in honor of the inventor Wolfgang Paul), use dynamic electric fields to trap charged particles, represented by the green and blue dots in Figure 2.11. The QIT setup consist of one ring electrode and two hyperbolic end cap electrodes. An

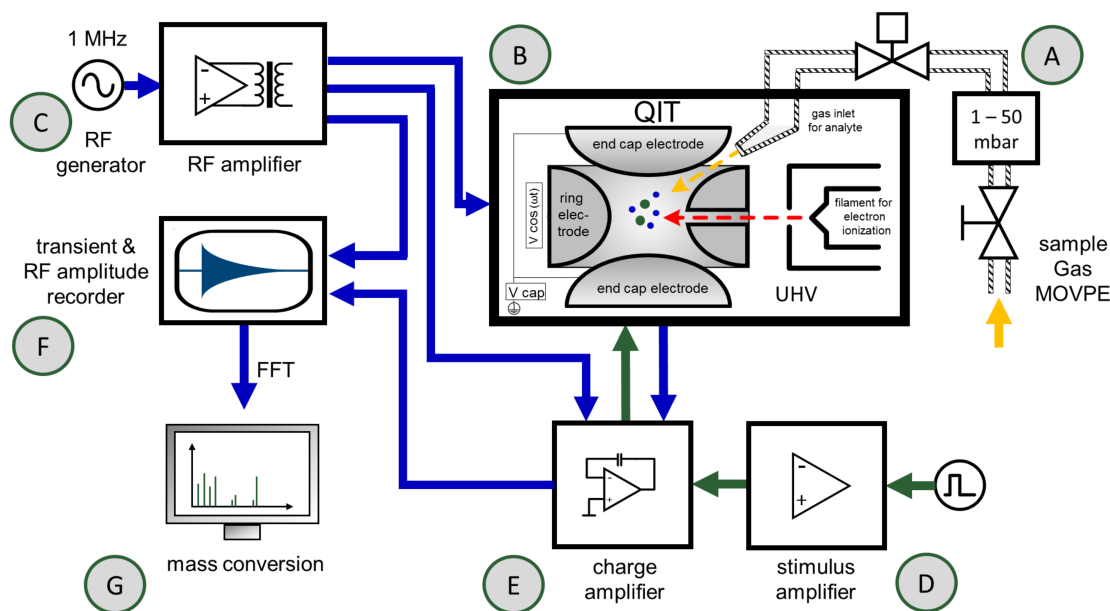


Figure 2.11: Simplified sketch of the functional principle of the MS *iTrap*, developed and provided by *Carl Zeiss SMT GmbH*. Green arrows represent the stimulation of the ions, while blue arrows mark measured and post processed signals, including the radio frequency for ion storage. Output is a mass spectrum (intensity vs mass).

AC radio frequency (RF) voltage oscillates between the two end cap electrodes, and a

driving AC voltage is applied to the ring electrode, see Figure 2.11. Those voltages force the ions to move up and down (end cap electrodes) and radially (ring electrode). The motion of the ions in the electric field is mathematically described by solutions of the *Mathieu equations*^{118,119}. The QIT is located in a stainless steel UHV process chamber (B in Figure 2.11), which is directly connected to a turbo pump (not shown), which provides a UHV better than $1 \cdot 10^{-8}$ mbar. The UHV is necessary to enable sub-pptV detection of analyte species. Higher pressures in the measurement chamber would disturb the measurement, as ions and molecules from the measurement chamber itself are ionized and stored as well. A tungsten filament provides electrons for EI. Furthermore, the QIT is directly connected to an RF amplifier (C), which amplifies the generated RF voltage for storage of the ionized analyte. A stimulus amplifier makes it possible to stimulate the trapped ions (D). Thereafter, using a charge amplifier (E) and a highly sophisticated signal compensation concept with selective ion excitation techniques enables the detection of the image current in the QIT induced by the oscillating ions. As the ions or molecules in the trap have different masses, their resonance behavior after the stimulus will be different. However, the end cap electrodes detect the image current of the overlay of all the different resonances. Hence, a fast fourier transformation (FFT) is necessary to transform the measured transient into all the single eigenfrequencies of the different ions and molecules (G). Calculations then allow the conversion from frequencies to masses.

Since the instrument used is a prototype, the measurement procedure with all parameters needed to be analyzed and understood. Therefore, an overview about the measurement procedure is shown in Figure 2.12. Beginning with the inlet of the analyte gas into the

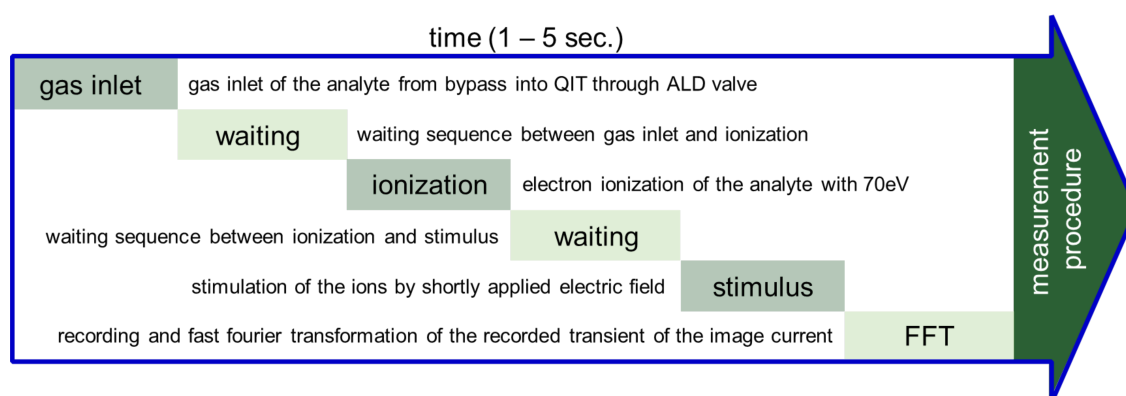


Figure 2.12: Illustration of the measurement procedure. Starting with gas inlet into the measurement chamber, first the vacuum needs to stabilize before the analyte left will be ionized. After ionization and another waiting sequence, the ionized analyte will be stimulated and the resulting electric field of the ions will be measured. The recorded transient then is fast fourier transformed, which leads to the corresponding mass spectrum.

stainless steel chamber, the analyte is ionized after some ms (waiting time), which is necessary for the vacuum to stabilize again, so that the right amount of analyte to be ionized is reached. If the ionization process starts too early, too much analyte is trapped in the RF field, and no clear transient of the stimulated ions can be recorded. If the ionization

starts too late, not enough ions of the chemical species are stored, which again makes the analyzation of the corresponding mass spectrum difficult. The time of the ionization process itself is also important, since it is responsible for the number of ions. Furthermore, the interaction between the analyte molecules and the electron beam changes the structure of the molecules themselves, which makes a fine adjustment important. Another waiting sequence between the ionization and the stimulation gives the ionized molecules time to *repair* the damage caused by the ionization process¹¹⁶. But also structural and chemical changes can occur if this waiting sequence is too long. Finally, the stimulus is applied in order to record the electric image current of the stimulated ions. The recorded transient of this induced image current is transformed using a FFT, and the resulting spectrum of frequencies is calculated into a mass spectrum, see Figure 2.11. This procedure, described and depicted (2.12) above, illustrates how relevant every single parameter is and underlines the importance of careful parameter adjustment.

Since the comprehension of the different parameters of the recently developed mass spectrometer, their influence on the measurement, and especially their influence on each other were the subjects of this work, further discussion will take place in chapter 4.1.

CHAPTER 3

Dilute Bi Containing III/V Semiconductors

This chapter covers the results of the development and characterization of bismide containing III/V semiconductors. The exploitation of alternative Bi and Ga precursors and their influence on the growth surface will be discussed in section 3.1. Sections 3.2 and 3.3 will deal with the growth and characterization of quaternary bismides. Section 3.2 focuses on the question of whether $\text{GaAs}_{1-y-x}\text{P}_y\text{Bi}_x$ on GaAs is a suitable alloy for solar cell applications, while section 3.3 aims to unveil the role of strain for the limitation of Bi incorporation in III/Vs, which was investigated by growing and comparing $\text{GaAs}_{1-y-x}\text{P}_y\text{Bi}_x$ and $\text{GaAs}_{1-y-x}\text{N}_y\text{Bi}_x$ on GaAs. Furthermore, in section 3.4, the deposition of $\text{GaP}_{1-x}\text{Bi}_x$ on GaP and GaP on Si will be discussed, considering the material as a candidate for optoelectronic applications on Si. Finally, the recent achievements made on the deposition of $\text{GaAs}_{1-x}\text{Bi}_x$ lasers on GaAs will be covered in section 3.5.

3.1 $\text{GaAs}_{1-x}\text{Bi}_x$ MOVPE with Alternative Bi and Ga Precursors

In order to understand the influence and role of hydrocarbon residues on the growth chemistry, different MO Ga and Bi precursors were used to deposit GaAs and $\text{GaAs}_{1-x}\text{Bi}_x$ layers. More precisely, the behavior of the growth rate and the Bi incorporation for growth with various precursors with different hydrocarbon groups was of interest. It was investigated if and how the growth characteristics change, due to a changed surface availability caused by different hydrocarbon groups at the growth surface. Furthermore, the question of chemical interactions of the different precursors during decomposition and at the surface was also part of the investigation.

$\text{GaAs}_{1-x}\text{Bi}_x$ and GaAs growth between 350 °C and 625 °C, with three different Bi precursors, TIPBi, TTBBi and TMBi, and two different Ga precursors, TEGa and TTBGa, was performed. As already reported in previous studies^{9,64,65,120}, the growth rate decreases with increasing TMBi supply. Simultaneously, the Bi incorporation increases up to a certain saturation level, which depends on growth temperature, group III supply, and TBAs/TEGa ratio. In contrast to the initial hypothesis, the experiments of this work also

showed the same behavior for the growth with TIPBi and TTBBi as well¹⁷. For all three Bi precursors, the Bi incorporation increases and the growth rate decreases with increasing Bi supply (Figure 6, section 6.2.5). Even the saturation level and the level of the decrease of the growth rate were almost identical at this growth temperature for all precursors used. That means that the original idea that the Bi incorporation and the growth rate should be higher when using the alternative precursors TIPBi and TTBBi, due to a higher decomposition efficiency at low temperatures and no methyl groups that block the growth surface, was not confirmed⁶⁵. However, this makes it possible to make important conclusions about the growth behavior. First, it means that (for the case of $\text{GaAs}_{1-x}\text{Bi}_x$ at the given growth temperature) the methyl groups in particular are not responsible for the limited Bi incorporation. The fact that the decrease of the growth rate is the same for all three precursors used also indicates that, most likely, not even the hydrocarbon groups (coming from the Bi precursors) in general are **the** limiting factor at those growth temperatures, which does not mean that they do not have an influence on the surface chemistry, which could be an important factor at even lower growth temperatures, where a higher decomposition efficiency becomes important. Furthermore, the independence of the Bi incorporation limit from the Bi source shows that surface processes, like formation of Bi surface reconstructions, which are not related to the type of hydrocarbon residues on the growth surface, are fundamental to understanding the growth process. Those reconstructions and their formation are currently under investigation.

The comparison of the growth with different Ga precursors was not only important because of the different hydrocarbon residues, which could have a different influence on the growth surface, but also because of the fact that the group III supply is growth limiting. Therefore, using a precursor with a higher decomposition efficiency¹²¹ at the low growth temperatures used could lead to a higher group III supply and therefore to a higher growth rate, by simultaneously keeping the precursor consumption constant. Hence, the $\text{GaAs}_{1-x}\text{Bi}_x$ growth using TEGa and TTBGa was compared. However, results¹⁷ of these experiments showed a significantly lower growth rate for the growth with TTBGa than for TEGa (Figure 6, section 6.2.5). Additionally, the Bi incorporation drops earlier, when the TBAs/Ga-source ratio is increased. This indicates that in addition to possible gas phase reactions, the tertiarybutyl groups, coming from TBAs and TTBGa, suppress the growth rate. This behavior can be ascribed to the larger size of the tertiarybutyl groups combined with the relatively low growth temperatures. The number and size of the tertiarybutyl groups using TTBGa instead of TEGa leads to a blocking of the growth front or makes adhesion more difficult and therefore leads to a decrease of the growth rate, even if the decomposition efficiency of TTBGa is higher than the one of TEGa at 400 °C^{17,121}.

Also a comparison of unintentional C incorporation, which is a crucial point when growing at low temperatures, was performed for growth with all different precursors. All three Bi sources showed the same low C incorporation. This is remarkable when one considers that an industry grade TMBi precursor is compared to self synthesized TIPBi

and TTBBi, and underlines the efficiency of the Bi surfactant effect²⁹. The growth of TTBGa compared to TEGa showed a significantly reduced C incorporation by an order of magnitude (for TTBGa). This underlines again the importance of research for alternative precursors, as the trend leads to lower growth temperatures for many material systems⁶⁴.

The results of the MOVPE growth of GaAs_{1-x}Bi_x layers discussed above showed how crucial a more detailed understanding of the growth chemistry is. In order to understand and overcome the limitations of this material system, further experiments must be done in order to finally be able to grow device-quality material with Bi contents above 10 %. Therefore, an experiment for in-situ gas phase investigations was developed, which will be discussed in chapter 4.

3.2 Quaternary GaAs_{1-x-y}P_yBi_x for Solar Cell and Laser Applications

The main motivation for growing GaAs_{1-y-x}P_yBi_x was the intention to realize a lattice matched alloy for optoelectronic applications on GaAs, as for example 1 eV sub cells for multi-junction solar cells. Therefore, it was investigated if high quality GaAs_{1-y-x}P_yBi_x can be deposited using MOVPE, as well as its structural and optical properties.

Due to a low decomposition efficiency of TBP at 400 °C ($T_{50}=475-500$ °C), gallium arsenide phosphide (GaAs_{1-y}P_y) layers have been deposited first, in order to verify if the growth at those temperatures is even possible. Results of these growth experiments showed a surprisingly high P incorporation efficiency of about 30 %¹⁸. Furthermore, it was observed that a TBAs/TEGa ratio of one is ideal, since for the higher TBAs/TEGa of two, an extremely high TBP partial pressure (three times higher) is necessary to incorporate the same amount of P. After deposition of GaAs_{1-y}P_y with P fractions up to 35 %, GaAs_{1-y-x}P_yBi_x structures were deposited.

Before interpreting the results of the growth, it is important to discuss the composition determination process of quaternary materials, as already mentioned in chapter 2.4.2. (004) HR-XRD experiments alone do not provide enough information for a distinct composition determination, since the composition of the group V lattice sites can be simulated with an infinite number of pairs of values. In order to determine distinct composition information of the quaternary layers, HR-XRD and SIMS measurements were used. By growing a specific layer structure, depicted in Figure 3.1 a), the P (or N) and Bi counts per second of the ternary layers of the SIMS analysis were correlated to the peak position of the HR-XRD diffraction pattern, Figure 3.1 b). Thereby, the ratio of counts per second and volume fractions of P (or N) and Bi were determined. This procedure allowed the conversion from P and Bi counts of the SIMS measurements to a P and Bi fraction in %, see Figure 3.1 c). APT investigations (not shown here) on some of the samples showed good agreement with the data obtained from the procedure described above.

When summarizing the growth experiments, it was observed that the Bi incorporation into GaAs_{1-x-y}P_yBi_x increases into a saturation level with increasing TMBi supply, which

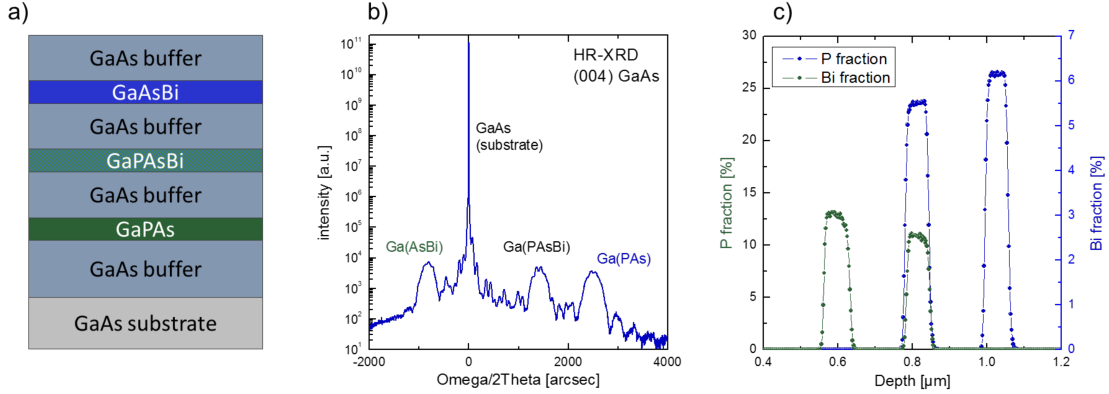


Figure 3.1: Illustration of the composition determination process for quaternary alloys, using HR-XRD (b) and SIMS (c), applied on the layer structure (a).

confirms the results of present literature^{17,65,122,123}. However, it was also examined that the Bi fraction limit can be shifted upwards to higher Bi fractions in the saturation region by increasing the P incorporation (see Figure 3, section 6.2.4). This observation is underlined by the fact that the formation of droplets at the surface can also be suppressed by increasing the P fraction when growing in the saturation region¹⁸. This behavior can be explained by the fact that P atoms compensate the local strain of Bi atoms in the GaAs host lattice. That means that the Bi incorporation is not only limited by metastability and surface chemistry, but that also the strain has to be taken into account. The strain compensation, using group V atoms with a smaller covalent radius, was further investigated and will be discussed in section 3.3. Studies on the structural quality of $\text{GaAs}_{1-y-x}\text{P}_y\text{Bi}_x$ showed excellent material quality with a homogeneous chemical distribution, as long as the TMBi supply was below or at the border of the saturation region.

Additionally, it was possible to observe the first PL activity of $\text{GaAs}_{1-y-x}\text{P}_y\text{Bi}_x$ (see Figure 6, section 6.2.4). A broad distinct double s-shape of the PL maximum at higher temperatures implies band edge PL of the $\text{GaAs}_{1-y-x}\text{P}_y\text{Bi}_x$ layer. The determined value of the band gap for both samples measured agreed with the calculated values. It can be concluded that optical activity of $\text{GaAs}_{1-y-x}\text{P}_y\text{Bi}_x$ on GaAs and agreement with calculated values was successfully demonstrated. However, further experiments should be done to improve the material quality necessary to achieve material for high performance device quality.

3.3 The Influence of Strain on the Bi Incorporation Limit

As already mentioned in chapters 3.1 and 3.2, the incorporation of significant amounts of Bi still remains a challenge. In order to verify the influence of local strain introduced by Bi, the MOVPE growth of $\text{GaAs}_{1-y-x}\text{N}_y\text{Bi}_x$, $\text{GaAs}_{1-y-x}\text{P}_y\text{Bi}_x$, and $\text{GaAs}_{1-x}\text{Bi}_x$ structures

at low growth temperatures of 400 °C was compared. The comparison of the growth of two different quaternary materials with two different group V atoms (N and P, both with a smaller covalent radius than As) with GaAs_{1-x}Bi_x could unveil the influence of strain on the limitation of Bi incorporation. A positive effect on the Bi incorporation limit was already observed while introducing P while growing GaAs_{1-y-x}P_yBi_x (section 3.2), but the exact mechanism needs to be verified by comparison with a second quaternary system⁵².

All compositions of quaternary compounds were determined using the method introduced in chapter 3.2. GaAs_{1-x}Bi_x, GaAs_{1-y-x}P_yBi_x and GaAs_{1-y-x}N_yBi_x layers were deposited under the same growth conditions, using a growth temperature of 400 °C and the same group III supply. To determine if the N atoms in GaAs_{1-y-x}N_yBi_x would have the same effect on the Bi saturation level as P in GaAs_{1-y-x}P_yBi_x, the Bi incorporation in quaternary GaAs_{1-y-x}N_yBi_x and GaAs_{1-y-x}P_yBi_x was plotted versus the tensile strain from N and P in ternaries GaAs_{1-y}P_y and gallium arsenide nitride (GaAs_{1-y}N_y). The results observed were significant. In both cases, for GaAs_{1-y-x}N_yBi_x and GaAs_{1-y-x}P_yBi_x, a given strain compensation by the smaller group V atoms led to the same increase in Bi incorporation. The Bi saturation level increased linearly with increasing P or N content (see Figure 3, section 6.2.3). Those results indicated that the strain is in fact a crucial parameter for the limitation of Bi incorporation. However, it is important to mention that the Bi fraction was only increased in the region of Bi saturation, where surplus Bi was available¹²⁴. Below the saturation region, almost all of the Bi supplied was incorporated anyway; hence no effect of the P or N could be observed, except for a slight decrease of the Bi fraction due to a significant change of the gas phase (high TBP or UDMHy fluxes). The influence of the Bi surface coverage on the incorporation of P and N was also investigated (see Figure 4 and 5, section 6.2.3). Analysis of the characterization of the deposited samples showed a linear decrease of P or N incorporation with increasing TMBi supply. This result was expected, since the Bi surface coverage has a positive surfactant effect, which suppresses carbon incorporation and improves device properties, but it also blocks the surface for other species, which are trying to connect to the growth surface.

Summarizing, it can be concluded that the assumption that strain is a very important factor on the limitation of Bi incorporation was proved. This is an interesting result, which might also open up ways to strain-engineer the Bi incorporation into III/V materials in the future.

3.4 GaP_{1-x}Bi_x on GaP and GaP on Si

GaP_{1-x}Bi_x on GaP could be a promising candidate for optoelectronic applications on Si, but has not been deposited by MOVPE so far. Hence, suitable growth conditions for this highly metastable material had to be found. Optimum growth conditions were observed to be at around 400 °C growth temperature, and a relatively high group III

supply of $25.5 \mu\text{mol}/\text{min}$. Before optoelectronic characterization, the MOVPE growth characteristics and the structural quality were systematically investigated (see Figure 3, section 6.2.2). The TMBi supply, the TBP/TEGa ratio, the growth temperature, and the TEGa flux were varied, and Bi incorporation as well as growth rate were determined by HR-XRD. The results showed an increasing Bi fraction up to a certain saturation level, when TMBi supply is increased. This behavior has already been reported for $\text{GaAs}_{1-x}\text{Bi}_x$ and $\text{GaAs}_{1-y-x}\text{P}_y\text{Bi}_x$. However, the Bi incorporation limit was significantly higher for $\text{GaP}_{1-x}\text{Bi}_x$ than for $\text{GaAs}_{1-x}\text{Bi}_x$. This was unexpected, since the lattice mismatch of $\text{GaP}_{1-x}\text{Bi}_x$ to GaP per percent Bi is much larger than the one for $\text{GaAs}_{1-x}\text{Bi}_x$ on GaAs, which indicates that the surface chemistry is a crucial point when growing $\text{GaP}_{1-x}\text{Bi}_x$. A catalytical reaction between TB(P) and TM(Bi) species seemed to be responsible for the surprisingly high Bi incorporation, as a doubling of the TBP/TEGa ratio led to a Bi incorporation in the saturation region higher by 25 %. This idea was underlined by the fact that the growth rate was stable for the higher TBP/TEGa ratio, while the Bi incorporation decreased drastically at higher TMBi supplies for the lower TBP/TMBi ratio. Also temperature and group III supply variation underlined the importance of an interaction between TB(P) and TM(Bi). Hence, gas phase investigations are planned and currently under investigation, in order to understand the interaction between those species. A detailed description and interpretation of the growth characteristics observed can be found in¹⁹. Additionally, the possibility of depositing $\text{GaP}_{1-x}\text{Bi}_x$ structures on GaP on Si was explored, and the material could be successfully grown with similar properties and Bi contents compared to the growth on GaP substrates.

Also the structural quality was analyzed by using STEM (see Figure 5, section 6.2.2). All interfaces deposited below the saturation region showed sharp interfaces and a good chemical homogeneity, which would be necessary for utilization for optoelectronic applications¹⁹. Furthermore, STEM analysis showed that $\text{GaP}_{1-x}\text{Bi}_x$ structures provide excellent properties for investigations of various electron microscopy methods and effects, as the Z-contrast of P and Bi is large. Belz et al. investigated the influence of column occupancy and static atomic disorder on the analysis of chemical ordering in $\text{GaP}_{1-x}\text{Bi}_x$ ¹⁰¹. They showed that the effects of z-position, static atomic disorder, and column crosstalk are important when considering atomic ordering analysis in $\text{GaP}_{1-x}\text{Bi}_x$ using STEM. This becomes important when acquiring an accurate distribution model for Bi in GaP. Moreover, in collaboration with Christopher Broderick^{53,62} and Zoe Bushell^{53,125}, the deposited $\text{GaP}_{1-x}\text{Bi}_x$ structures were analyzed theoretically and experimentally, by using spectroscopic ellipsometry, see sections 6.2.7 and 6.2.6. Thereby, it was found that the material is unlikely to lead to efficient light emitters, since even with significant amounts of Bi, the band gap remains indirect and the material suffers from a breakdown of band edge Bloch character due to short-range alloy disorder. This was underlined by the fact that despite excellent crystal quality, no PL nor photorefectance (PR) activity could be observed. However, the ellipsometry experiments confirmed the theoretical calculations,

which predicted the strongest band gap reduction and largest increase of the spin-orbit energy observed for a III/V material so far⁵³. This makes the material interesting from a theoretical point of view, since this is the first time the impurity states, caused by Bi, were found to be located in the band gap of the host material⁵³.

3.5 Progress on GaAs_{1-x}Bi_x Lasers

P. Ludewig et al. published on the first electrically pumped GaAs_{1-x}Bi_x laser in 2013⁶⁶. Furthermore, GaAs_{1-x}Bi_x edge-emitters grown by MOVPE with Bi fractions up to 4.4 % have been reported⁶⁷. Recently, Marko and Sweeney published on the progress toward GaAs_{1-x}Bi_x lasers and provided a good overview of the current situation of III-Bi-V laser devices⁶⁸. A hybrid structure with 6 % Bi deposited using MOVPE (for cladding- and separate confinement hetero (SCH) structure) and MBE (GaAs_{1-x}Bi_x QW) was successfully developed and showed room temperature lasing¹²⁶. However, MOVPE grown GaAs_{1-x}Bi_x lasers with room temperature lasing are still limited to 2.5 % Bi^{6,68,69}. The challenge regarding those laser structures is to maintain the balance between incorporation of sufficient amounts of Bi and simultaneously ensure a high crystal quality to enable laser operation. Additionally, the design of SCH structures as well as the cladding is crucial to enable room temperature lasing of those devices^{66,69}.

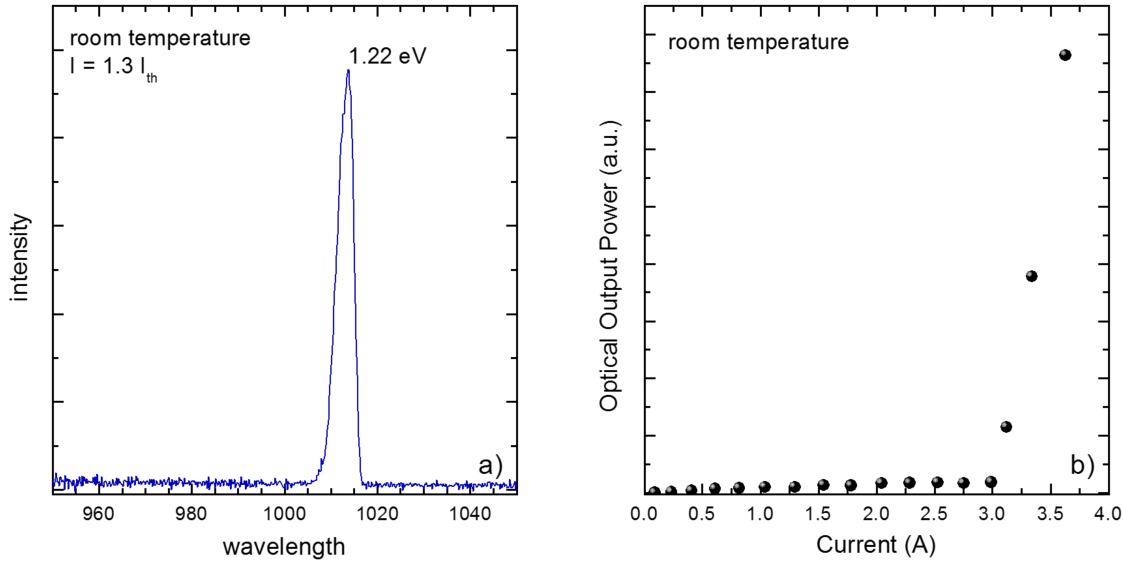


Figure 3.2: Lasermode and L-I curve for a 50 x 2060 μm GaAs_{1-x}Bi_x/aluminum gallium arsenide (Al_yGa_{1-y}As) SQW laser diode at room temperature.

Starting from the experience with the structures published previously^{66,67} and the knowledge obtained through the present work, further developed GaAs_{1-x}Bi_x laser structures were deposited, processed, and measured. The SCH was optimized in the way that the Al_{0.2}Ga_{0.8}As layers (or GaAs layers, respectively) around the GaAs_{1-x}Bi_x⁶⁶ QW were

exchanged by $\text{Al}_{0.12}\text{Ga}_{0.88}\text{As}$ layers. Thereby, the band offsets between $\text{GaAs}_{1-x}\text{Bi}_x$ QW and the $\text{Al}_y\text{Ga}_{1-y}\text{As}$ layers and the electrical confinement were improved. Furthermore, a new $\text{GaAs}_{1-x}\text{Bi}_x$ test sample was chosen as a starting point and a new test structure series was grown for optimizing the Bi incorporation, interface quality, and chemical homogeneity. The results of the characterization of the deposited laser structures are shown in Figure 3.2. The characterization of the laser diode showed room temperature lasing at 1015 nm (Figure 3.2 a). The threshold current (I_{th}) was measured to be 2.96 kA/cm^2 (Figure 3.2 b). Regarding future optimization, it was found that the Bi preflow before $\text{GaAs}_{1-x}\text{Bi}_x$ QW deposition needs to be longer in order to realize a higher Bi incorporation as well as to improve the interface between GaAs and $\text{GaAs}_{1-x}\text{Bi}_x$. Moreover, the doping in the p- and n-contact needs to be optimized. The device discussed here, as well as further laser devices, are still under investigation and the results will be published separately after additional optimization.

CHAPTER 4

MOVPE In-Situ Gas Phase Analysis

This chapter covers the development of a mass spectrometer setup on a MOVPE system, using a MS prototype (iTrap), provided and invented by *Carl Zeiss SMT GmbH*. The first challenge was the implementation of the MS in the MOVPE system (see section 4.1). Subsequently, the optimization of MS performance and its parameters for gas phase investigations was accomplished, which allowed the first proof of concept, the thermal decomposition analysis of TBAs (see section 4.2).

4.1 Quadrupole Ion Trap Based Mass Spectrometer Setup on a MOVPE System

First MOVPE gas phase investigations using MS started in the late 1980s, when alternative group V precursors such as TBAs and TBP were developed. Due to the toxicity of the MOs and the sensitivity of the MOVPE process, gas phase analysis of decomposition processes are highly complex^{127,128}. Many different approaches for gas phase investigations on MOVPE systems were tested in previous experiments^{129–139}. Advantages and disadvantages of the previous experiments are discussed in detail in chapter 6.2.1. The first aim of building a setup for in-situ gas phase investigations was to maintain the balance between transferring the analyte as unmodified as possible from the reactor chamber into the MS and simultaneously not influencing the MOVPE process itself too much. The final approach, realized after a diverse number of optimizations, will be described in the following section.

Figure 4.1 depicts the setup, which consists of three parts: the adjusted MOVPE reactor chamber (see section 2.4.1 for details) and the liner, the bypass for the process gas from the reactor chamber to the exhaust gas system, and finally, the MS itself, which is connected to the bypass and the exhaust gas system. Firstly, it was important to realize the possibility of a constant gas sampling out of the reactor, by simultaneously ensuring an almost undisturbed MOVPE growth. Therefore, a quartz glass nozzle (D) and a quartz glass flange (E) were installed in the back part of the growth chamber for gas

sampling (as depicted in figure 4.1). Thereby, gas turbulences caused by the nozzle are minimized to ensure a constant reactor flow pattern. Afterwards, the analyte gas flux through the nozzle into the bypass was kept under stable conditions with high gas flow rates and a pressure close to the pressure of the growth chamber. This was realized by utilizing a needle valve (J), a pressure controller (L), and a backing pump (N). Since it was ascertained that stable gas sample conditions are important for the MS in order to obtain reliable and comparable mass spectra, an atomic layer deposition (ALD) valve (K) was located between the needle valve and the pressure controller, where flux- and pressure conditions were stable. The ALD valve allowed short gas pulses (ms range) of the analyte, to flow through the bypass into the UHV MS chamber. Additionally, it turned out that heating the bypass was necessary to prevent condensation of analyte chemicals at the inner pipe walls. Therefore, heating wires were used to keep the bypass temperature at 90 °C. Finally, in the MS chamber itself, the gas was analyzed. The analyte gas in

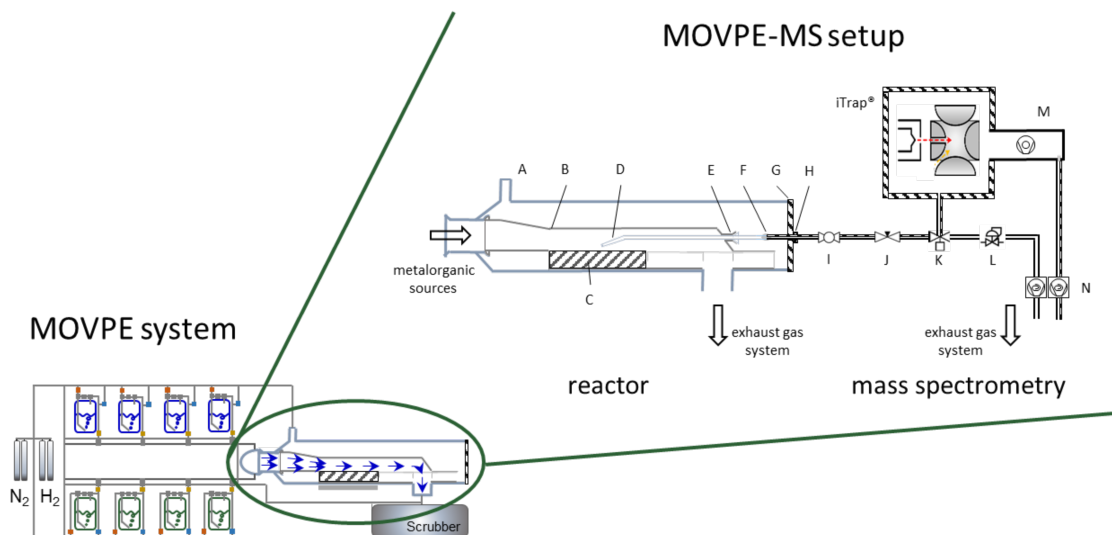


Figure 4.1: Sketch of the setup for in-situ gas phase investigations using a 3D ion trap based MS on a commercially available MOVPE system. Liner purge A, silica-glass liner B, susceptor C, nozzle for analyte suction D, quartz-glass flange E, glass-metal-transition F, reactor gate G, O-ring seal H, ball valve I, needle valve J, ALD valve (gas supply to mass spectrometer) K, pressure controller L, turbo molecular pump M, backing pumps (for analyte bypass and for turbo pump) N. Parts of the figure were adopted from²⁰.

the MS chamber was finally also pumped into the scrubber after analysis (M and N). An optimization of the MS parameters (see section 2.4.5) was necessary to obtain reliable and reproducible data. However, the optimization process was highly analyte dependent so that further discussion will take place in section 4.2. After discussion of the setup, results of the first investigation on TBAs and important parameter optimization of the MS will be described in the next section.

4.2 Gas Phase Analysis on the Thermal Decomposition of TBAs

This section covers the results of the first gas phase decomposition investigations. Part of the results were published²⁰ and can be found in chapter 6.2.1.

After it was ensured that it was possible to sample relatively unchanged process gas from the reactor chamber into the MS (section 4.1), the MS's measurement procedure itself had to be optimized and investigated, since this MS was not tested in a similar environment (analyte species and complexity of experimental setup) before. Due to a large number of important parameters, such as waiting sequences, ionization parameters, and stimulus conditions (see section 2.4.5), the impact of every parameter on the measurement procedure had to be analyzed. One, or even more *detuned* parameters, such as a too short waiting sequence before ionization, a too long ionization time, or a too strong stimulus pulse, would lead, for example, to multiple fractures of the analyte, an overfilled ion trap, strong interaction of the analyte molecules, failure of the electrical signal timing, or other problems. This made an interpretation of the first mass spectra almost impossible. By investigating TBAs at room temperature, suitable waiting sequences between gas inlet and ionization, as well as between ionization and stimulus, were found. Furthermore, the ionization time and the current of the electron filament were adjusted, and the duration and intensity of the stimulus were tuned. Thereby, first reliable TBAs room temperature spectra were recorded (Figure 4.2), using literature data for comparison^{129,130,140}. Figure

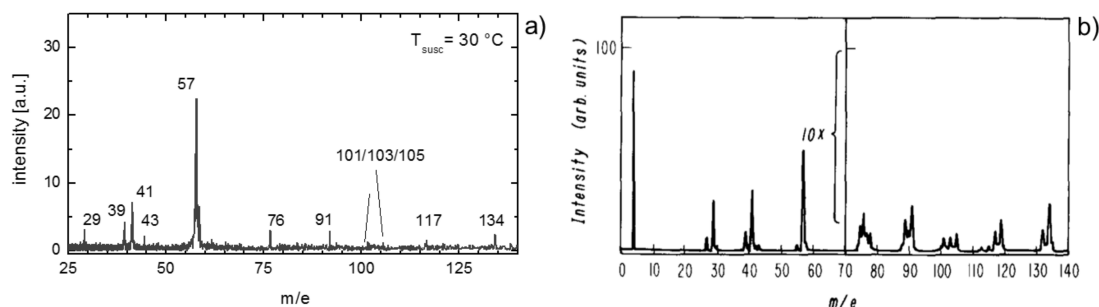


Figure 4.2: Mass spectrum of TBAs at room temperature, recorded with the setup developed for this work a), in comparison to literature data b), taken from^{20,140}.

4.2 shows a recorded mass spectrum of TBAs at room temperature (a) and the mass spectrum of TBAs obtained by Larsen et al. (b) recorded under similar conditions, but using a commercially available quadrupole MS¹⁴⁰. The spectra clearly show the influence of the ionization procedure, which is typical for all MSs using a 70 eV ionization technique. The parent molecule of TBAs can be seen at 134 amu, but also a variety of additional peaks, which partly have an even higher intensity than the TBAs peak at 134 itself. First, there is the dominant peak at 57 amu, which is caused by tertiarybutyl groups, fractured from the TBAs molecule by the electron beam during the ionization process. Furthermore, there are peaks at 39, 41, 43 (C₃-chains) and 29 amu (C₂-chain), which are present due to an electron

beam fracturing of the tertiarybutyl group (57 amu). Also detected were AsH (76 amu), monomethylarsine (91 amu), dimethylarsine (101-105 amu), and a fragmentation product at 117 amu, caused by loss of 2H and CH₃. It is important to keep in mind that all these products are caused by a fracturing of the TBAs parent molecule at room temperature, due to the EI. None of the products is caused by a thermal decomposition process, which, of course, makes interpretation of the actual thermal decomposition complex, since cracking due to EI and thermal decomposition will overlap when recording temperature-dependent mass spectra of the thermal decomposition process^{129,130,140}. Large databases, as for example, the *NIST data base*¹⁴¹ provide typical mass spectra measured under operation with 70 eV ionization. Those databases are usually necessary to compare recorded MS spectra, in order to correlate all the features to different molecules caused by the thermal decomposition, which is actually of interest. This procedure of mass spectra interpretation was explained well by G. Zimmermann¹⁴², see figure 4.3. The Figure shows mass spectra recorded using 70 eV EI. The influence of the thermal decomposition becomes clear by comparing the TBAs spectrum measured at room temperature (b) with the one recorded at 400 °C (c). Further comparison to spectra a), d), and e) (can be found in databases), show the formation of arsine, isobutane, and isobutene, due to a thermal decomposition at 400 °C. The Figure was inherited and edited from¹⁴².

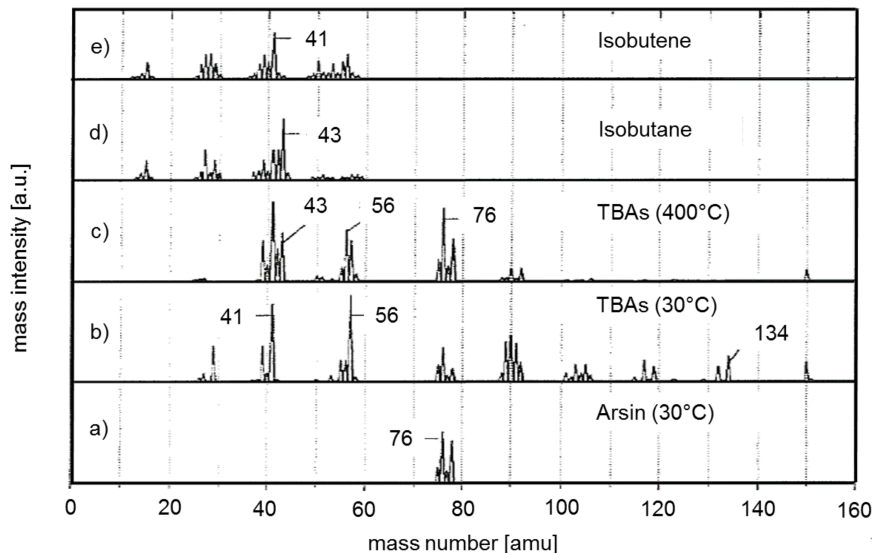


Figure 4.3: The figure shows mass spectra recorded using 70 eV EI. The influence of the thermal decomposition becomes clear by comparing the TBAs spectrum measured at room temperature (b)) with the one recorded at 400 °C, (c). Further comparison to spectra a), d), and e) shows the formation of arsine, isobutane, and isobutene due to a thermal decomposition at 400 °C. Figure taken and edited from¹⁴².

An important result of this work is that the large set of parameters which made the recording of reliable mass spectra complex in the first place actually opens up the possibility for an *ultra sensitive ionization*. The MS parameters of the instrument used can be adjusted

so that the parent molecule does not fracture, as it does while using commercially available MSs. This is shown in figure 4.4 a) and b). The peak caused by TBAs at 134 amu is

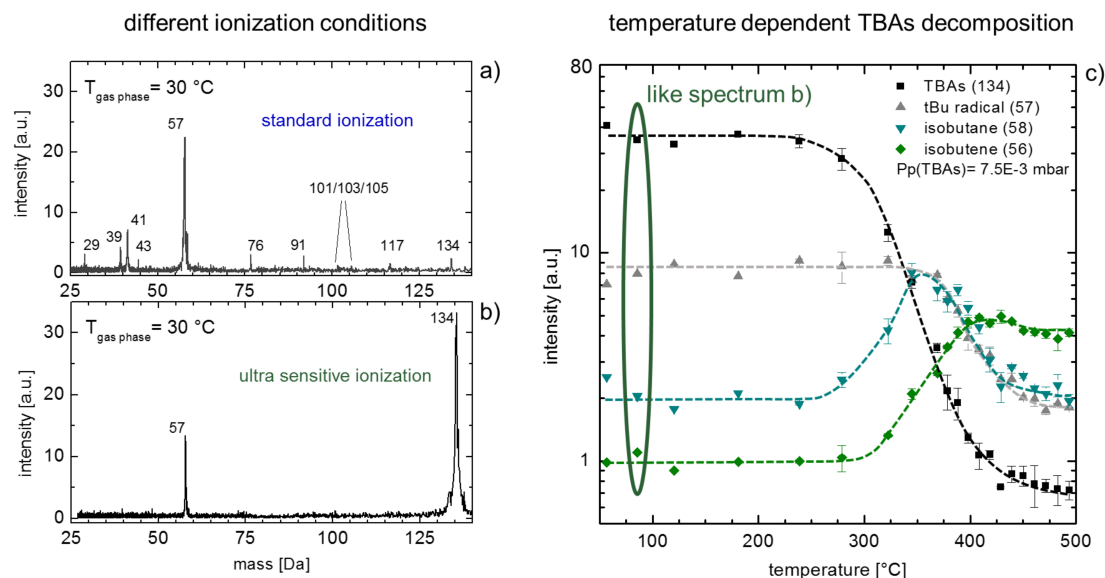


Figure 4.4: Figure a) shows the TBAs room temperature mass spectrum under standard 70 eV EI conditions. In Figure b) the spectrum was recorded under the same analyte conditions, but with different MS parameters. Figure a) depicts the temperature-dependent decomposition behavior of TBAs and clearly indicates the β -H-elimination as the dominant mechanism at higher temperatures. All spectra in Figure c) were recorded using sensitive ionization conditions, like for the spectrum in Figure b). Figures inherited from²⁰.

clearly the highest peak in the spectrum, and only one additional peak, due to fracturing, was detected at 57 amu (tertiarybutyl). The ultra sensitive ionization (Figure 4.4 b)), and thereby the suppression of strong EI fracturing, opens up the possibility of a straightforward interpretation of the mass spectra. This is especially helpful for recording the temperature-dependent thermal decomposition behavior of precursors, as shown for TBAs in Figure 4.4 c).

Starting below 100°C , where no thermal decomposition takes place, the temperature was increased and mass spectra were recorded at every temperature step up to 500°C , where TBAs is fully decomposed. Instead of tracking the different decomposition fragments by dominating peaks^{140,142}, the products important for the TBAs decomposition mechanism, isobutane (58 amu), isobutene (56 amu), tertiarybutyl radical (57 amu), and, of course, the TBAs itself, were tracked directly by their actual mass. This made the mass spectra clearer and the interpretation significantly easier. The thermal decomposition started at around 275°C , where the TBAs signal started decreasing. First, the isobutane signal increased, but at slightly higher temperatures the isobutene signal also rose, until it became the dominant signal at around 400°C . Since isobutene is produced due to β -H-elimination, while isobutane is caused by a radical cleavage process, this behavior confirms the β -H-elimination as the dominant decomposition pathway at temperatures

above 400 °C^{140,142–145}. Further information on TBAs decomposition behavior and the interpretation of Figure 4.4 c) can be found in²⁰.

In addition to the compelling progress of mass tracking in order to unveil decomposition pathways, another possibility also opened up due to the suppression of the TBAs ionization fracturing. Foster et al. were the first ones who stated a thermal cleavage of H and H₂ molecules from the TBAs, even before the radical cleavage or β -H-elimination of the tertiarybutyl group occurs¹⁴⁶. This is very important, as a β -H-elimination of TBAs would lead to AsH₃ instead of AsH or AsH₂. Indeed, AsH₃ decomposes at higher temperatures, which is one of the main reasons why a part of the MOVPE processes switched from AsH₃ to TBAs, whereas AsH easily connects to the surface and additionally provides H to satisfy hydrocarbon residues. Therefore, a H or H₂ cleavage from the TBAs molecule is important for explaining the experimentally confirmed higher decomposition and incorporation efficiencies of TBAs compared to Arsin (AsH₃). This experimental confirmation was possible with the MS setup developed for this work, as the ultra sensitive ionization made it possible to distinguish between TBAs and tBuAs (TBAs with loss of H₂). Figure 4.5 shows the results of the experiments to measure the temperature-dependent ratio between tBuAs and TBAs. With increasing temperature the ratio of tBuAs to TBAs increased

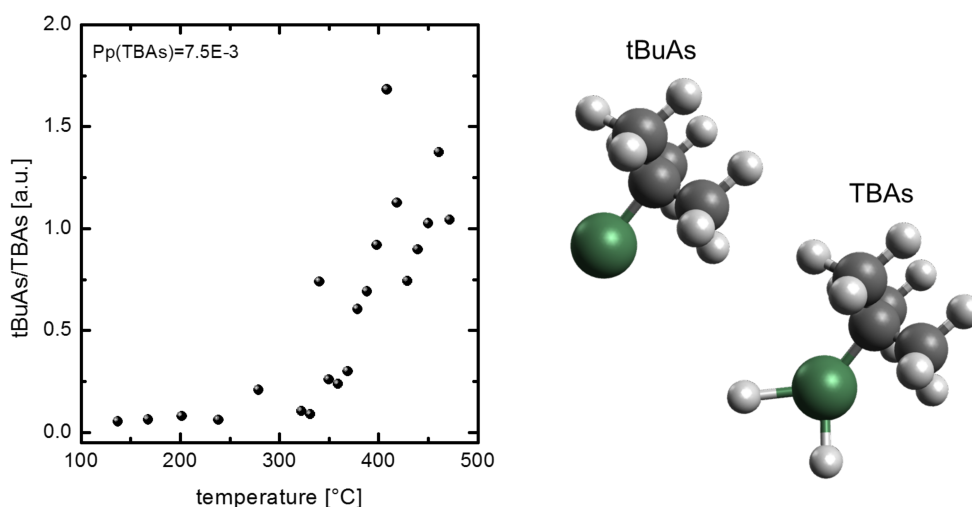


Figure 4.5: On the left side, demonstration of the cleavage of H and H₂ fragments from TBAs molecule before β -H-elimination occurs predicted by Foster et al.. Plotted is the ratio of tBuAs and TBAs over the temperature. On the right-hand side, the two molecules tBuAs and TBAs are depicted for illustration.

significantly, which indicates an H₂ cleavage from the TBAs. This finally confirms the theory by Foster et al.¹⁴⁶, which is essential for fully interpreting the decomposition and especially the growth characteristics of TBAs. Altogether, the investigations of TBAs discussed above showed the suitability of the developed MOVPE MS setup for detailed decomposition and gas phase studies. The next steps currently under investigation are

the decomposition analysis of different Ga and Bi MOs. Those results will be published separately from this work. Furthermore, the influence of GaAs (and other III/V) surfaces on the decomposition characteristics will be observed. Finally, the in-situ analysis of GaAs growth and later on $\text{GaAs}_{1-x}\text{Bi}_x$ growth will be investigated with this setup.

CHAPTER 5

Summary and Outlook

The strong rise of mobile and tethered data communication has a significant impact on global electricity consumption. Due to inefficient $\text{In}_y\text{Ga}_{1-y}\text{As}_z\text{P}_{1-z}$ telecommunication lasers (around 2 % efficiency with cooling efforts), 3 % of global electricity is consumed for optical data transfer. The low efficiency of those $\text{In}_y\text{Ga}_{1-y}\text{As}_z\text{P}_{1-z}$ telecommunication lasers is caused by loss processes, such as Auger recombination and IVBA, which lead to the heating of the devices. Other fields of III/V optoelectronics are also seeking more efficient candidates for device materials, like the search for 1 eV sub-cell alloys in multi-junction solar cells as well as a laser material on Si base. Different Bi containing III/V alloys are discussed as promising candidates. For example, $\text{GaAs}_{1-x}\text{Bi}_x$ on GaAs with 10 % Bi would be a highly efficient laser material for optical data transmission and provide a temperature insensitive band gap with $1.55\text{ }\mu\text{m}$ emission wavelength. The main reason for the high potential of III-Bi-V semiconductors is the fact that already small fractions of Bi, substituting group V host atoms, lead to a significant change of the band structure, which leads to suppression of Auger recombination and IVBA for sufficient compositions. However, the deposition of these highly metastable materials is challenging and still the subject of current research.

In the present work, different dilute Bi containing III/V alloys were investigated. $\text{GaAs}_{1-x}\text{Bi}_x$, $\text{GaAs}_{1-y-x}\text{P}_y\text{Bi}_x$, $\text{GaAs}_{1-y-x}\text{N}_y\text{Bi}_x$, and $\text{GaP}_{1-x}\text{Bi}_x$ were epitaxial grown using MOVPE and characterized using various structural and optical characterization techniques. The challenge here was to deposit structures with sufficient Bi fractions, while simultaneously realizing high quality layers and interfaces.

The deposition of $\text{GaAs}_{1-x}\text{Bi}_x$ with Bi fractions close to 10 % has not been realized thus far. In the present work, the reasons for the Bi incorporation limit were under investigation. Therefore, alternative Bi MOs were used to unveil the influence of the thermal decomposition characteristics of the different precursors and the associated surface processes at the growth surface. It was shown that the incorporation limit is not dependent on the type of hydrocarbon residues (different precursors). Rather it was shown that the growth using different MOs led to nearly identical growth characteristics. Therefore it was

concluded that at the temperature used neither the Bi incorporation limit is related to a specific hydrocarbon molecule at the growth surface, nor is an insufficient decomposition of one of the alternative MOs responsible.

Quaternary layers $\text{GaAs}_{1-y-x}\text{P}_y\text{Bi}_x$ and $\text{GaAs}_{1-y-x}\text{N}_y\text{Bi}_x$ were deposited. They enable the lattice matched growth on GaAs, while simultaneously the band gap can be tuned independently over a wide range. $\text{GaAs}_{1-y-x}\text{P}_y\text{Bi}_x$ was investigated as a potential candidate for a 1 eV sub-cell material in multi-junction solar cells. It was possible to demonstrate the first PL activity in this quaternary alloy, which makes the material interesting for further optoelectronic applications. Furthermore, it was found that the smaller covalent radius of the P atoms led to an increased Bi incorporation limit. Hence, $\text{GaAs}_{1-y-x}\text{P}_y\text{Bi}_x$, $\text{GaAs}_{1-y-x}\text{N}_y\text{Bi}_x$, and $\text{GaAs}_{1-x}\text{Bi}_x$ structures were deposited and compared. The two different quaternary materials in comparison to $\text{GaAs}_{1-x}\text{Bi}_x$ showed that with increasing P (or N) incorporation the Bi incorporation limit was increased. Thereby, it was possible to prove the assumption that local strain is a crucial factor for the Bi incorporation limit. This is an important finding for future III-Bi-V studies, as it might open up the possibility of strain-engineering the Bi incorporation into III/Vs.

Moreover, $\text{GaP}_{1-x}\text{Bi}_x$ layers were deposited on GaP and GaP on Si. $\text{GaP}_{1-x}\text{Bi}_x$ was a relatively new material, and the first deposition by MOVPE was successfully demonstrated. Furthermore, it was possible to incorporate high quality structures and Bi fractions up to 8.5 %. Originally considered to be a promising candidate for a laser material on Si, it was found that despite the large band gap reduction, the alloy is unlikely to lead to efficient light emitters. This is mainly related to a breakdown of the band edge Bloch character due to short-range alloy disorder and the indirect band gap. However, the findings are highly interesting for the Bi community from a theoretical point of view.

Finally, it was possible to realize an improved $\text{GaAs}_{1-x}\text{Bi}_x$ laser structure with an emission wavelength of 1015 nm at room temperature.

The second project of this work was the development of a new in-situ setup of a MS connected to an MOVPE system. The new setup is meant to enable in-situ investigations of the deposition procedures discussed above. Especially of interest is the decomposition of MO precursors and analysis of MOVPE process desorption products. Therefore, with the support of *Carl Zeiss SMT GmbH*, a 3D ion trapped based MS prototype was prepared, and an in-situ setup to the MOVPE system was developed. The main challenge was to maintain the balance between transferring the analyte as unmodified as possible from the reactor chamber into the mass spectrometer and simultaneously not influencing the MOVPE process itself. Despite initial difficulties, the setup was successfully developed, and the potential was demonstrated by investigating the decomposition of TBAs. The main advantages of the new setup are the short measurement time for a mass spectrum over a large range and the ultra sensitive ionization conditions. The investigations on further MOs and growth processes are still under investigation at the moment of submission of this work and will be published separately.

Altogether, it can be concluded that the investigations of this work led to various new insights into the growth of bismide containing III/V materials. Furthermore, the developed in-situ setup of the MS at an MOVPE system allows decomposition and growth investigations on a new level, which was demonstrated by TBAs decomposition experiments.

CHAPTER 6

Author's Contribution

In the following chapter, I will briefly describe the original contributions during the three years of my PhD, see 6.1. In section 6.2, the full publications, which are actually part of this work, will follow with information about my personal contributions to every publication. Finally, further publications with a significant contribution by me not directly connected to bismides nor to mass spectrometry studies, but also published during my PhD, will be listed (section 6.3).

6.1 Original Contributions

All studies and findings in this work are the result of many different experiments, discussions, group meetings, and collaborations. The main topic of this work is the MOVPE deposition of bismide containing III/Vs. I started my thesis with the results on the MOVPE growth of $\text{GaAs}_{1-x}\text{Bi}_x$ using alternative precursors from my master thesis and the knowledge Peter Ludewig gathered during his PhD thesis. Among other questions, those results led to the questions of gas phase and decomposition reactions during the growth of bismide containing materials. Therefore, further growth studies were performed, and the first peer-review paper on the growth with alternative metalorganics (MOs) was written, see section 6.2.5. Simultaneously, I started to develop the MS setup at one of our MOVPE systems to enable further insights into the complex growth of III-Bi-V semiconductors. This was a collaboration with *Carl Zeiss SMT GmbH*. They provided the MS prototype, and my task was to find a setup that enables in-situ studies at the MOVPE system. During the first year, we worked on the preparation of the MS for the special environment of our MOVPE machine. Simultaneously, I planned the setup for the connection between MS and MOVPE with technical support from Thomas Ochs and through supportive discussions with Kerstin Volz, Wolfgang Stolz, and the research team of Carl Zeiss. The second year was used to implement the setup and to connect the MS to the MOVPE. After various difficulties with the MS itself and after the challenges of the setup were tackled, the first actual decomposition studies could finally start in the beginning of 2017. Finally, the

decomposition analysis of the well described TBAs precursor enabled the demonstration of the potential of the newly developed setup. Kerstin Volz, Wolfgang Stolz, and Ralf Tonner provided helpful theoretical input for the interpretation of the collected data. The technical implementation of the MS-MOVPE setup and the proof of concept using TBAs was published in a peer-review paper, see section 6.2.1.

Since the work with the MS prototype was challenging and there were many smaller and bigger interruptions due to MS problems which needed to be fixed by the Carl Zeiss team, there was time to work on further studies on bismide III/Vs over the last three years. The studies on $\text{GaAs}_{1-y-x}\text{P}_y\text{Bi}_x$ were inspired by fruitful discussions at the international Bi Workshop in Cork (Ireland). With the assistance of Thilo Hepp as well as Peter Ludewig and with advice from Kerstin Volz, I worked with Stephen Sweeney, Shirong Jin, and Konstanze Hild from the University of Surrey to calculate the band structure for this material system on GaAs. Sangam Chatterjee and Nils Rosemann from the University of Marburg demonstrated first $\text{GaAs}_{1-y-x}\text{P}_y\text{Bi}_x$ PL on our samples. This collaboration is summarized in the paper published with *Applied Materials Today* (section 6.2.4). Further studies on the $\text{GaAs}_{1-y-x}\text{P}_y\text{Bi}_x$ samples were carried out in cooperative work with Susan Babcock and Weixin Chen from the University of Wisconsin, Madison. During my two-month stay in Madison, we prepared different quaternary Bi samples and investigated the composition on a high spatial 3D resolution using atom probe tomography (APT). Thereby, it was possible to confirm the method of composition determination applied on the quaternary materials. Additionally, further spectral ellipsometry measurements on various samples grown in Marburg were done by Zoe Bushell and Stephen Sweeney from the University of Surrey. Those studies led to the determination of important optical constants and critical points of dilute bismide alloys, see section 6.2.7.

The growth of $\text{GaAs}_{1-y-x}\text{P}_y\text{Bi}_x$ showed that local strain might play an important role regarding the Bi incorporation limit in III/V semiconductors. Therefore, further $\text{GaAs}_{1-y-x}\text{N}_y\text{Bi}_x$ was epitaxially grown and compared to $\text{GaAs}_{1-x}\text{Bi}_x$. This led to the publication about the role of strain in bismide containing III/V materials, where Eduard Sterzer and Kerstin Volz provided supportive input, see section 6.2.3.

The idea to deposit $\text{GaP}_{1-x}\text{Bi}_x$ was born at the international Bi workshop in Madison in 2015, where Oleg Rubel talked about the band structure unfolding of this material. After the successful deposition of this highly meta-stable material was demonstrated in Marburg (section 6.2.2), the samples were further investigated in close collaboration with Christopher Broderick from the Tyndall Institut in Cork Ireland and with Zoe Bushell and Stephen Sweeney in Surrey (section 6.2.6). Furthermore, during STEM experiments on $\text{GaP}_{1-x}\text{Bi}_x$ by Andreas Beyer¹⁹, it was found that this material is excellent for investigations of STEM methods, which are under investigation by Jürgen Belz, see section 6.2.8.

6.2 Publications of this Work

6.2.1 MOVPE Gas Phase Analysis Setup - With Newly Designed, Highly Sensitive and Real-Time Quadrupole Ion Trap Mass Spectrometer

L. Nattermann, O. Maßmeyer, E. Sterzer, V. Derpmann, H. Y. Chung, W. Stolz, K. Volz, submitted to Scientific Reports (2017)

Abstract

This is a report about the first setup of a recently developed, extremely sensitive, and very fast 3D quadrupole ion trap mass spectrometer inline in a metalorganic vapor phase epitaxy (MOVPE) system. This setup was developed ultimately for the decomposition- and the interaction analysis of different established and novel metalorganic sources for MOVPE deposition of III/V semiconductors. To make insitu gas-phase and growth interaction analysis on a new level of sensitivity possible without disturbing the MOVPE growth process itself, an optimized experimental connection of the mass spectrometer to the MOVPE system is required. This work reports on the realization of such an experimental setup and provides first proof of concept for decomposition analysis. In addition, a comparison to previous studies and gas-phase analysis at MOVPE systems will be given in this work.

The Authors contribution

My contribution to this work was the planning, development and execution of the experimental setup and all decomposition experiments. The support for the mass spectrometer itself came from V. Derpmann and H. Y. Chung. All co-authors helped to interpret the data and to improve the manuscript written by me.

MOVPE gas-phase analysis setup - with newly designed, highly sensitive and real-time 3D quadrupole ion trap mass spectrometer

L. Nattermann^{1*}, O. Maßmeier¹, E. Sterzer¹, V. Derpmann², H. Y. Chung², W. Stolz¹, K. Volz¹

¹*Material Sciences Center and Faculty of Physics, Philipps-Universität Marburg, Germany*

²*Carl Zeiss SMT GmbH, Oberkochen, Germany*

email: lukas.nattermann@physik.uni-marburg.de

Lukas Nattermann, WZMW & Philipps-Universität Marburg, Hans-Meerwein-Str. 6 MzGb
Kern D 02D 35a

Keywords: gas-phase reaction analysis; mass spectrometry; in situ MOVPE; III/V semiconductors;

Abstract

This is a report about the first setup of a recently developed, extremely sensitive and very fast 3D quadrupole ion trap mass spectrometer inline in a metalorganic vapour phase epitaxy (MOVPE) system. This setup was developed ultimately for the decomposition- and the interaction analysis of different established and novel metalorganic sources for MOVPE deposition of III/V semiconductors. To make in situ gas-phase and growth interaction analysis on a new level of sensitivity possible without disturbing the MOVPE growth process itself, an optimized experimental connection of the mass spectrometer to the MOVPE system is required. This work reports on the realization of such an experimental setup and provides first proof of concept for decomposition analysis. In addition, a comparison to previous studies and gas-phase analysis at MOVPE systems will be given in this work.

1. Introduction

Metalorganic vapour phase epitaxy (MOVPE), first used for semiconductor growth on an industrial scale in the eighties [1], is a well-established and essential method for processes in large areas of the semiconductor industry today [2], [3]. From light emitting diode (LED) manufacturing and computer chip production to deposition of semiconductor lasers and solar cells, a billion dollar market is based on MOVPE [4]. Hence, a thorough understanding of the gas-phase processes as well as in situ process gas analysis can help make manufacturing consistently more efficient and the development of new semiconductor materials possible. In particular, the deposition of III/V semiconductors requires high technical standards and purified metalorganic precursors (MOs), as impurities even in the parts per million (ppm) range can cause high defect densities and often lead to inoperable devices [5]. Additionally, even the smallest changes in gas-phase and partial pressure ratios of the different sources can have a large influence on the growth characteristics of semiconductor materials.

Decomposition analysis on MOs for III/V semiconductor growth was first performed in the late eighties and early nineties, when novel precursors like tertiarybutylarsine (TBAs) and triethylgallium (TEGa) entered the market. As already reported by others, these studies are highly complex [6], [7]. Different experimental approaches for gas-phase investigations on MOVPE systems were tested in previous experiments. Some of the first experiments were performed by Yoshida and Watanabe [8], who reported on mass spectrometry studies of trimethylgallium (TMGa) and TEGa decomposition reaction in H₂ and N₂ and introduced one of the first setups for decomposition measurements of MO sources. One experimental barrier that needs to be overcome is the different pressure regimes between the MOVPE growth system on one side and the mass spectrometer system on the other. For most studies linear quadrupole mass spectrometers (QMS) were used. Hence, at least two expensive pressure reduction stages were necessary to reduce the pressure from MOVPE conditions (mbar range) down to 1E-5 mbar needed for QMS operation [9]. Furthermore, the pressure reduction can lead to changes in the gas-phase so that in situ measurements become even more challenging [6]. Lee et al. published a study on mass spectrometry investigations on the MOVPE growth of GaAs in which they developed a setup to prevent these effects [6]. However, a disadvantage of their experimental approach is that the whole system is meant to investigate decomposition reactions and is not designed for growing semiconductors on a large scale. The problem is that decomposition characteristics will change when growth conditions are changed [4]–[9], so that a setup for decomposition

investigations alone is an important first step, but ultimately an inline process analysis tool is needed to provide the possibility of understanding gas-phase reactions and surface reactions under real MOVPE growth conditions [8], [10]–[15].

Additionally, previous studies showed that the addition of precursors, a change of V/III ratios, and, of course, temperature variations can lead to an alteration of the decomposition pathways and their products and therefore often to an important change of growth characteristics [13], [16]. Mashita et al. for example, observed that the mass spectrum of a TEGa and trimethylaluminum (TMAI) mixture does not correspond to a simple sum of the spectra, measured for the two individual alkyls [9].

As an example and currently under investigation are gas-phase analyses of the growth of $\text{GaAs}_{1-x}\text{Bi}_x$ and $\text{GaP}_{1-x}\text{Bi}_x$, since MOVPE growth studies showed that the limitation of the Bi incorporation in these two different ternaries is not only explainable by strain and solubility barriers, but also gas-phase reactions or surface reactions between different precursors seem to play a role [17]–[19].

In addition to the investigations on gas-phase processes during the growth and the combination of established precursors, studies with novel precursors are of interest as well. Recently, several precursors have been introduced for the growth of III/V semiconductors [20]–[22]. Some of those precursors showed promising properties for dilute nitride III/V semiconductor growth, but also gave rise to questions about the gas-phase interactions, as large differences compared to the growth with conventional precursors were observed. The N incorporation efficiency in GaAs for the growth with the novel precursor (DTBAA) was orders of magnitude higher than the N incorporation efficiency of the conventional N precursor (UDMHy). Gas phase calculations lead to the assumption that the decomposition mechanism plays a significant role [20].

Furthermore, C incorporation in III/V semiconductors is crucial in terms of device performance. As the source of C incorporation is not yet fully understood for several III/V semiconductors and especially dilute nitrides, gas-phase investigations could help to understand and to decrease the C content. This becomes an even more important question because low temperature MOVPE growth has recently been gaining attention [23].

In this work we will present a new experimental setup of a real-time and highly sensitive mass spectrometer inline connected to a conventional horizontal MOVPE system as the first step for future gas-phase investigations of MOVPE processes. The setup thereby enables in situ MOVPE growth investigations, without disturbing or changing the growth process itself. The experimental setup with its advantages and challenges will be discussed in detail. Furthermore, as a proof of concept, decomposition studies on TBAs will be shown and discussed in context to the literature [10].

2. Experimental Equipment

2.1 MOVPE

The MOVPE system used for this work is a horizontal reactor design Aixtron Aix 200 with gas foil rotation. The system is separated into three parts, the gas supply-and mixing-cabinet, the reactor chamber with glove box for sample exchange, and the exhaust gas system. Both, H_2 and N_2 , can be used as carrier gas and are purified to at least 9N purity. All pipes are made of electron beam polished stainless steel and are always kept under room temperature to prevent both pre-reactions of the carrier gas and MOs and condensation or deposition of chemicals on the inner pipe walls. For group III-and group-V MOs, two gas pipes are available for each gas supply to the reactor chamber. Hence, pre-reactions of the different MOs are detained. The total flow rate in the reactor chamber was 6800 sccm. The susceptor temperature was between room temperature and 850 °C. The susceptor is located in a quartz liner and the temperature is controlled by a thermocouple in the center of the susceptor. The difference between inner susceptor temperature and surface temperature is determined by observing a phase change of Al coated Si substrates on the susceptor. The reactor chamber surface is 720 cm², including silica liner surface and susceptor surface (100 cm²).

2.2 Mass Spectrometer

The instrument used here is a recently developed 3D quadrupole ion trap (QIT) based mass spectrometer (Zeiss iTrap®, Carl Zeiss SMT GmbH). Figure 1 shows a sketch of the mass spectrometer and its electronics. The QIT itself is located in a stainless steel cube, which is directly connected to a turbo molecular pump, which generates an ultra-high vacuum (UHV) in the measurement chamber. As an interface between the analyte source and the mass spectrometer a fast atomic layer deposition (ALD) valve, with pulse times below 50 ms, is used. Inside the

QIT an integrated electron gun ionizes the analyte with an energy of 70 eV. After ionization the newly created ions are stored by applying a radio frequency (RF) to the ring electrode inside the QIT. Then the stored ions are excited by a stimulus to assure a correlated movement of the ions. A highly sophisticated signal compensation concept with selective ion excitation techniques and advanced low-noise charge amplifiers close to the measurement chamber (see figure 1) makes it then possible to detect the mirror current induced by the oscillating ions in the QIT. This mirror current is analyzed by a software tool and after fast Fourier transformation (FFT) leads to the corresponding mass spectrum.

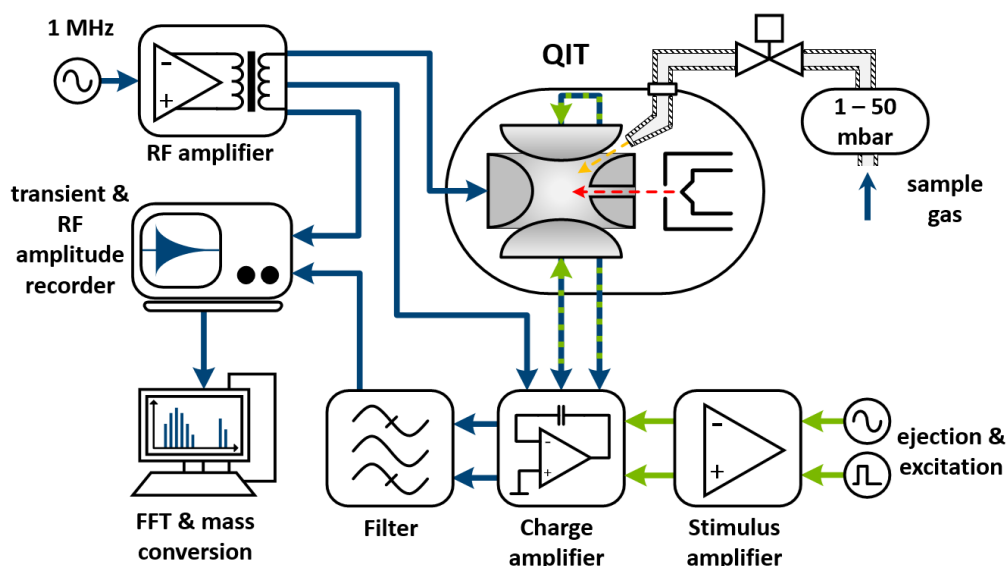


Figure 1: Sketch of the signal path of the quadrupole ion trap based mass spectrometer.

This mass spectrometer was chosen, as it does not have any detector surfaces that can degenerate by hydrogen or covered by MOVPE gases. Furthermore all surfaces are inert to reduce reactions with the analyte and assure reproducible measurements. This is also ensured by heating the mass analyzer to approximately 100°C at all time. To reduce the amount of precursor ions the stored waveform inverse Fourier Transform (SWIFT) technique can be applied to selectively eject ions from the QIT and increase the sensitivity for the decomposition or product ions. The resolution ($\Delta m/m$) of the instrument is better than 1000, however due to shortcomings of the mass calibration in the current experimental setup the mass accuracy is only giving nominal masses.

3. Results and Discussion

3.1 Mass spectrometer – MOVPE setup

Firstly, the connection between the MOVPE system and mass spectrometer will be described in detail. Afterwards, a discussion of the advantages and challenges of the setup, the new mass spectrometer, and its applicability for MOVPE gas-phase investigations will follow.

The setup consists of three different parts (see figure 2). First, the adjusted MOVPE reactor and liner system, second, the bypass, which transports the analyte from the reactor chamber to the mass spectrometer and then to the exhaust gas system; and third, the mass spectrometer itself, which is also connected to the exhaust gas system. The quartz glass liner (B) in the Aixtron Aix 200 horizontal reactor (A) was extended by a glass flange (E) at the end of the liner to keep gas flow turbulences before and above the growth area as small as possible. A tapered quartz glass nozzle (D) is used to sample gas from exactly the center of the growth area, approximately 0.8 mm above the susceptor, through the extended glass flange. This nozzle is connected to a ¼ inch diameter, electron polished, stainless steel pipe by a glass metal transition (F), to absorb the different thermal expansions of quartz glass and stainless steel. This first part of the setup, located in the reactor chamber, was already successfully used by our group in previous studies [24]–[27]. The analyte then enters the bypass and passes the reactor gate through an O-ring seal (H). A needle valve at the beginning of the bypass makes it possible to keep the bypass under constant vacuum ($50 \text{ mbar} < \text{bypass} < 5\text{E-}3 \text{ mbar}$) for when the reactor needs to be opened in order to change samples or clean the quartz glass components. Contamination of the bypass is thereby avoided. The ALD valve

(K), which allows very short gas pulses in the mass spectrometer chamber, is located between a needle valve (J) and a pressure controller (L) to provide constant gas flow and pressure conditions for the measurements. Additionally, the bypass between the reactor gate and the pressure controller is heated to 100°C, in order to prevent accumulation and condensation of analyte on the pipe walls. After the pressure controller a backing pump (N) provides a constant gas flow through the bypass. The bypass ends at the connection of the exhaust of the backing pump to the scrubber of the MOVPE system.

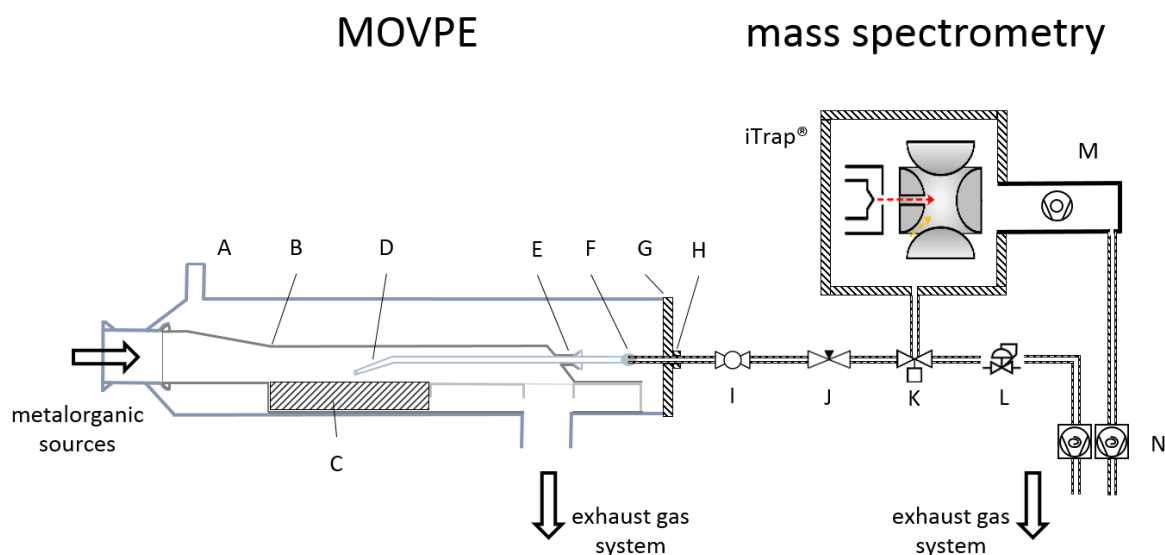


Figure 2: Experimental setup of MOVPE (reactor) and connection to mass spectrometer system. Liner purge **A**, silica glass liner **B**, susceptor **C**, nozzle for analyte suction **D**, quartz glass flange **E**, glass-metal-transition **F**, reactor gate **G**, O-ring seal **H**, ball valve **I**, needle valve **J**, ALD valve (gas supply to mass spectrometer) **K**, pressure controller **L**, turbo molecular pump **M**, backing pumps (for analyte bypass and for turbo pump) **N**

The ALD valve located between needle valve and pressure controller pulses analyte into the mass spectrometer. Directly connected to the mass spectrometer, a turbo molecular pump (M) generates an ultra-high vacuum inside the measurement chamber. A second backing pump (N) (also connected to the scrubber) generates the pre-vacuum for the turbo pump.

The main challenge of gas-phase investigations of MOVPE growth processes in general is to maintain the balance between transferring the analyte as unmodified as possible into the mass spectrometer and simultaneously not influencing the MOVPE process itself. This balance has been realized in this work by operating the bypass under stable conditions, similar to the reactor pressure in the growth chamber. Expensive pressure reduction stages, which can change the analyte itself, are thereby avoided. The backing pump in combination with the needle valve and the pressure controller allows for a constant and stable flux of the analyte (between the needle valve and pressure controller) directly from the gas-phase above the sample, where the decomposition takes place. Simultaneously, the flow turbulences in the reactor, caused by the nozzle, are minimized and engineered to be located behind the actual growth area.

Additionally, the recording time for a single spectrum is below 2 sec, so that a high data point density and a large number of measurements for improved statistics are possible. However, experiments have shown that a recovery time of about 20 sec for the ultra-high vacuum in the mass spectrometer chamber is recommended (depending on the bypass pressure) to achieve clear spectra. Furthermore, a fine adjustment of parameters of the mass spectrometer makes a sensitive ionization possible. Thereby, the analyte is not fractured, as for standard 70 eV ionization, and makes interpretation of the recorded spectra easier. Altogether this makes the new mass spectrometer setup in the MOVPE system a highly effective tool for investigating and controlling gas-phase processes.

In regards to the challenges, which are under research at the moment, another important point of the described experiment is the large number of parameters of the mass spectrometer itself. Although, this opens up the possibility of sensitive and exact real-time measurements on one hand, it requires a sophisticated adjustment of all the parameters on the other. In order to find suitable parameters for gas-phase investigations and to understand the

parameter characteristics of the mass spectrometer, the well-known TBAs precursor was investigated. Results of these experiments are presented and discussed in the following.

3.2 Proof of concept – decomposition investigations of TBAs

3.2.1 Results

In order to verify the functionality of the experimental setup, results of TBAs investigations are presented and discussed in context to the literature.

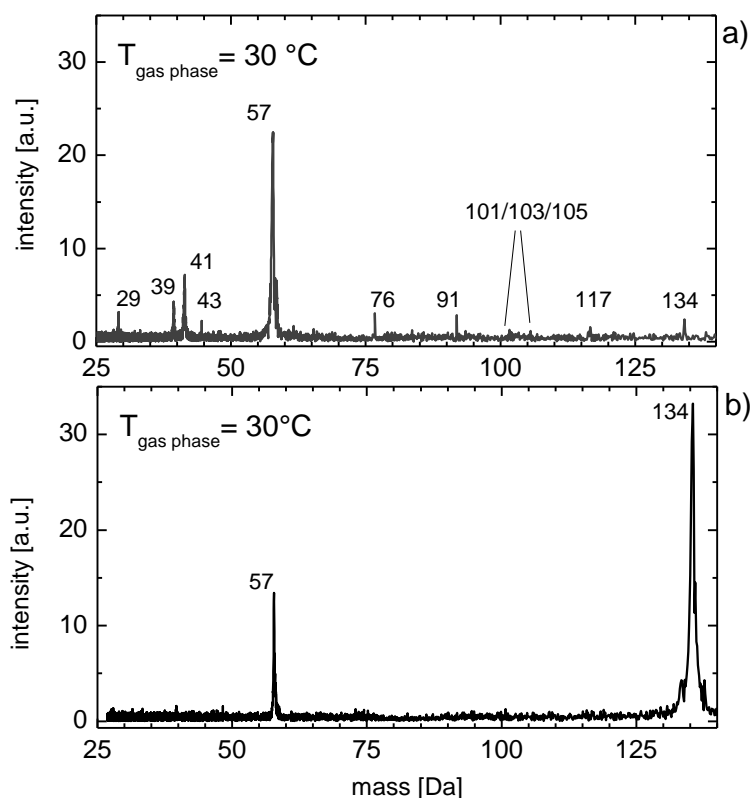


Figure 3: Mass spectrum of TBAs at 30°C for standard ionization conditions a) and sensitive ionization b). The partial pressure was 7.5E-3 mbar, the ionization potential = 70 eV.

Figure 3a shows the mass spectrum of TBAs at 30 °C with a TBAs partial pressure of 7.5E-3 mbar. Mass spectrometer parameters as RF and pulse width of the stimulus were optimized for detection of a mass range from 15 amu to 160 amu. The most prominent peak (principal peak) is located at 57 amu. This peak is related to ^tBu-radicals from the fragmentation of TBAs. But also C₂-chains (29 amu) and C₃-chains (39, 41 and 43 amu) are clearly visible. AsH was also detected (76 amu), as well as monomethylarsine (91 amu), dimethylarsine (101-105 amu), and the parent molecule at 117 amu (loss of 2H, CH₃) and 134 amu (TBAs). The spectrum in figure 3b was taken under sensitive ionization conditions. The parent peak of TBAs is most prominent at 134 amu. The only fragmentation product due to EI is the ^tBu peak at 57 amu, but also this peak is smaller than for standard 70 eV ionization conditions. No further significant fragmentation products were found.

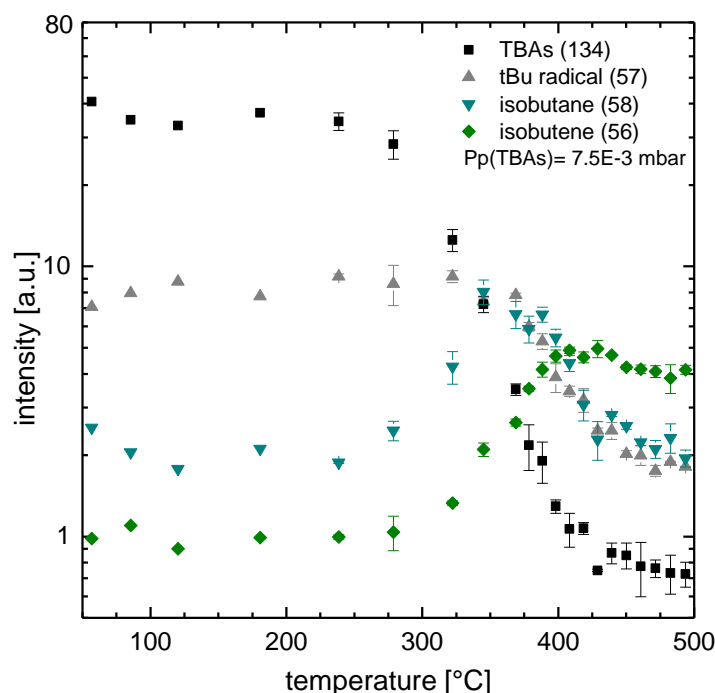


Figure 4: Plot of the most relevant TBAs decomposition- and fragmentation- products, the parent molecule TBAs (134 amu) the ^tBu-radical (57 amu) and Isobutene (56 amu) vs. temperature. The temperature was determined by correlation with data from [10], as only the susceptor temperature could be measured during experiments.

Additionally, temperature dependent measurements of the decomposition products were performed. Results of these experiments are plotted in figure 4. All temperature dependent measurements are recorded without GaAs substrates or GaAs coating of the susceptor or the liner. Since the thermocouple is located in the susceptor, the gas-phase temperature was determined by the correlation of the decomposition rate with results from [6]. Three mass spectra were recorded for every temperature point from 240 °C on, where the thermal decomposition begins. The intensity plotted is the mean value of these three measurements; the error bar shows the standard deviation. The most relevant decomposition products of TBAs are isobutene (C₄H₈) and isobutane (C₄H₁₀) [28]. The intensity could be monitored by mass 56 amu and 58 amu directly, since sensitive ionization conditions were used, which is different from previous studies where isobutane was tracked by 43 amu [10], [29]. At around 250 °C gas-phase temperature, the TBAs signal decreases with increasing temperature. The parent peak disappears fully at around 450 °C. Increasing isobutane production, starts slightly before 300 °C, and the isobutene signal starts to increase at 325 °C, about 50 °C after the isobutane signal increases. The ^tBu radical (57 amu) decreases slightly after the TBAs signal at 350 °C. It is then tracked by the isobutane signal and decreases down to a constant level at 450 °C.

3.2.2 Comparison to literature

Figure 3a shows a typical room temperature mass spectrum of a metal organic precursor. Most of the peaks are caused by the fragmentation of the TBAs molecule due to the electron ionization (70 eV), inside the mass spectrometer. The influence of the EI process on the analyte is always important and the first step that needs to be taken into account in order to interpret the mass spectra. Various databases of fragmentation spectra of different molecules and fragments are available for the 70 eV EI technique. For these studies the database *Chemistry WebBook* of the *National Institute of Standards and Technology (NIST)* was used for identification [29]. The results observed are in good agreement with the literature [10], [30], [31]. In the study published by Larsen, Buchan and Stringfellow [6], the same fragmentation spectrum was found for TBAs at room temperature. This is an important finding, as it shows that the results obtained with the experimental setup discussed here, is suitable for direct comparison with data from previous studies. It also indicates that established mass spectrometer databases can be used for interpretation of mass spectra collected with the new mass spectrometer, which was not clear in the first place, since different ionization techniques often lead to a different fragmentation of molecules during the ionization process in mass spectrometers (see 2.2). This enables a straightforward comparison to previous studies.

However, the fragmentation of the analyte due to ionization often makes interpretation of the obtained mass spectra more complicated, especially when temperature dependent measurements are performed and the thermal decomposition of the analyte is under investigation. Figure 3b shows a spectrum of TBAs, also recorded at 30°C as in figure 3a, but under fine adjustment of mass spectrometer parameters for sensitive ionization conditions. One can see that the only fragmentation product is the ^tBu radical (57 amu) and the most prominent peak comes from the TBAs (134 amu) itself. Thereby it is possible to directly interpret the mass spectra by the weight of the molecules produced due to thermal decomposition.

The results of the temperature dependent measurements in figure 4 provide insights into the thermal decomposition characteristics of TBAs. While isobutane and isobutene are products of the thermal decomposition of the TBAs molecule, the ^tBu radicals are both, a fragmentation product of the ionization and a decomposition product of the thermal induced decomposition of the precursor at higher temperatures. In previous studies TBAs was tracked by the 57 amu peak as the parent molecule was mostly fractured by EI [10]. The sensitive ionization used here makes it possible to distinguish between TBAs and ^tBu molecules as can be seen in fig. 4. From room temperature up to 250 °C, the concentration of the all products is caused by a small number of fractured TBAs molecules. From 250 °C, the spectra change when the thermal decomposition of the TBAs starts. The ^tBu concentration (57 amu) decreases slightly after the TBAs due to the thermal induced generation of free radicals. The fact that the isobutane signal (58 amu) tracks the ^tBu signal from about 375°C could also be caused by EI cracking of an H atom from the isobutane molecules.

The observation that the production of isobutane starts slightly before the generation of isobutene confirms the findings of Larsen et al. and Lee et al. [10], [28]. They found that the abundance of isobutane dominates at lower temperatures before the production of isobutene as a product of β-H-elimination increases significantly at temperatures above 400 °C. Also Foster et al. and Zimmermann et al. reported that there are two decomposition pathways, first a free radical process producing isobutane and second a β-H-elimination process, generating isobutene as a side product [30], [31]. Hence, the observations made in these experiments as well confirm β-H-elimination as the main decomposition mechanism at temperatures above 390°C [32], [33].

All findings agree well with previous experimental investigations, so that the functionality of the setup discussed here is confirmed to be suitable for future gas-phase and decomposition investigations. Furthermore, it seems to be a promising candidate to enable deeper insights into decomposition gas phase processes of metal organic precursors during MOVPE.

4. Summary

A new setup for inline gas-phase investigations on a MOVPE system was introduced. The characteristics, advantages and challenges of the developed experimental setup were illustrated and discussed in context of previous experimental studies on metalorganic decomposition pathways. TBAs experiments showed good agreement with the literature.

Acknowledgments

We gratefully acknowledge support from German Science Foundation (DFG) in the framework of the RTG1782 "Functionalization of Semiconductors" as well as from the HMWK in the framework of the project EGALITE. We are also grateful to funding from EPSRC (UK) under grant EP/H005587/1.

References

- [1] R. L. Moon, "MOVPE: is there any other technology for optoelectronics?," *J. Cryst. Growth*, vol. 170, no. 1–4, pp. 1–10, 1997.
- [2] G. B. Stringfellow, "Development and current status of organometallic vapor phase epitaxy," *J. Cryst. Growth*, vol. 264, no. 4, pp. 620–630, 2004.
- [3] I. Garcia, B. Galiana, I. Rey-Stolle, and C. Algora, "MOVPE technology for the growth of III-V semiconductor structures," *2007 Spanish Conf. Electron Devices, Proc.*, pp. 17–20, 2007.
- [4] P. Roussel and E. Virey, *MOCVD and MBE epitaxy trends for compound semiconductors*. Solid State Technology, 2012.
- [5] A. Brauers, "Alternative Precursors for III-V MOVPE - Promises and Problems," vol. 22, pp. 1–18, 1991.
- [6] P. W. Lee, T. R. Omstead, D. R. McKenna, and K. F. Jensen, "In Situ Mass Spectroscopy And Thermogravimetric Studies Of GaAs MOCVD Gas Phase And Surface Reactions," vol. 85, pp. 165–174, 1987.
- [7] J. T. Francis, S. W. Benson, and T. T. Tsotsis, "Observation of the methyl radical during the surface decomposition reaction of trimethylgallium," *J. Phys. Chem.*, vol. 95, no. 12, pp. 4583–4586, 1991.
- [8] M. Yoshida, H. Watanabe, and F. Uesugi, "Mass Spectrometric Study of Ga(CH₃)₃ and Ga(C₂H₅)₃ Decomposition Reaction in

- H₂ and N₂," *J. Electrochem. Soc. Solid-State Sci. Technol.*, vol. 132, no. 3, pp. 677–679, 1985.
- [9] M. Mashita *et al.*, "THE PYROLYSIS TEMPERATURE OF TRIETHYLGALLIUM IN THE PRESENCE OF ARSINE OR TRIMETHYLALUMINUM," *J. Cryst. Growth*, vol. 77, pp. 194–199, 1986.
- [10] C. A. Larsen, S. H. Li, and G. B. Stringfellow, "Decomposition mechanisms of TBAs," *J. Cryst. Growth*, vol. 94, pp. 663–672, 1989.
- [11] N. I. Buchan, C. A. Larsen, and G. B. Stringfellow, "A mass spectrometric study of the simultaneous reaction mechanism of TMIn and PH₃ to grow InP," *J. Cryst. Growth*, vol. 92, no. 3–4, pp. 605–615, 1988.
- [12] C. H. Chen, C. A. Larsen, G. B. Stringfellow, D. W. Brown, and A. J. Robertson, "MOVPE growth of InP using isobutylphosphine and tert-butylphosphine," *J. Cryst. Growth*, vol. 77, no. 1–3, pp. 11–18, 1986.
- [13] C. A. Larsen, S. H. Li, N. J. Buchan, and G. B. Stringfellow, "Mechanisms Of GaAs Growth Using Tertiarybutylarsine And Trimethylgallium," *J. Cryst. Growth*, vol. 94, pp. 673–682, 1989.
- [14] C. A. Larsen, N. I. Buchan, and G. B. Stringfellow, "Mass spectrometric studies of phosphine pyrolysis and OMVPE growth of InP," *J. Cryst. Growth*, vol. 85, pp. 148–153, 1987.
- [15] C. A. Larsen, C. H. Chen, M. Kitamura, G. B. Stringfellow, D. W. Brown, and A. J. Robertson, "Organometallic vapor phase epitaxial growth of InP using new phosphorus sources," *Appl. Phys. Lett.*, vol. 48, no. 22, pp. 1531–1533, 1986.
- [16] C. A. Larsen, N. I. Buchan, and G. B. Stringfellow, "Reaction mechanisms in the organometallic vapor phase epitaxial growth of GaAs," *Appl. Phys. Lett.*, vol. 52, no. 6, pp. 480–482, 1987.
- [17] L. Nattermann *et al.*, "MOVPE growth of Ga(AsBi)/GaAs using different metalorganic precursors," *J. Cryst. Growth*, vol. 426, pp. 54–60, 2015.
- [18] L. Nattermann, A. Beyer, P. Ludewig, T. Hepp, E. Sterzer, and K. Volz, "MOVPE growth of Ga(PBi) on GaP and GaP on Si with Bi fractions up to 8%," *J. Cryst. Growth*, vol. 463, pp. 151–155, 2017.
- [19] K. Forghani *et al.*, "Self-limiting growth when using trimethyl bismuth (TMBi) in the metal-organic vapor phase epitaxy (MOVPE) of GaAs 1 {Å} y Bi y," *J. Cryst. Growth*, vol. 395, pp. 38–45, 2014.
- [20] E. Sterzer *et al.*, "(GaIn)(NAs) growth using di-tertiary-butyl-arsano-amine (DTBAA)," *J. Cryst. Growth*, 2017.
- [21] E. Sterzer *et al.*, "Novel nitrogen/gallium precursor [Ga(bdma)H₂] for MOVPE," *J. Cryst. Growth*, vol. 454, pp. 173–179, 2016.
- [22] E. Sterzer *et al.*, "Efficient nitrogen incorporation in GaAs using novel metal organic As-N precursor di-tertiary-butyl-arsano-amine (DTBAA)," *J. Cryst. Growth*, vol. 439, pp. 19–27, 2016.
- [23] B. Kunert, K. Volz, I. Nemeth, and W. Stolz, "Luminescence investigations of the GaP-based dilute nitride Ga(NAsP) material system," *J. Lumin.*, vol. 121, no. 2 SPEC. ISS., pp. 361–364, 2006.
- [24] G. Zimmermann *et al.*, "New Developments of Less Toxic Group-V Precursors for the Metalorganic Vapour Phase Epitaxy of III – V-Semiconductors : In -Situ-Formation of As – H Functions by Thermal β- Elimination of Specific As-Trialkyl Compounds," *J. Appl. Phys.*, vol. 35, pp. 2035–2042, 1996.
- [25] R. Dorn *et al.*, "New group III aluminium and gallium hydride precursors for metal-organic vapour-phase epitaxy," *Mater. Sci. Eng. B*, vol. 17, no. 1–3, pp. 21–24, 1993.
- [26] G. Zimmermann *et al.*, "Amino-arsine and -phosphine compounds for the MOVPE of III-V semiconductors," *J. Cryst. Growth*, vol. 129, no. 1–2, pp. 37–44, 1993.
- [27] G. Zimmermann, H. Protzmann, W. Stolz, and E. O. Göbel, "In-situ formation of As-H functions by Beta-elimination of specific metalorganic arsenic compounds for the MOVPE of III/V semiconductors," *J. Cryst. Growth*, vol. 124, pp. 136–141, 1992.
- [28] P. W. Lee, T. R. Omstead, D. R. McKenna, and K. F. Jensen, "In situ mass spectroscopy studies of the decomposition of organometallic arsenic compounds in the presence of Ga(CH₃)₃ and Ga(C₂H₅)₃," *J. Cryst. Growth*, vol. 93, no. 1–4, pp. 134–142, 1988.
- [29] NIST Mass Spectrometry Data Center, "Standart Reference Database Nr 69, <http://webbook.nist.gov/chemistry/>," *Choice Reviews Online*. U.S. Secretary of Commerce, on behalf of the United States of America, 2017.
- [30] G. Zimmermann, *Einfluss neuartiger Ausgangsmaterialien in der MOVPE auf die physikalischen Eigenschaften von III/V Halbleitern*, 1st ed. Marburg: Cuvillier Verlag Göttingen, 1994.
- [31] D. F. Foster, C. Glidewell, and D. J. Cole-Hamilton, "Probing the Mechanisms of Growth of Gallium Arsenide by Metalorganic Vapor Phase Epitaxy Using Experimental and Theoretical Studies of Designed Precursors," *J. Electron. Mater.*, vol. 23, no. 2, 1994.
- [32] A. Stegmüller and R. Tonner, "Hydrogen Elimination Mechanism in the Absence of Low-Lying Acceptor Orbitals in EH₂(t-C₄H₉) (E = N-Bi)," *Inorg. Chem.*, vol. 54, no. 13, pp. 6363–6372, 2015.
- [33] A. Stegmüller and R. Tonner, "A quantum chemical descriptor for CVD precursor design: Predicting decomposition rates of TBP and TBAs isomers and derivatives," *Chem. Vap. Depos.*, vol. 21, no. 7–9, pp. 161–165, 2015.

6.2.2 MOVPE Growth of Ga(PBi) on GaP and GaP on Si With Bi Fractions up to 8% ¹

L. Nattermann, A. Beyer, P. Ludewig, T. Hepp, E. Sterzer, K. Volz,
Journal of Crystal Growth **463**, pp. 151-155 (2017). DOI: 10.1016/j.jcrysgro.2017.02.021

Abstract

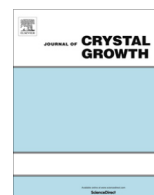
Dilute bismide containing materials can play an important role in addressing the issue of finding new highly efficient lasers for telecommunications as well as sensing applications. In the last several years a growing body of literature has emerged, particularly on the growth of Ga(AsBi). However, the metal organic vapor phase epitaxy growth of Ga(AsBi) with high amounts of Bi, which are necessary to overcome Auger recombination and reach telecommunications wavelengths, still remains a challenge. Ga(PBi) could be a promising alternative, but has not been deposited with significant amounts of Bi so far. A second argument for Ga(PBi) is that it could be grown on GaP, which was already deposited on Si. A number of researchers have reported theoretical calculations on the band structure of Ga(PBi), but experimental results are still lacking.

In this work we present the first Ga(PBi) structures, grown by metal organic vapor phase epitaxy on GaP and on GaP on Si. By careful characterization with high resolution X-ray diffraction, atomic force microscopy, secondary ion mass spectrometry and scanning transmission electron microscopy, we will show that we have realized high quality Ga(PBi) with Bi fractions over 8%.

The Authors contribution

My contribution to this work was the planning, execution and interpretation of all experiments including the MOVPE growth and analysis by HR-XRD. The preparation and investigation of the samples with STEM was performed by A. Beyer. All co-authors helped to interpret the data and to improve the manuscript that was written by me.

¹ Reprinted from *Journal of Crystal Growth* **463** (2017) 151-155, Copyright 2016, with permission from Elsevier.



MOVPE growth of Ga(PBi) on GaP and GaP on Si with Bi fractions up to 8%



L. Nattermann*, A. Beyer, P. Ludewig, T. Hepp, E. Sterzer, K. Volz

Material Sciences Center and Faculty of Physics, Philipps-Universität Marburg, Germany

ARTICLE INFO

Article history:

Received 22 November 2016
Received in revised form 13 February 2017
Accepted 14 February 2017
Available online 16 February 2017
Communicated by C. Caneau

Keywords:

A1. High resolution X-ray diffraction
A3. Metalorganic vapor phase epitaxy
B2. Semiconducting III–V materials
B2. Semiconducting compounds on silicon
B3. Infrared device

ABSTRACT

Dilute bismide containing materials can play an important role in addressing the issue of finding new highly efficient lasers for telecommunications as well as sensing applications. In the last several years a growing body of literature has emerged, particularly on the growth of Ga(AsBi). However, the metal organic vapor phase epitaxy growth of Ga(AsBi) with high amounts of Bi, which are necessary to overcome Auger recombination and reach telecommunications wavelengths, still remains a challenge. Ga(PBi) could be a promising alternative, but has not been deposited with significant amounts of Bi so far. A second argument for Ga(PBi) is that it could be grown on GaP, which was already deposited on Si. A number of researchers have reported theoretical calculations on the band structure of Ga(PBi), but experimental results are still lacking.

In this work we present the first Ga(PBi) structures, grown by metal organic vapor phase epitaxy on GaP and on GaP on Si. By careful characterization with high resolution X-ray diffraction, atomic force microscopy, secondary ion mass spectrometry and scanning transmission electron microscopy, we will show that we have realized high quality Ga(PBi) with Bi fractions over 8%.

© 2017 Elsevier B.V. All rights reserved.

1. Introduction

One of the main reasons for the growing body of publications [1] on Bi containing III/Vs is the substantial reduction of band gap energy achieved by adding small amounts of Bi. For example, a band gap reduction between 80 and 90 meV per % Bi has been calculated and experimentally confirmed for Ga(AsBi) [2–5]. Additionally, it was found in previous studies that an Auger recombination process leading to the excitation of a hot hole into the spin-orbit split-off sub-band is responsible for the majority of the injected current in currently used near-infrared lasers [6,7]. As the spin-orbit splitting increases drastically with increasing Bi fraction, this heat generating loss process can be suppressed for Bi fractions higher than 10% in Ga(AsBi), since then the spin-orbit splitting becomes larger than the band gap [5]. Other Bi containing materials, such as (GaIn)(AsBi), Ga(PAsBi), Ga(NAsBi), In(PBi), In(SbBi) or Ga(SbBi) have been presented, and similar properties have been observed [8–11]. The main challenge faced by many metal organic vapor phase experiments (MOVPE) is realizing high quality material for highly efficient optoelectronic applications

with a high enough Bi-incorporation as needed for the application. Ga(PBi) could be a promising candidate for realizing a telecommunication wavelength emission laser [12,13] and additionally presents the possibility of realizing laser applications on Si, as Ga(PBi) is grown on GaP and GaP can be deposited nearly lattice-matched on Si [14]. P was already used for the growth of another Bi containing III/V semiconductor, Ga(PAsBi) [15,16]. However, Ga(PAsBi) was grown lattice matched on GaAs and large differences of the gas phase due to TBAs supply make a direct comparison to the growth characteristics of Ga(PBi) on GaP difficult. Samajdar et al. and Polak et al. recently reported on theoretical band structure calculations for Ga(PBi) [12,13]. They calculated different band shifts per percent Bi, 67 meV [12] and 206 meV [13]. Christian et al. published results on MBE grown Ga(PBi) samples up to 1.1% Bi [17,18]. Publications on the growth of Ga(PBi) with significant higher amounts of Bi and experimental results of Ga(PBi) for comparison and verification of theoretical calculations [1,12,13] are still lacking.

This work focuses on how the highly metastable material Ga(PBi) could be deposited by MOVPE. The first MOVPE grown Ga(PBi) layers will be presented and structurally characterised by means of scanning transmission electron microscopy (STEM), high resolution X-ray diffraction (HRXRD) and atomic force microscopy (AFM).

* Corresponding author.

E-mail address: lukas.nattermann@physik.uni-marburg.de (L. Nattermann).

2. Experimental procedure

All layers were grown using a commercially available Aixtron horizontal reactor system (AIX 200-reactor) with gas foil rotation. Pd purified H_2 carrier gas (10 N) was used at a reduced reactor pressure of 50 mbar. All Ga(PBi) layers were grown on exact n-type GaP (001) substrates or on GaP on Si templates [14]. For the growth on the GaP substrates, a 200 nm GaP buffer layer, deposited at 675 °C, implemented a high quality growth surface for the growth of all Ga(PBi) bulk structures. All Ga(PBi) layers in this study are between 50 and 200 nm thick. For the growth on GaP on Si, a 600 μ m thick Si substrate with a 35 nm GaP buffer layer was used, whereby 28 nm of the GaP were nucleated in an Aixtron closed coupled showerhead cluster reactor and 7 nm were grown in the horizontal reactor, right before the growth of the Ga(PBi) bulk layer. The nucleation of GaP on exact Si (001) substrates has been described before [14]. During the temperature ramps between the GaP buffer layers and Ga(PBi) layers, the GaP surface was TBP stabilized to prevent desorption of P atoms during the temperature change. The growth temperature of the Ga(PBi) layers was 400 °C or 450 °C. Triethylgallium (TEGa), tertiary-butylphosphine (TBP) and trimethylbismuth (TMBi) were used as precursors for gallium, phosphorus and bismuth, respectively.

For the investigations of the different layers we used (HRXRD) in a Panalytical X'Pert Pro diffractometer to determine the growth rate as well as Bi-incorporation. The HRXRD pattern was simulated around the (004)-GaP substrate peak, assuming the GaBi lattice constant to be 6.33 Å [19]. AFM images were taken with a Nanoscope IIIa in tapping mode to study surface morphologies and metallic droplets on the surface. The STEM HAADF (high angle annular dark field) micrographs were taken with a double C_s corrected JEOL 2200FS microscope operating at 200 kV. Image series consisting of seven individual images were acquired and aligned non-rigidly using the Smart-Align software [20] to enhance the signal-to-noise ratio.

First, the results of the variation of Bi supply, TBP/TEGa ratio, temperature and group III supply for the deposition on GaP substrates will be discussed. Afterwards, the results on the growth of Ga(PBi) on GaP on Si will be presented. Finally, the first STEM micrographs of Ga(PBi) layers will be introduced.

3. Ga(PBi) on GaP

3.1. Results

As there is no literature on the growth parameters of Ga(PBi) at all, experience from previous studies on dilute Ga(AsBi) [21,22] was used to begin the deposition of the novel material. A suitable parameter set was found where growth of this highly metastable material is possible. At 400 °C growth temperature, a TBP/TEGa ratio of 20 and a high partial pressure of group III - $Pp(TEGa) = 0.042$ mbar (25.484 μ mol/min) - and a total flux of 6800 ml, the first Bi incorporation was observed. Afterwards, at first, the Bi supply was systematically varied. Fig. 1 shows the HRXRD measurements of the resulting samples. As the TMBi supply increases, the Bi fraction in the layer increases until a certain saturation level, where further increase of the Bi supply does not lead to a higher Bi incorporation, but droplets on the surface and a decreasing growth rate occur [23]. The disappearance of the Pendellösung fringes of the Ga(PBi) layer also indicates a decreasing layer- and interface quality, when the TMBi supply is further increased after the region of saturation was entered. AFM scans were performed to get information about surface quality and formation of Bi droplets. Fig. 2a and b show two AFM images depicting the surfaces of structures A and B, marked in Figs. 1 and 3a. Smooth surfaces

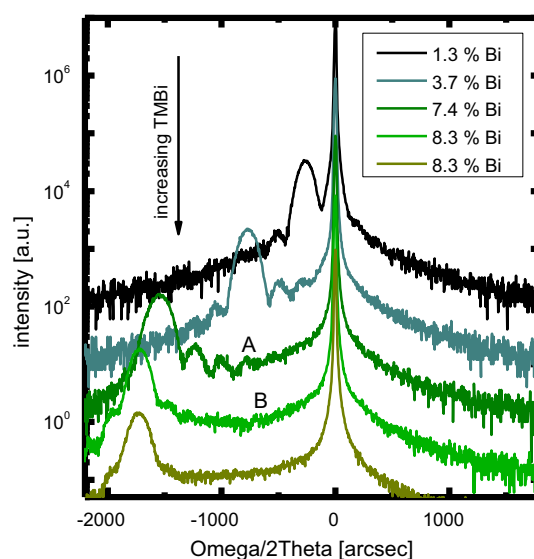


Fig. 1. HRXRD measurements on Ga(PBi) layers from 1.3 to 8.3% Bi.

were realized. In Fig. 2a, which shows a layer below the saturation region, one can see a droplet-free surface, while 2b shows a layer above the saturation level, with a high density of Bi droplets. This behaviour of droplet formation was observed for all growth parameter sets discussed in Fig. 3. Before the region of Bi saturation, the surface gets smoother with increasing TMBi supply; as the region of Bi saturation is entered, increasing TMBi supply leads to increasing roughness and density of droplets.

An overview of the growth results and the different influences of growth parameter variations are given in Fig. 3. First the figure will be described and an interpretation of the data will follow.

The Bi incorporation vs. the partial pressure of the Bi source is shown in Fig. 3a; the growth rate is depicted in Fig. 3b. With increasing $Pp(TMBi)$, the Bi fraction in the layer increases up to 8.3% Bi, to a saturation of Bi incorporation for a TBP/TEGa ratio of 20 (round filled data points) as illustrated in the HRXRD plots in Fig. 1. The TBP/TEGa ratio was varied, in order to determine the dependence of the Bi incorporation and the growth rate on the TBP/TEGa ratio. As one can see, the saturation level of the Bi incorporation decreases down to Bi fractions of 6.4% when the TBP/TEGa ratio is halved by decreasing the TBP by a factor of two (triangular data points).

As low temperatures could lead to a higher defect density and a higher C incorporation due to inefficient decomposition of the metalorganic chemicals, the growth characteristics at a higher temperature were also investigated. Fig. 3c and d shows the comparison of the growth at 400 °C as discussed before (round filled data points) and the growth at 450 °C (circular data points) under otherwise identical growth conditions. In Fig. 3c one can see that the saturation level of the Bi fraction shifts downwards for the higher growth temperature. At 450 °C, the growth rate (Fig. 3d) is higher compared to 400 °C by more than a factor of four, but the growth rate of Ga(PBi) drops suddenly to that at 400 °C for $Pp(TMBi) > 0.001$ mbar (0.606 μ mol/min). The large error bars for the two experiments at 450 °C in Fig. 3d are caused by a broader main peak and the disappearance of the Pendellösung fringes in the XRD pattern which leads to a larger uncertainty.

As a third parameter the TEGa partial pressure was of interest, as it is known from previous studies on Ga(AsBi) that the growth rate, varied by the group III supply, affects the Bi incorporation [21]. As the $Pp(TEGa)$ was decreased by a factor of two (TBP/TEGa was kept constant), the Bi fraction saturation level decreased, and the saturation region starts at lower TMBi supplies (see Fig. 3e).

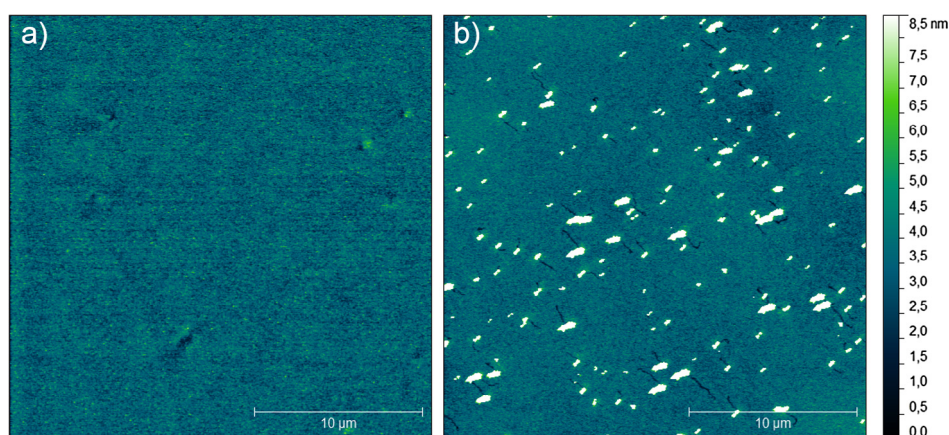


Fig. 2. AFM images of two Ga(PBi) layers A and B, see also Figs. 1 and 3a.

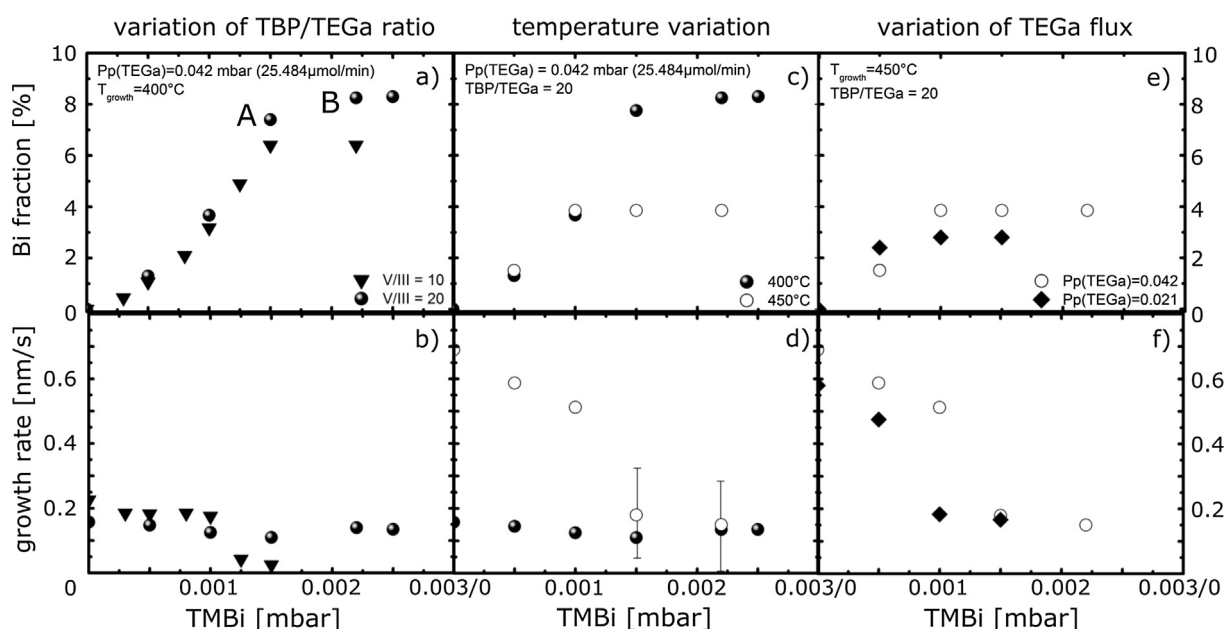


Fig. 3. Growth characteristics for Ga(PBi). Plotted is the Bi fraction and the growth rate vs. TMBi supply for different TBP/TEGa ratios (a and b), temperatures (c and d) and TEGa partial pressures (e and f). The large error bar in figure (d) is caused by a broader main peak of the XRD pattern and a disappearance of the Pendelösung fringes which leads to a larger uncertainty. The other uncertainties are within the size of the data points.

The growth rate of the growth with the lower group III supply decreases earlier, already at $P_p(\text{TMBi}) = 0.001$ mbar, Fig. 3f.

3.2. Discussion

Coming to the interpretation of the data obtained, it is noteworthy that the TBP/TEGa ratio has an impact on the Bi fraction only when the growth takes place in the region of Bi saturation. When the TMBi supply is below the saturation level, the TBP/TEGa does not have any influence on the Bi fraction. While the growth rate decreases rapidly with increasing TMBi supply and when coming closer to the region of Bi saturation for the lower TBP/TEGa of 10, the growth rate stays approximately constant for the higher TBP/TEGa = 20. These findings lead to the assumption that surface reactions between (TB)P and (TM)Bi might enable a higher Bi incorporation - and in consequence a more constant growth rate -, since this behaviour is observable only if there is surplus Bi at the surface (saturation region) and such a behaviour has not been observed for

the growth of Ga(AsBi), so that an interaction between TEGa and TMBi seems to be unlikely. The details of the mechanism that leads to the higher Bi fraction and constant growth rate at higher TBP/TEGa (3a and b) need to be investigated by future gas-phase and surface in-situ measurements. However, the fact that only the TBP supply was varied and that the change is only observable in the region of Bi saturation leads to the assumption that reactions between TBP and TMBi, or some of their decomposition fragments, are responsible. Also Fig. 3e and f underline the argument of the importance of the TB(P)-(TM)Bi reactions, since the halved TBP/TMBi ratio leads to a lower Bi incorporation. Nevertheless, one has to be careful with this interpretation at this point, as also the halved group III supply has an impact on the Bi incorporation here (discussed below), so that there are multiple effects which are responsible for the changed Bi incorporation observed between the two parameter sets in Fig. 3e and f. The decrease of the growth rate for the lower TBP/TEGa, slightly before the Bi saturation region is entered, is also caused by another fact. Due to the low

decomposition rate of the TBP at 400 °C, even a small surface coverage of Bi already hinders connection to the surface and incorporation of the small decomposed amount of TBP.

The decrease in Bi incorporation by a factor of two from 400 °C to 450 °C can be explained by the fact that the segregation of Bi atoms to the surface is increased and less Bi stays in the crystal. Hence, also more Bi remains at the surface, blocking the growth front so that the crystal quality decreases (increasing uncertainty for growth rate) and the growth rate decreases down to that at 400 °C and finally the growth drops at $P_p(\text{TMBi}) = 0.0022$ mbar. This is different compared to the growth at 400 °C where deposition with this TMBi supply is still possible. The increasing growth rates at 450 °C for the lower TMBi supplies, indicate the low decomposition rates of TEGa, and especially TBP, at 400 °C and underline that gas-phase investigations would be of great interest to determine the gas-phase reactions and desorbed species from the growth surface, in order to make a detailed description of the growth mechanisms possible.

The variation of group III supply in Fig. 3e and f reveals, at halved TEGa supply, an expected decrease of the growth rate and a reduced Bi incorporation with an earlier beginning of saturation. This shift of the saturation region to lower Bi layer fractions and lower TMBi supplies is caused by a relatively higher amount of Bi atoms, segregating to the growth front, compared to the faster growth at higher TEGa partial pressures. However, the growth rate for the growth without TMBi supply decreases only by 15% when the TEGa supply is halved, although the group III supply was reduced by a factor of two. This can be explained by the fact that at these low temperatures not only TEGa is growth limiting but also TBP, as the decomposition rate of TBP is very low at these temperatures. Hence, also the absolute TBP/TEGa ratio must be adjusted to compare the growth rates, as the decomposition rates of TEGa and TBP change differently between 400 °C and 450 °C.

4. Ga(PBi) on GaP on Si

To verify whether Ga(PBi) can also be grown on Si substrate, some of the test layers before and after the saturation region were

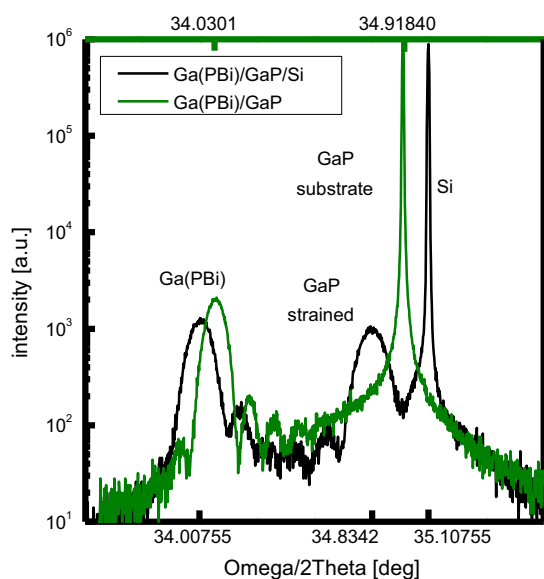


Fig. 4. HR-XRD results of a Ga(PBi) layer on GaP (green) and a Ga(PBi) layer on GaP on Si (black), grown under otherwise same growth conditions. The growth conditions were the one of sample B in Fig. 3a. (For interpretation of the references to color in this figure legend, the reader is referred to the web version of this article.)

deposited on a GaP on Si template under the same conditions used (Fig. 3a) for the growths on GaP. Results of HRXRD measurements on a Ga(PBi) layer on GaP in comparison to Ga(PBi) on GaP on Si are depicted in Fig. 4. The samples shown here are sample A from Figs. 1 and 3a and the Ga(PBi) layer grown under the same conditions, but on GaP on Si. Although there is a small lattice mismatch between the Si substrate and the GaP buffer layer, the Ga(PBi) layer on Si base contains the same amount of Bi under similar growth conditions as the layer grown on GaP substrate.

To look at the structural quality of the deposited Ga(PBi) layers in more detail, a dedicated STEM sample was grown and investigated by applying the HAADF technique.

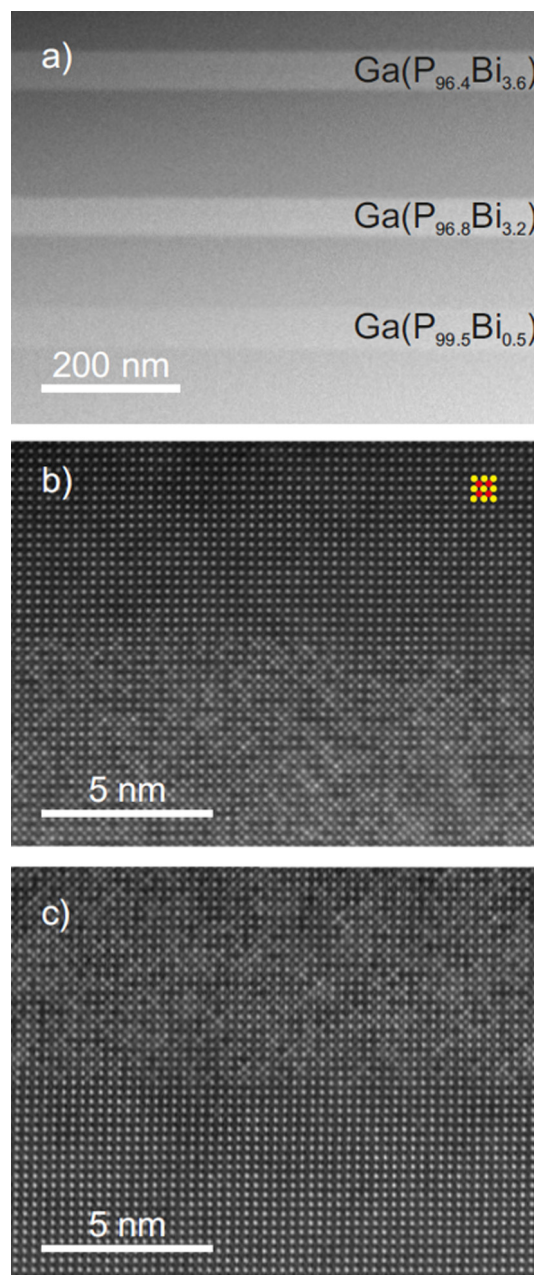


Fig. 5. HAADF overview image of the dedicated TEM structure containing Ga(PBi) layers with different compositions (a). Atomic resolution HAADF images of the upper and lower interface of the $\text{Ga}(\text{P}_{96.4}\text{Bi}_{3.6})$ layer (b) and (c), respectively. In all images the viewing direction is [010] and the growth direction is from bottom to top.

An overview image of the sample viewed along the [010] zone axis is depicted in Fig. 5a; the growth direction is from bottom to top. All three layers have Bi fractions below the saturation region. The first layer was grown under a TBP/TEGa ratio of 10, the second and the third layer were grown with a TBP/TEGa ratio of 20 (from bottom to top). The Bi containing layers appear bright in the darker GaP matrix due to Z contrast [24]. The individual layers exhibit a homogenous intensity distribution, which means no phase separation or segregation is present. Additionally, the interfaces between the Ga(PBi) layers and the GaP barriers appear abrupt.

To further confirm this finding, exemplary atomic resolution images of the upper and lower interface of the layer with a Bi fraction of 3.6% are shown in 5b and c, respectively. A two dimensional unit cell of GaP is marked in the upper right corner of 5b. Here yellow circles represent group III atomic columns, whereas red¹ circles represent the group V columns. The Ga(PBi) can be clearly distinguished from the pure GaP by the increased intensity of the group V lattice sites. At both interfaces, the transition from GaP to Ga(PBi) and vice versa occurs within a few monolayers, confirming the abruptness of the interfaces.

5. Summary

The first experimental results on the Ga(PBi) samples were presented. Comprehensive growth studies show strong dependencies between Bi incorporation and growth rate and TBP/TEGa ratio, temperature and group III supply. By doubling the TBP/TEGa ratio, a 25% higher Bi incorporation was achieved, while the growth rate was kept approximately constant independently of the supply of TMBi, even for the highest TMBi supplies used. 400 °C turned out to be the optimum growth temperature, since an increase of the growth temperature up to 450 °C led to a decrease of Bi incorporation by 50% and a diminishing structural quality. A variation of group III supply showed a slight increase of Bi incorporation and growth rate for a higher TEGa supply. AFM and STEM studies showed that the deposition of high structural quality Ga(PBi) with Bi fractions over 8% were realized on GaP and on GaP on Si substrates. From a structural point of view, excellent III/V material deposition on Si substrates was achieved. Further optoelectronic experiments have to show if Ga(PBi) can be a promising candidate for various lasing and sensing applications.

Acknowledgments

We gratefully acknowledge support from German Science Foundation (DFG) in the framework of the RTG1782 “Functionalization of Semiconductors” as well as from the HMWK in the framework of the project EGALITE.

References

- [1] H. Li, Z.M. Wang, *Bismuth-Containing Compounds*, vol. 186, Springer New York, New York, NY, 2013.
- [2] K. Alberi, O.D. Dubon, W. Walukiewicz, K.M. Yu, K. Bertulis, A. Krotkus, Valence band anticrossing in GaBi_xAs_{1-x}, *Appl. Phys. Lett.* 91 (5) (2007) 051909.
- [3] M. Usman, C.A. Broderick, A. Lindsay, E.P. O'Reilly, Tight-binding analysis of the electronic structure of dilute bismide alloys of GaP and GaAs, *Phys. Rev. B* 84 (24) (2011) 245202.
- [4] P. Ludewig, N. Knaub, N. Hossain, S. Reinhard, L. Nattermann, I.P. Marko, S.R. Jin, K. Hild, S. Chatterjee, W. Stolz, S.J. Sweeney, K. Volz, Electrical injection Ga (AsBi)/(AlGa)As single quantum well laser, *Appl. Phys. Lett.* 102 (24) (2013).
- [5] S.J. Sweeney, S.R. Jin, Bismide-nitride alloys: promising for efficient light emitting devices in the near- and mid-infrared, *J. Appl. Phys.* 113 (4) (2013) 043110.
- [6] A.F. Phillips et al., The temperature dependence of 1.3 μm and 1.5 μm compressively strained InGaAs(P) MQW semiconductor lasers, *IEEE J. Sel. Top. Quantum Electron.* 5 (1999) 401.
- [7] S.J. Sweeney et al., Dependence of threshold current on QW position and on pressure in 1.5 μm InGaAs(P) lasers, *Phys. Status Solidi B* 211 (1999) 525.
- [8] W. Bennarndt, G. Boehm, M.-C. Amann, Domains of molecular beam epitaxial growth of Ga(In)AsBi on GaAs and InP substrates, *J. Cryst. Growth* 436 (2015) 56–61.
- [9] C.A. Broderick, P.E. Harnedy, R.J. Manning, E.P.O'Reilly, P. Ludewig, Z.L. Bushell, K. Volz, Determination of band offsets in dilute bismide GaBi_xAs_{1-x} quantum wells using polarization-resolved photovoltage spectroscopy and 12-band kp calculations, 2015.
- [10] Z.L. Bushell, P. Ludewig, N. Knaub, Z. Batool, K. Hild, W. Stolz, S.J. Sweeney, K. Volz, Growth and characterisation of Ga(NAsBi) alloy by metal–organic vapour phase epitaxy, *J. Cryst. Growth* 396 (2014) 79–84.
- [11] K. Wang, Y. Gu, H.F. Zhou, L.Y. Zhang, C.Z. Kang, M.J. Wu, W.W. Pan, P.F. Lu, Q. Gong, S.M. Wang, InPBi single crystals grown by molecular beam epitaxy, *Sci. Rep.* 4 (2014) 5449.
- [12] D.P. Samajdar, T.D. Das, S. Dhar, Valence band anticrossing model for GaSb1 – xBi_x and GaP1 – xBi_x using k.p method, *Mater. Sci. Semicond. Process.* 40 (2015) 539–542.
- [13] M.P. Polak, P. Scharoch, R. Kudrawiec, First-principles calculations of bismuth induced changes in the band structure of dilute Ga–V–Bi and In–V–Bi alloys: chemical trends versus experimental data, *Semicond. Sci. Technol.* 30 (9) (2015) 94001.
- [14] K. Volz, A. Beyer, W. Witte, J. Ohlmann, I. Németh, B. Kunert, W. Stolz, GaP-nucleation on exact Si (001) substrates for III/V device integration, *J. Cryst. Growth* 315 (1) (2011) 37–47.
- [15] K. Forghani, Y. Guan, M. Losurdo, G. Luo, D. Morgan, S.E. Babcock, A.S. Brown, L. J. Mawst, T.F. Kuech, GaAsPBi, an alternative reduced band gap alloy system lattice-matched to GaAs, *Appl. Phys. Lett.* 105 (111101) (2014).
- [16] L. Nattermann, P. Ludewig, N. Knaub, N.W. Rosemann, T. Hepp, E. Sterzer, S.R. Jin, K. Hild, S. Chatterjee, S.J. Sweeney, W. Stolz, K. Volz, MOVPE growth and characterization of quaternary Ga(PAsBi)/GaAs alloys for optoelectronic applications, *Appl. Mater. Today* 5 (209–214) (2016).
- [17] T.M. Christian, D.A. Beaton, K. Alberi, B. Fluegel, A. Mascarenhas, Mysterious absence of pair luminescence in gallium phosphide bismide, *Appl. Phys. Express* 8 (061202) (2015).
- [18] T.M. Christian, B. Fluegel, D.A. Beaton, K. Alberi, A. Mascarenhas, Bismuth-induced Raman modes in GaPBi, *J. Appl. Phys.* 55 (108002) (2016).
- [19] S. Tixier, M. Adamczyk, T. Tiedje, S. Francoeur, A. Mascarenhas, P. Wei, F. Schiettekatte, Molecular beam epitaxy growth of GaAs_{1-x}Bi_x, *Appl. Phys. Lett.* 82 (14) (2003) 2245–2247.
- [20] L. Jones, H. Yang, T.J. Pennycook, M.S.J. Marshall, S. Van Aert, N.D. Browning, M. R. Castell, P.D. Nellist, Smart align – a new tool for robust non-rigid registration of scanning microscope data, *Adv. Struct. Chem. Imag.* (2015) 1–16.
- [21] P. Ludewig, Z.L. Bushell, L. Nattermann, N. Knaub, W. Stolz, K. Volz, Growth of Ga(AsBi) on GaAs by continuous flow MOVPE, *J. Cryst. Growth* 396 (2014) 95–99.
- [22] L. Nattermann, P. Ludewig, L. Meckbach, B. Ringler, D. Keiper, C. Von Hänisch, W. Stolz, K. Volz, MOVPE growth of Ga(AsBi)/GaAs using different metalorganic precursors, *J. Cryst. Growth* 426 (2015) 54–60.
- [23] E. Sterzer, N. Knaub, P. Ludewig, R. Straubinger, A. Beyer, K. Volz, Investigation of the microstructure of metallic droplets on Ga(AsBi)/GaAs, *J. Cryst. Growth* 408 (2014) 71–77.
- [24] S.J. Pennycook, Z-contrast stem for materials science, *Ultramicroscopy* 30 (1989) 58–69.

¹ For interpretation of color in Fig. 5, the reader is referred to the web version of this article.

6.2.3 Exploiting Strain to Enhance the Bi Incorporation in GaAs-based III/V Semiconductors Using MOVPE ¹

L. Nattermann, P. Ludewig, E. Sterzer, K. Volz,
Journal of Crystal Growth **470**, pp. 15-19 (2017). DOI: 10.1016/j.jcrysgro.2017.04.005

Abstract

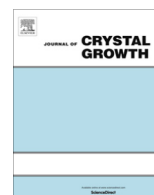
Bi containing III/V semiconductors are frequently mentioned for their importance as part of the next generation of optoelectronic devices. Bi containing ternary and quaternary materials like Ga(AsBi), Ga(NAsBi) or Ga(PAsBi) are promising candidates to meet the requirements for new laser structures for telecommunications and solar cell applications. However, in previous studies it was determined that the incorporation of sufficient amounts of Bi still poses a challenge, especially when using MOVPE (metalorganic vapour phase epitaxy) as the growth technique. In order to figure out which mechanisms are responsible for the limitation of Bi incorporation, this work deals with the question of whether there is a relationship between strain, induced by the large Bi atoms, and the saturation level of Bi incorporation in Ga(AsBi).

Ga(NAsBi) structures were grown by MOVPE at a low temperature, 400 °C, and compared to Ga(PAsBi) as well as Ga(AsBi) growth. By using the two group V atoms P and N, which have a smaller covalent radius than Bi, the effect of local strain compensation was investigated systematically. The comparison of Bi incorporation in the two quaternary materials systems proved the importance of local strain for the limitation of Bi incorporation, in addition to other effects, like Bi surface coverage and hydrocarbon groups at the growth surface. This, of course, also opens up ways to strain-state-engineer the Bi incorporation in semiconductor alloys.

The Authors contribution

My contribution to this work was the planning, execution and interpretation of all experiments including the MOVPE growth and analysis by HR-XRD and AFM. The preparation and investigation of the samples with SIMS was performed by *RTG Mikroanalyse GmbH Berlin*. All co-authors helped to interpret the data and to improve the manuscript that was written by me.

¹ Reprinted from *Journal of Crystal Growth* **470** (2017) 15-19, Copyright 2017, with permission from Elsevier.



Exploiting strain to enhance the Bi incorporation in GaAs-based III/V semiconductors using MOVPE



L. Nattermann*, P. Ludewig, E. Sterzer, K. Volz

Material Sciences Center and Faculty of Physics, Philipps-Universität Marburg, Hans-Meerwein-Str. 6, MzGb 02D 35a, 35032 Marburg, Germany

ARTICLE INFO

Article history:

Received 23 January 2017

Received in revised form 3 April 2017

Accepted 5 April 2017

Available online 7 April 2017

Communicated by T.F. Kuech

Keywords:

A3. Metalorganic vapour phase epitaxy

A1. Characterization

A1. High resolution X-ray diffraction

B1. Bismuth compounds

B2. Semiconducting III–V materials

ABSTRACT

Bi containing III/V semiconductors are frequently mentioned for their importance as part of the next generation of optoelectronic devices. Bi containing ternary and quaternary materials like Ga(AsBi), Ga(NAsBi) or Ga(PAsBi) are promising candidates to meet the requirements for new laser structures for telecommunications and solar cell applications. However, in previous studies it was determined that the incorporation of sufficient amounts of Bi still poses a challenge, especially when using MOVPE (metalorganic vapour phase epitaxy) as the growth technique. In order to figure out which mechanisms are responsible for the limitation of Bi incorporation, this work deals with the question of whether there is a relationship between strain, induced by the large Bi atoms, and the saturation level of Bi incorporation in Ga(AsBi).

Ga(NAsBi) structures were grown by MOVPE at a low temperature, 400 °C, and compared to Ga(PAsBi) as well as Ga(AsBi) growth. By using the two group V atoms P and N, which have a smaller covalent radius than Bi, the effect of local strain compensation was investigated systematically. The comparison of Bi incorporation in the two quaternary materials systems proved the importance of local strain for the limitation of Bi incorporation, in addition to other effects, like Bi surface coverage and hydrocarbon groups at the growth surface. This, of course, also opens up ways to strain-state-engineer the Bi incorporation in semiconductor alloys.

© 2017 Elsevier B.V. All rights reserved.

1. Introduction

The incorporation of bismuth (Bi) in III/V semiconductors can play an important role in addressing the development of the new generation of highly efficient optoelectronics devices [1–4]. A major problem of most of the currently used telecommunications lasers is their low efficiency, which is approximately 20% [5,6]. The need for cooling due to heat generating loss processes decreases the efficiency again by an order of magnitude. Bi leads to a strong reduction of the band gap by 80 meV per % Bi in GaAs and simultaneously shifts the spin orbit split-off band to lower energies. Therefore, Auger processes could be suppressed for Bi fractions above 11% Bi in GaAs [1,7–9]. Furthermore, a decreased sensitivity of band gap energy to temperature has been observed, which additionally increases the overall efficiency of Bi containing devices [10]. The quaternary materials systems Ga(PAsBi) and Ga(NAsBi) are also promising candidates for a 1 eV sub-cell in multi-junction solar cells, as the band gap and the lattice constant can be tuned independently from each other.

Nevertheless, as significant amounts of Bi are required, the metalorganic vapour phase epitaxy (MOVPE) growth of these Bi containing materials is challenging. In previous studies a saturation level of the Bi incorporation in GaAs has been reported [11–14]. This saturation level depends on temperature, growth rate and As/Ga input ratio; indeed the Bi incorporation in high quality Ga(AsBi) grown using MOVPE is still limited to a Bi fraction of 7%. Only in MBE grown samples have Bi fractions of more than 10% been realized, but temperatures as low as 200 °C are required. The growth of Ga(AsBi) above the saturation level of Bi incorporation leads to the formation of Bi- and GaBi-droplets at the surface [12,15]. The influence of strain on the composition of other III–V materials was investigated in several studies before, like for example in [16]–[18], but was not yet investigated for Bi containing materials. The influence of strain on the composition of quaternary bismides is the subject of this work.

In previous studies we and others have already reported on the influence of hydrocarbon groups on the surface and Bi surface coverage on the Bi incorporation [12,13]. We found that the use of Bi sources with different hydrocarbon rest groups does not show any difference in the influence on the growth of Ga(AsBi) [12]; consequently there is no large influence of the kind of alkyl groups on the surface on the blocking of the growth. Therefore, Ga(PAsBi)

* Corresponding author.

E-mail address: lukas.nattermann@physik.uni-marburg.de (L. Nattermann).

samples were realized in order to determine what effect the increasing tensile strain of Ga(PAs) has on the incorporation of Bi [19,20]. We have shown that the Bi incorporation can be increased by increasing the phosphorus (P) fraction while the supply of Bi is kept constant, as long as the growth takes place in the saturation region of Ga(AsBi) [20].

To determine whether the dependency between the supply of P and the Bi incorporation increase is strain induced, in this work Ga(NAsBi) layers were deposited and compared to the Ga(PAsBi) layers from [20]. By growing two different kinds of quaternary Bi layers, both with a group V element (P and nitrogen (N)) that has a smaller covalent radius than Bi, it can be demonstrated that compensating the local strain by P and N leads to an increasing Bi incorporation.

2. Experimental procedure

All samples presented in this work were grown by metal organic vapour phase epitaxy at 400 °C using a horizontal Aixtron Aix 200 GFR reactor and Pd purified H₂ as carrier gas (10 N). The reactor pressure was 50 mbar, and temperature control was provided by an infrared heating and water-cooling system. The temperature factor between the thermocouple in the susceptor and the sample surface was found by observing a phase change of the surface of an Al coated Si substrate. As metal organic precursors, triethylgallium (TEGa), tertiarybutylarsine (TBAs), tertiarybutylphosphine (TBP), trimethylbismuth (TMBi) and 1,1-dimethylhydrazine (UDMHy) were used to deposit the ternary and quaternary structures on semi insulating, exact GaAs (001) substrates. The partial pressures of TEGa and TBAs were $P_p(\text{TEGa}) = P_p(\text{TBAs}) = 0.042$ mbar, which resulted in growth rates between 0.1 and 0.5 nm per second.

For composition determination of the ternary layers, we used high resolution X-ray diffraction (HR-XRD) and the simulation software X'Pert Epitaxy by Panalytical. The HR-XRD pattern was simulated around the (004) GaAs-substrate peak, assuming the GaBi lattice constant to be 6.33 Å [21]. In order to get information about the composition of the quaternary layers Ga(PAsBi) and Ga(NAsBi), HR-XRD and secondary ion mass spectrometry (SIMS) were used, as HR-XRD alone does not provide enough information for composition determination of quaternary layer structures. Fig. 1a shows a HR-XRD pattern of a Ga(PAsBi) layer stack grown for SIMS investi-

gations. The layer structure of this example is GaAs substrate, Ga(PAs), GaAs, Ga(PAsBi), GaAs, Ga(AsBi) and a GaAs layer on top. With SIMS the Bi- and P- (or N-) content were determined in counts per second. The count rate from the SIMS measurements of the two ternary layers Ga(PAs) (or Ga(NAs)) and Ga(AsBi) were then used to determine the composition of P and Bi in % in correlation with the HR-XRD results in Fig. 1a. This procedure allows the conversion from a P- and Bi-count rate of the SIMS measurements to a P- and Bi-fraction in %, see Fig. 1b. The procedure was the same for all Ga(PAsBi) and Ga(NAsBi) samples.

3. Results and discussion

First the relation between strain and Bi incorporation will be examined. Afterwards, the results concerning relation between Bi surface coverage and P and N incorporation will be discussed.

Ga(AsBi), Ga(PAsBi) and Ga(NAsBi) layers were deposited under the same growth conditions. Fig. 2 illustrates the Bi incorporation characteristics and the growth rates for the growth of Ga(AsBi), Ga(PAsBi) and Ga(NAsBi). The Bi fraction in the layer vs. the partial pressure of TMBi is plotted for different partial pressures of TBP (figure a) and UDMHy (figure b). The growth rate vs TMBi is plotted for different partial pressures of TBP (figure c) and UDMHy (figure d). As shown in Fig. 2a the Bi incorporation saturates at a certain saturation level in Ga(AsBi). The start of the saturation level is defined as the point where further increase of the Bi supply does not lead to linearly increasing further Bi incorporation, but the formation of droplets on the surface. When TBP is introduced, the saturation level increases with increasing $P_p(\text{TBP})$. Further details about this behaviour can be found in [20]. A similar behaviour is illustrated in Fig. 2b for the growth with UDMHy instead of TBP. In general, the parameter window where the growth of Ga(NAsBi) is possible, was found to be smaller than for Ga(PAsBi). Additionally, the growth of Ga(NAsBi) is more sensitive to changes of the gas phase. Nevertheless, with increasing UDMHy supply, the Bi incorporation increases by shifting the saturation region, although the supply of Bi is constant. The growth rate decreases constantly with increasing Bi supply for both materials systems, see Fig. 2c and d. The decrease of the growth rate with $p(\text{TMBi})$ is reduced with increasing TBP and UDMHy supply, respectively. This was already found and discussed in previous studies [20] and is probably related to the Bi surface coverage.

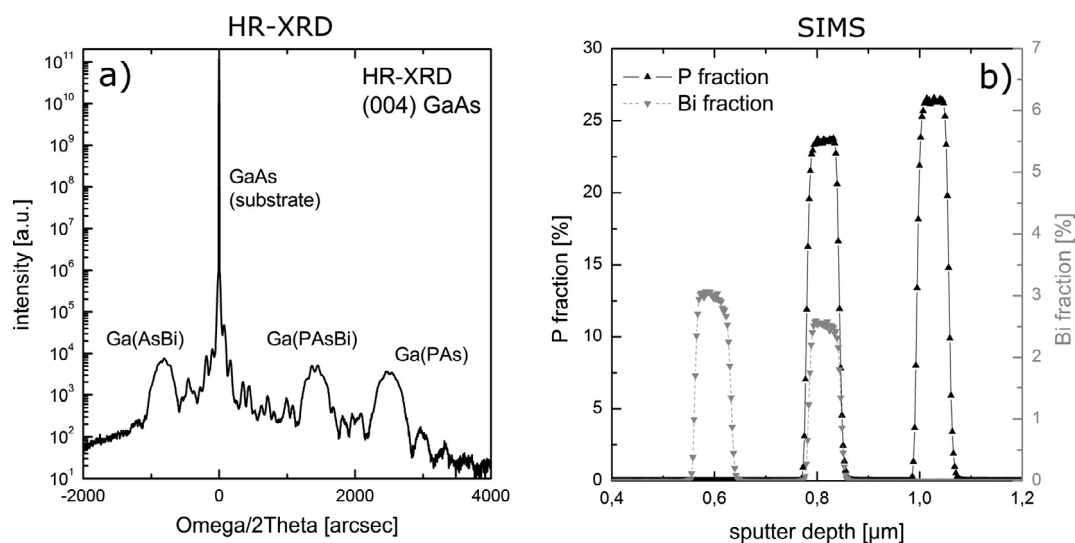


Fig. 1. HR-XRD pattern of a SIMS sample (a) and the SIMS results of the same sample (b). The P- and Bi-fractions are plotted in % after correlation of the SIMS count rate of the ternary layers with the HR-XRD pattern.

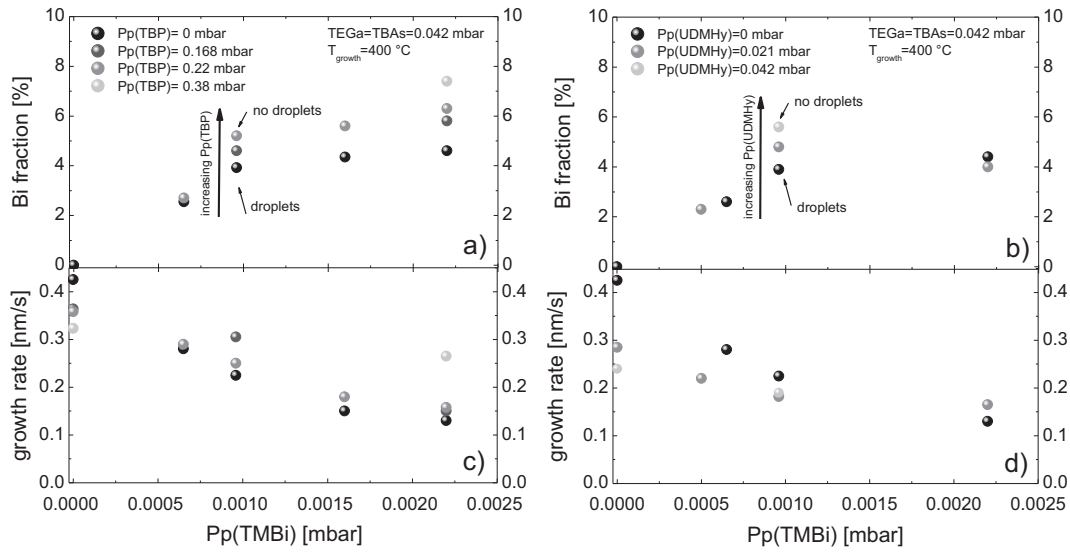


Fig. 2. Bi incorporation characteristics during the growth of Ga(PAsBi) (a) from [20] and Ga(NAsBi) (b), and growth rate of Ga(PAsBi) (c) and Ga(NAsBi) (d).

In the case of Ga(NAsBi), the decrease of the Bi fraction in the layer for the highest Bi supply is probably related to an increase of the UDMHy/TBAs ratio, which leads to a decrease of the Bi incorporation first and for even higher UDMHy/TBAs ratios to a drop of the Ga(NAsBi) growth rate. However, it is important that an increase of Bi fraction with increasing TBP or UDMHy can only be observed in the Bi saturation region. Below the saturation domain, the supply of TBP or UDMHy does not lead to a higher Bi fraction, which implies that all the Bi is already incorporated in the crystal. Once the Pp(TMBi) is in the Ga(AsBi) saturation region, additional P and N atoms can reduce the Bi induced compressive strain, due to the tensile strain of P and N and consequently increase the Bi incorporation. To prove this argument, Ga(NAsBi) layers were grown in order to investigate whether the same tensile strain introduced by N leads to the same increase of the Bi fraction as for the tensile strain from P.

Fig. 3a displays the dependency of strain induced by P, Bi and N in Ga(PAs), Ga(AsBi) and Ga(NAs) on the fraction of P, Bi and N. Following the addition of P and N, a tensile strain results, whereas

the addition of Bi leads to a compressive strain in GaAs. In Fig. 3b the Bi incorporation in quaternaries Ga(PAsBi) and Ga(NAsBi) is plotted vs. the strain from P and N in ternaries Ga(PAs) and Ga(NAs). The circular data points show the Bi fraction in the Bi saturation region. The diamond-shaped data points mark the Bi fraction below the saturation. It is obvious that in both cases, for Ga(PAsBi) and Ga(NAsBi), a given strain compensation by the smaller group V atoms leads to the same increase in Bi incorporation. This indicates that the strain is an important parameter, which is responsible for the limitation of Bi incorporation in GaAs based crystals.

The open circles in Fig. 3b depict the Bi fraction for a higher Bi supply. The increase of the Bi fraction with increasing Pp(TBP) is even higher for higher Pp(TMBi). Hence, the effect of strain compensation increases for the growth further in the saturation region, as more Bi is at the growth surface and can be incorporated.

The diamond-shaped data points illustrate that, below the saturation domain, most of the Bi is already incorporated into the Ga(AsBi) crystal. The introduction of P or N does not have an effect on

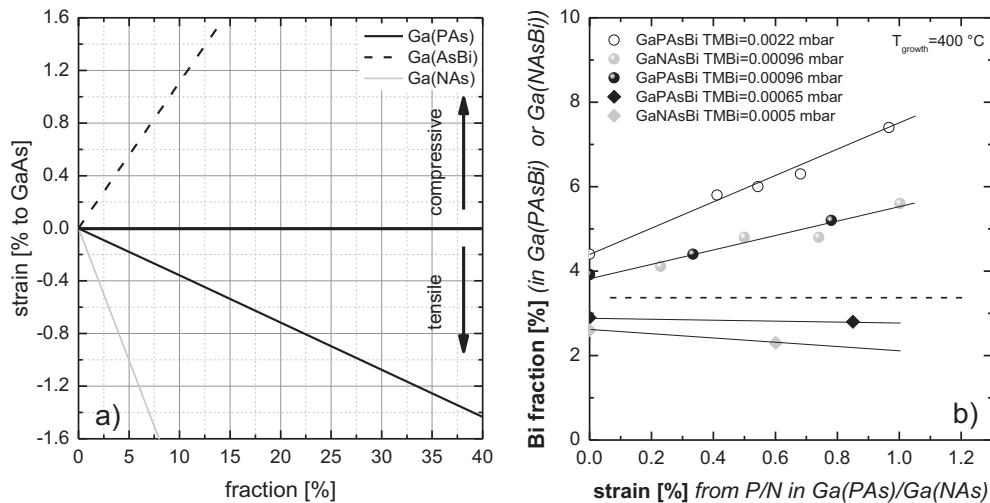


Fig. 3. Strain in ternary alloys plotted vs. fraction. Relation between Bi incorporation in quaternary Ga(PAsBi) and Ga(NAsBi) and the strain which is compensated by P and N in Ga(PAs) and Ga(NAs), respectively. The dashed line separates the samples grown with a Bi supply below and above the saturation for pure Ga(AsBi).

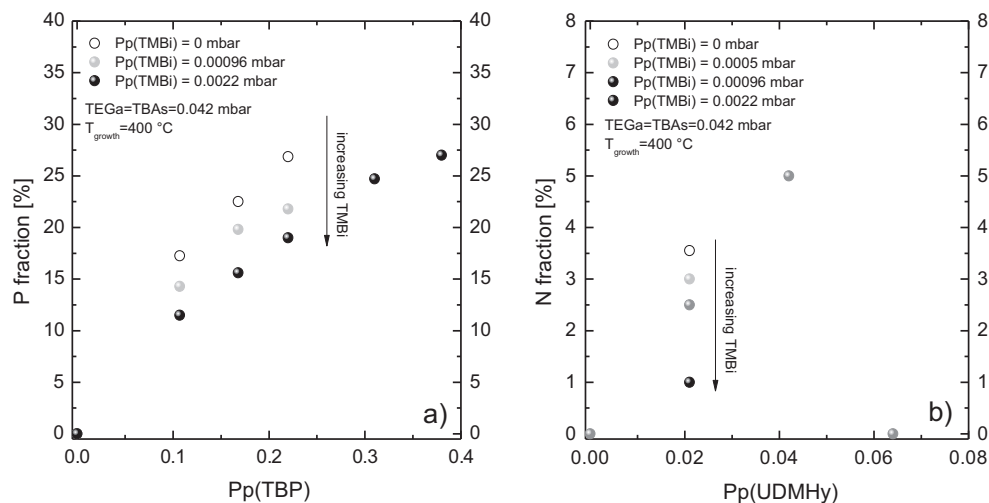


Fig. 4. P and N incorporation characteristics in Ga(PAsBi) (a) and Ga(NAsBi) (b). Plotted is the P fraction vs. the supply of TBP (a) and the N fraction vs. the supply of UDMHy (a) for different partial pressures of TMBi.

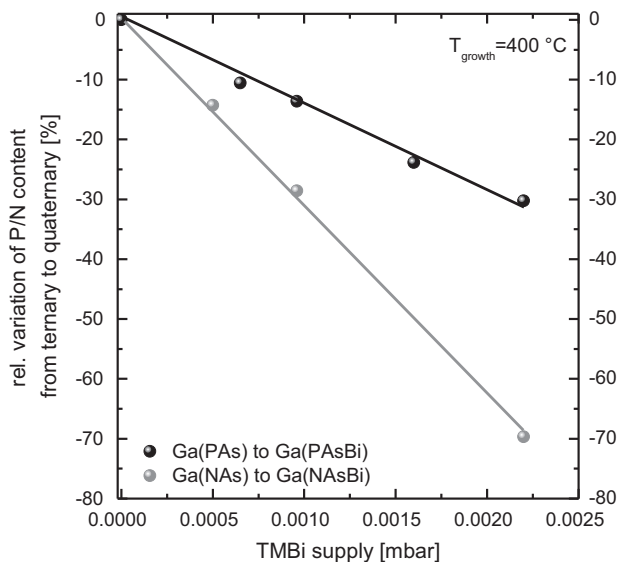


Fig. 5. P and N incorporation characteristics. Plotted is the relative variation of P/N content from the growth of Ga(PAs)/Ga(NAs) to Ga(PAsBi)/Ga(NAsBi) vs. the supply of TMBi. The growth temperature was 400°C . All growth conditions were constant except for Pp(TMBi).

the Bi incorporation, except for a slight decrease of the Bi fraction related to a significant change of the gas phase and growth surface, probably due to the relatively high partial pressures of TBP or UDMHy.

The incorporation characteristics of P and N are different from the incorporation mechanisms of Bi in Ga(PAsBi) and Ga(NAsBi). Fig. 4a displays the P fraction vs. Pp(TBP), Fig. 4b illustrates the dependency between N fraction and Pp(UDMHy) for different TMBi supplies. With increasing Pp(TBP), the P fraction increases. The same behaviour is observed for Ga(NAsBi) with increasing UDMHy supply. The highest P and N fractions can be observed without TMBi supply. With increasing TMBi supply, the P fraction in Ga(PAsBi), as well as the N fraction in Ga(NAsBi), decreases. This is probably due to the Bi surface coverage that blocks the growth surface and hinders the P and N molecules from connecting to the surface and, of course, a V/V competition between Bi and P. With

increasing Bi surface coverage the blocking increases; hence the incorporation of P or N decreases. The drop of the growth rate of Ga(NAsBi) for Pp(UDMHy) > 0.045 mbar is not fully understood yet and still under investigation. A change of the surface reconstruction during the growth due to an increase of the V/III ratio could be responsible for this behaviour.

To verify whether the Bi surface coverage is responsible for the decreasing P and N incorporation with increasing TMBi supply, the relative variation of the P or N content from ternary to quaternary growth ((quaternary content/ternary content)/ternary content * 100) is plotted vs. the Pp(TMBi) in Fig. 5. One can see that the decrease of the P and N content increases linearly with increasing TMBi supply. The reason for that is not definitively clarified, but the stronger decline of the N incorporation compared to the decrease of the P incorporation could be due to the order of magnitude higher partial pressures of the P source. In addition, the gas phase and surface reactions are different for UDMHy and TBP; hence a direct comparison of P and N incorporation is precarious in this case.

4. Summary

To address the question of the relation between strain and Bi incorporation, several Ga(PAsBi) and Ga(NAsBi) structures were grown with MOVPE at low temperature under variation of TMBi-, P-, and N-supply. It was shown that the saturation level for a certain Pp(TMBi) can be shifted to higher Bi fractions with additional group V atoms like P or N. This proves the assumption that strain is a very important factor of the limitation of Bi incorporation in GaAs. This might also open up a way to strain-engineer the Bi incorporation in III/V semiconductors. The incorporation of N and P on the other side is limited by the Bi surface coverage and hydrocarbon groups at the growth surface. It was observed that the N and P incorporation in Ga(PAsBi) and Ga(NAsBi) decreases with increasing the Bi supply.

Acknowledgment

We gratefully acknowledge support from German Science Foundation (DFG) in the framework of the RTG1782 "Functionalization of Semiconductors" as well as from the HMWK in the framework of the project EGALITE.

References

- [1] S.J. Sweeney, S.R. Jin, Bismide-nitride alloys: promising for efficient light emitting devices in the near- and mid-infrared, *J. Appl. Phys.* 113 (4) (2013) 043110, <http://dx.doi.org/10.1063/1.4789624>.
- [2] K. Alberi, O.D. Dubon, W. Walukiewicz, K.M. Yu, K. Bertulis, A. Krotkus, Valence band anticrossing in $\text{GaBi}_x\text{As}_{1-x}$, *Appl. Phys. Lett.* 91 (5) (2007) 051909, <http://dx.doi.org/10.1063/1.2768312>.
- [3] Z. Batool, K. Hild, T.J.C. Hosea, X. Lu, T. Tiedje, S.J. Sweeney, The electronic band structure of GaBiAs/GaAs layers: influence of strain and band anti-crossing, *J. Appl. Phys.* 111 (11) (2012) 113108, <http://dx.doi.org/10.1063/1.4728028>.
- [4] B. Breddermann, A. Bäumner, S.W. Koch, P. Ludewig, W. Stolz, K. Volz, J. Hader, J.V. Moloney, C.A. Broderick, E.P. O'Reilly, Luminescence properties of dilute bismide systems, *J. Lumin.* 154 (2014) 95–98, Oct. <<http://www.sciencedirect.com/science/article/pii/S0022231314002518>>.
- [5] S.J. Sweeney, A.F. Phillips, A.R. Adams, E.P. O'Reilly, P.J.A. Thijs, The effect of temperature dependent processes on the performance of 1.5- μm compressively strained InGaAs(P) MQW semiconductor diode lasers, *IEEE Photon. Technol. Lett.* 10 (8) (1998) 1076–1078, <http://dx.doi.org/10.1109/68.701507>, Aug..
- [6] A.F. Phillips, S.J. Sweeney, A.R. Adams, P.J.A. Thijs, The temperature dependence of 1.3- and 1.5- μm compressively strained InGaAs(P) MQW Semiconductor Lasers, *IEEE J. Selcted Top Quantum Electron.* 5 (3) (1999) 401–412, <http://dx.doi.org/10.1109/2944.788398>.
- [7] K. Alberi, J. Wu, W. Walukiewicz, K.M. Yu, O.D. Dubon, S. Watkins, C. Wang, X. Liu, Y.-J. Cho, J. Furdyna, Valence-band anticrossing in mismatched III–V semiconductor alloys, *Phys. Rev. B* 75 (4) (2007) 045203, <http://dx.doi.org/10.1103/PhysRevB.75.045203>, Jan..
- [8] M. Usman, C.A. Broderick, A. Lindsay, E.P. O'Reilly, Tight-binding analysis of the electronic structure of dilute bismide alloys of GaP and GaAs , *Phys. Rev. B* 84 (24) (2011) 245202, <http://dx.doi.org/10.1103/PhysRevB.84.245202>, Dec..
- [9] C.A. Broderick, P.E. Harnedy, R.J. Manning, E.P. O'Reilly, P. Ludewig, Z.L. Bushell, K. Volz, Determination of band offsets in dilute bismide GaBiAs_{1-x} quantum wells using polarization-resolved photovoltage spectroscopy and 12-band kp calculations (2015), <http://dx.doi.org/10.1088/0268-1242/30/9/094009>.
- [10] K. Oe, H. Okamoto, New semiconductor alloy $\text{GaAs}_{1-x}\text{Bi}_x$ grown by metal organic vapor phase epitaxy, *Jpn. J. Appl. Phys.*, vol. 37, no. Part 2, No. 11A, pp. L1283–L1285, Nov. 1998, <http://dx.doi.org/10.1143/JJAP.37.L1283>.
- [11] P. Ludewig, N. Knaub, W. Stolz, K. Volz, MOVPE growth of Ga(AsBi)/GaAs multi quantum well structures, *J. Cryst. Growth* 370 (2013) 186–190, <http://dx.doi.org/10.1016/j.jcrysgro.2012.07.002>, Jul..
- [12] L. Nattermann, P. Ludewig, L. Meckbach, B. Ringler, D. Keiper, C. von Hänisch, W. Stolz, K. Volz, MOVPE growth of Ga(AsBi)/GaAs using different metalorganic precursors, *J. Cryst. Growth* 426 (2015) 54–60, <http://dx.doi.org/10.1016/j.jcrysgro.2015.05.015>.
- [13] K. Forghani, Y. Guan, A.W. Wood, A. Anand, S.E. Babcock, L.J. Mawst, T.F. Kuech, Self-limiting growth when using trimethyl bismuth (TMBi) in the metal-organic vapor phase epitaxy (MOVPE) of $\text{GaAs}_{1-x}\text{Bi}_x$, *J. Cryst. Growth* 395 (2014) 38–45, <http://dx.doi.org/10.1016/j.jcrysgro.2014.03.014>.
- [14] I. Moussa, H. Fitouri, A. Rebey, B. El Jani, Atmospheric-pressure metalorganic vapour phase epitaxy optimization of GaAsBi alloy, *Thin Solid Films* 516 (23) (2008) 8372–8376, <http://dx.doi.org/10.1016/j.tsf.2008.04.062>.
- [15] E. Sterzer, N. Knaub, P. Ludewig, R. Straubinger, A. Beyer, K. Volz, Investigation of the microstructure of metallic droplets on Ga(AsBi)/GaAs , *J. Cryst. Growth* 408 (2014) 71–77, <http://dx.doi.org/10.1016/j.jcrysgro.2014.09.006>, Dec..
- [16] J.C. Harmand, A. Caliman, E.V.K. Rao, L. Largeau, J. Ramos, R. Teissier, L. Travers, G. Ungaro, B. Theys, I.F.L. Dias, GaNASb how does it compare with other dilute III–V-nitride alloys?, *Semicond. Sci. Technol.* 17 (8) (2002) 778–784, <http://dx.doi.org/10.1088/0268-1242/17/8/306>.
- [17] D.M. Wood, A. Zunger, Epitaxial effects on coherent phase diagrams of alloys, *Phys. Rev. B* 40 (6) (1989) 4062–4089, <http://dx.doi.org/10.1103/PhysRevB.40.4062>.
- [18] E. Sterzer, B. Ringler, L. Nattermann, A. Beyer, C. von Hänisch, W. Stolz, K. Volz, GaIn(NAs) growth using di-tertiary-butyl-arsano-amine (DTBAA), *J. Cryst. Growth* (2017), <http://dx.doi.org/10.1016/j.jcrysgro.2017.01.014>.
- [19] K. Forghani, Y. Guan, M. Losurdo, G. Luo, D. Morgan, S.E. Babcock, A.S. Brown, L. J. Mawst, T.F. Kuech, $\text{GaAs}_{1-y-z}\text{P}_y\text{Bi}_z$, an alternative reduced band gap alloy system lattice-matched to GaAs , *Appl. Phys. Lett.* 105 (11) (2014) 111101, <http://dx.doi.org/10.1063/1.4895116>.
- [20] L. Nattermann, P. Ludewig, N. Knaub, N.W. Rosemann, T. Hepp, E. Sterzer, S.R. Jin, K. Hild, S. Chatterjee, S.J. Sweeney, W. Stolz, K. Volz, MOVPE growth and characterization of quaternary Ga(PAsBi)/GaAs alloys for optoelectronic applications, *Appl. Mat. Today* 5 (2016) 209–214, <http://dx.doi.org/10.1016/j.apmt.2016.09.018>, Dec..
- [21] S. Tixier, M. Adamcyk, T. Tiedje, S. Francoeur, A. Mascarenhas, P. Wei, F. Schiettekatte, Molecular beam epitaxy growth of $\text{GaAs}_{1-x}\text{Bi}_x$, *Appl. Phys. Lett.* 82 (14) (2003) 2245–2247, <http://dx.doi.org/10.1063/1.1565499>.

6.2.4 MOVPE Growth and Characterization of Quaternary Ga(PAsBi)/GaAs Alloys for Optoelectronic Applications ¹

L. Nattermann, P. Ludewig, N. Knaub, N. W. Rosemann, T. Hepp, E. Sterzer, S. R. Jin, K. Hild, S. Chatterjee, S. J. Sweeney, W. Stolz, K. Volz,
Applied Materials Today **5**, pp. 209-214 (2016). DOI: 10.1016/j.apmt.2016.09.018

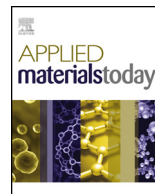
Abstract

Dilute bismide Ga(PAsBi)-based structures are promising candidates for highly efficient optoelectronic applications, like the 1 eV sub-cell in multi-junction solar cells or the active region in infra-red laser diodes. The band gap can be tuned independently from the lattice constant, which theoretically enables the deposition of lattice-matched layers in a wide range of band gap energies on GaAs substrate. In this work, firstly, the shifts in the band edge positions as a function of composition that are possible with the Ga(PAs(Bi)) alloy were estimated using the virtual crystal approximation and valence band anti-crossing theory. Secondly, systematic investigations on MOVPE growth of Ga(PAsBi) layers are presented. Finally, we show the first photoluminescence activity of quaternary Ga(PAsBi) and compare the experimental results to theory.

The Authors contribution

My contribution to this work was the planning, execution and interpretation of all experiments including the MOVPE growth and analysis by HR-XRD, and AFM. The theoretical data were calculated by S. R. Jin, K. Hild and S. J. Sweeney. The preparation and investigation of the STEM samples was performed by N. Knaub. The PL measurements were done by N. W. Rosemann and S. Chatterjee. All co-authors helped to interpret the data and to improve the manuscript that was written by me.

¹ Reprinted from *Applied Materials Today* **5** (2016) 209-214, Copyright 2016, with permission from Elsevier.



MOVPE growth and characterization of quaternary Ga(PAsBi)/GaAs alloys for optoelectronic applications

L. Nattermann^{a,*}, P. Ludewig^a, N. Knaub^a, N.W. Rosemann^a, T. Hepp^a, E. Sterzer^a, S.R. Jin^b, K. Hild^b, S. Chatterjee^a, S.J. Sweeney^b, W. Stolz^a, K. Volz^a

^a Material Sciences Center and Faculty of Physics, Philipps-Universität Marburg, Germany

^b Advanced Technology Institute and Department of Physics, University of Surrey, Guildford, Surrey GU2 7XH, UK

ARTICLE INFO

Article history:

Received 17 August 2016

Received in revised form

27 September 2016

Accepted 29 September 2016

Keywords:

Solar cells

Laser material

Metal organic chemical vapour deposition

Bismuth compounds

Semiconducting III-V materials

Characterization

Crystal morphology

ABSTRACT

Dilute bismide Ga(PAsBi)-based structures are promising candidates for highly efficient optoelectronic applications, like the 1 eV sub-cell in multi-junction solar cells or the active region in infra-red laser diodes. The band gap can be tuned independently from the lattice constant, which theoretically enables the deposition of lattice-matched layers in a wide range of band gap energies on GaAs substrate. In this work, firstly, the shifts in the band edge positions as a function of composition that are possible with the Ga(PAsBi) alloy were estimated using the virtual crystal approximation and valence band anti-crossing theory. Secondly, systematic investigations on MOVPE growth of Ga(PAsBi) layers are presented. Finally, we show the first photoluminescence activity of quaternary Ga(PAsBi) and compare the experimental results to theory.

© 2016 Elsevier Ltd. All rights reserved.

1. Introduction

Dilute bismuth (Bi) containing materials play an important role in developing highly efficient optoelectronic devices operating in the infrared wavelength region. A key advantage of alloying III/V semiconductors with Bi is the large band gap reduction by 80 meV per % Bi in GaAs [1,2]. Due to the large band gap reduction caused by Bi incorporation in GaAs, fundamental loss processes like Auger recombination can be suppressed, as the energetic difference between valence band and spin-orbit split-off band becomes larger than the band gap [2–5]. Additionally, a decreased sensitivity of band gap energy to temperature has been observed, which again increases the efficiency of Bi-containing devices [6]. These features have resulted in a growing body of literature that recognizes the importance of Bi-containing semiconductors for future optoelectronic devices [7]. However, the synthesis of Bi-containing materials with a significant amount of Bi remains a major challenge, especially when using MOVPE (metal organic vapour phase epitaxy), as high growth temperatures are needed [8–10]. In addition to the metastability, the deposition of Ga(AsBi) with Bi fractions

of more than 7% is technically challenging, since there is a large difference between the covalent radii of Bi and As, which leads to increasing strain with increasing Bi content [9], [11]. In order to compensate the compressive strain introduced by Bi, smaller P could be incorporated. Forghani et al. have first shown that in MOVPE grown Ga(PAsBi) layers, growth with PH₃ is possible [12].

In this work, firstly, the shifts in the band edge positions as a function of composition were estimated using the virtual crystal approximation and valence band anti-crossing theory. Secondly, systematic investigations on the growth of Ga(PAs) and Ga(PAsBi) layers with tertiarybutylphosphine (TBP) as P source were realized. In order to incorporate a significant amount of Bi, relatively low growth temperatures of 400 °C are required. Therefore, the growth of Ga(PAs) was investigated as a first step; as a second step, Bi was added to Ga(PAs). After comprehensive parameter variations and careful characterization, the growth characteristics of Ga(PAsBi) are discussed. Finally, we show the first photoluminescence activity of quaternary Ga(PAsBi) alloys and compare experimental results to theoretical predictions of the band extrema.

2. Structure modelling

To estimate the shifts in the band edge positions as a function of composition that are possible with the Ga(PAs(Bi)) alloy, the virtual crystal approximation (VCA) [13] and valence band anti-crossing

* Corresponding author at: Philipps-Universität Marburg, Hans-Meerwein-Str. 6 MzGb, Kern D02D 35a, Germany.

E-mail address: lukas.nattermann@physik.uni-marburg.de (L. Nattermann).

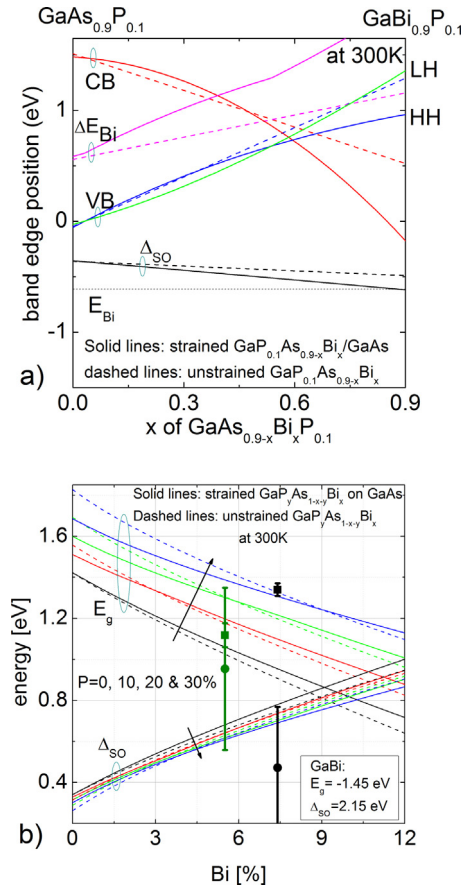


Fig. 1. (a) Shifts of CB, VB and SO bands of GaAs_{0.9-x}Bi_xP_{0.1} relative to the valence band maximum of GaAs with increasing Bi fraction at 300 K based on the VCA. (b) Unstrained and fully strained band gap and spin-orbit splitting energy of GaAs_{1-x-y}Bi_xP_y (on GaAs) at 300 K. Measured band gap (rectangles) and spin-orbit split-off (filled circles) for two different compositions in context to calculations (black 18284: 28% P, 7.4% Bi and green 18145: 15% P, 5.5% Bi). (For interpretation of the references to color in this figure legend, the reader is referred to the web version of this article.)

(VBAC) theory [4,14] were utilized. The conduction band, valence band and spin-orbit splitting band energies for Ga(PAs(Bi)) grown on a GaAs substrate were determined where strain was accounted for. All band and material parameters of Ga(PAs(Bi)) were used from the literature [4,13,14]. As an example, Fig. 1a shows the VCA-only shifts of CB, VB and SO bands of Ga(P_{0.1}As_{0.9-x}Bi_x) relative to the valence band maximum of GaAs with increasing Bi concentration at 300 K. There are three steps to calculate the fully strained band gap and spin-orbit splitting energy of Ga(PAsBi) on GaAs, as per other studied bismide alloys such as Ga(SbBi) [15], In(AsBi) and In(SbBi) [16]. Firstly, from the CB, VB and SO band edge positions of Ga(As_{0.9}P_{0.1}) (i.e. $x=0$) and Ga(P_{0.1}Bi_{0.9}) (i.e. $x=0.9$), the Ga(P_{0.1}As_{0.9-x}Bi_x) CB, VB and SO bands can be estimated (dashed lines in the figure) using linear interpolation for the unstrained Ga(P_{0.1}As_{0.9-x}Bi_x) values. Secondly, the strain-induced shifts (solid lines in the figure) of the CB, VB and SO bands are calculated, using the approach of Krijn [17]. The VBAC model is further applied to the valence band of Ga(P_{0.1}As_{0.9-x}Bi_x), which leads to an additional shift of the VB bands. The separation energy, ΔE_{Bi} , between the VBM and Bi level is found from the figure while the coupling parameter, C_{Bi} , may be estimated from the measured band gap reduction. For other Ga(PAsBi) alloys, C_{Bi} is estimated from the $C_{Bi}-\Delta E_{Bi}$ relation using linear interpolation. Based on these calculations, both the unstrained and fully strained band gap E_g of Ga(P_yAs_{1-x-y}Bi_x) were determined as shown in Fig. 1b (0% (black), 10% (red), 20% (green)

and 30% (blue) phosphorus). The spin-orbit splitting energies Δ_{SO} of strained Ga(P_yAs_{1-x-y}Bi_x) are also given in the figure. It shows that the addition of Bi in Ga(PAs) leads to a significant reduction of E_g and a strong increase in Δ_{SO} . The incorporation of P in Ga(AsBi) increases E_g but has only a small influence on Δ_{SO} . Furthermore, since P atoms are smaller than As atoms, the incorporation of P in GaAs leads to tensile strain. Conversely, since bismuth atoms are larger than arsenic atoms, incorporating Bi atoms in GaAs leads to compressive strain. Therefore, as can be seen, Ga(P_yAs_{1-x-y}Bi_x) can be flexibly designed with zero or a small degree of strain on GaAs depending on the P and Bi compositions. This opens up a number of possibilities for device design, like a lattice-matched Ga(PAsBi) layer on GaAs with a band gap of 1 eV for a sub-cell in a multi-junction solar cell.

3. Experimental procedure

All Ga(PAs) and Ga(PAsBi) layers were grown on exact GaAs (001) substrates using a commercially available Aixtron horizontal reactor system (AIX 200-reactor) with gas foil rotation. Pd purified H₂ carrier gas (10 N) was used at a reduced reactor pressure of 50 mbar. The growth temperature of the Ga(PAs) and Ga(PAsBi) layers was 400 °C. Firstly, a 250-nm thick GaAs buffer layer was grown at 625 °C in order to realize a high-quality surface for the growth of the Ga(PAs) and Ga(PAsBi) layers on top of the buffer layer. Triethylgallium (TEGa), Tertiarybutylarsine (TBAs), Trimethylbismuth (TMBi) and Tritertiarybutylbismuth (TTBBi) were used as precursors for gallium, arsenic and bismuth, respectively. As a phosphorus source, Tertiarybutylphosphine (TBP) was used instead of PH₃, since TBP has a better decomposition efficiency at 400 °C than PH₃ [18]. Furthermore, the cleaning effort of the exhaust gas system is much higher when using PH₃ and TBP has a by three orders of magnitude lower value of toxicity [18] compared to PH₃. For thickness and composition determination of the different layers, we used high-resolution X-ray diffraction (HRXRD) and secondary ion mass spectroscopy (SIMS) to determine the growth rate as well as P and Bi incorporation, since HRXRD alone is insufficient for composition investigations of quaternary compounds. The HRXRD pattern was simulated around the (004)-GaAs substrate peak, assuming the GaBi lattice constant to be 6.33 Å [19]. STEM (scanning transmission electron microscopy) HAADF (high-angle annular dark field) micrographs were taken with a double Cs corrected JEOL 2200FS – system operating at 200 keV. Atomic force microscope (AFM) images were taken to study surface morphologies and potential metallic droplets on the surface. Temperature-dependent photoluminescence (PL) was measured using a standard PL setup. The light (30 mW) of a stabilized 532 nm diode pumped solid-state (DPSS) laser was focused on the sample to a spot size of 6.5×10^{-5} cm². The samples PL were collimated and focused on the entrance slit of a Czerny-Turner monochromator equipped with 150 grooves/mm grating blazed at 1200 nm. To block residual laser light and prevent detection of the second diffraction order, a colour glass long-pass filter (3 mm OG570) or a dichroic long-pass filter (H450) was placed in front of the monochromator. For detection, either a liquid nitrogen cooled (Ga,In)As linear array detector for photon energies below 1.2 eV or a thermoelectrically cooled Si charge-coupled device for photon energies above 1.2 eV were used. The modulated reflectance spectra of the samples are measured at room temperature using photomodulation and standard lock-in technique in line-scan mode. The emission from a tungsten-halogen bulb is focused onto the entrance of a 1 m focal length Czerny-Turner type monochromator and dispersed by a 600 grooves/mm grating blazed at 1250 nm. The resolution of the system is set to 1.5 nm to ensure high throughput. Different filters are placed directly behind the exit port of the monochromator to block higher diffraction

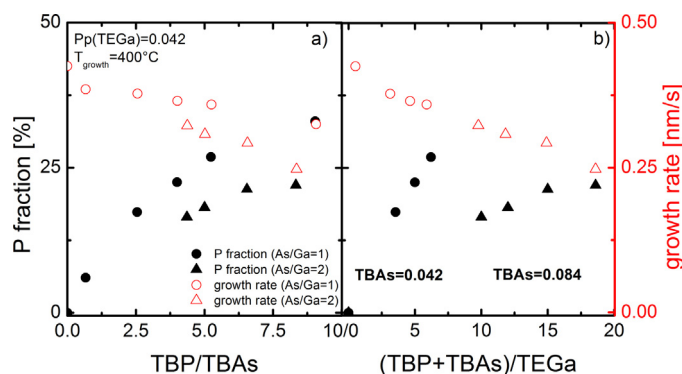


Fig. 2. Growth of Ga(PAs) at 400 °C. P fraction and growth rate vs. TBP/TBAs ratio (a) and vs. V/III ratio (b). In both graphs, P fraction and growth rate are plotted for two different TBAs/TEGa ratios. Partial pressure of TEGa was 0.042; the partial pressure of the TBAs was 0.042 and 0.084, respectively.

orders. In particular, a colour glass filter (RG780), a dielectric filter (FELH1500) and an anti-reflection-coated germanium window are used for wavelength ranges such as 800–1550 nm, 1500–2200 and 2200–2500 nm, respectively. The monochromatic light is relayed onto the sample using all-reflective optics to avoid chromatic aberrations. It is focused to a spot size of about 0.5 mm in diameter on the sample, incident under an angle of about 30° to the sample's surface normal. The reflected light is collimated and then focused onto either a Si photodiode or a long-wavelength enhanced (Ga,In)As photodiode, depending on the respective detection wavelength. Both diodes are thermoelectrically cooled yielding an enhanced signal-to-noise ratio. The modulation is achieved by focusing a mechanically chopped 405 nm laser beam onto the sample. A long-pass colour glass filter (GG420) is placed in front of the photodiode to suppress the detection of scattered laser light. The unmodulated and modulated signal are separated electronically using a passive frequency crossover. Recording of both signals is done simultaneously by the same lock-in amplifier. The normalized differential reflectance $\Delta R/R$ is calculated from the differential reflectance, i.e., the modulated signal (ΔR) and the absolute reflectance, i.e., the unmodulated signal ($R = R^M - PL$) that is corrected for the luminescence background (PL).

4. Results and discussion

First, systematic investigations on the growth of Ga(PAs) with TBP at 400 °C are presented as no data on Ga(PAs) growth at these low temperatures are available so far. Afterwards the results concerning the growth of the quaternary Ga(PAsBi) layers are introduced and discussed in detail. Finally, optical measurements are presented and discussed in context to the theoretical predictions.

4.1. Growth

Initially, Ga(PAs) layers were deposited to verify if the growth with TBP at these low temperatures is even possible, as the decomposition of TBP should be very low at these temperatures ($T_{50} = 475$ –500 °C). A variation of TBP supply also gives results on the P incorporation characteristics in GaAs, independent of the influence of TMBi and elemental Bi on the surface. In this way, it is possible to understand and separate the effects and influences coming from the decomposition characteristics of TBP on the one hand and from TMBi on the other. Fig. 2 shows the results of the growth of Ga(PAs) at 400 °C. The P incorporation and the growth rate vs. the partial pressure of TBP are plotted, while the

TBAs and TEGa supply are kept constant. The TBAs/TEGa ratio is 1 ($Pp(TBAs) = Pp(TEGa) = 0.042$ mbar). P incorporation increases with increasing TBP supply, whereas the growth rate decreases for increasing TBP/TBAs ratios. A TBP/(TBP + TBAs) ratio of 9 leads to a P fraction of 33% (of group V lattice sites), which means the P incorporation efficiency is about 30% under the conditions chosen here. The decrease of the growth rate is due to the increasing V/III ratio leading to a larger number of hydrocarbon radicals, which cannot desorb from the surface any more. This needs to be taken into account, especially in this temperature regime. This is shown by the linear decrease of the growth rate with increasing V/III in Fig. 2. From this, it can be concluded that as low V/III ratios as possible should be chosen while still keeping a good crystal quality. In order to verify the influence of TBAs supply, variation of TBP was carried out at two different TBAs/TEGa ratios, which are 1 and 2, respectively. The P fraction and the growth rate of these layers are shown in Fig. 2. For both TBAs/TEGa ratios, increasing P incorporation and decreasing growth rates with increasing $Pp(TBP)$ are found. For the higher TBAs/TEGa ratios, however, a more than three times higher partial pressure of TBP is required in order to realize the same P fraction. Hence, the TBAs/TEGa ratio of 1 was selected for the following experiments. In order to get a comprehensive understanding of the growth process of Ga(PAsBi), several parameters were varied. Both Bi and P fractions, as well as the growth rate, were investigated by varying the TMBi supply at different TBP supplies. Ga(PAsBi) layers were grown at 400 °C. The partial pressures of TEGa and TBAs were again kept constant at 0.042 mbar.

The dependency of Bi incorporation on the partial pressure of TMBi at different TBP supplies is illustrated in Fig. 3. Initially, the Bi incorporation increases with increasing TMBi supply. This confirms present literature [8,9,20,21], where these dependencies have already been investigated for ternary Ga(AsBi). At certain $Pp(TMBi)$, the Bi incorporation saturates and cannot be increased without changing growth conditions. This is also the region where Bi droplets start forming on the surface [22]. With increasing $Pp(TBP)$, the saturation level of the Bi fraction increases. Hence, it is possible to increase the Bi incorporation in the saturation regime by increasing the TBP supply, while $Pp(TMBi)$ is kept constant. This unexpected behaviour is depicted in Fig. 3, where the Bi fraction of Ga(PAsBi) is plotted vs. the partial pressure of TBP at a fixed $Pp(TMBi) = 0.0022$ mbar. The Bi fraction increases linearly with increasing TBP. It is important to keep in mind that these dependencies are only valid in the Bi saturation regime. Otherwise, there is no increase in Bi incorporation by offering P, since all Bi atoms are already incorporated in the crystal, even without P supply. The surplus Bi segregates at the surface in the case when growing Ga(AsBi) is consumed and incorporated. In the case where no surplus Bi is riding the surface (linear incorporation regime in Fig. 3), the Bi content cannot be increased when adding P to the crystal. This behaviour is due to the fact that Bi induces compressive strain in the GaAs lattice, which increases with increasing Bi content and hinders the incorporation of further Bi at a certain saturation level. By adding P atoms, this compressive strain can be compensated so that more Bi can be incorporated into the crystal. The assumption that the Bi incorporation is not only limited due to the metastability but also by strain needs to be verified by the growth and comparison of Ga(PAsBi) and Ga(NAsBi) in future experiments. Fig. 3c shows results from HR-XRD measurements of the series with $Pp(TBP) = 0.22$ and increasing TMBi supply (see Fig. 3a). The peak of the Ga(PAsBi) layer shows distinct thickness fringes for every composition and shifts with increasing TMBi supply from tensile to compressive strain.

Fig. 4 illustrates the incorporation characteristics of P in Ga(PAsBi). The P fraction is plotted vs. the partial pressure of TBP for different TMBi supplies. The P fraction increases with increasing TBP supply and decreases with increasing $Pp(TMBi)$. A similar

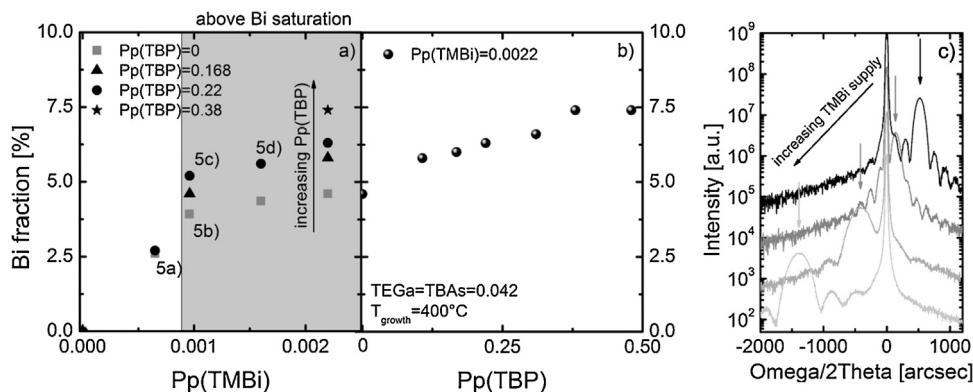


Fig. 3. Growth of Ga(PAsBi) at 400 °C. Plotted is the Bi fraction vs. partial pressure of TMBi (a) and Bi fraction of Ga(PAsBi) vs. partial pressure of TBP (b). Shaded region in (a) indicates the region of Bi saturation. Indices (a–d) correspond to the AFM images in Fig. 5. Indices in (a) correspond with AFM images from Fig. 5a. (c) The HR-XRD of the series with Pp(TBP) = 0.22 (a) and increasing Pp(TMBi). The Ga(PAsBi) layers show a high crystal quality and shift from tensile to compressive with increasing TMBi supply.

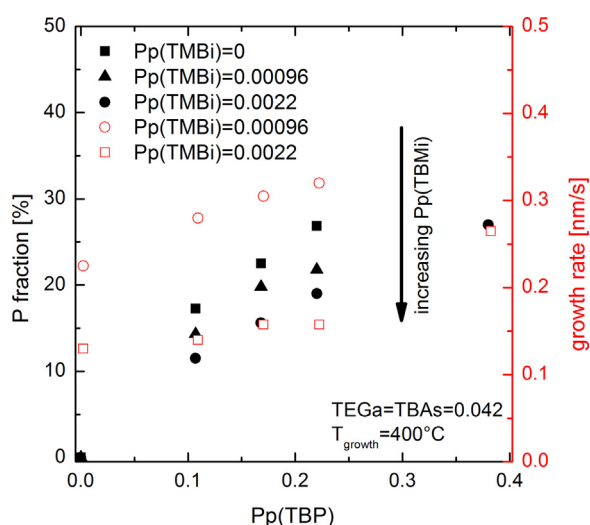


Fig. 4. Growth of Ga(PAsBi) at 400 °C. P fraction and growth rate are plotted vs. Pp(TBP) for different TMBi supplies.

trend was observed for P incorporation without TMBi supply; see Fig. 2. The decreasing P incorporation for increasing TMBi supply is due to the Bi surface coverage, which increases with increasing Pp(TMBi). The growth rate for the growth of Ga(PAsBi) is depicted

in Fig. 4. The growth rate of Ga(PAsBi) increases with increasing TBP and constant TMBi supply but decreases with constant Pp(TBP) and increasing Pp(TMBi). With increasing TMBi supply, the surface coverage of TMBi and elemental Bi increases so that the growth surface becomes passivated. However, the increase of the growth rate with increasing TBP supply is probably due to the fact that more Bi can be incorporated with increasing TBP. Hence, the Bi surface coverage decreases and the growth rate can increase, as more Ga can reach the growth front.

4.2. Structure and surface

The surface and crystal quality of the quaternary layers were analyzed by AFM and STEM. Results from these investigations are depicted in Fig. 5. In previous Ga(AsBi) experiments, it was already shown that the Bi droplets and Ga–Bi droplets occur, as soon as the Bi fraction reaches the saturation regime [8–10]. This is due to the fact that Bi can incorporate only until a specific saturation level, which depends on Pp(TEGa), V/III ratio and temperature. For Bi supplies above these saturation levels, droplet formation on the surface appears, because of the remaining Bi, which cannot be incorporated in the crystal [22]. This behaviour is also found for Ga(PAsBi). In Fig. 5, it is shown that the occurrence of droplets on the Ga(PAsBi) surface shifts with saturation level, which is increased with increasing P incorporation. Fig. 5a and b shows a Ga(AsBi) surface before

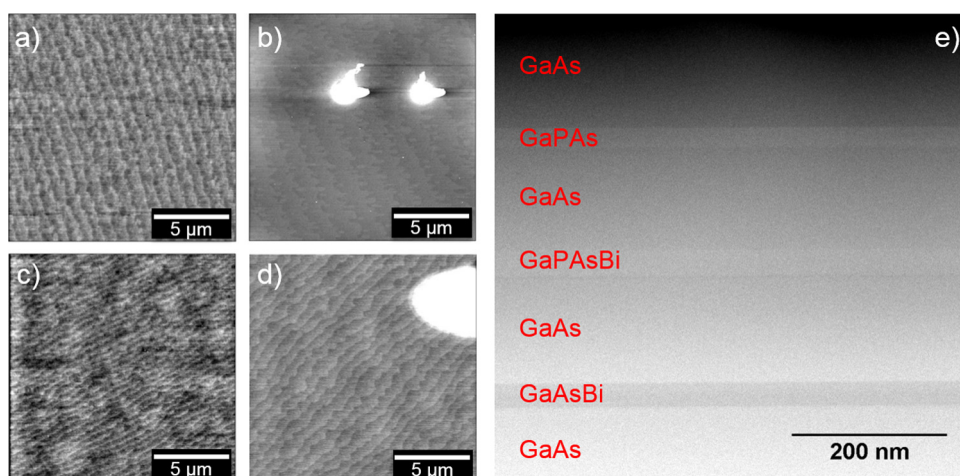


Fig. 5. AFM and STEM HAADF micrographs of Ga(PAsBi) surfaces a–d and interfaces e, respectively. Figure a and b shows a Ga(AsBi) surface before a and after saturation b. Figure c shows a Ga(PAsBi) surface with the same TMBi supply like for the growth of the sample in figure b was used, but without droplets. The saturation level is shifting with TBP supply as well as the droplet formation does. With further increase of TMBi supply, the formation of droplets on the surface is also visible for Ga(PAsBi); see figure d. See also Fig. 3a.

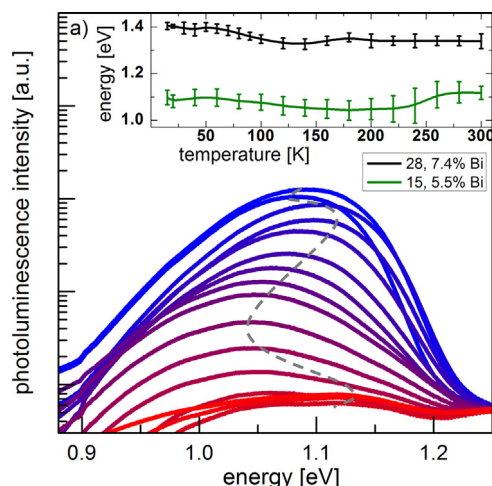


Fig. 6. Typical temperature-dependent PL spectra (15% P, 5.5% Bi), measured from 15 K (blue) to 300 K (red). Double s-shape of the PL maximum indicated by guidance to the eye (grey line). Inset: PL-peak position for all temperatures for two samples with different compositions (black: 28% P, 7.4% Bi and green: 15% P, 5.5% Bi). (For interpretation of the references to color in this figure legend, the reader is referred to the web version of this article.)

and after saturation, respectively. Fig. 5c shows a Ga(PAsBi) surface where the same TMBi supply like for the growth of the sample in Fig. 5b was used, but no droplets can be detected on the surface. The Bi saturation level is shifting with TBP supply as well as does the droplet formation; see also corresponding indices in Fig. 3a. With further increase of TMBi supply, the formation of droplets on the surface is also visible for Ga(PAsBi); see Fig. 5d.

Interfaces of Ga(PAsBi) and Ga(PAs) as well as the crystal quality were analyzed by STEM HAADF measurements. Fig. 5e shows a [010] STEM HAADF micrograph of a layer stack as it was grown for SIMS measurements for composition determination. It can be seen clearly that all layers are well established and no significant Bi segregation is observed.

The surface coverage of Bi during the growth, which decreases the growth rate and is related to droplet formation on the surface, has one very positive impact, as already found for Ga(AsBi) [10]. With increasing Bi surface coverage, the C incorporation, which is around 1×10^{18} atoms per cm^3 at these low temperatures for Bi-free GaAs, decreases, and is dependent on the P supply, by up to two orders of magnitude.

4.3. Photoluminescence

Fig. 6 shows the results of temperature-dependent measurements between 15 K and 300 K. A broad distinct double s-shape of the PL maximum at higher temperatures indicates band edge PL of the GaPAsBi layer [23]. The composition of the measured sample is about 15% P and 5.5% Bi. The inset shows the PL-peak position for all temperatures for two samples with different compositions. In Fig. 1b, the band gap and spin-orbit split-off positions at room temperature are plotted in context to the theory for these two samples with different compositions, which are 15% P and 5.5% Bi and 28% P and 7.4% Bi, respectively. As one can see, the sample with the higher P and Bi content shows good agreement with the calculated value for the band gap. For the sample with 15% P and 5.5% Bi, the band gap energy is slightly different from the expected value. The values of the calculated spin-orbit split-off correspond with the values obtained by photoreflectance measurements; however, the error bars for the calculated values are very large.

5. Summary

The shifts in the band edge positions as a function of composition that are possible with the Ga(PAs(Bi)) alloy were estimated using the virtual crystal approximation and valence band anti-crossing theory. It was shown that the growth of Ga(PAs) and Ga(PAsBi) at low temperatures of 400°C is possible. The saturation level of Bi incorporation increases with increasing P incorporation. The P incorporation is related to the Bi surface coverage just as the growth rate of Ga(PAsBi) is. Hence, the formation of Bi droplets at the surface can be inhibited with increasing TBP supply, and well-stepped surfaces with high-TMBi supplies can be realized, if the TMBi supply is in the saturation regime. First, PL results show good agreement with theoretically calculated band gap.

Acknowledgments

We gratefully acknowledge the support from German Science Foundation (DFG) in the framework of the RTG1782 “Functionalization of Semiconductors” as well as from the HMWK in the framework of the project EGALITE. We are also grateful to funding from EPSRC (UK) under grant EP/H005587/1.

References

- [1] K. Alberi, O.D. Dubon, W. Walukiewicz, K.M. Yu, K. Bertulis, A. Krotkus, Valence band anticrossing in $\text{GaBi}_x\text{As}_{1-x}$, *Appl. Phys. Lett.* 91 (5) (2007) 051909.
- [2] S.J. Sweeney, S.R. Jin, Bismide-nitride alloys: promising for efficient light emitting devices in the near- and mid-infrared, *J. Appl. Phys.* 113 (4) (2013) 043110.
- [3] K. Alberi, J. Wu, W. Walukiewicz, K.M. Yu, O.D. Dubon, S. Watkins, C. Wang, X. Liu, Y.-J. Cho, J. Furdyna, Valence-band anticrossing in mismatched III-V semiconductor alloys, *Phys. Rev. B* 75 (January (4)) (2007) 045203.
- [4] M. Usman, C.A. Broderick, A. Lindsay, E.P. O'Reilly, Tight-binding analysis of the electronic structure of dilute bismide alloys of GaP and GaAs, *Phys. Rev. B* 84 (December (24)) (2011) 245202.
- [5] C.A. Broderick, P.E. Harnedy, R.J. Manning, E.P. O'Reilly, P. Ludewig, Z.L. Bushell, K. Volz, Determination of band offsets in dilute bismide $\text{GaBi}_x\text{As}_{1-x}$ quantum wells using polarization-resolved photovoltage spectroscopy and 12-band k_p calculations, 2015.
- [6] K. Oe, H. Okamoto, New semiconductor alloy $\text{GaAs}_{1-x}\text{Bi}_x$ grown by metal organic vapor phase epitaxy, *Jpn. J. Appl. Phys.* 37 (November (Part 2)) (1998) L1283–L1285, No. 11A.
- [7] H. Li, Z. Wang, Bismuth – Containing Compounds, Springer New York Heidelberg Dordrecht London, Springer S. New York, 2013.
- [8] P. Ludewig, N. Knaub, W. Stolz, K. Volz, MOVPE growth of Ga(AsBi)/GaAs multi quantum well structures, *J. Cryst. Growth* 370 (July) (2013) 186–190.
- [9] L. Nattermann, P. Ludewig, L. Meckbach, B. Ringler, D. Keiper, C. Von Hänisch, W. Stolz, K. Volz, MOVPE growth of Ga(AsBi)/GaAs using different metalorganic precursors, *J. Cryst. Growth* 426 (2015) 54–60.
- [10] P. Ludewig, Z.L. Bushell, L. Nattermann, N. Knaub, W. Stolz, K. Volz, Growth of Ga(AsBi) on GaAs by continuous flow MOVPE, *J. Cryst. Growth* 396 (2014) 95–99.
- [11] P. Ludewig, N. Knaub, N. Hossain, S. Reinhard, L. Nattermann, I.P. Marko, S.R. Jin, K. Hild, S. Chatterjee, W. Stolz, S.J. Sweeney, K. Volz, Electrical injection Ga(AsBi)/(AlGa)As single quantum well laser, *Appl. Phys. Lett.* 102 (24) (2013).
- [12] K. Forghani, Y. Guan, M. Losurdo, G. Luo, D. Morgan, S.E. Babcock, A.S. Brown, L.J. Mawst, T.F. Kuech, $\text{GaAs}_{1-y-z}\text{Py}_z\text{Bi}_z$, an alternative reduced band gap alloy system lattice-matched to GaAs, *Appl. Phys. Lett.* 105 (11) (2014) 111101.
- [13] I. Vurgaftman, J.R. Meyer, L.R. Ram-Mohan, Band parameters for III–V compound semiconductors and their alloys, *J. Appl. Phys.* 89 (11) (2001) 5815.
- [14] C.A. Broderick, M. Usman, E.P. O'Reilly, Derivation of 12- and 14-band $k \cdot p$ Hamiltonians for dilute bismide and bismide-nitride semiconductors, *Semicond. Sci. Technol.* 28 (December (12)) (2013) 125025.
- [15] M.K. Rajpalke, W.M. Linhart, M. Birkett, K.M. Yu, D.O. Scanlon, J. Buckeridge, T.S. Jones, M.J. Ashwin, T.D. Veal, Growth and properties of GaSbBi alloys, *Appl. Phys. Lett.* 103 (14) (2013) 142106.
- [16] D.P. Samajdar, S. Dhar, Valence band structure of $\text{InAs}_{1-x}\text{Bi}_x$ and $\text{InSb}_{1-x}\text{Bi}_x$ alloy semiconductors calculated using valence band anticrossing model, *Sci. World J.* 2014 (2014) 704830.
- [17] M.P.C.M. Krijn, Heterojunction band offsets and effective masses in III–V quaternary alloys, *Semicond. Sci. Technol.* 6 (1) (1999) 27–31.
- [18] G.B. Stringfellow, *Organometallic Vapor-phase Epitaxy: Theory and Practice*, 2nd ed., Academic Press, 1998.
- [19] S. Tixier, M. Adamczyk, T. Tiedje, S. Francoeur, A. Mascarenhas, P. Wei, F. Schiettekatte, Molecular beam epitaxy growth of $\text{GaAs}_{1-x}\text{Bi}_x$, *Appl. Phys. Lett.* 82 (14) (2003) 2245–2247.

- [20] K. Forghani, Y. Guan, A.W. Wood, A. Anand, S.E. Babcock, L.J. Mawst, T.F. Kuech, Self-limiting growth when using trimethyl bismuth (TMBi) in the metal-organic vapor phase epitaxy (MOVPE) of GaAs 1 Å y Bi y, *J. Cryst. Growth* 395 (2014) 38–45.
- [21] I. Moussa, H. Fitouri, A. Rebey, B. El Jani, Atmospheric-pressure metalorganic vapour phase epitaxy optimization of GaAsBi alloy, *Thin Solid Films* 516 (23) (2008) 8372–8376.
- [22] E. Sterzer, N. Knaub, P. Ludewig, R. Straubinger, A. Beyer, K. Volz, Investigation of the microstructure of metallic droplets on Ga(AsBi)/GaAs, *J. Cryst. Growth* 408 (December) (2014) 71–77.
- [23] S. Imhof, A. Thränhardt, A. Chernikov, M. Koch, N.S. Köster, K. Kolata, S. Chatterjee, S.W. Koch, X. Lu, S.R. Johnson, D.A. Beaton, T. Tiedje, O. Rubel, Clustering effects in Ga(AsBi), *Appl. Phys. Lett.* 96 (13) (2010) 1–4.

6.2.5 MOVPE Growth of Ga(AsBi)/GaAs Using Different Metalorganic Precursors ¹

L. Nattermann, P. Ludewig, L. Meckbach, B. Ringler, D. Keiper, C. von Hänisch,
Journal of Crystal Growth, Journal of Crystal Growth **426**, pp. 54-60 (2015)
DOI: 10.1016/j.jcrysgro.2015.05.015

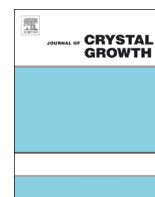
Abstract

In this paper different metalorganic Bismuth- and Gallium-precursors such as Triisopropylbismuth, Tritertiarybutylbismuth, Trimethylbismuth, Triethylgallium and Tritertiarybutylgallium, were investigated to grow Ga(AsBi) by metal organic vapour phase epitaxy (MOVPE). Use of different precursors which dissociate at different temperatures and have various decomposition pathways can lead to an understanding of the complex growth chemistry at low temperatures, possibly enabling the growth of Ga(AsBi) at very low growth temperatures in order to further increase the Bi fraction. The growth conditions were varied over a wide range in order to investigate the Bi-incorporation and growth rate comprehensively. Using different methods like high resolution X-ray diffraction, scanning electron microscopy and secondary ion mass spectroscopy, we found that especially in the low temperature regime not only the decomposition of the precursors is important but also the interaction between the different molecules and processes at the surface, like surface coverage and pyrolysis of the precursors, needs to be taken into account. Furthermore, it is demonstrated that the growth of Ga(AsBi) with the novel precursors is possible and results in high quality Ga(AsBi) samples.

The Authors contribution

My contribution to this work was the planning, execution and interpretation of all experiments including the MOVPE growth and analysis by HR-XRD, AFM and PL spectroscopy. It is important to mention that part of the results for this paper were collected for my Masters Thesis with the titel *Wachstum und Charakterisierung verdünnt Bi-haltiger Schichten mittels MOVPE mit alternativen Präkursoren*. The metalorganic sources were synthesized by B. Ringler in collaboration with D. Keiper and C. von Hänisch. The preparation and investigation of the SEM samples were performed by L. Meckbach in close collaboration with me. All co-authors helped to interpret the data and to improve the manuscript that was written by me.

¹ Reprinted from *Journal of Crystal Growth* **426** (2015) 54-60, Copyright 2015, with permission from Elsevier.



MOVPE growth of Ga(AsBi)/GaAs using different metalorganic precursors

L. Nattermann^{a,*}, P. Ludewig^a, L. Meckbach^a, B. Ringler^b, D. Keiper^b, C. von Hänisch^b, W. Stolz^a, K. Volz^a

^a Material Sciences Center and Faculty of Physics, Philipps-Universität Marburg, Germany

^b Faculty of Chemistry and Materials Science Center, Philipps-Universität Marburg, Germany

ARTICLE INFO

Article history:

Received 9 January 2015

Received in revised form

13 May 2015

Accepted 15 May 2015

Communicated by: C. Caneau

Available online 25 May 2015

Keywords:

A1. Characterization

A1. Crystal morphology

A2. Metalorganic chemical vapour deposition

B1. Bismuth compounds

B2. Semiconducting III–V materials

B3. Laser diodes

ABSTRACT

In this paper different metalorganic Bismuth- and Gallium-precursors such as Triisopropylbismuth, Tertiarybutylbismuth, Trimethylbismuth, Triethylgallium and Tertiarybutylgallium, were investigated to grow Ga(AsBi) by metal organic vapour phase epitaxy (MOVPE). Use of different precursors which dissociate at different temperatures and have various decomposition pathways can lead to an understanding of the complex growth chemistry at low temperatures, possibly enabling the growth of Ga(AsBi) at very low growth temperatures in order to further increase the Bi fraction. The growth conditions were varied over a wide range in order to investigate the Bi-incorporation and growth rate comprehensively. Using different methods like high resolution X-ray diffraction, scanning electron microscopy and secondary ion mass spectroscopy, we found that especially in the low temperature regime not only the decomposition of the precursors is important but also the interaction between the different molecules and processes at the surface, like surface coverage and pyrolysis of the precursors, needs to be taken into account. Furthermore, it is demonstrated that the growth of Ga(AsBi) with the novel precursors is possible and results in high quality Ga(AsBi) samples.

© 2015 Elsevier B.V. All rights reserved.

1. Introduction

Dilute bismide Ga(AsBi) based laser diodes are promising candidates for high efficiency infrared light sources, since for Bi > 10%, hot-hole generating Auger recombination and inter-valence band absorption (IVBA) processes could be suppressed [1–3]. In addition, it was shown that the temperature sensitivity of the band gap of Ga(AsBi) is reduced in comparison to the one of GaAs [4–5]. Hence, dilute bismide systems are promising candidates for many applications, like lasers or highly efficient solar cells, because of their interesting electronic properties [6–9].

However, the growth of this highly metastable material system is very challenging, especially when using metalorganic vapour phase epitaxy (MOVPE) as very low growth temperatures are required in order to incorporate significant amounts of Bi. Experiments with the conventional precursors Triethylgallium (TEGa) and Trimethylbismuth (TMBi) as well as Tertiarybutylarsine (TBAs) show that growth temperatures of 375–400 °C are most suitable in order to realize high quality Ga(AsBi) structures, since a sufficient

precursor decomposition is needed [10,11]. However, so far, only TMBi, TEBi, TEGa and TBAs/AsH₃ were used to grow Ga(AsBi) structures [10–13]. Indeed, it has been reported [10] that the Bi fraction is limited to about 7% in this temperature regime. Furthermore, the interaction between the molecules as well as between the molecules and the growing surface cannot be neglected at these low temperatures as decomposition fragments do not easily desorb from the surface any more. This leads for example to a decreasing growth rate if the Bi-precursor partial pressure is increased while the Ga-precursor partial pressure is kept constant. It has been suggested that the decreasing growth rate is caused by a surface passivation with methyl groups resulting from the TMBi [13]. Because of these methyl-groups the TEGa molecule or one of its dissociation products is no longer able to connect to the surface and will not be fully decomposed or will not reach the growth front, respectively. This would mean that the surface passivation could be prevented by using another Bi precursor – especially a precursor such as TTBBi (Tertiarybutylbismuth) and TIPBi (Triisopropylbismuth), which decomposes more efficiently at lower temperatures. Better decomposition of these precursors at low temperatures results from the positive inductive effect [14], which causes a better stabilization of the desorbing hydro carbon radicals.

* Corresponding author.

E-mail address: lukas.nattermann@physik.uni-marburg.de (L. Nattermann).

Hence, Ga(AsBi)/GaAs layers were grown on GaAs (001) substrates using alternative precursors that are supposed to dissociate at lower temperatures and have different decomposition pathways in order to study the incorporation characteristics and to obtain a better understanding of the surface chemistry occurring at these low temperatures. The results of these investigations are discussed in comparison to the results of the growth with the conventional source materials.

2. Experimental procedure

Ga(AsBi) layers were grown on exact GaAs (001) substrates using a commercially available horizontal reactor system (AIX 200-reactor) with gas flow rotation. We used a reduced reactor pressure of 50 mbar and Pd purified H₂ as carrier gas. The growth temperature of the Ga(AsBi) layers was 400 °C.

First a 250 nm GaAs buffer layer was grown at 625 °C in order to make sure that there is a high quality surface for the growth of the Ga(AsBi) layers on top of the buffer layer. The temperature ramps between the GaAs and Ga(AsBi) layers were TBAs stabilized to prevent a desorption of As atoms during the temperature change. The Ga(AsBi) layers were grown with both alternative Gallium- and Bismuth-precursors such as TTbGa (Tritertiarybutyl-gallium), TIPBi and TTbBi and with the conventional precursors TEGa and TMbI in order to compare the growth processes. The Arsenic precursor was TBAs in all cases. The alternative Ga precursor TTbGa was not synthesized by ourselves but is commercially available.

The use of organometallic bismuth compounds as potential precursors for the MOVPE process requires the possibility of large scale production. Therefore the enhancement of yields in chemical synthesis is an important aspect when examining the applicability of these compounds for industrial use.

In 1975 the first preparation of TTbBi was mentioned by Schumann and Breunig [15] and slightly better yields could be achieved by Herberhold et al. [16]. The yield is more than doubled via our preparation method. Likewise an improvement of the yield is achieved for the synthesis of TIPBi. Breunig and Müller reported a yield of 43% in 1982, which we increased up to 68% [17].

All working procedures to synthesize the metalorganic compounds were conducted under rigorous exclusion of oxygen using standard Schlenk technique and an argon atmosphere. Solvents were dried and freshly distilled before use. All air sensitive substances were stored and handled in a glove-box under an argon atmosphere. The starting material *tert*-butylchloride was purchased from Acros Organics, magnesium and *iso*-propylchloride from SigmaAldrich and bismuthtrichloride from Alfa Aesar. Bismuthtrichloride was purified by sublimation prior to use. NMR-spectra were recorded with a Bruker Avance 300 spectrometer. Both source molecules TTbBi and TIPBi should be handled under exclusion of light and stored at –32 °C, otherwise decomposition will occur.

2.1. Synthesis of TTbBi

The synthesis is based on the method described by Herberhold et al. [16]. 7.25 g Mg powder (298 mmol) was suspended in 200 mL Et₂O. Subsequently 31.3 ml *tert*BuCl (26.29 g, 283 mmol) dissolved in 150 ml Et₂O were added drop wise. This Grignard solution was added drop wise to a solution of 19.90 g BiCl₃ (63 mmol) in 300 ml 1,2-dimethoxyethane at –40 °C. The obtained dark solution was warmed slowly to room temperature. After filtration, the solvent was removed under reduced pressure. The purification was done by fractional distillation under dynamic

vacuum (38 °C, 10^{–3} mbar) to afford 11.9 g TTbBi as green yellow oil with a yield of 50%.¹

2.2. Synthesis of TIPBi

The synthesis is based on the methods described by Breunig et al. [17]. 7.48 g Mg turnings (308 mmol) were suspended in 300 ml Et₂O and 30.0 ml *iso*PrCl (25.86 g, 329 mmol) were added drop wise. This Grignard solution was added to 32.33 g BiCl₃ (103 mmol) dissolved in 300 ml Et₂O at 0 °C. After warming to room temperature the solution was cooled to 0 °C and degassed water was added carefully. Subsequently the phases were separated and the organic phase was dried over MgSO₄ which was filtered. The solvent was removed under reduced pressure. The purification was done by condensation under dynamic vacuum to afford 23.7 g TIPBi as yellow oil with a yield of 68%.²

For the investigations of the different layers we used high resolution X-ray diffraction (HR-XRD) to determine the growth rate and Bi-incorporation. For that purpose, the high resolution X-ray pattern was simulated around the (004)-GaAs substrate peak, assuming the GaBi lattice constant to be 6.33 Å [18]. Room temperature photoluminescence spectroscopy (PL) was used to analyse the optical properties of the samples. The measurements were carried out using the 514 nm line of an Argon-ion laser for excitation, a 1 m grating monochromator (THR 1000, Jobin-Yvon) and a cooled germanium detector with the standard lock-in technique to disperse and collect the PL signal. The SEM (scanning electron microscopy) images were taken with a JEOL JIB 4601F-System.

3. Results and discussion

First the Bi incorporation and the growth rate of Ga(AsBi) layers grown with conventional and alternative Bi precursors will be compared and discussed. Then the results concerning the growth with TTbGa in comparison to the growth with TEGa will be presented.

In Fig. 1(a) the Bi incorporation and the growth rate of Ga(AsBi), grown with TEGa, TBAs and TMbI, are plotted against the partial pressure of the TMbI (Pp(TMbI)). The growth temperature was 400 °C, Pp(TEGa) was 0.042 mbar and the As/Ga ratio was 1.9 (filled circles) or 1 (empty circles). The parameters were chosen after careful optimizations of the growth conditions in order to optimize the quality of the Ga(AsBi) layers. As already figured out for continuous [10] and pulsed growth [11,13], the growth rate decreases with increasing Pp(TMbI). This is also observed for the continuous growth scheme used for the samples presented in this paper. Furthermore, the Bi incorporation saturates at around 4% Bi fraction. The level of Bi saturation depends on the growth temperature, the As/Ga ratio and the TEGa partial pressure. So far the Bi fraction using MOVPE is limited to about 7% in this temperature regime [10]. For the growth with TMbI it is shown in Fig. 1(a) that the Bi fraction and the growth rate vary with the As/Ga ratio.

Similar results from the growth of Ga(AsBi) using the alternative Bi precursors are shown in Fig. 1(b) for TIPBi and in Fig. 1(c) for TTbBi, respectively. The Bi incorporation and the growth rate are plotted against partial pressure in arbitrary units of the Bi source. The vapour pressures of the alternative Bi sources are not

¹ ¹H NMR (300 MHz, C₆D₆) δ=1.80 (s, C(CH₃)₃, 27H) ppm. ¹³C NMR (75 MHz, C₆D₆) δ=32.5 (s, C(CH₃)₃), 47.3 (bs, C(CH₃)₃) ppm. The abbreviations for the multiplicity of the signals are s=singlet, bs=broad singlet.

² ¹H NMR (300 MHz, C₆D₆) δ=1.83 (d, ³J_{HH}=7.3 Hz, CH(CH₃)₂, 18H), 2.15 (sept, ³J_{HH}=7.3 Hz, CH(CH₃)₂, 3H) ppm. ¹³C NMR (75 MHz, C₆D₆) δ=23.7 (s, CH(CH₃)₂), 28.8 (bs, CH(CH₃)₂) ppm. The abbreviations for the multiplicity of the signals are s=singlet, bs=broad singlet, d=doublet, sept=septet.

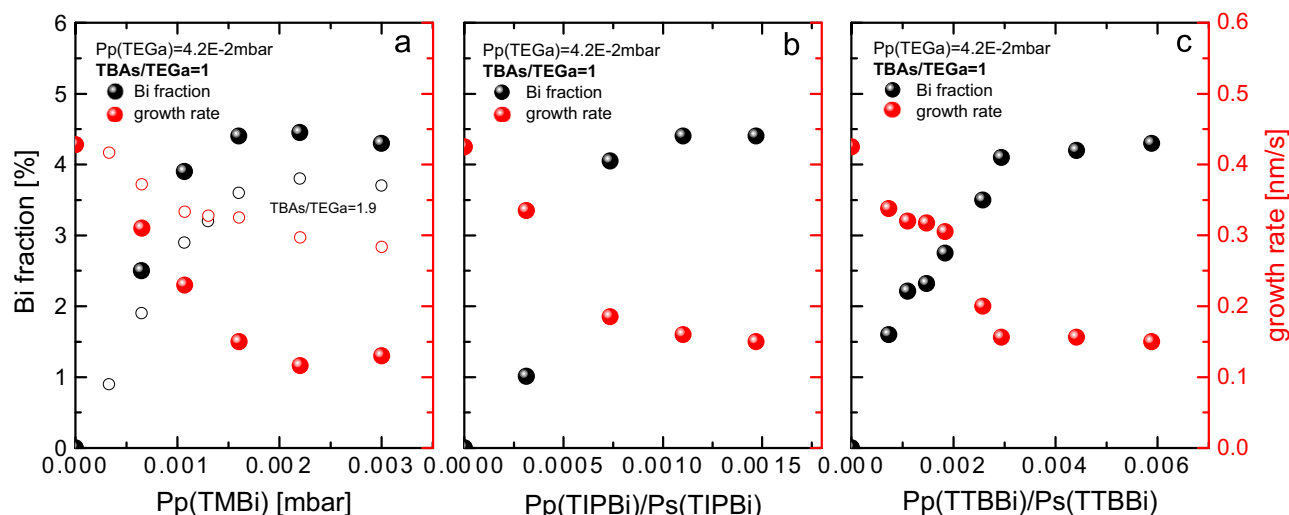


Fig. 1. Growth of Ga(AsBi) layers at 400 °C using three different Bi sources, TMBi (a), TIPBi (b) and TTBi (c). The Bi-fraction in the crystal (black and grey data points, left axis) and the growth rate (red data points, right axis) are plotted as functions of the partial pressure of the Bi-sources used. All lines are guides to the eye, not a fit. The partial pressures of TIPBi and TTBi are given in units of the vapour pressure (P_s), which is estimated to be about 1 mbar in both cases. (For interpretation of the references to color in this figure legend, the reader is referred to the web version of this article.)

precisely known and are estimated to be about 1 mbar. Growth parameters are otherwise identical to the parameters of the growth with the conventional precursors in order to compare the growth with the different Bi sources, while varying the Bi supply. To demonstrate how the Bi fraction and growth rate were determined, Fig. 2 shows XRD patterns of four different Ga(AsBi) layers grown with TTBi. For the growth with all three Bi sources the Bi fraction increases with offer of Bi, while the growth rate decreases. Fig. 1 illustrates that the trend of the Bi fraction and growth rate is not depending on the Bi source if the partial pressures of the TBAs and TEGa are comparable in the investigations. As already figured out in [13], the surface is covered with Bi and Bi-Ga droplets if Bi supply is in the saturation regime for both As/Ga ratios. A similar behaviour is also observed for the growth with TIPBi and TTBi. This is depicted in Fig. 3.

In contrast to the initial guess that the growth rate and the Bi incorporation should be higher with the alternative sources, because of the higher decomposition efficiency and the fact that no methyl groups are supplied to the surface, the Bi incorporation and the growth rate are similar for all – highly different – precursor molecules. This gives rise to the assumption that the methyl groups in particular are not responsible for a decrease of the growth rate and the limited Bi fraction as a consequence. However, a surface passivation through hydrocarbon groups in general or/and elemental Bi at the surface [10] could be cause for the dropping growth rate, as Ga could not reach the growth front any more.

At low growth temperatures high carbon (C) incorporation could be an issue, since the sources may not be fully decomposed. Therefore, the C incorporation was investigated and is also compared for the growths with different Bi precursors. Fig. 4 shows the dependence of the C incorporation on the Pp (Bi source). The C incorporation is reduced with an increasing amount of Bi during growth, which was already reported in [10]. Furthermore, it becomes apparent that the C incorporation is similar for all three Bi precursors. This is a further hint that, if there are alkyl fragments at the surface, at least they are not leading to a higher incorporation of carbon atoms in the growing layer. C incorporation in Ga(AsBi) grown at these low temperatures is lower than C incorporation in GaAs layers grown under the same conditions without Bi. Hence, it also becomes clear that Bi acts as a surfactant to decrease the C incorporation [10] as the C incorporation decreases with increasing Bi content.

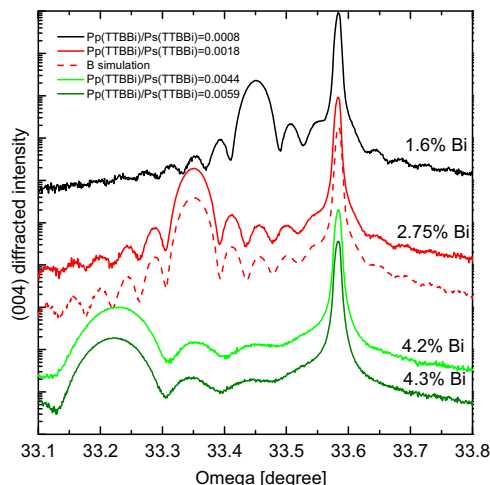


Fig. 2. XRD patterns of four Ga(AsBi) layers grown at 400 °C with different flows of TTBi (data are part of Fig. 1(c)).

Despite the low growth temperature, the samples show very good optical properties. In Fig. 5 room temperature PL spectra of the Ga(AsBi) layers grown with all three different Bi precursors are shown. The intensity is similar for all three Bi sources tested. It is remarkable that the high PL intensity of the first Ga(AsBi) layers grown with TTBi and TIPBi is close to the PL intensity of the layers grown with the commercially available TMBi. This shows that a low concentration of carrier traps has been achieved.

Summarizing the growths with the alternative Bi sources, it was shown that it is possible to grow high quality Ga(AsBi) structures with TIPBi and TTBi. The growth at even lower temperatures should be possible due to the promising crystal quality, low C incorporation and good decomposition characteristics shown here.

Nevertheless, the results from the growth of Ga(AsBi) with the alternative Bi precursors showed that the Bi source and its decomposition characteristics do not have an influence on the Bi incorporation or the growth rate in the investigated temperature range. Hence, the Bi incorporation is not limited by the decomposition or the decomposition pathway of the different Bi-precursors. It has been shown in previous experiments that higher Bi incorporation under otherwise unchanged growth conditions can be achieved by

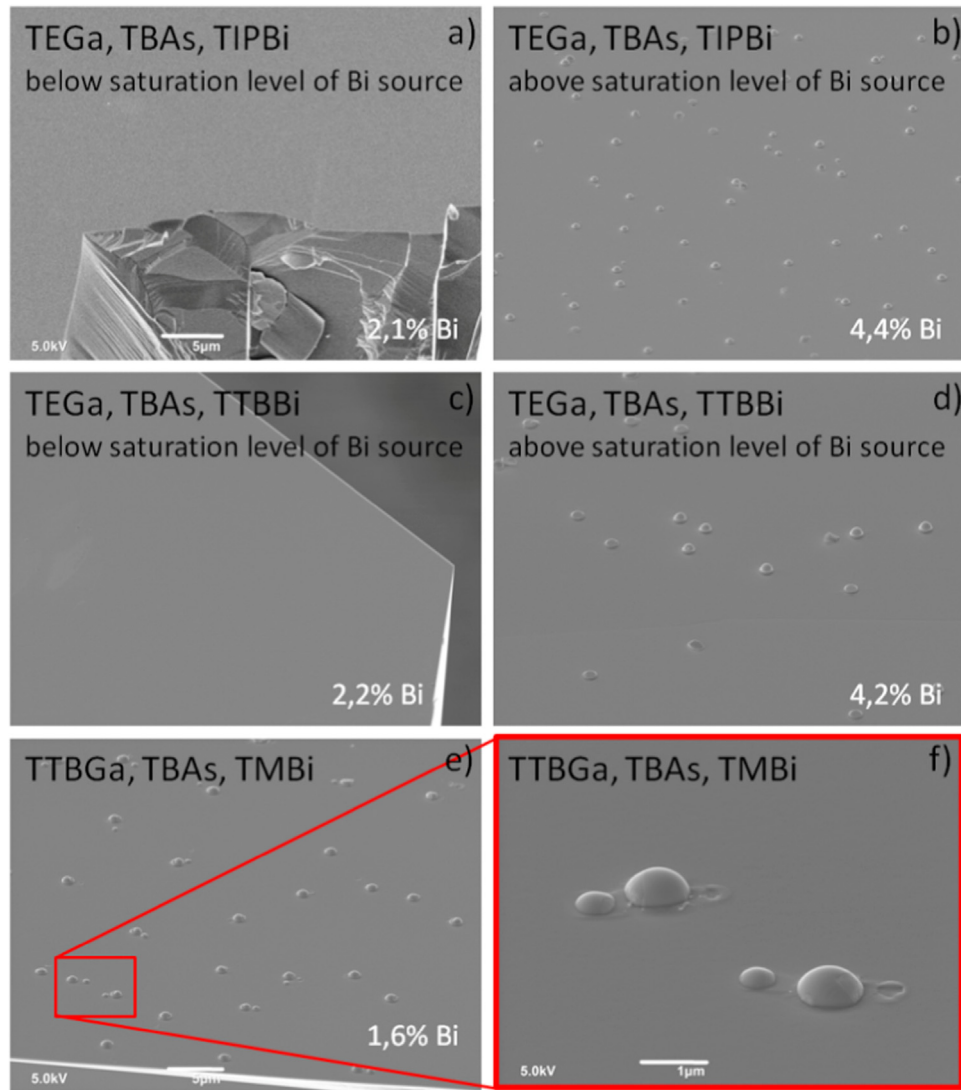


Fig. 3. SEM images from the surface of Ga(AsBi) layers grown with the alternative precursors TIPBi (a and b), TTBBi (c and d) and TTBGa (e and f). There are no droplets on layers which are grown below the saturation level (a and c) and a lot of droplets on the layers which are grown above the saturation level (b and d). For the growth with TTBGa there are droplets on every GaAsBi layer. This is due to the lower growth rate during the growth of Ga(AsBi) with the new Ga precursor.

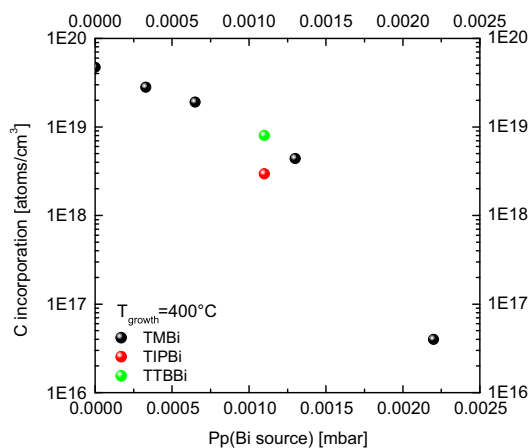


Fig. 4. C incorporation in Ga(AsBi) from SIMS (secondary ion mass spectrometry) analysis as a function of Bi partial pressure. The vapour pressure of the alternative Bi sources was estimated to be 1 mbar. Growth temperature was 400 °C.

increasing the growth rate by increasing the partial pressure of the Ga-precursor [10]. The partial pressures of As and Bi source have to be adjusted to the higher Ga partial pressure afterwards in order to

keep the ratios constant. To achieve that at these low growth temperatures using TEGa is very difficult, as this molecule is only decomposed to a small fraction at these temperatures. Hence, a different group III precursor (TTBGa), which decomposes at lower temperatures ($T_{50}=150\text{--}200\text{ °C}$) was used. Furthermore, the use of this precursor allows to investigate if there is an influence of the tertiarybutyl (TB) decomposition fragments on the surface chemistry and hence, on the growth characteristics.

Fig. 6 compares the results of the growth using TEGa and TTBGa. TMBi was used as the Bi source for these experiments. The Bi fraction and the growth rate are plotted vs. TBAs/TEGa ratio. Fig. 6(a) shows the results for the growth with TEGa and Fig. 4 (b) for TTBGa. The offer of TBAs was varied, while the partial pressures of the Ga- and Bi-sources were kept constant. While the Bi incorporation is similar for the growth for both Ga precursors, the growth rate drops with increasing TBAs when TTBGa is used, but not when Ga is supplied by TEGa. Due to the higher decomposition rate of the TTBGa relative to TEGa, this is the opposite of the result that was expected. The reason for that is probably the different size and number of the different hydrocarbon-rest fragments on the surface in experiments using TEGa compared to TTBGa. The higher number of huge TB-fragments which are bigger than the ethyl fragments is problematic, because it is more difficult

for the TTBGa to connect to the surface, which is already covered by elemental Bi or hydrocarbon-groups from the sources. Nevertheless, these results are very promising as – despite a very low growth rate – a significant Bi incorporation has been achieved. It should be possible to increase the Bi fraction in the crystal using this group III precursor, if the partial pressure of the TTBGa is increased or the growth temperature is lowered, provided the problem with the TB groups can be fully understood and solved. The potential possibility to increase Bi incorporation and growth rate is due to the highly efficient decomposition characteristics and especially to the fact that the ratio between Bi incorporation and growth rate is higher with TTBGa than the one for the growth with TEGa. We have seen that the Bi incorporation are increasing with increasing the growth rate by group III supply.

To verify that TTBGa is decomposed to a larger fraction than TEGa at this temperature and that the hydrocarbon rest groups are blocking the growth surface, resulting in a lowering of the growth rate, GaAs layers were grown with TEGa and TTBGa in order to check the growth rate with the two different precursors without the influence of the Bi precursor or the metallic Bi at the surface. In Fig. 7 the results of these experiments are plotted at different temperatures (Fig. 7(a)) and at different As/Ga ratios (Fig. 7(b)).

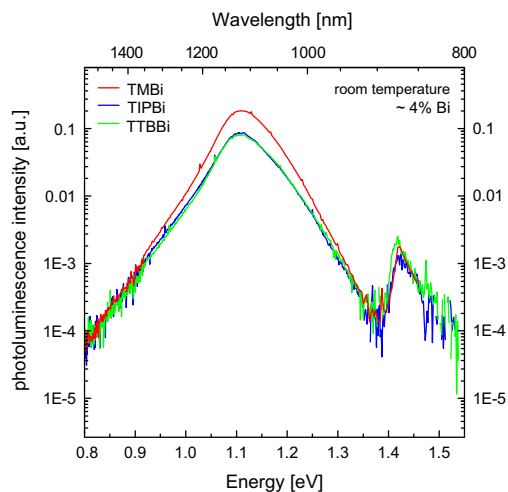


Fig. 5. Room temperature PL spectra of Ga(AsBi) grown with TMBi, TIPBi and TTBBi having similar Bi fractions. On the left side the peak coming from the Ga(AsBi), on the right the GaAs-peak. All three spectra are from measurements performed under same conditions to assure the comparability. Growth temperature was 400 °C.

The growth rate is the same with both Ga-sources for each set of parameters, over the whole range of parameters investigated. Fig. 7(b) shows that not only the TB-groups from the TTBGa are responsible for the observed growth rate characteristics, but in addition there is an influence of the TB groups of the TBAs on the growth rate. This becomes obvious from the observed drop in growth rate when just increasing the TBAs partial pressure under otherwise unchanged conditions (Fig. 7(b)). Such a behaviour is not observed for the growth using TBAs at higher temperatures.

In order to prove that TTBGa has a more efficient decomposition pathway than TEGa at 400 °C SEM investigations are shown in Fig. 8. Two experiments, where only Ga was offered to the GaAs surface, one experiment with TTBGa (right) and one with TEGa (left), show that the decomposition of TTBGa is more efficient than the one of TEGa, since the volumetric density of Ga droplets is higher at the GaAs surface of the TTBGa experiment. The growth parameters were identical (400 °C growth temperature, $P_p(\text{Ga})=0.042$ mbar, growth time 200 s). For the estimation of the total volumetric density of Ga-droplets on the surface images from different angles were taken into account and a higher Ga-droplet volume of at least 30% was found. These findings confirm studies in the literature [19].

These experiments prove that there is a significant influence of hydrocarbon fragments sticking to the growth surface on growth characteristics and that pure source decomposition cannot be used at those low temperatures as an argument for the choice of sources. Worth mentioning is that we observe an extremely low C incorporation (even without Bi) if TTBGa is used as Ga-precursor. Values which are more than one order of magnitude below the values which have been achieved with TEGa in GaAs can be realized easily. Finally, it is not possible to give a definite answer or explanation for the behaviour during the growth with TTBGa. Further experiments and theoretical studies will follow to fully understand and explain the decomposition processes.

4. Summary

It was shown that the growth of high quality Ga(AsBi) layers with alternative Bi- and Ga-precursors is possible. Bi fractions of up to 4% were achieved. A strong room temperature PL signal was observed for all three Bi precursors pointing towards an excellent crystal quality for the first low temperature growth studies using those chemicals. It was shown that there is low C incorporation for all Bi sources in Ga(AsBi) at 400 °C for all precursors investigated although they have significantly

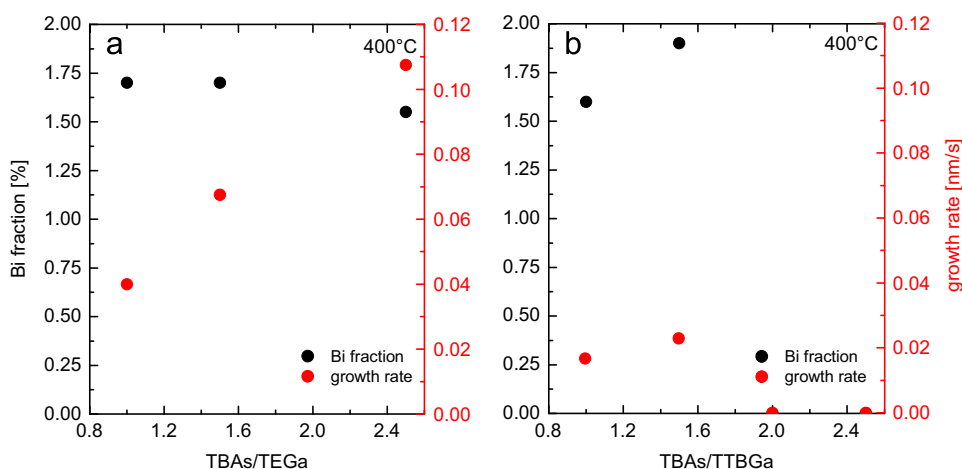


Fig. 6. Growth of Ga(AsBi) layers at 400 °C using TEGa (a) and TTBGa (b), respectively. The Bi-fraction in the crystal (black data points, left axis) and the growth rate (red data points, right axis) are plotted as function of the As/Ga ratio used, while $P_p(\text{TMBi})$ is fix. For the TTBGa (b) the Bi incorporation dropped already at a As/Ga ratio between 2 and 2.5 so that there is no information about the growth rate. (For interpretation of the references to color in this figure legend, the reader is referred to the web version of this article.)

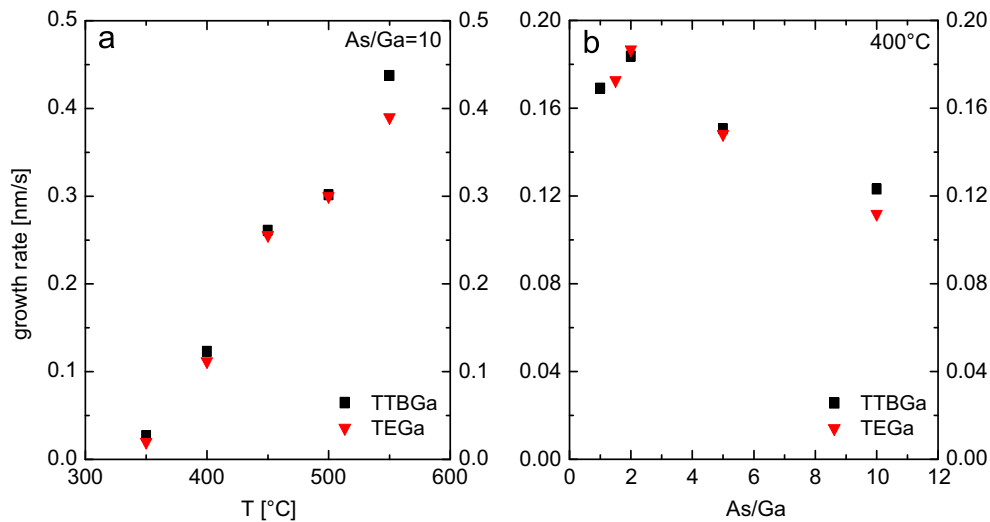


Fig. 7. Growth rate of pure GaAs layers grown with TEGa (black data points) and TTBGa (red data points), respectively. (a) shows the growth rate at different growth temperatures and (b) shows the influence of a variation of the TBAs partial pressure on the growth rate at 400 °C. (For interpretation of the references to color in this figure legend, the reader is referred to the web version of this article.)

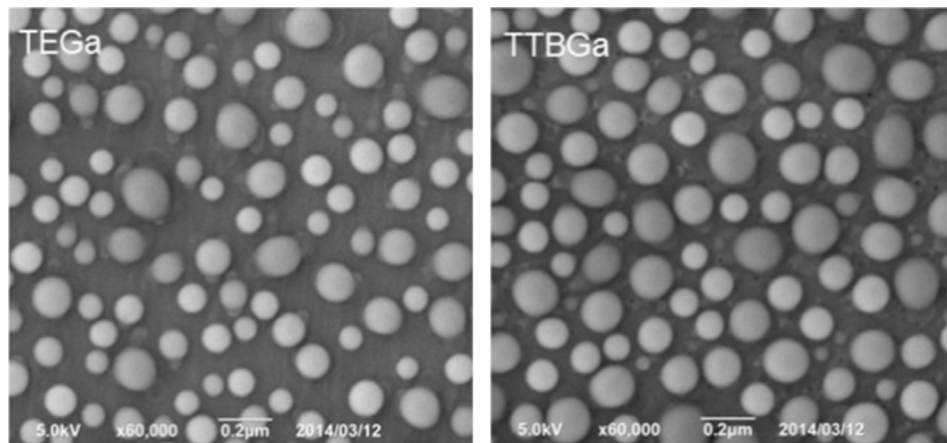


Fig. 8. SEM images of Ga droplets on a GaAs surface. The droplets were deposited using TEGa (left) and TTBGa (right) at 400 °C under identical conditions.

different hydrocarbon ligands. For the growth of GaAs with TTBGa there is even a one order of magnitude lower C incorporation compared to the growth with TEGa.

It has been shown that for the low growth temperatures needed for the growth of metastable materials like dilute bismides, one has to take into account a significant effect of hydrocarbon groups from the metal organic precursor decomposition, which do not desorb from the surface any more but also do not incorporate, on the growth characteristics. Effects of size and number of hydrocarbon residue groups blocking surface sites can be more important than arguments of pure source stability and thermal decomposition. Overall TTBGa, TIPBi and TTBi are promising candidates for the growth of Ga(AsBi) at even lower growth temperatures, which should be helpful in order to increase the Bi incorporation.

Acknowledgements

We gratefully acknowledge support from German Research Foundation (DFG) in the framework of the RTG1782 “Functionalization of Semiconductors” as well as from the HMWK in the framework of the project EGALITE.

References

- [1] C.A. Broderick, M. Usman, S.J. Sweeney, E.P. O'Reilly, *Semicond. Sci. Technol.* 27 (2012) 094011. <http://dx.doi.org/10.1088/0268-1242/27/9/094011>.
- [2] S.J. Sweeney, S.R. Jin, *J. Appl. Phys.* 113 (2013) 043110. <http://dx.doi.org/10.1063/1.4789624>.
- [3] K. Alberi, et al., *Appl. Phys. Lett.* 91 (2007) 051909. <http://dx.doi.org/10.1063/1.2768312>.
- [4] K. Oe, H. Okamoto, *Jpn. J. Appl. Phys.* 37 (1998) L1283–L1285. <http://dx.doi.org/10.1143/JJAP.37.L1283>.
- [5] J. O'Gorman, A.F.J. Levi, T. Tanbun-Ek, D.L. Coblenz, R.A. Logan, *Appl. Phys. Lett.* 60 (1992) 1058. <http://dx.doi.org/10.1063/1.106443>.
- [6] Y.L. Chen, et al., *Science* 325 (2009) 178. <http://dx.doi.org/10.1126/science.1173034>.
- [7] M.K. Rajpalke, W.M. Linhart, M. Birkett, K.M. Yu, D.O. Scanlon, J. Buckeridge, T. S. Jones, M.J. Ashwin, T.D. Veal, *Appl. Phys. Lett.* 103 (2013) 142106. <http://dx.doi.org/10.1063/1.4824077>.
- [8] Z.L. Bushell, P. Ludewig, N. Knaub, Z. Batool, K. Hild, W. Stolz, S.J. Sweeney, K. Volz, *J. Cryst. Growth* 396 (2014) 79–84. <http://dx.doi.org/10.1016/j.jcrysgro.2014.03.038>.
- [9] J.P. Petropoulos, Y. Zhong, J.M.O. Zide, *Appl. Phys. Lett.* 99 (3) (2011) 031110. <http://dx.doi.org/10.1063/1.3614476>.
- [10] P. Ludewig, Z.L. Bushell, L. Nattermann, N. Knaub, W. Stolz, K. Volz, *J. Cryst. Growth* 396 (2014) 95–99. <http://dx.doi.org/10.1016/j.jcrysgro.2014.03.041>.
- [11] P. Ludewig, N. Knaub, W. Stolz, K. Volz, *J. Cryst. Growth* 370 (2013) 186–190. <http://dx.doi.org/10.1016/j.jcrysgro.2012.07.002>.
- [12] K. Oe, et al., *Jpn. J. Appl. Phys.* 41 (2002) 2801–2806. <http://dx.doi.org/10.1143/JJAP.41.2801>.

- [13] K. Forghani, Y. Guan, A.W. Wood, A. Anand, S.E. Babcock, L.J. Mawst, T.F. Kuech, J. Cryst. Growth 395 (2014) 38–45. <http://dx.doi.org/10.1016/j.jcrysgro.2014.03.014>.
- [14] Joachim Buddrus, Grundlagen der organischen Chemie, Page 90, De Gruyter.
- [15] H. Schumann, H.J. Breunig, J. Organomet. Chem. 87 (1975) 83–92.
- [16] M. Herbold, W. Ehrenreich, K. Guldner, Chem. Ber. 117 (1984) 1999–2005.
- [17] H.J. Breunig, D. Müller, Z. Naturfor. 38B (1983) 125–129.
- [18] S. Tixier, M. Adamczyk, T. Tiedje, S. Francoeur, M.-J. Seong, A. Mascarenhas, Appl. Phys. Lett. 82 (2003) 22. <http://dx.doi.org/10.1063/1.1581983>.
- [19] N. Bahlawane, et al., Mass-spectrometric monitoring of the thermal induced decomposition of trimethylgallium, tris(tert-butyl)gallium, and triethylantimony at low pressure conditions Elsevier Inc., Am. Soc. Mass Spectrom. 19 (2008) 947–954. <http://dx.doi.org/10.1016/j.jasms.2008.04.015>, 1044–0305.

6.2.6 Valence Band-Anticrossing in Ga(PBi) Dilute Bismide Alloys: Giant Bowing of the Band Gap and Spin-Orbit Splitting Energy

Z. Bushell, C. Broderick, L. Nattermann, R. Joseph, J. Keddie, J. Rorison, K. Volz, S. Sweeney

submitted to Physical Review Materials (Rapid Communications) (2017)

Abstract

We present an experimental and theoretical study of the band structure evolution with bismuth (Bi) composition x in the dilute bismide alloy $\text{GaP}_{1-x}\text{Bi}_x$. Using spectroscopic ellipsometry measurements on $\text{GaP}_{1-x}\text{Bi}_x/\text{GaP}$ epitaxial layers up to $x = 3.7\%$ we confirm the predicted giant bowing of the direct band gap (E_g) and valence band spin-orbit splitting energy (ΔSO). E_g (ΔSO) is measured to decrease (increase) by approximately 220 meV with the incorporation of 1% Bi, corresponding to a greater than fourfold increase in ΔSO in going from GaP to $\text{GaP}_{1-0.99}\text{Bi}_{0.01}$. The evolution of E_g and ΔSO with x is characterised by strong, composition-dependent bowing. We demonstrate that a simple valence band-anticrossing model - parametrised directly from atomistic supercell calculations - is sufficient to quantitatively describe the measured evolution of E_g and ΔSO with x . In contrast to the well-studied $\text{GaAs}_{1-x}\text{Bi}_x$ alloy, in $\text{GaP}_{1-x}\text{Bi}_x$ substitutional Bi creates localised impurity states lying energetically within the GaP band gap. This corresponds to the emergence of an optically active impurity band of Bi-hybridised states, accounting explicitly for the overall large bowing of E_g and ΔSO , and in particular for the giant bowing observed for $x \lesssim 1\%$. Our analysis provides insight into the action of Bi as an isovalent impurity when incorporated in conventional III-V semiconductors, and constitutes the first detailed analysis of the $\text{GaP}_{1-x}\text{Bi}_x$ alloy band structure.

The Authors contribution

My contribution to this work was the planning and execution of the MOVPE growth and first structural characterization of all samples investigated. The performance of all ellipsometry measurements was done by Z. Bushell in close collaboration with R. Joseph. C. Broderick performed all calculations. S. Sweeney and K. Volz as well as all co-authors helped to interpret the data and to improve the manuscript that was written by Z. Bushell, C. Broderick and me.

Valence band-anticrossing in $\text{GaP}_{1-x}\text{Bi}_x$ dilute bismide alloys: giant bowing of the band gap and spin-orbit splitting energy

Zoe L. Bushell,¹ Christopher A. Broderick,^{2,3} Lukas Nattermann,⁴ Rita M. Joseph,¹
Joseph L. Keddle,¹ Judy M. Rorison,³ Kerstin Volz,⁴ and Stephen J. Sweeney^{1,*}

¹*Advanced Technology Institute & Department of Physics, University of Surrey, Guildford, GU2 7XH, U.K.*

²*Tyndall National Institute, Lee Maltings, Dyke Parade, Cork T12 R5CP, Ireland*

³*Department of Electrical and Electronic Engineering, University of Bristol, Bristol BS8 1UB, U.K.*

⁴*Materials Science Center & Faculty of Physics, Philipps-Universität Marburg, 35032 Marburg, Germany*
(Dated: September 20, 2017)

We present an experimental and theoretical study of the band structure evolution with bismuth (Bi) composition x in the dilute bismide alloy $\text{GaP}_{1-x}\text{Bi}_x$. Using spectroscopic ellipsometry measurements on $\text{GaP}_{1-x}\text{Bi}_x/\text{GaP}$ epitaxial layers up to $x = 3.7\%$ we confirm the predicted giant bowing of the direct band gap (E_g^Γ) and valence band spin-orbit splitting energy (Δ_{SO}). E_g^Γ (Δ_{SO}) is measured to decrease (increase) by approximately 200 meV (240 meV) with the incorporation of 1% Bi, corresponding to a greater than fourfold increase in Δ_{SO} in going from GaP to $\text{GaP}_{0.99}\text{Bi}_{0.01}$. The evolution of E_g^Γ and Δ_{SO} with x is characterised by strong, composition-dependent bowing. We demonstrate that a simple valence band-anticrossing model – parametrised directly from atomistic supercell calculations – is sufficient to quantitatively describe the measured evolution of E_g^Γ and Δ_{SO} with x . In contrast to the well-studied $\text{GaAs}_{1-x}\text{Bi}_x$ alloy, in $\text{GaP}_{1-x}\text{Bi}_x$ substitutional Bi creates localised impurity states lying energetically within the GaP host matrix band gap. This leads to the emergence of an optically active band of Bi-hybridised states, accounting for the overall large bowing of E_g^Γ and Δ_{SO} and in particular for the giant bowing observed for $x \lesssim 1\%$. Our analysis provides insight into the action of Bi as an isovalent impurity, and constitutes the first detailed analysis of the $\text{GaP}_{1-x}\text{Bi}_x$ alloy band structure.

Highly-mismatched III-V semiconductor alloys containing dilute concentrations of Bi have attracted significant attention in recent years¹ since their unique electronic properties open up a range of possibilities for practical applications in near- and mid-infrared semiconductor lasers,^{2–13} photovoltaics,^{14,15} spintronics,^{16–18} photodiodes,^{19–22} and thermoelectrics.²³ Research on dilute bismide alloys has primarily focused to date on $\text{GaAs}_{1-x}\text{Bi}_x$, where incorporation of Bi brings about a strong reduction of the direct band gap (E_g^Γ) – by up to 90 meV per % Bi at low Bi compositions x ^{24–28} – characterised by strong, composition-dependent bowing.^{26,29} This unusual behaviour derives from the large differences in size (covalent radius) and chemical properties (electronegativity) between As and Bi: Bi, being significantly larger and more electropositive than As, acts as an isovalent impurity which primarily impacts and strongly perturbs the valence band (VB) structure.^{27,30,31} This is in contrast to dilute nitride alloys, in which small electronegative nitrogen (N) atoms strongly perturb the conduction band (CB) structure in $\text{GaN}_x\text{As}_{1-x}$ and related alloys.^{32–35} Additionally Bi, being the largest stable group-V element, has strong relativistic (spin-orbit coupling) effects.³⁶ As such, the reduction of E_g^Γ in $(\text{In})\text{GaAs}_{1-x}\text{Bi}_x$ is accompanied by a strong increase in the VB spin-orbit splitting energy (Δ_{SO}).^{27,28,37}

Epitaxial growth of $\text{GaP}_{1-x}\text{Bi}_x$ alloys – via molecular beam epitaxy^{38,39} and metal-organic vapour phase epitaxy⁴⁰ (MOVPE) – has been only recently established. Here, we present the first detailed analysis of the $\text{GaP}_{1-x}\text{Bi}_x$ electronic structure. Initial experiments⁴¹ revealed that Bi dopants generate bound localised im-

purity states in GaP – i.e. Bi-related localised impurity states lying energetically within the GaP host matrix band gap – but little further data is available regarding the $\text{GaP}_{1-x}\text{Bi}_x$ band structure. We explicitly verify that the evolution of the main features of the $\text{GaP}_{1-x}\text{Bi}_x$ VB structure with x can be understood straightforwardly in terms of a Bi composition-dependent valence band-anticrossing (VBAC) interaction between the extended states of the GaP VB edge and highly localised bound impurity states associated with substitutional Bi impurities. Our measurements reveal giant bowing of E_g^Γ and Δ_{SO} : E_g^Γ (Δ_{SO}) decreases (increases) by ≈ 200 meV (240 meV) when 1% Bi is incorporated substitutionally in GaP. Comparison between theory and experiment highlights the emergence of an impurity band of primarily Bi-derived states, lying energetically within the GaP band gap but close in energy to the unperturbed GaP VB edge. The VBAC interaction leads to these states acquiring an admixture of localised (Bi) and extended Γ_{8v} VB edge (Bloch) character, enabling optical coupling to the comparatively unperturbed Γ_{6c} CB states.

Spectroscopic ellipsometry (SE) was used to study bulk-like $\text{GaP}_{1-x}\text{Bi}_x/\text{GaP}$ epitaxial layers containing up to 3.7% Bi. The samples upon which our analysis was performed were grown on (001)-oriented GaP by MOVPE. Full details of the sample growth and characterisation can be found in Ref. 40. The SE measurements were performed at room temperature using a J. A. Woolam Co. variable angle spectroscopic ellipsometer system. Three incident beam angles were used to generate sufficient data to provide confidence in modelling fits to the measured spectra. Angles of 73.5°, 74.0° and 74.5° were

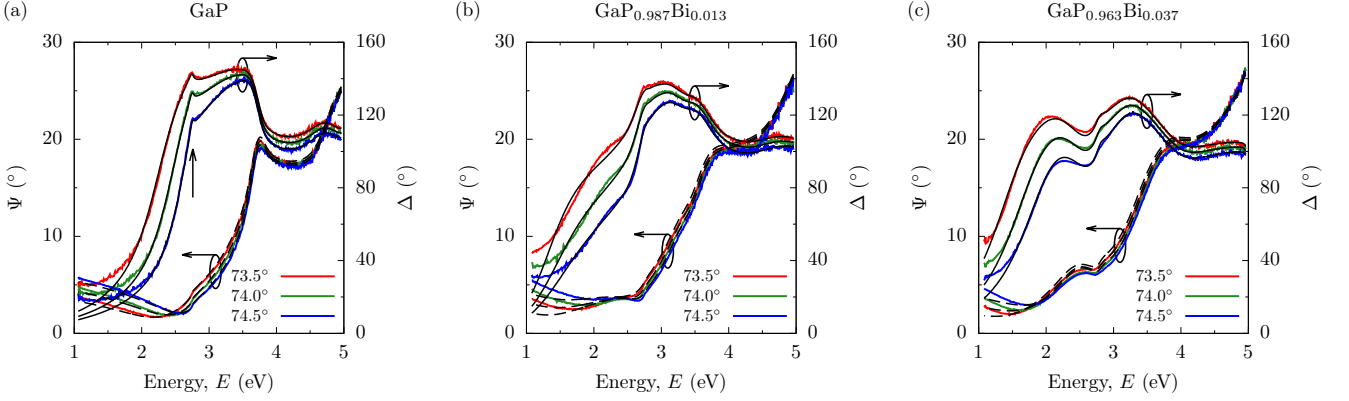


FIG. 1. Measured SE spectra for the MOVPE-grown (a) GaP (Bi-free, $x = 0$), (b) $\text{GaP}_{0.987}\text{Bi}_{0.013}$ ($x = 1.3\%$), and (c) $\text{GaP}_{0.963}\text{Bi}_{0.037}$ ($x = 3.7\%$) samples described in the text and in Ref. 40. Solid red, green and blue lines respectively denote data measured for incident beam angles of 73.5° , 74.0° and 74.5° . Solid (dashed) black lines show the fits to the measured Δ (Ψ) spectra; the SE model and associated fitting procedure are outlined in the text.

chosen since they are close to the pseudo-Brewster angles of the samples under investigation, thereby ensuring that the phase change on reflection Δ remained close to 90° . The sensitivity of the rotating analyser ellipsometer configuration is reduced when Δ is close to 0° or 180° – keeping Δ close to 90° therefore maximises the accuracy of the measurements.⁴² A carefully defined modelling and fitting procedure is required to extract the energies corresponding to critical points in the band structure from the measured SE data. The semiconductor layers were described using a parametrised model which represents the sample dielectric constant as a sum of multiple Gaussian oscillators.⁴³ The presence of a native oxide layer on the surface of each sample was accounted for explicitly via tabulated dielectric constant data.⁴⁴ Using the appropriately parametrised model for each sample an iterative fitting procedure was then implemented to minimise the difference between the measured and simulated SE data, allowing the energies corresponding to the E_g^Γ and $E_g^\Gamma + \Delta_{\text{SO}}$ interband transitions to be extracted.

The solid red, green and blue lines in Figs. 1(a), (b) and (c) respectively show the measured SE data – where $\tan(\Psi)$ is the amplitude ratio of the p - and s -polarisations after reflection⁴² – for incident beam angles of 73.5° , 74.0° and 74.5° in the GaP, $\text{GaP}_{0.987}\text{Bi}_{0.013}$ and $\text{GaP}_{0.963}\text{Bi}_{0.037}$ samples. Solid (dashed) black lines show the corresponding fits to Δ (Ψ) obtained using the procedure outlined above. The GaP sample consists of an epitaxial GaP buffer layer grown on a GaP substrate, and was analysed first in order to obtain accurate input parameters for the SE fits. These parameters were then used to describe the substrate and buffer layer in the subsequent models of the Bi-containing samples. Following this procedure it was possible to achieve good fits to the key features observed in the measured $\text{GaP}_{1-x}\text{Bi}_x$ SE spectra (cf. Figs. 1(b) and (c)). In Fig. 1(a) a clear feature associated with E_g^Γ is visible in the measured Δ and Ψ spectra, which is well described by a modelling fit

corresponding to a direct GaP room temperature band gap $E_g^\Gamma = 2.76$ eV – denoted in Fig. 1(a) by a vertical arrow. The slight deviation from the accepted value of 2.78 eV is possibly attributable to the growth taking place on n-doped GaP substrates.

Turning to Figs. 1(b) and (c) it is clear from the measured Δ spectra that Bi incorporation gives rise to an additional feature which appears on the low energy side of the GaP direct band gap and shifts to lower energies with increasing x . This indicates a large reduction of E_g^Γ , in accordance with theoretical predictions.^{27,45,46} The features associated with E_g^Γ are significantly broader in the Bi-containing samples than in GaP. This is likely associated with the presence of Bi composition fluctuations across the samples, as well as short-range alloy disorder and structural defects, leading to reduced material quality.^{47,48} Using the multiple oscillator approach described above it was also possible to extract the energies associated with the $E_g^\Gamma + \Delta_{\text{SO}}$ transitions in each sample. The values of E_g^Γ and Δ_{SO} extracted in this manner are shown respectively in Figs. 2(b) and (c), using closed red circles and blue squares. We note that the uncertainties in these data are associated with the broadening of the associated features in the measured spectra. Overall, the SE measurements indicate that incorporation of dilute concentrations of Bi is sufficient to cause a giant reduction (increase) and bowing of E_g^Γ (Δ_{SO}).

To understand this unusual behaviour we have used atomistic supercell calculations to analyse the contributions to the Bi-induced changes in the band edge energies, and to parametrise a suitable VBAC model for $\text{GaP}_{1-x}\text{Bi}_x$. This approach does not rely on post hoc fitting to alloy band structure data, thereby providing a predictive capability commonly lacking in models of this type.²⁹ In Ref. 27 we employed an atomistic tight-binding (TB) model to analyse the electronic structure of ordered and disordered $\text{GaP}_{1-x}\text{Bi}_x$ alloys. By directly constructing the T_2 -symmetric localised states $|\psi_{\text{Bi}}\rangle$ as

sociated with an isolated, substitutional Bi impurity we predicted the presence of a VBAC interaction having a composition dependence $\beta\sqrt{x}$. In the dilute doping (large supercell) limit we computed that the Bi-related localised states in GaP:Bi lie approximately 120 meV above the unperturbed GaP VB edge, in good agreement with experiment.⁴¹ Analysis of the electronic structure of ordered Ga(P,As)_{1-x}Bi_x alloys elucidates the differences in the impact of Bi incorporation on the band structure: the natural VB offsets between GaP, GaAs and GaBi lead to the 6*p* valence orbitals of Bi lying below the 4*p* valence orbitals of As in energy, but higher in energy than the 3*p* valence orbitals of P. As such, a substitutional Bi impurity forms a resonant localised state lying energetically below the VB edge in GaAs, but a bound localised state lying above the VB edge in energy in GaP.²⁷

Building on our initial analysis of Ga(P,As)_{1-x}Bi_x we have derived an extended basis set 12-band (VBAC) **k**·**p** Hamiltonian to describe the dilute bismide band structure.²⁹ Using the TB model of Ref. 27 we have directly evaluated the Bi-related parameters of this model, including the distinct VBAC, virtual crystal (VC) and strain-related contributions to the Bi-induced shifts in the band edge energies.⁴⁹ To analyse the SE measurements we focus on the band edge energies at the zone centre: at Γ the 12-band Hamiltonian diagonalises into decoupled blocks describing the CB, heavy-hole (HH), and light- and spin-split-off-hole (LH and SO) band edges.⁴⁹ As in GaAs_{1-x}Bi_x, the GaP_{1-x}Bi_x Γ -point CB edge energy is well described as $E_{\text{CB}}(x) = E_g^{\Gamma}(0) - \alpha x + \delta E_{\text{CB}}^{\text{hy}}$, where the zero of energy has been chosen at the unperturbed GaP VB edge, $E_g^{\Gamma}(0) = 2.78$ eV is the host matrix band gap, α describes the VC shift of the CB edge energy, and $\delta E_{\text{CB}}^{\text{hy}}$ is the energy shift associated with the hydrostatic component of the compressive pseudomorphic strain in a GaP_{1-x}Bi_x/GaP epitaxial layer.⁴⁹

The energies of the HH-like alloy VB states are given in the 12-band VBAC model as the eigenvalues of^{27,49}

$$\begin{pmatrix} \Delta E_{\text{Bi}} + \delta E_{\text{Bi}}^{\text{hy}} - \delta E_{\text{Bi}}^{\text{ax}} & \beta\sqrt{x} \\ \beta\sqrt{x} & \kappa x + \delta E_{\text{VB}}^{\text{hy}} - \delta E_{\text{VB}}^{\text{ax}} \end{pmatrix} \begin{pmatrix} |\psi_{\text{Bi}}^{\text{HH}}\rangle \\ |\psi_{\text{HH}}^{(0)}\rangle \end{pmatrix}, \quad (1)$$

where $\kappa x + \delta E_{\text{VB}}^{\text{hy}} - \delta E_{\text{VB}}^{\text{ax}}$ describes the VC, hydrostatic and axial strain-induced shifts to the GaP HH band edge energy, and $\Delta E_{\text{Bi}} + \delta E_{\text{Bi}}^{\text{hy}} - \delta E_{\text{Bi}}^{\text{ax}}$ is the energy of the HH-like Bi-related localised states relative to the zero of energy at the unperturbed GaP VB edge.⁴⁹ The energies of the LH- and SO-like VB states are given as the eigenvalues of a 3×3 matrix which can be found, along with full details of the model, in Ref. 49.

The Bi-related band parameters computed for GaP_{1-x}Bi_x are summarised in Table I, where they are compared to those computed previously for GaAs_{1-x}Bi_x. The calculated VC parameters α , κ and γ – the latter describing the SO band edge energy^{29,49} – are close to those calculated for GaAs_{1-x}Bi_x, reflecting (i) the larger (smaller) CB and VB (SO) offsets between GaP and GaBi than between GaAs and GaBi,²⁷ and (ii) the larger lattice

TABLE I. Bi-related parameters for the 12-band (VBAC) **k**·**p** Hamiltonian of Ga(P,As)_{1-x}Bi_x, computed using atomistic TB calculations on ordered alloy supercells. The energy ΔE_{Bi} of the Bi-related localised impurity states is given relative to the unperturbed Ga(P,As) host matrix VB edge.^{29,49}

Parameter	GaP _{1-x} Bi _x	GaAs _{1-x} Bi _x
ΔE_{Bi} (eV)	0.122	-0.183
α (eV)	3.22	2.82
β (eV)	1.41	1.13
γ (eV)	0.24	0.55
κ (eV)	1.47	1.01

mismatch between GaP and GaBi ($\approx 14\%$) than between GaAs and GaBi ($\approx 11\%$). The calculated VBAC coupling strength β is larger in GaP_{1-x}Bi_x, reflecting the larger differences in size and electronegativity between P and Bi than between As and Bi. We note that β in GaP_{1-x}Bi_x is comparable to that calculated previously for the GaN_xP_{1-x} CB ($\beta = 1.74$ eV).^{35,50}

Figure 2(a) shows the calculated variation of the Γ -point band edge energies with x in pseudomorphically strained GaP_{1-x}Bi_x/GaP, for the CB (E_{CB} , solid green line), HH (E_{\pm}^{HH} , solid red lines), and LH and SO (E_{\pm}^{LH} and E_{SO} , dashed blue lines) states respectively. At Γ the hydrostatic component of the pseudomorphic strain acts to push the CB (HH, LH and SO) edge(s) upwards (downwards) in energy, while the axial component lifts the degeneracy of VB edge to push HH-like states higher in energy than the LH-like states. In GaP_{1-x}Bi_x/GaP we calculate that E_{CB} reduces linearly with increasing x , by 18 meV per % Bi. The VBAC interaction produces two Bi-hybridised HH-like bands, the energies E_{\pm}^{HH} of which vary strongly with x , displaying strong composition-dependent bowing. Beginning from $E_{-}^{\text{HH}} = 0$ and $E_{+}^{\text{HH}} = \Delta E_{\text{Bi}}$ at $x = 0$, we calculate that E_{-}^{HH} (E_{+}^{HH}) decreases (increases) by 79 meV (103 meV) between $x = 0$ and 1%. Similarly, the VBAC interaction produces a set of LH- and SO-like Bi-hybridised bands,⁴⁹ the energies of which are again strongly dependent on x and characterised by strong composition-dependent bowing. As E_{-}^{LH} moves downwards in energy towards E_{SO} with increasing x the coupling between the LH- and SO-like states – brought about by the axial component of the pseudomorphic strain⁴⁹ – leads to an anticrossing which is manifested in an abrupt increase in the rate at which E_{SO} decreases for $x \gtrsim 1\%$. We note also that this axial strain-induced anticrossing between the LH- and SO-like states leads to a change of the VB ordering at Γ , with $E_{-}^{\text{LH}} > E_{-}^{\text{HH}}$ for $x \gtrsim 1\%$.

To compare the composition dependence of E_g^{Γ} and ΔE_{SO} inferred from the SE measurements to the theoretical calculations it is necessary to analyse the character of the VB eigenstates, in order to identify the presence of optically active states in the highly perturbed GaP_{1-x}Bi_x VB. Since GaP_{1-x}Bi_x/GaP epitaxial layers are in a state

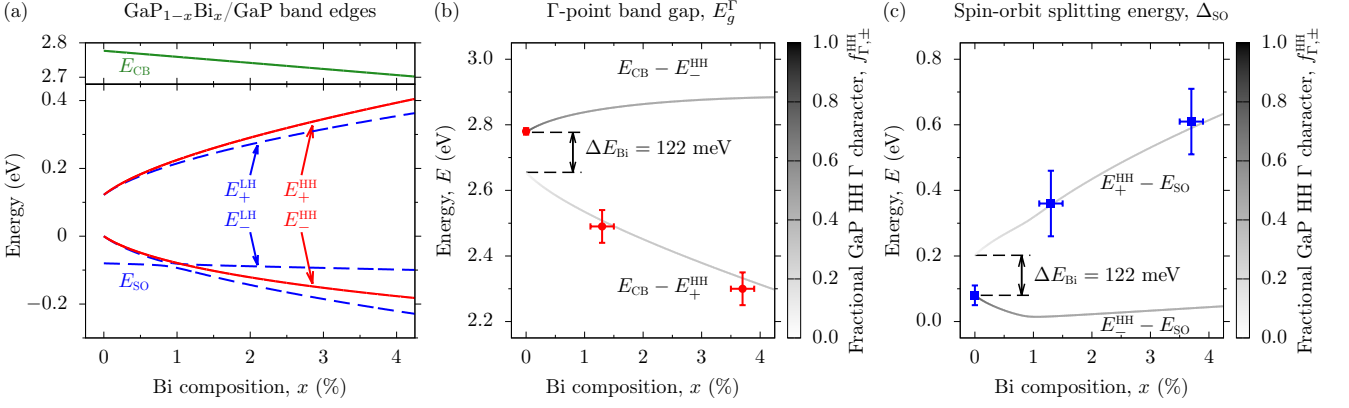


FIG. 2. (a) Calculated variation of the Γ -point band edge energies with x in pseudomorphically strained $\text{GaP}_{1-x}\text{Bi}_x/\text{GaP}$. Solid red, dashed blue and solid green lines respectively show the variation of the HH-like, LH/SO-like, and CB edge energies. (b) Variation of the $\text{GaP}_{1-x}\text{Bi}_x/\text{GaP}$ Γ -point band gaps $E_{\text{CB}} - E_{\pm}^{\text{HH}}$ with x , calculated (shaded lines) and extracted from SE measurements (closed red circles). The line shading is determined by the fractional GaP HH Γ character $f_{\Gamma,\pm}^{\text{HH}}$ of the associated HH-like $\text{GaP}_{1-x}\text{Bi}_x$ VB states E_{\pm}^{HH} . (c) Variation of the $\text{GaP}_{1-x}\text{Bi}_x/\text{GaP}$ VB spin-orbit splitting energies $E_{\pm}^{\text{HH}} - E_{\text{SO}}$ with x , calculated (shaded lines) and extracted from SE measurements (closed blue circles). The line shading is as in (b).

of compressive pseudomorphic strain the highest energy alloy VB states are expected to be HH-like (cf. Fig. 2(a)). It is therefore sufficient to investigate the character of the eigenstates $|\psi_{\pm}^{\text{HH}}\rangle = a_{\text{HH}}^{(\pm)} |\psi_{\text{HH}}^{(0)}\rangle + a_{\text{Bi}}^{(\pm)} |\psi_{\text{Bi}}^{\text{HH}}\rangle$ of Eq. (1) – corresponding respectively to the eigenvalues E_{\pm}^{HH} – which are a linear combination of the extended HH band edge state $|\psi_{\text{HH}}^{(0)}\rangle$ of the unperturbed GaP host matrix, and the HH-like Bi-related localised state $|\psi_{\text{Bi}}^{\text{HH}}\rangle$.

Since $\Delta E_{\text{Bi}} > 0$ in $\text{GaP}_{1-x}\text{Bi}_x$ the higher energy E_{+}^{HH} eigenstate $|\psi_{+}^{\text{HH}}\rangle$ of Eq. (1) is primarily Bi-derived ($|a_{\text{HH}}^{(+)}|^2 < \frac{1}{2}$). Furthermore, given that the Bi-related localised states $|\psi_{\text{Bi}}^{\text{HH}}\rangle$ do not couple optically to the Γ_{6c} CB edge states,²⁹ any optical transitions between $|\psi_{+}^{\text{HH}}\rangle$ and the Γ -point CB edge, having energy $E_{\text{CB}} - E_{+}^{\text{HH}}$, result from the VBAC interaction imparting GaP HH fractional Γ character $f_{\Gamma,+}^{\text{HH}} \equiv |\langle \psi_{\text{HH}}^{(0)} | \psi_{+}^{\text{HH}} \rangle|^2 = |a_{\text{HH}}^{(+)}|^2$ to $|\psi_{+}^{\text{HH}}\rangle$. Using Eq. (1), $f_{\Gamma,+}^{\text{HH}}$ can be determined analytically as

$$f_{\Gamma,+}^{\text{HH}} = \frac{\beta^2 x}{\beta^2 x + (E_{+}^{\text{HH}} - \kappa x - \delta E_{\text{VB}}^{\text{hy}} + \delta E_{\text{VB}}^{\text{ax}})^2}. \quad (2)$$

As x increases the increase in the strength $\beta\sqrt{x}$ of the VBAC interaction leads to $|\psi_{+}^{\text{HH}}\rangle$ acquiring significant GaP HH Γ character which, despite being limited to values $< \frac{1}{2}$, is sufficient to produce appreciable optical coupling to the Γ_{6c} CB states. For example, at $x = 1\%$ we calculate $f_{\Gamma,+}^{\text{HH}} = 0.315$, indicating that the optical transition strength between $|\psi_{+}^{\text{HH}}\rangle$ and Γ_{6c} in an ordered $\text{GaP}_{0.99}\text{Bi}_{0.01}$ alloy should be close to one-third of that between Γ_{8v} and Γ_{6c} in GaP. Our analysis therefore suggests the emergence of an optically active band of primarily Bi-derived impurity states at energy E_{+}^{HH} .

In order to reflect this admixture of GaP Bloch and Bi localised character, we have calculated each of the potentially observable energy gaps $E_g^{\Gamma} = E_{\text{CB}} - E_{\pm}^{\text{HH}}$ and $\Delta_{\text{SO}} = E_{\pm}^{\text{HH}} - E_{\text{SO}}$. The results of these calculations are

shown respectively in Figs. 2(b) and 2(c) for E_g^{Γ} and Δ_{SO} (shaded lines), where they are compared to the measured values of E_g^{Γ} and Δ_{SO} extracted from the SE measurements of Figs. 1(a) – (c). To describe the potential optical activity of these transitions the lines denoting the calculated transition energies are shaded according to the GaP HH Γ character $f_{\Gamma,\pm}^{\text{HH}}$ of the corresponding HH-like alloy VB edge states $|\psi_{\pm}^{\text{HH}}\rangle$, with solid black describing a purely GaP-like state having $f_{\Gamma,-}^{\text{HH}} \equiv |a_{\text{HH}}^{(-)}|^2 = 1$. No clear features were distinguishable in the measured SE spectra close to the calculated transition energies $E_{\text{CB}} - E_{-}^{\text{HH}}$, while the calculated transition energies $E_{-}^{\text{HH}} - E_{\text{SO}}$ lie outside the spectral range of the experiment.

The quantitative agreement between the calculated and measured data in Figs. 2(b) and (c) confirms that the extremely large observed reduction (increase) and bowing of E_g^{Γ} (Δ_{SO}) results from the emergence of an optically active band of primarily Bi-derived impurity states lying energetically within the GaP band gap. That this impurity band lies energetically within the host matrix band gap accounts quantitatively for the observed trends: the contribution of the strong, composition-dependent bowing of E_{+}^{HH} to the decrease (increase) of E_g^{Γ} (Δ_{SO}) is combined with the decaying energy ΔE_{Bi} of the Bi-related localised states. This behaviour is qualitatively distinct from that in $\text{GaAs}_{1-x}\text{Bi}_x$, where substitutional Bi impurities generate localised states which are resonant with the GaAs VB,^{27,30,51,52} but similar to that in the dilute nitride alloy $\text{GaN}_x\text{P}_{1-x}$, where substitutional N impurities produce a band of primarily N-derived states lying deep within the GaP band gap, several hundred meV below the CB edge at Γ .^{34,35,50,53–57}

From the SE measurements we extract $E_g^{\Gamma} = 2.49$ eV at $x = 1.3\%$ ($f_{\Gamma,+}^{\text{HH}} = 0.338$), an extremely large reduction of 290 meV compared to the unperturbed GaP Γ -point band gap $E_g^{\Gamma}(0) = 2.78$ eV. This is in good agreement

with the calculated reduction of 270 meV. Given the calculated reduction of 23 meV in E_{CB} between $x = 0$ and 1.3%, we conclude that the majority (91%) of the reduction in E_g^Γ is associated with the emergence of the E_{+}^{HH} impurity band. Similarly, we measure an extremely large ($>$ fourfold) increase of Δ_{SO} , from 80 meV in GaP to approximately 360 meV at $x = 1.3\%$. This is again in good agreement with the calculated value $\Delta_{SO} = 357$ meV, with the majority (92%) of the increase in Δ_{SO} associated with the emergence of the E_{+}^{HH} band.

Increasing the Bi composition from 1.3 to 3.7% we note that the relative change in E_g^Γ and Δ_{SO} per % Bi is significantly reduced. The measured (calculated) value $E_g^\Gamma = 2.30$ eV (2.33 eV) at $x = 3.7\%$ ($f_{\Gamma,+}^{HH} = 0.421$) represents a further reduction of 190 meV (175 meV) from $x = 1.3\%$, while the measured (calculated) value $\Delta_{SO} = 0.61$ eV (0.59 eV) at $x = 3.7\%$ Bi represents a further increase of 250 meV (230 meV) from $x = 1.3\%$. For E_g^Γ this change is only 86% of that between $x = 0$ and 1.3%, despite occurring over a 2.4% increase in x . The measured and calculated changes of Δ_{SO} between $x = 1.3$ and 3.7% are approximately equal to those between $x = 0$ and 1.3%, again representing a significantly reduced change per % Bi. These trends highlight the strong dependence of the bowing of E_g^Γ and Δ_{SO} on x . We note that our calculated variations of E_g^Γ and Δ_{SO} with x differ significantly from those predicted using first principles calculations,⁴⁵ but are close to those calculated via a VBAC model using parameter estimates extracted based on the available data for related alloys.⁴⁶

We now turn our attention to two key qualitative features of the $\text{GaP}_{1-x}\text{Bi}_x$ electronic structure. Firstly, GaP has an indirect band gap due to the X_{6c} CB states lying ≈ 0.4 eV below Γ_{6c} , while in semimetallic GaBi the X_{6c} states lie ≈ 2 eV below Γ_{6c} .^{27,58} Applying the VC approximation in conjunction with the TB model, we estimate that the X_{6c} states are shifted downwards in energy by $\approx \text{XXX}$ meV per % Bi in free-standing $\text{GaP}_{1-x}\text{Bi}_x$. This is more than the 32 meV reduction per % Bi in the energy of the Γ_{6c} states described by the VC parameter $\alpha = 3.22$ eV, suggesting that Bi incorporation decreases the indirect Γ_{8v} - X_{6c} band gap relative to E_g^Γ . Our analysis therefore suggests that $\text{GaP}_{1-x}\text{Bi}_x$ is an indirect-gap alloy, in agreement with the first principles calculations of Ref. 45. This highlights an important qualitative difference between the $\text{GaP}_{1-x}\text{Bi}_x$ and $\text{GaN}_x\text{P}_{1-x}$ band structures: substitutional N in GaP generates localised states lying below the host matrix X_{6c} states in energy, bringing about a direct band gap.^{34,50,53–56}

Secondly, our analysis in Ref. 27 demonstrated that the VBAC description of the $\text{GaP}_{1-x}\text{Bi}_x$ VB structure breaks down rapidly with increasing x in the presence of short-range alloy disorder. Bi clustering creates a distribution of Bi-related localised states – lying across a range of energies within the GaP band gap – with which the GaP VB edge states strongly hybridise. This leads to a distribution of GaP VB edge Γ character over a multiplicity of impurity levels, suggesting that there is no single

band that possesses sufficient Bloch character to allow for appreciable absorption or emission of light. While our results above demonstrate that the VBAC model provides a useful approach to analyse the main features of the band structure, the details of the electronic structure are in practice determined primarily by the impact of short-range alloy disorder. The high crystalline quality of, and inability to obtain photoluminescence from, the samples studied here⁴⁰ supports this interpretation: the $\text{GaP}_{1-x}\text{Bi}_x$ optical properties are intrinsically limited not by defects associated with the low growth temperatures required to incorporate Bi, but instead by a combination of an indirect band gap and a breakdown in VB edge Bloch character.

Despite their having lattice constants commensurate with growth on Si, our analysis suggests that refinement of the epitaxial growth of $\text{GaP}_{1-x}\text{Bi}_x$ alloys is unlikely to lead to efficient light emitters: the optical properties are expected to be intrinsically limited by the nature of the material band structure. However, just as quaternary $\text{GaN}_x\text{As}_y\text{P}_{1-x-y}$ alloys have found applications in III-V semiconductor lasers monolithically integrated on Si,⁵⁹ it is possible that similar progress could be made using As-rich quaternary $\text{GaP}_{1-x-y}\text{As}_y\text{Bi}_x$ alloys for, e.g., applications in multi-junction solar cells due to the fact that they can be grown lattice-matched to either GaAs or germanium (Ge) while having band gaps close to 1 eV.^{60–62}

In conclusion, we have presented a combined experimental and theoretical investigation of the $\text{GaP}_{1-x}\text{Bi}_x$ band structure. Measurements performed on $\text{GaP}_{1-x}\text{Bi}_x/\text{GaP}$ epitaxial layers reveal giant bowing of E_g^Γ and $\Delta_{SO} - E_g^\Gamma$ (Δ_{SO}) decreases (increases) by approximately 200 meV (240 meV) between $x = 0$ and 1% – the respective extremely large decrease and increase of which with increasing x is characterised by strong, composition-dependent bowing. Electronic structure calculations confirm that substitutional Bi impurities in GaP generate localised impurity states lying energetically within the GaP band gap, and that the main features of the $\text{GaP}_{1-x}\text{Bi}_x$ band structure can be understood in terms of a VBAC interaction between the extended states of the GaP VB edge, and highly localised Bi-related impurity states. A VBAC model was derived and parametrised directly from atomistic supercell calculations, allowing quantitative prediction of the evolution of the main features of the band structure with x . Our analysis suggests that the highest energy VB in $\text{GaP}_{1-x}\text{Bi}_x$ is a hybridised impurity band: admixture of GaP VB edge Γ character into this primarily Bi-derived band allows optical coupling to the comparatively unperturbed CB states. Aspects of the $\text{GaP}_{1-x}\text{Bi}_x$ band structure are broadly comparable to $\text{GaN}_x\text{P}_{1-x}$, but key qualitative differences highlight the distinction between Bi and N as isovalent impurities in conventional III-V semiconductors.

This work was supported by the Engineering and Physical Sciences Research Council, U.K. (EP-SRC; project nos. EP/H005587/1, EP/H050787/1, and

EP/K029665/1), by Science Foundation Ireland (SFI; project no. 15/IA/3082), and by the German Science Foundation (DFG; project no. GRK 1782). Z.L.B. acknowledges support from the University of Surrey Mar-

ion Redfearn and Advanced Technology Institute Scholarships. The data associated with this work are available from the University of Surrey publications repository at <http://epubs.surrey.ac.uk/XXXXXX/>.

-
- * s.sweeney@surrey.ac.uk
- ¹ H. Li and S. M. Wang, eds., *Bismuth-Containing Compounds* (Springer, New York, 2013).
 - ² S. J. Sweeney, Z. Batool, K. Hild, S. R. Jin, and T. J. C. Hosea, in proceedings of the 13th International Conference on Transparent Optical Networks p. 1 (2011).
 - ³ C. A. Broderick, M. Usman, S. J. Sweeney, and E. P. O'Reilly, *Semicond. Sci. Technol.* **27**, 094011 (2012).
 - ⁴ S. J. Sweeney and S. R. Jin, *J. Appl. Phys.* **113**, 043110 (2013).
 - ⁵ P. Ludewig, N. Knaub, N. Hossain, S. Reinhard, L. Nattermann, I. P. Marko, S. R. Jin, K. Hild, S. Chatterjee, W. Stolz, et al., *Appl. Phys. Lett.* **102**, 242115 (2013).
 - ⁶ T. Fuyuki, K. Yoshida, R. Yoshioka, and M. Yoshimoto, *Appl. Phys. Express* **7**, 082101 (2014).
 - ⁷ R. Butkutė, A. Geizutis, V. Pačebutas, B. Čechavičius, V. Bukauskas, R. Kundrotas, P. Ludewig, K. Volz, and A. Krotkus, *Electron. Lett.* **50**, 1155 (2014).
 - ⁸ I. P. Marko, C. A. Broderick, S. R. Jin, P. Ludewig, W. Stolz, K. Volz, J. M. Rorison, E. P. O'Reilly, and S. J. Sweeney, *Sci. Rep.* **6**, 28863 (2016).
 - ⁹ H. Kim, Y. Guan, K. Forghani, T. F. Keuch, and L. J. Mawst, *Semicond. Sci. Technol.* **32**, 075007 (2017).
 - ¹⁰ X. Wu, W. Pan, Z. Zhang, Y. Li, C. Cao, J. Liu, L. Zhang, Y. Song, H. Ou, and S. M. Wang, *ACS Photonics* **4**, 1322 (2017).
 - ¹¹ I. P. Marko and S. J. Sweeney, *IEEE J. Sel. Topics Quantum Electron.* **23**, 1501512 (2017).
 - ¹² S. R. Jin and S. J. Sweeney, *J. Appl. Phys.* **114**, 213103 (2013).
 - ¹³ C. A. Broderick, W. Xiong, and J. M. Rorison, in proceedings of the 16th International Conference on Numerical Simulation of Optoelectronic Devices p. 47 (2016).
 - ¹⁴ T. Thomas, A. Mellor, N. P. Hylton, M. Führer, D. Alonso-Álvarez, A. Braun, N. J. Ekins-Daukes, J. P. R. David, and S. J. Sweeney, *Semicond. Sci. Technol.* **30**, 094010 (2015).
 - ¹⁵ R. D. Richards, F. Harun, J. S. Cheong, A. Mellor, N. P. Hylton, T. Wilson, T. Thomas, N. J. Ekins-Daukes, and J. P. R. David, in proceedings of the 43rd IEEE Photovoltaics Specialists Conference p. 1135 (2016).
 - ¹⁶ S. Mazzucato, T. T. Zhang, H. Carrère, D. Lagarde, P. Boonpeng, A. Arnoult, G. Lacoste, A. Balocchi, T. Amand, C. Fontaine, et al., *Appl. Phys. Lett.* **102**, 252107 (2013).
 - ¹⁷ B. Pursley, M. Luengo-Kovac, G. Vardar, R. S. Goldman, and V. Sih, *Appl. Phys. Lett.* **102**, 022420 (2013).
 - ¹⁸ R. A. Simmons, S. R. Jin, S. J. Sweeney, and S. K. Clowes, *Appl. Phys. Lett.* **107**, 142401 (2015).
 - ¹⁹ J. J. Lee, J. D. Kim, and M. Razeghi, *Appl. Phys. Lett.* **70**, 3266 (1997).
 - ²⁰ C. J. Hunter, F. Bastiman, A. R. Mohmad, R. Richards, J. S. Ng, S. J. Sweeney, and J. P. R. David, *IEEE Photon. Tech. Lett.* **24**, 2191 (2012).
 - ²¹ I. C. Sandall, F. Bastiman, B. White, R. Richards, D. Mendes, J. P. R. David, and C. H. Tan, *Appl. Phys. Lett.* **104**, 171109 (2014).
 - ²² Y. Gu, Y. G. Zhang, X. Y. Chen, Y. J. Ma, S. P. Xi, B. Du, and H. Li, *Appl. Phys. Lett.* **108**, 032102 (2016).
 - ²³ P. Dongmo, Y. Zhong, P. Attia, C. Bomberger, R. Cheaito, J. F. Ihlefeld, P. E. Hopkins, and J. M. O. Zide, *J. Appl. Phys.* **112**, 093710 (2012).
 - ²⁴ S. Francoeur, M.-J. Seong, A. Mascarenhas, S. Tixier, M. Adamczyk, and T. Tiedje, *Appl. Phys. Lett.* **82**, 3874 (2003).
 - ²⁵ J. Yoshida, T. Kita, O. Wada, and K. Oe, *Jpn. J. Appl. Phys.* **42**, 371 (2003).
 - ²⁶ K. Alberi, J. Wu, W. Walukiewicz, K. M. Yu, O. D. Dubon, S. P. Watkins, C. X. Wang, X. Liu, Y.-J. Cho, and J. Furdyna, *Phys. Rev. B* **75**, 045203 (2007).
 - ²⁷ M. Usman, C. A. Broderick, A. Lindsay, and E. P. O'Reilly, *Phys. Rev. B* **84**, 245202 (2011).
 - ²⁸ Z. Batool, K. Hild, T. J. C. Hosea, X. Lu, T. Tiedje, and S. J. Sweeney, *J. Appl. Phys.* **111**, 113108 (2012).
 - ²⁹ C. A. Broderick, M. Usman, and E. P. O'Reilly, *Semicond. Sci. Technol.* **28**, 125025 (2013).
 - ³⁰ Y. Zhang, A. Mascarenhas, and L.-W. Wang, *Phys. Rev. B* **71**, 155201 (2005).
 - ³¹ H.-X. Deng, J. Li, S.-S. Li, H. Peng, J.-B. Xia, L.-W. Wang, and S.-H. Wei, *Phys. Rev. B* **82**, 193204 (2010).
 - ³² W. Shan, W. Walukiewicz, J. W. A. III, E. E. Haller, J. F. Geisz, D. H. Friedman, J. M. Olson, and S. R. Kurtz, *Phys. Rev. Lett.* **82**, 1221 (1999).
 - ³³ M. Kondow, T. Kitatani, S. Nakatsuka, M. C. Larson, K. Hakahara, Y. Yazawa, M. Okai, and K. Uomi, *IEEE J. Sel. Topics Quantum Electron.* **3**, 719 (1997).
 - ³⁴ P. R. C. Kent and A. Zunger, *Phys. Rev. B* **64**, 115208 (2001).
 - ³⁵ E. P. O'Reilly, A. Lindsay, P. J. Klar, A. Polimeni, and M. Capizzi, *Semicond. Sci. Technol.* **24**, 033001 (2009).
 - ³⁶ P. Carrier and S.-H. Wei, *Phys. Rev. B* **70**, 035212 (2004).
 - ³⁷ B. Fluegel, S. Francoeur, A. Mascarenhas, S. Tixier, E. C. Young, and T. Tiedje, *Phys. Rev. Lett.* **97**, 067205 (2006).
 - ³⁸ T. M. Christian, D. A. Beaton, K. Alberi, B. Fluegel, and A. Mascarenhas, *Appl. Phys. Express* **8**, 061202 (2015).
 - ³⁹ T. M. Christian, B. Fluegel, D. A. Beaton, K. Alberi, and A. Mascarenhas, *Jpn. J. Appl. Phys.* **55**, 108002 (2016).
 - ⁴⁰ L. Nattermann, A. Beyer, P. Ludewig, T. Hepp, E. Sterzer, and K. Volz, *J. Cryst. Growth* **463**, 151 (2017).
 - ⁴¹ F. A. Trumbore, M. Gershenson, and D. G. Thomas, *Appl. Phys. Lett.* **9**, 4 (1966).
 - ⁴² J. A. Woollam Co., *A Short Course in Ellipsometry* (2001).
 - ⁴³ C. C. Kim, J. W. Garland, H. Abad, and P. M. Raccach, *Phys. Rev. B* **45**, 11749 (1992).
 - ⁴⁴ S. Zollner, *Appl. Phys. Lett.* **63**, 2523 (1993).
 - ⁴⁵ M. P. Polak, P. Scharoch, and R. Kudrawiec, *Semicond. Sci. Technol.* **30**, 094001 (2015).
 - ⁴⁶ D. P. Samadjar, T. D. Das, and S. Dhar, *Mater. Sci. Semicond. Process.* **40**, 539 (2015).
 - ⁴⁷ M. Usman, C. A. Broderick, Z. Batool, K. Hild, T. J. C. Hosea, S. J. Sweeney, and E. P. O'Reilly, *Phys. Rev. B* **87**,

- 115104 (2013).
- ⁴⁸ G. Luo, S. Yang, G. R. Jenness, Z. Song, T. F. Kuech, and D. Morgan, *NPG Asia Materials* **9**, 345 (2017).
 - ⁴⁹ C. A. Broderick, P. E. Harnedy, P. Ludewig, Z. L. Bushell, K. Volz, R. J. Manning, and E. P. O'Reilly, *Semicond. Sci. Technol.* **30**, 094009 (2015).
 - ⁵⁰ C. Harris, A. Lindsay, and E. P. O'Reilly, *J. Phys.: Condens. Matter* **20**, 295211 (2008).
 - ⁵¹ R. S. Joshya, A. J. Ptak, R. France, A. Mascarenhas, and R. N. Kini, *Phys. Rev. B* **90**, 165203 (2014).
 - ⁵² K. Alberi, D. A. Beaton, and A. Mascarenhas, *Phys. Rev. B* **92**, 241201 (2015).
 - ⁵³ W. Shan, W. Walukiewicz, K. M. Yu, J. W. A. III, E. E. Haller, H. P. Xin, and C. W. Tu, *Appl. Phys. Lett.* **76**, 3251 (2000).
 - ⁵⁴ Y. Zhang, B. Fluegel, A. Mascarenhas, H. P. Xin, and C. W. Tu, *Phys. Rev. B* **62**, 4493 (2000).
 - ⁵⁵ J. Wu, W. Walukiewicz, K. M. Yu, J. W. A. III, E. E. Haller, Y. G. Hong, H. P. Xin, and C. W. Tu, *Phys. Rev. B* **65**, 241303(R) (2002).
 - ⁵⁶ B. Fluegel, Y. Zhang, J. F. Geisz, and A. Mascarenhas, *Phys. Rev. B* **72**, 073203 (2005).
 - ⁵⁷ M. Güngerich, P. J. Klar, W. Heimbrodtt, G. Weiser, J. F. Geisz, C. Harris, A. Lindsay, and E. P. O'Reilly, *Phys. Rev. B* **74**, 241202 (2006).
 - ⁵⁸ A. Janotti, S.-H. Wei, and S. B. Zhang, *Phys. Rev. B* **65**, 115203 (2002).
 - ⁵⁹ S. Liebich, M. Zimprich, A. Beyer, C. Lange, D. J. Franzbach, S. Chatterjee, N. Hossain, S. J. Sweeney, K. Volz, B. Kunert, et al., *Appl. Phys. Lett.* **99**, 071109 (2011).
 - ⁶⁰ K. Forghani, Y. Guan, M. Losurdo, G. Luo, D. Morgan, S. E. Babcock, A. S. Brown, L. J. Mawst, and T. F. Kuech, *Appl. Phys. Lett.* **105**, 111101 (2014).
 - ⁶¹ L. Nattermann, P. Ludewig, N. Knaub, N. W. Rosemann, T. Hepp, E. Sterzer, S. R. Jin, K. Hild, S. Chatterjee, S. J. Sweeney, et al., *Applied Materials Today* **5**, 209 (2016).
 - ⁶² L. Nattermann, P. Ludewig, E. Sterzer, and K. Volz, *J. Cryst. Growth* **470**, 15 (2017).

6.2.7 Optical Constants and Critical Points of Dilute Bismide Alloys Studied by Spectroscopic Ellipsometry

Z. Bushell, R. M. Joseph, L. Nattermann, P. Ludewig, K. Volz, J. L. Keddie, S. J. Sweeney submitted to Journal of Applied Physics (2017)

Abstract

Critical point transition energies and optical constants of the novel GaAs-based dilute bismide alloys GaAsBi, GaNAsBi and GaPAsBi were determined using spectroscopic ellipsometry. The band gap and spin-orbit splitting were measured for samples with a range of compositions. The first experimental measurements of the spin-orbit splitting in the GaNAsBi quaternary alloy were obtained, which showed that it is approximately independent of N content, in agreement with theory. The real component of refractive index in the transparent region below the band gap was found to decrease as the band gap increased for all of the alloys studied, following the usual relations for conventional semiconductors. This work provides key electronic and optical parameters for the development of photonic devices based on these novel alloys.

The Authors contribution

My contribution to this work was the planning and execution of the MOVPE growth and first structural characterization of the investigated samples. The performance of all ellipsometry measurements was done by Z. Bushell in close collaboration with R. Joseph and J. L. Keddie. S. Sweeney and K. Volz as well as all co-authors helped to interpret the data and to improve the manuscript that was written by Z. Bushell.

Optical constants and critical points of dilute bismide alloys studied by spectroscopic ellipsometry

Z. L. Bushell¹, R. M. Joseph¹, L. Nattermann², P. Ludewig², K. Volz², J. L. Keddie¹ and S. J. Sweeney^{1a)}

¹ *Advanced Technology Institute and Department of Physics, University of Surrey, Guildford, GU2 7XH, UK*

² *Material Sciences Center and Faculty of Physics, Philipps-Universität Marburg, 35032 Marburg, Germany*

Critical point transition energies and optical constants of the novel GaAs-based dilute bismide alloys GaAsBi, GaNAsBi and GaPAsBi were determined using spectroscopic ellipsometry. The band gap and spin-orbit splitting were measured for samples with a range of compositions. The first experimental measurements of the spin-orbit splitting in the GaNAsBi quaternary alloy were obtained, which showed that it is approximately independent of N content, in agreement with theory. The real component of refractive index in the transparent region below the band gap was found to decrease as the band gap increased for all of the alloys studied, following the usual relations for conventional semiconductors. This work provides key electronic and optical parameters for the development of photonic devices based on these novel alloys.

I. INTRODUCTION

Dilute bismide semiconductor alloys have gained increasing attention over recent years as promising materials for producing high efficiency, temperature insensitive devices in the near infrared telecommunications range^{1,2} as well as further into the mid infrared,^{3,4} where there are numerous possible applications such as gas sensing.⁵ This is due to a combination of useful properties. Firstly, a band anti-crossing (BAC) interaction in the valence band (VB) due to the incorporation of dilute amounts of bismuth into GaAs leads to an upward shift in the VB edge energy and therefore a strong reduction in the band gap (E_g).^{6,7} Secondly, the incorporation of bismuth also increases the spin-orbit splitting (Δ_{so}), as this increases strongly with the atomic mass of the group V element in III-V semiconductors.^{8,9} The combination of these

properties could allow for suppression of CHSH (Conduction-Heavy hole Spin-orbit-Heavy hole) Auger recombination and inter-valence band absorption (IVBA) processes involving transitions to the spin-orbit band, which dominate the threshold current of typical InP-based telecoms lasers.¹⁰⁻¹³ This can be achieved if the spin-orbit splitting is made larger than the band gap, which occurs for bismuth concentrations $> 10\%$ in GaAsBi.^{7,14} The quaternary alloy GaNAsBi, also incorporating dilute concentrations of nitrogen, offers additional flexibility in band structure engineering,^{3,15} arising from a BAC interaction in the conduction band (CB) that lowers the CB energy. Tuning the Bi and N compositions therefore gives control of both the VB and CB energies. Due to the compensation in strain between the relatively small N atoms and relatively large Bi atoms, it is also possible to keep the material lattice matched

^{a)} Author to whom correspondence should be addressed.
Electronic mail: s.sweeney@surrey.ac.uk

to GaAs whilst covering a range of band gaps from 0.2 eV to 1.4 eV.³

Since the dilute bismide materials are a relatively new class of semiconductor alloy, there are relatively few or even no existing experimental measurements of key properties such as band gap, spin-orbit splitting and optical constants in many of these different materials. These properties are crucial for a material's use in any photonic device, hence this work characterizes a range of interesting dilute bismide alloys using spectroscopic ellipsometry in order to determine these values.

II. METHODS AND SAMPLES

Spectroscopic ellipsometry was used to study three dilute bismide alloys: GaAsBi, GaNAsBi and GaPAsBi, all grown on a GaAs substrate. All of the samples were grown by metal-organic vapor phase epitaxy (MOVPE) in a commercially available AIX 200-GFR horizontal reactor system, using Pd-purified H₂ carrier gas at a reduced reactor pressure of 50 mbar. Full details of the particular growth conditions, such as temperature and precursors used, can be found in our previous publications relating to the growth of each material.^{16–18} The samples consisted of a bulk epilayer of the given alloy (thicknesses within the range of 20 – 200 nm), and some were also capped with a 20 nm GaAs layer. Epilayer thickness and compositions were determined using dynamical modelling to fit the experimental results from high resolution X-ray diffraction (HR-XRD) ω -2 θ scans around the GaAs (004) reflection and correlation of HR-XRD data with secondary ion mass spectrometry (SIMS) results for the composition determination of the quaternary alloys (described in Refs. [17] and [18]).

The ellipsometry measurements were made using a J. A. Woollam Variable Angle Spectroscopic Ellipsometer (VASE) (J.A. Woollam Co., Lincoln, NE, USA) with a rotating analyzer. Three angles-of-incidence, θ (measured from the normal direction), were used to provide more data and to improve the confidence in fits generated from the results. The three angles (73.5°, 74.0° and 74.5°) were chosen to be close to the pseudo-Brewster angle of the semiconductors being measured, which ensures that the value of ellipsometric parameter Δ remains close to 90°. This is important because with the rotating analyzer ellipsometer configuration, sensitivity is reduced when Δ is near 0° and 180°, and therefore keeping Δ around 90° ensures more accurate measurements.¹⁹

Spectroscopic scans were made over the wavelength range from 250 nm to 1150 nm.

A modelling and fitting procedure was used in order to extract useful results from the measured ellipsometry spectra, consisting of the parameters ψ and Δ . This procedure was carried out within the J. A. Woollam 'V.A.S.E. for Windows' software. The samples were modelled as multi-layer slabs, consisting of the substrate, epilayer, GaAs cap layer (if present), and a GaAs native oxide surface layer. A parameterized model was used for each of the semiconductor layers, which represents the dielectric constant as the sum of multiple oscillators with Gaussian broadening, each centered on a critical point in the semiconductor band structure. It is based on the model of Kim and Garland for the optical dielectric function of zinc-blende semiconductors.²⁰ Each oscillator is characterized by parameters to describe the critical point center energy, amplitude, broadening and shape of the tails to either side of the critical point. The optical constants of the native oxide surface layer were described using tabulated data taken from the literature.²¹

A piece of plain GaAs substrate was first measured and analyzed in order to ensure accurate parameters for this layer were obtained, since these provide the foundation for subsequent fitting of the epilayers. An iterative fitting procedure was followed, using a Marquardt-Levenberg fitting algorithm²² built into the software to minimize the mean square error (MSE) between the generated from the model and the experimental data. The critical point center energies, amplitudes and broadenings, as well as the native oxide thickness, were used as fitting parameters. The parameters for one critical point at a time were allowed to vary, and the fitting procedure was repeated until the MSE could not be reduced further. The final best fit parameters for the substrate were then used in the models for the epilayer samples and remained fixed. When analyzing the samples with epilayers, the critical point center energies, amplitudes and broadenings for the epilayer only and the native oxide thickness were used as fitting parameters in the iterative fitting procedure.

III. RESULTS AND DISCUSSION

In this section the electrical and optical properties as determined from the spectroscopic ellipsometry measurements are presented. This is divided into subsections for clarity. Subsection A presents the

ellipsometry data and the critical point transition energies for each of the four dilute bismide alloys in turn. Subsection B then presents the optical constants of the three alloys.

A. Ellipsometry data and electronic properties

1. GaAsBi

A set of GaAsBi samples were chosen to begin the ellipsometry study since this is the most well studied of the dilute bismide alloys both theoretically^{7,15,23–25} and experimentally.^{9,14,26–28} Hence there is a relatively high level of confidence in expected properties, such as band gap and spin-orbit splitting. This allows for comparison of the ellipsometry results to those from other methods to verify the technique before going on to study other less developed alloys. This alloy is of particular interest for 1.55 μm telecoms lasers based on GaAs with $\Delta_{SO} > E_g$ to suppress CHSH Auger recombination and IVBA²⁹.

The raw ellipsometry data and best fits produced by the modelling procedure are shown in Figure 1 for three representative examples. In all cases, a good fit was made to the experimental data, characterized by MSE

values of 0.31, 1.44 and 0.76 for the data in Figure 1 (a), (b) and (c), respectively. The GaAs critical points, as determined from fitting the substrate data, are marked. It is clear, especially in the Δ spectra, that an additional feature appears on the low energy side of the GaAs band gap and shifts to lower energies with increasing Bi fraction. This is consistent with the reducing band gap of the GaAsBi layer with increasing Bi content.

The critical point energies for the GaAsBi layers were recorded, along with 90% confidence intervals as calculated by the fitting algorithm. The band gap (E_g) and spin-orbit splitting (Δ_{SO}) are presented in Figure 2. These show very good agreement with the theoretical values as determined using the virtual crystal approximation and band anti-crossing model with parameters from Ref. [15], as well as many previous experimental measurements on samples across this range of bismuth concentrations.¹⁴ This provides verification of the validity of the spectroscopic ellipsometry method and modelling procedure applied here for extracting critical point energies from semiconductor alloys.

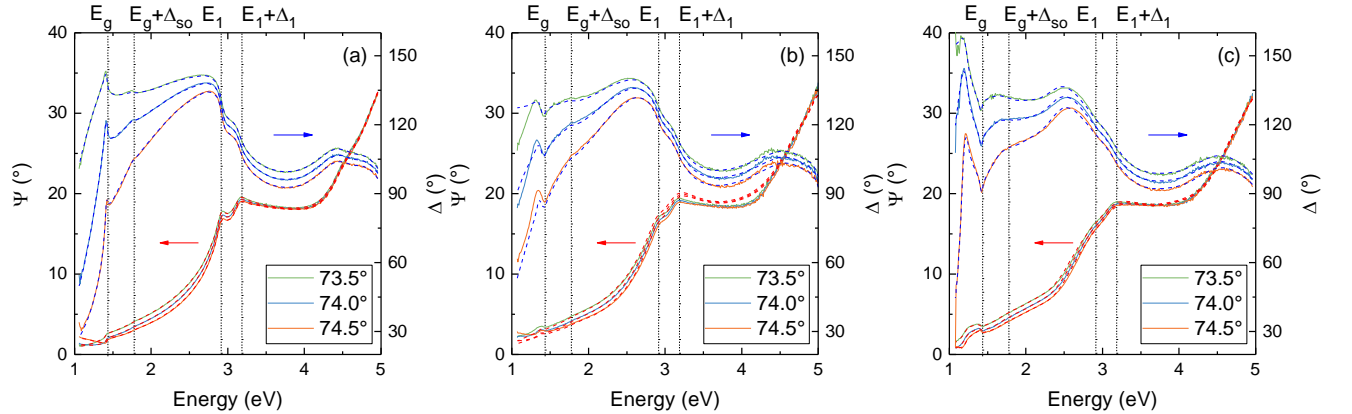


FIG. 1. Experimental spectroscopic ellipsometry data for GaAs (a) and GaAsBi samples with 1.0 % (b) and 3.5 % (c) bismuth. Best fits to the data are also shown as red / blue dashed lines for ψ / Δ .

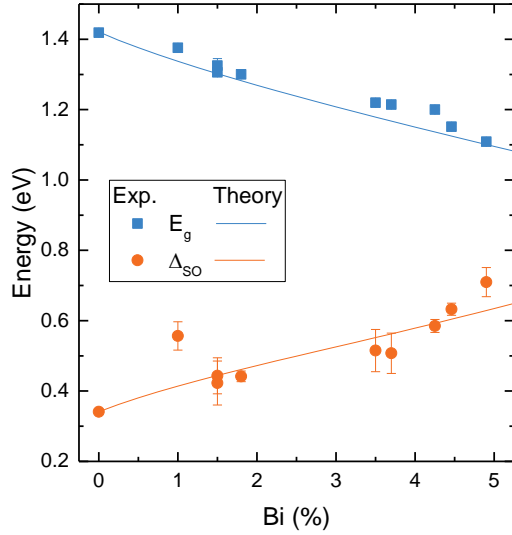


FIG. 2. Band gap (E_g) and spin-orbit splitting (Δ_{so}) of GaAsBi alloys as a function of bismuth concentration, as determined from ellipsometry measurements. Theoretical values calculated according to Ref. [15] also shown.

The values of higher energy critical points in the band structure were also extracted from the analysis procedure. The E_I and $E_I + \Delta_I$ points could consistently be identified and fitted across the range of compositions. The results are plotted in Figure 3. The data show approximately linear decreases in the energy of both critical points with increasing bismuth concentration. The E_I energy decreases by 40 ± 3 meV/%Bi, while the $E_I + \Delta_I$ energy decreases by 10 ± 1 meV/%Bi. Consequently, the Δ_I splitting energy must increase by 30 ± 3 meV/%Bi. These results contrast with the previously reported values of a decrease of 18 meV/%Bi for the E_I transition and 12 meV/%Bi for the $E_I + \Delta_I$ transition, giving an increase of 6 meV/%Bi for the Δ_I splitting.³⁰ From both sets of results, however, it is clear that the incorporation of bismuth has a smaller effect on the band gap and spin-orbit splitting energies at the Λ -point away from the zone center than it does at the Γ point. This is analogous to the behavior of the E_I transition in the dilute nitride GaNAs alloy. In this material there is a band anti-crossing interaction between a nitrogen state and the GaAs conduction band edge, which causes a large decrease in E_g of around 0.15 eV with the addition 1 % N.³¹ By contrast, measurements have shown that E_I has much weaker dependence on nitrogen fraction, with an increase of less than 0.05 eV with the addition of 1 % N.^{32,33} It appears that the same behavior is occurring in the GaAsBi alloy, where the band anti-crossing effect

occurs in the valance band, with the E_I transition away from the Brillouin zone center being much less strongly affected by the bismuth.

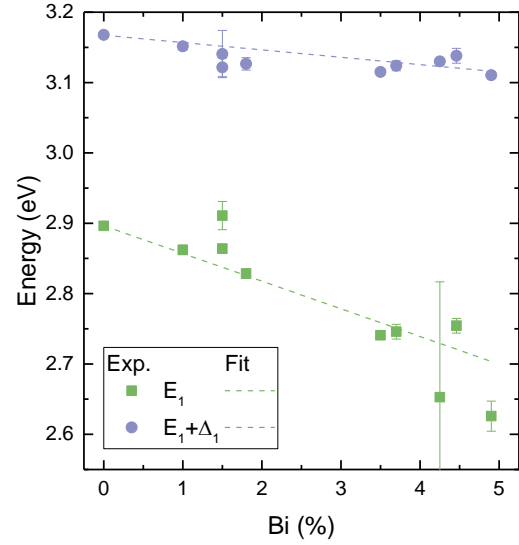


FIG. 3. Energies of the E_I and $E_I + \Delta_I$ transitions in GaAsBi as a function of bismuth concentration, as determined from ellipsometry measurements. Linear fits are also shown.

2. GaNAsBi

The quaternary alloy GaNAsBi is of interest as a sub-cell with band gap ~ 1 eV lattice matched to GaAs or Ge for multi-junction photovoltaics^{34,35} as well as for optoelectronic devices in the near- and mid-infrared.³ In the literature there are theoretical predictions of the band gap and spin-orbit splitting,^{15,36} as well as a small number of experimental measurements of the band gap by photoluminescence (PL) and photo/electroreflectance (PR/ER) spectroscopy,^{17,37,38} but there are not yet any experimental reports of the spin-orbit splitting for this novel alloy. This work therefore adds to the understanding of GaNAsBi and aids the design of future photonic devices.

The GaNAsBi samples investigated here are based on the GaAsBi sample containing 1.8% bismuth analyzed in the previous section. Details of their growth and initial optical characterization are reported in Ref. [17]. Fitting of the experimental data was carried out using the same procedure as outlined previously. Again, it was possible to achieve good fits to the experimental ellipsometry data. The critical point energies were used to find the band gap and spin-orbit splitting as a function of nitrogen content for these four samples with nominally equal bismuth contents of 1.8

%. The results are plotted in Figure 4. Previous measurements of the band gap by PR spectroscopy on the same set of samples are included for comparison.¹⁷ The ellipsometry results show good agreement with the band gap from the PR results and theory across the composition range. The spin-orbit splitting does not vary significantly with increasing nitrogen content. This is expected, since the addition of nitrogen mainly affects the conduction band by the band anti-crossing interaction, whilst the spin-orbit splitting is instead dominated by the effect of the bismuth. The spin-orbit splitting energies show very good agreement with the theoretical values, plotted as the dashed curve. This is the first experimental measurement of spin-orbit splitting in this alloy. Thus, it is a significant result for verifying the accuracy of the theoretical models for the quaternary alloy.

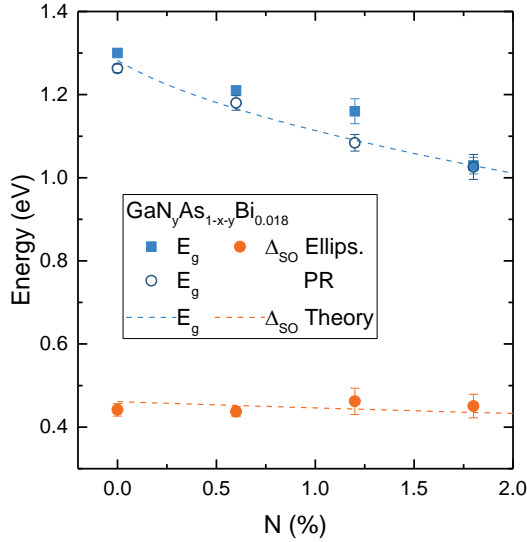


FIG. 4. Band gap and spin-orbit splitting for GaNAsBi alloys with 1.8 % Bi as a function of N content, as determined by ellipsometry. Band gap as measured by PR for same samples included for comparison.¹⁷ Theoretical values calculated according to Ref. [15] also shown.

3. GaPAsBi

The quaternary GaPAsBi alloy is another novel dilute bismide alloy of interest for applications in a variety of photonic devices. Similarly to the GaNAsBi alloy, the opposing effects of the large bismuth and smaller phosphorous atoms allow control of the lattice constant such that the quaternary can be either be lattice matched, or under tensile or compressive strain, on GaAs as desired. The addition of phosphorous acts to

increase the band gap compared to GaAs, hence it has been calculated that band gaps in the range from 1.7 eV to 0.7 eV (wavelengths from 0.73 μm – 1.8 μm) could be achieved with bismuth fractions up to 12 % and phosphorous fractions up to 40 %.¹⁸ This would make it potentially suitable for NIR devices, and one particular area of interest is as a 1 eV band gap sub-cell in multi-junction solar cells lattice matched on GaAs. It could also act as a barrier material in GaAsBi lasers due to the increase in the conduction band energy with the addition of phosphorous. Initial growth of this material by MOVPE has only recently been reported,^{18,39} so there is currently relatively little experimental data available to verify these predicted useful electronic properties.

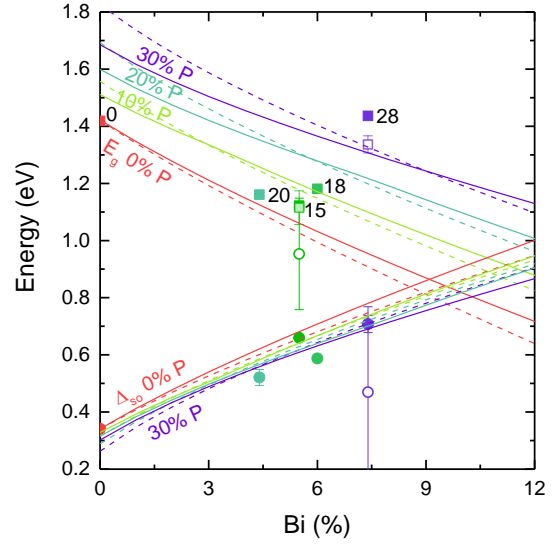


FIG. 5. Band gap and spin-orbit splitting for GaPAsBi alloys with varying P content (% shown next to marker) as a function of Bi content, as determined by ellipsometry (filled markers). Values as measured previously by PR for two samples included for comparison (open markers).¹⁸ Theoretical values from Ref. [18] for strained (solid lines) and unstrained (dashed lines) materials are also shown.

The GaPAsBi samples investigated here have varying concentrations of both P and Bi.¹⁸ The energies of the band gap and spin-orbit splitting in each sample were determined from the fitting procedure and are plotted in Figure 5. Since both phosphorous and bismuth content vary, the data is plotted as a function of bismuth content, with the different colors of the data points representing the phosphorous content. Theoretical calculations made using the virtual crystal approximation (VCA) and BAC model, as published in Ref. [18], are also shown. These relied on interpolation of many parameters to describe this quaternary alloy,

hence there is a degree of uncertainty associated with the calculated values. The experimental values of band gap and spin-orbit splitting all lie close to the expected range given by the theoretical calculations. For the two samples on which PR measurements had previously been carried out, there is a relatively large discrepancy between the spin-orbit splitting values obtained by the two methods, with the ellipsometry results lying much closer to the theoretical values. By combining these results it is possible to estimate the overall uncertainty associated with the experimental measurements, which is relatively large at 100s of meV. This could in part be due to the significant broadening of the features, which is likely to originate from alloy inhomogeneities and clustering in this new quaternary material, as has also been observed in other related alloys.^{23,40,41}

B. Optical properties

In addition to parameters describing the electronic band structure, the optical constants of the materials could also be determined by ellipsometry. The real (n) and imaginary (k) components of the refractive index as a function of photon energy for the GaAsBi and

GaNAsBi samples are plotted in Figure 8. At low photon energies both the real and imaginary parts of the refractive index increase with increasing bismuth and nitrogen fraction (decreasing band gap). The features around the E_I critical point become broadened by the addition of bismuth and the maximum real part of the refractive index decreases.

For most photonic device applications it is the refractive index around the band gap energy that is important, since this will be the energy of photons being generated / absorbed. The real part of the refractive index (n) in the transparent region below the band gap was therefore extracted from the fitting results for each sample. This value was taken at a photon energy of 1.07 eV in all cases, which was the minimum energy covered by the ellipsometry scan. The results are shown in Figure 9. There is a clear inverse relationship between the band gap and refractive index that applies to all of the different alloys. There are various equations proposed in the literature to describe the relationship between band gap and refractive index.⁴² For example, the Ravindra relation⁴³ is a simple empirical linear fit, giving $n = 4.084 - 0.62E_g$.

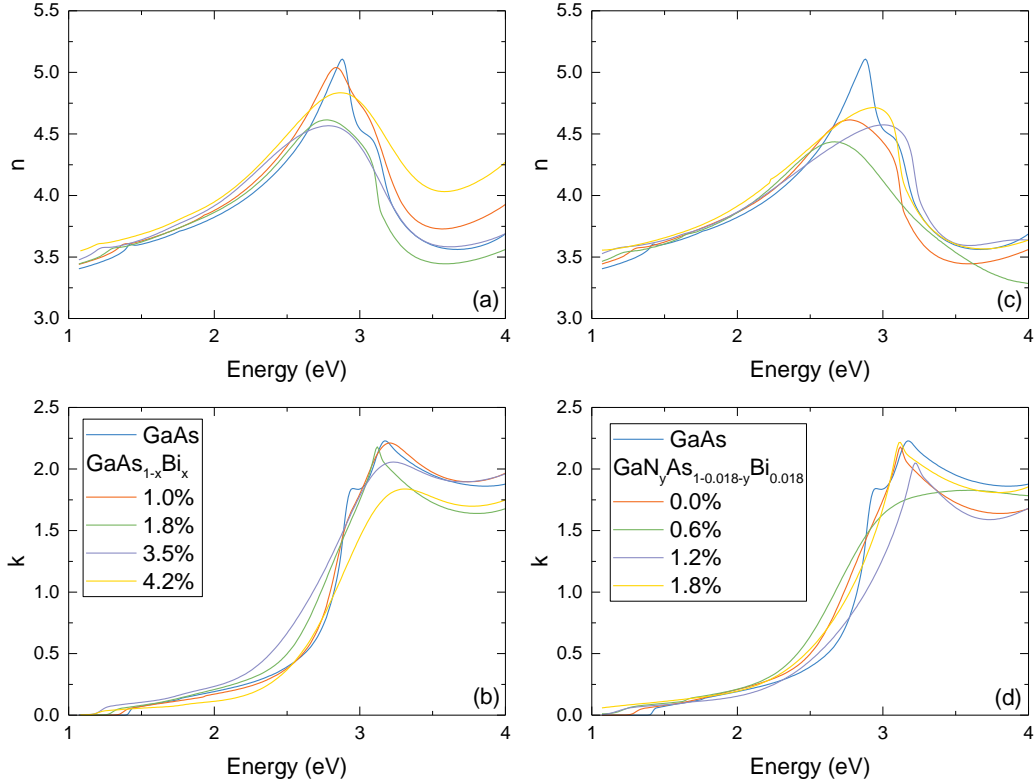


FIG. 8. Real (a,c) and imaginary (b,d) components of the refractive index for the dilute bismide alloys GaAsBi (a,b) and GaNAsBi (c,d).

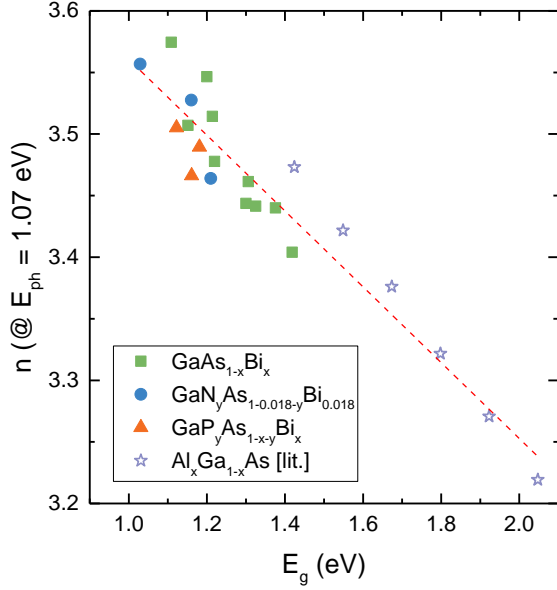


FIG. 9. Real part of refractive index (n) as a function of material band gap (E_g) at a photon energy of 1.07 eV for all samples.

To test whether this relationship holds for the dilute bismide alloys, a linear fit was made to the data in Figure 9, as shown by the dashed red line. The equation for this line is $n = (3.87 \pm 0.03) - (0.31 \pm 0.02)E_g$. It therefore appears that the refractive index can be well described with a linear dependence on the band gap, but with a much shallower gradient than in the standard Ravindra relation. The relationship found in this work provides a means of estimating the refractive index of dilute bismide alloys from the band gap. Knowing this parameter is useful in the design of photonic devices, such as for optimizing laser waveguides. The refractive index of AlGaAs alloys at 10 % steps in Al content, taken from Ref. [44], are also included in Figure 9 as the open stars for comparison, as this is known to provide very good refractive index contrast for use in waveguides and Bragg reflectors. It can be seen that the GaAsBi samples studied here with 0 – 5 % Bi span an equivalent refractive index range to AlGaAs alloys with 0 – 40 % Al. This highlights the potential of dilute bismide alloys for designing good optical structures, as well as providing beneficial electronic properties.

IV. CONCLUSIONS

In this work a variety of novel dilute bismide alloys were studied using spectroscopic ellipsometry. It was possible to achieve good fitting of the experimental data and to extract critical point transition energies and optical properties of the materials. The analysis method

was first verified by measuring GaAsBi samples, which have been studied extensively in the literature, and showing that the analysis produced the expected band gap and spin-orbit splitting. The E_I and Δ_I transition energies were also measured. The E_I band gap decreased by 40 ± 3 meV/%Bi, while the Δ_I splitting energy increased by 30 ± 3 meV/%Bi, which are both smaller changes than occur at the Γ point.

Two novel dilute bismide quaternary alloys were then studied and the band gap and spin-orbit splitting were determined for all samples. The first ever experimental measurements of spin-orbit splitting in the quaternary GaNAsBi alloy were made and showed that it is approximately independent of nitrogen content, in excellent agreement with theory. Measurements were also made on the new GaPAsBi quaternary alloy and showed reasonably good agreement with theory and previous measurements. Since there are only two previous reports in the literature on this alloy, with limited experimental data, this a useful contribution to refining understanding of its properties.

The final key outcome of this work was the measurement of the optical constants of the dilute bismide alloys. The real part of refractive index in the transparent region below the band gap was found to decrease as the band gap increases for all of the alloys studied. It is well described by the linear relationship $n = (3.87 \pm 0.03) - (0.31 \pm 0.02)E_g$. This relationship allows the refractive index to be calculated for different compositions of dilute bismide alloys if the band gap is known, which will be useful for optimizing the optical design of practical photonic devices.

ACKNOWLEDGEMENTS

This work was partially supported by the Engineering and Physical Sciences Research Council, U.K. (project nos. EP/H005587/01, EP/H050787/1 and EP/N021037/1) and the European Union Framework programme (EU-FP7 project “BIANCHI” (FP7-257974) and the German Research Foundation (DFG) in the framework of the RTG1782 “Functionalization of Semiconductors”. Z.L.B. gratefully acknowledges support from the Marion Redfearn Scholarship and the University of Surrey Advanced Technology Institute Scholarship. Details of the data and how to request access are available from the University of Surrey publications repository at <http://epubs.surrey.ac.uk/XXXXXX>.

- ¹ S.J. Sweeney, Z. Batool, K. Hild, S.R. Jin, and T.J.C. Hosea, in *13th Int. Conf. Transparent Opt. Networks* (Stockholm, Sweden, 2011), pp. 26–30.
- ² K. Oe, *Jpn. J. Appl. Phys.* **41**, 2801 (2002).
- ³ S.J. Sweeney and S.R. Jin, *J. Appl. Phys.* **113**, 43110 (2013).
- ⁴ S. Jin and S.J. Sweeney, *J. Appl. Phys.* **114**, 1 (2013).
- ⁵ K.C. Cossel, E.M. Waxman, I.A. Finneran, G.A. Blake, J. Ye, and N.R. Newbury, *J. Opt. Soc. Am. B* **34**, 104 (2017).
- ⁶ S.J. Sweeney, in *22nd IEEE Int. Semicond. Laser Conf.* (Kyoto, Japan, 2010), pp. 111–112.
- ⁷ M. Usman, C.A. Broderick, A. Lindsay, and E.P. O'Reilly, *Phys. Rev. B* **84**, 245202 (2011).
- ⁸ P. Carrier and S.-H. Wei, *Phys. Rev. B* **70**, 35212 (2004).
- ⁹ B. Fluegel, S. Francoeur, A. Mascarenhas, S. Tixier, E. Young, and T. Tiedje, *Phys. Rev. Lett.* **97**, 67205 (2006).
- ¹⁰ T. Higashi, S.J. Sweeney, A.F. Phillips, A.R. Adams, E.P. O'Reilly, T. Uchida, and T. Fujii, *IEEE J. Sel. Top. Quantum Electron.* **5**, 413 (1999).
- ¹¹ S.J. Sweeney, A.R. Adams, M. Silver, E.P. O'Reilly, J.R. Watling, A.B. Walker, and P.J.A. Thijs, *Phys. Status Solidi* **211**, 525 (1999).
- ¹² M. Silver, E.P. O'Reilly, and A.R. Adams, *IEEE J. Quantum Electron.* **33**, 1557 (1997).
- ¹³ A.R. Adams, M. Asada, Y. Suematsu, and S. Arai, *Jpn. J. Appl. Phys.* **19**, L621 (1980).
- ¹⁴ Z. Batool, K. Hild, T.J.C. Hosea, X. Lu, T. Tiedje, and S.J. Sweeney, *J. Appl. Phys.* **111**, 113108 (2012).
- ¹⁵ C.A. Broderick, M. Usman, and E.P. O'Reilly, *Semicond. Sci. Technol.* **28**, 125025 (2013).
- ¹⁶ L. Nattermann, P. Ludewig, L. Meckbach, B. Ringler, D. Keiper, C. von Hänisch, W. Stolz, and K. Volz, *J. Cryst. Growth* **426**, 54 (2015).
- ¹⁷ Z.L. Bushell, P. Ludewig, N. Knaub, Z. Batool, K. Hild, W. Stolz, S.J. Sweeney, and K. Volz, *J. Cryst. Growth* **396**, 79 (2014).
- ¹⁸ L. Nattermann, P. Ludewig, N. Knaub, N.W. Rosemann, T. Hepp, E. Sterzer, S.R. Jin, K. Hild, S. Chatterjee, S.J. Sweeney, W. Stolz, and K. Volz, *Appl. Mater. Today* **5**, 209 (2016).
- ¹⁹ J. A. Woollam Co. Inc., *A Short Course in Ellipsometry* (n.d.).
- ²⁰ C.C. Kim, J.W. Garland, H. Abad, and P.M. Racciah, *Phys. Rev. B* **45**, 749 (1992).
- ²¹ S. Zollner, *Appl. Phys. Lett.* **63**, 2523 (1993).
- ²² D.W. Marquardt, *J. Soc. Ind. Appl. Math.* **11**, 431 (1963).
- ²³ M. Usman, C.A. Broderick, Z. Batool, K. Hild, T.J.C. Hosea, S.J. Sweeney, and E.P. O'Reilly, *Phys. Rev. B - Condens. Matter Mater. Phys.* **87**, 1 (2013).
- ²⁴ D. Madouri, A. Boukra, A. Zaoui, and M. Ferhat, *Comput. Mater. Sci.* **43**, 818 (2008).
- ²⁵ M.P. Polak, P. Scharoch, and R. Kudrawiec, *Semicond. Sci. Technol.* **30**, 94001 (2015).
- ²⁶ K. Alberi, O.D. Dubon, W. Walukiewicz, K.M. Yu, K. Bertulis, and A. Krotkus, *Appl. Phys. Lett.* **91**, 51909 (2007).
- ²⁷ Z. Chine, H. Fitouri, I. Zaied, A. Rebey, and B. El Jani, *Semicond. Sci. Technol.* **25**, 65009 (2010).
- ²⁸ M. Masnadi-Shirazi, R.B. Lewis, V. Bahrami-Yekta, T. Tiedje, M. Chicoine, and P. Servati, *J. Appl. Phys.* **116**, 0 (2014).
- ²⁹ I.P. Marko and S.J. Sweeney, *IEEE J. Sel. Top. Quantum Electron.* (2017).
- ³⁰ N. Ben Sedrine, I. Moussa, H. Fitouri, A. Rebey, B. El Jani, and R. Chtourou, *Appl. Phys. Lett.* **95**, 1 (2009).
- ³¹ I. Vurgaftman and J.R. Meyer, *J. Appl. Phys.* **94**, 3675 (2003).
- ³² G. Leibiger, V. Gottschalch, A. Kasik, B. Rheinlander, J. Sik, and M. Schubert, in *Proc. IEEE Twenty-Seventh Int. Symp. Compd. Semicond.* (2000), pp. 7–12.
- ³³ J. Wu, W. Shan, and W. Walukiewicz, *Semicond. Sci. Technol.* **17**, 860 (2002).
- ³⁴ S.J. Sweeney, K. Hild, and S.R. Jin, in *39th IEEE Photovolt. Spec. Conf.* (Tampa Bay, Florida, 2013).
- ³⁵ A. Aissat, A.M. Benahmed, R. Bestam, and J.P. Vilcot, in *2014 Int. Renew. Sustain. Energy Conf.* (IEEE, Ouarzazate, 2014), pp. 181–184.
- ³⁶ M.M. Habchi, A. Ben Nasr, A. Rebey, and B. El Jani, *Infrared Phys. Technol.* (2013).
- ³⁷ W. Huang, K. Oe, G. Feng, and M. Yoshimoto, *J. Appl. Phys.* **98**, 53505 (2005).
- ³⁸ S. Tixier, S.E. Webster, E.C. Young, T. Tiedje, S. Francoeur, A. Mascarenhas, P. Wei, and F. Schiettekatte, *Appl. Phys. Lett.* **86**, 112113 (2005).
- ³⁹ K. Forghani, Y. Guan, M. Losurdo, G. Luo, D. Morgan, S.E. Babcock, A.S. Brown, L.J. Mawst, and T.F. Kuech, *Appl. Phys. Lett.* **105**, (2014).
- ⁴⁰ C. Gogineni, N.A. Riordan, S.R. Johnson, X. Lu, and T. Tiedje, *Appl. Phys. Lett.* **103**, 41110 (2013).
- ⁴¹ I.P. Marko, Z. Batool, K. Hild, S.R. Jin, N. Hossain, T.J.C. Hosea, J.P. Petropoulos, Y. Zhong, P.B. Dongmo, J.M.O. Zide, and S.J. Sweeney, *Appl. Phys. Lett.* **101**, 221108 (2012).
- ⁴² N.M. Ravindra, P. Ganapathy, and J. Choi, *Infrared Phys. Technol.* **50**, 21 (2007).
- ⁴³ V.P. Gupta and N.M. Ravindra, *Phys. Status Solidi* **100**, 715 (1980).
- ⁴⁴ S. Adachi, *J. Appl. Phys.* **58**, R1 (1985).

6.2.8 On The Effects of Column Occupancy and Static Atomic Disorder on the Analysis of Chemical Ordering in Ga(PBi) Compounds ¹

J. Belz, A. Beyer, L. Nattermann, K. Volz,
Microscopy and Microanalysis **23(S1)** (2017) pp.1774-1475.
DOI: 10.1017/S1431927617008030

The Authors contribution

My contribution to this work was the planning and execution of the MOVPE growth. The preparation and main investigation by STEM was performed by J. Belz in close collaboration with A. Beyer. K. Volz helped to interpret the data and to improve the manuscript that was written by J. Belz.

¹ Reprinted from *Microscopy and Microanalysis* **23(S1)** (2017) pp.1774-1475, Copyright Microscopy Society of America

On The Effects of Column Occupancy and Static Atomic Disorder on the Analysis of Chemical Ordering in $\text{Ga}(\text{P}_{(1-x)}\text{Bi}_x)$ Compounds

Jürgen Belz¹, Andreas Beyer¹, Lukas Nattermann¹ and Kerstin Volz¹

¹ Materials Science Center and Faculty of Physics, Philipps-Universität Marburg, Marburg, Germany

Dilute bismides have been considered promising materials for new highly efficient lasers for telecommunication applications due to their reduced Auger recombination [1]. Since electronic calculations can depend on ordering effects [2], the following work is aimed towards the characterization of clustering behavior of bismuth in gallium phosphide bismide ($\text{Ga}(\text{PBi})$) by scanning electron transmission microscopy (STEM). Hereto, we investigate the effects of static atomic disorder (SAD) on the intensity distribution in such a material as well as the implications of intra-column distributions of bismuth with respect to the scattered intensity.

The compound has been grown pseudomorphically on gallium phosphide (GaP) substrate by metal organic vapor phase epitaxy. A test structure containing multiple layers of $\text{Ga}(\text{PBi})$ with different bismuth fractions and separated by GaP layers is thinned along the [010] direction by broad argon ion beam milling. The microscopy was carried out with a double aberration corrected JEOL JEM-2200FS at 200kV in scanning mode using an annular dark field detector (ADF).

Upon investigation, the bismuth containing layers possess a remarkable appearance when investigated with STEM due to the highly different scattering power of bismuth (atomic number $Z = 83$) compared to that of phosphorous ($Z = 15$). Since both elements occupy the group V sub-lattice in the zinc blende structure, the overall image contrast is very significantly altered by small amounts of bismuth (fig. 1a).

In order to characterize the alloy with respect to ordering on the atomic scale by STEM measurements image simulations are carried out first. We hereto utilize our newly developed STEMsalabim code [3] in order to perform accurate multi slice simulations using the frozen lattice approach as well as modelling the probe of an aberration corrected STEM including the C_c induced defocus spread.

The impact of SADs is evaluated by the comparison of simulated STEM ADF intensities of rigid and valance force field relaxed supercells. It can be seen that on-column intensities are redistributed from every ADF scattering range into the diffuse background with a bias towards lower scattering angles. This finding can be directly correlated with the distortion of gallium position when they are neighboured by bismuth atoms.

On the other hand, in experimental images (cf. fig. 1a) gallium columns in the alloy show up to 15% higher intensities than those of the neighbouring undistorted binary material which is at first glance contrary to the aforementioned simulation results. Upon further investigation it can be concluded that the drastic increase of these intensities has to result from the huge scattering power of even single bismuth atoms and the resulting intensity overlap with the gallium columns.

The effect of intensity crosstalk is therefore considered in a systematic image simulation study. Hereto, we model a large supercell of pure GaP and substitute single phosphorous atoms (separated by one unit cell) with bismuth atoms at different z-positions along the electron beam direction. It can be seen that the

depth measured from the top surface is of great relevance when considering the distribution of bismuth in GaP. We show that when one atom lies in the vicinity of the top surface its scatter appears up to three times as intense as compared to a deep (> 15 nm) region, and that such an atom contributes a significant amount of scattered intensity to even the 2nd nearest neighbouring column.

Finally, an image simulation from a randomly ordered $\text{Ga}(\text{P}_{96.8\%} \text{Bi}_{3.2\%})$ supercell is used to derive the apparent number of bismuth atoms from the averaged group V on-column (fig. 1b). Here we can identify a region (red box) where intense columns (pointing to a high bismuth occupancy) are neighboured by other bismuth-rich columns. Nevertheless, this effect can be shown to be partially an artefact as described before when considering the actual supercell occupation (fig. 1c). In addition, we can find very bright columns (purple boxes) where very few bismuth atoms are present and only the central column intensity is high. This finding can be correlated with the large difference of the z-position of bismuth atoms within these neighbouring columns.

We can show that the effects of SADs, z-position and column crosstalk are of great relevance when considering atomic ordering analysis in Ga(PBi) using STEM. These complex effects have to be accounted for when deriving an accurate distribution model for bismuth in GaP on an atomic scale.

References:

- [1] Polak, M. P., P. Scharoch, and R. Kudrawiec, *Semicond. Sci. Technol.* 30.9 (2015): 094001.
- [2] Franceschetti et al., *Physical Review B* 52.19 (1995): 13992.
- [3] J.O. Oelerich et al., *Submitt. Publ.* (2016). <http://www.online.uni-marburg.de/stemsalabim/>.
- [4] The authors acknowledge support from the German Science Foundation (GRK 1782: “Functionalization of Semiconductors”) and the German Federal Ministry of Education and Research through the project “MehrSi”.

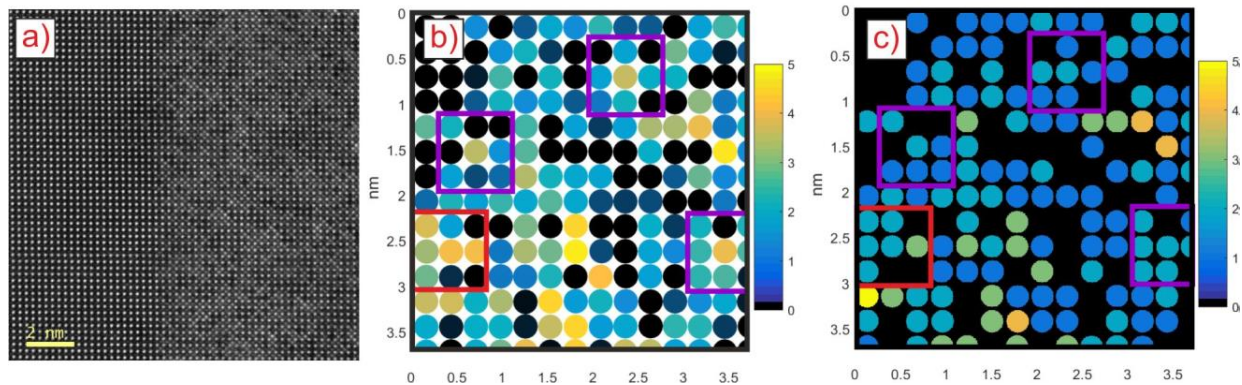


Figure 1. (a) Experimental STEM image of a $\text{GaP}/\text{Ga}(\text{P}_{96.8\%} \text{Bi}_{3.2\%})$ interface. (b) Bismuth occupancy derived from an image simulation of a supercell containing 3.2% bismuth (group V columns shown). (c) The actual supercell composition is shown in where atoms at the surface have high intensity and can raise the local intensity environment.

6.3 Further Publications

Peer-Review Paper

Listed below are the scientific papers which were published during my PhD but which do not directly bear a relation to the Bi containing III/Vs or the MS setup.

- P. Ludewig, L. Nattermann, W. Stolz, K. Volz
MOVPE growth mechanisms of dilute bismide III/Vs, Semicond. Sci. Technol., **30**, 9 (2015) DOI: 10.1088/0268-1242/30/9/094017
- E. Sterzer, A. Beyer, L. Duschek, L. Nattermann, B. Ringler, B. Leube, A. Stegmüller, R. Tonner, C. von Hänisch, W. Stolz, K. Volz,
Efficient nitrogen incorporation in GaAs using novel metal organic As-N precursor (DTBAA), J. Crys. Growth, **439**, 19-27 (2016) DOI: 10.1016/j.jcrysgro.2015.12.032
- E. Sterzer, A. Beyer, L. Nattermann, W. Schorn K.Schlechter, S. Pulz, J. Sundermeyer, W. Stolz, K. Volz
Novel nitrogen/gallium precursor [Ga(bdma)H₂] for MOVPE, J. Crys. Growth, **454**, 173-179 (2016) DOI: 10.1016/j.jcrysgro.2016.08.061
- E. Sterzer, B. Ringler, L. Nattermann, A. Beyer, C. von Hänisch, W. Stolz, K. Volz
(GaIn)(NAs) growth using di-tertiary-butyl-arsanoamine (DTBAA), J. Crys. Growth, **467**, 132-136 (2017) DOI: 10.1016/j.jcrysgro.2017.01.014
- C. Krammel, L. Nattermann, E. Sterzer, K. Volz, P. M. Koenraad,
Structural and Electronic Properties of Isovalent Boron Atoms in GaAs
submitted to Journal of Applied Physics (Special Issue) (2017)

Conference Presentations (Talks)

- L. Nattermann, P. Ludewig, L. Meckbach, B. Ringler, C. von Hänisch, W. Stolz, K. Volz
MOVPE growth of Ga(AsBi)/GaAs hetero structures using alternative sources
5th international Workshop on Bismide Containing Semiconductors (July 2014) Cork, Ireland
- L. Nattermann, P. Ludewig, L. Meckbach, B. Ringler, C. von Hänisch, W. Stolz, K. Volz
MOVPE growth of Ga(AsBi)/GaAs hetero structures
DGKK Arbeitskreistreffen Epitaxie von III-V Halbleitern (Dez 2014) Magdeburg, Germany

- L. Nattermann, N. Knaub, P. Ludewig, W. Stolz, K. Volz
MOVPE growth of Ga(PAsBi) on GaAs at low temperatures
6th international Workshop on Bismide Containing Semiconductors (July 2015)
Madison, WI, USA
- L. Nattermann, P. Ludewig, W. Stolz, K. Volz
MOVPE growth of dilute Bi containing quaternary alloys on GaAs
20th American Conference on Crystal Growth and Epitaxy (ACCGE-20) (Aug 2015)
Big Sky, MT, USA
- L. Nattermann, N. Knaub, A. Beyer, W. Stolz, K. Volz
MOVPE growth studies of Ga(PBi) on GaP and on GaP/Si
DPG Tagung (Mar 2016) Regensburg, Germany
- L. Nattermann, T. Hepp, N. Rosemann, P. Ludewig, A. Beyer, S. Chatterjee, W. Stolz and K. Volz
MOVPE growth of Ga(PBi) and Ga(NPBi) on GaP and GaP on Si ? laser material on Si base?
7th international Workshop on Bismide Containing Semiconductors (Jul 2016) Shanghai, China
- L. Nattermann, T. Hepp, R. Döring, N. Rosemann, P. Ludewig, A. Beyer, S. Chatterjee, W. Stolz, K. Volz
MOVPE growth of Ga(PBi) and Ga(NPBi) on GaP and on GaP/Si
DGKK Arbeitskreistreffen Epitaxie von III-V Halbleitern (Dez 2016) Duisburg, Germany

Acronyms

AFM: atomic force microscopy

Al_yGa_{1-y}As: aluminum gallium arsenide

APT: atom probe tomography

CBAC: conduction band anticrossing

CHSH: conduction heavy hole spin-orbit heavy hole

CW: continuous wave

DFT: density functional theory

DTBAA: ditertiarybutylarsanoamine

EI: electron ionization

FFT: fast fourier transformation

Ga_yIn_{1-y}As_zN_{1-z}: gallium indium arsenide nitride

GaAs: gallium arsenide

GaAs_{1-x}Bi_x: gallium arsenide bismide

GaAs_{1-y-x}N_yBi_x: gallium arsenide nitride bismide

GaAs_{1-y-x}P_yBi_x: gallium arsenide phosphide bismide

GaAs_{1-y}N_y: gallium arsenide nitride

GaAs_{1-y}P_y: gallium arsenide phosphide

GaP: gallium phosphide

GaP_{1-x}Bi_x: gallium phosphide bismide

HR-XRD: high resolution X-ray diffraction

In_{1-x-y}Ga_yAl_xAs: Indium gallium aluminum arsenide

In_yGa_{1-y}As_zP_{1-z}: Indium gallium arsenide phosphide

InP: indium phosphide

IR: infrared

IVBA: intervalence band absorption

laser: light amplification by stimulated emission of radiation

LED: light emitting diode

MBE: molecular beam epitaxy

MFC: mass flow controller

MIR: mid infrared

MO: metalorganic

MOs: metalorganics

MOVPE: metalorganic vapor phase epitaxy

MS: mass spectrometer

NIR: near infrared

PC: pressure controller

PL: photoluminescence

QIT: quadrupole ion trap

RF: radio frequency

SCH: separate confinement hetero

SIMS: secondary ion mass spectrometry

STEM: Scanning transmission electron microscopy

TBAs: tertiarybutylarsine

TBP: tertiarybutylphosphine

TEGa: triethylgallium

TIPBi: triisopropylbismuth

TMAI: trimethylaluminum

TMBi: trimethylbismuth

TMGa: trimethylgallium

TMIn: trimethylindium

TTBBi: tritertiarybutylbismuth

TTBGa: tritertiarybutylgallium

UDMHy: 1,1-dimethylhydrazine

UHV: ultra-high vacuum

VBAC: valence band anticrossing

VCA: virtual crystal approximation

Bibliography

- [1] T. Bawden, Global warming: Data centres to consume three times as much energy in next decade, experts warn, 2016, [Online; posted 23-Jan-2016].
- [2] S. J. Sweeney, A. F. Phillips, A. R. Adams, E. P. O'Reilly and P. J. A. Thijs, *IEEE Photonics Technol. Lett.* **10**, 8 (1998).
- [3] T. R. Chen, B. Chang, L. C. Chiu, K. L. Yu, S. Margalit and A. Yariv, *Appl. Phys. Lett.* **43**, 217 (1983).
- [4] A. R. Adams, M. Asada, Y. Suematsu and S. Arai, *Japanese Journal of Applied Physics* **19**, 10 (1980).
- [5] A. R. Adams, K. C. Heasman and J. Hilton, *Semicond. Sci. Technol.* **2**, 12 (1987).
- [6] H. Kim, Y. Guan, K. Forghani, T. F. Kuech and L. J. Mawst, *Semicond. Sci. Technol.* **32**, 7 (2017).
- [7] R. Butkute, V. Pačebutas, B. Čechavičius, R. Nedzinskas, A. Selskis, A. Arlauskas and A. Krotkus, *Journal of Crystal Growth* **391**, 116 (2014).
- [8] R. Y. Takuma Fuyuki, Kenji Yoshida and M. Yoshimoto, *Applied Physics Exp.* **7**, 082101 (2014).
- [9] P. Ludewig, N. Knaub, W. Stolz and K. Volz, *Journal of Crystal Growth* **370**, 186 (2013).
- [10] S. J. Sweeney and S. R. Jin, *J. Appl. Phys.* **113**, 043110 (2013).
- [11] C. Broderick, M. Usman, S. J. Sweeney and E. P. O'Reilly, *Semiconductor Science and Technology* **27**, 9 (2012).
- [12] R. D. Richards, F. Harun, J. S. Cheong, A. Mellor, N. P. Hylton, T. Wilson, T. Thomas, N. J. Ekins-Daukes and J. P. R. David, *IEEE Photovoltaic Specialists Conference* **43(S1)**, 1135 (2016).
- [13] T. Thomas, A. Mellor, N. P. Hylton, M. Führer, D. Alonso-Alvarez, A. Braun, N. G. Ekins-Daukes, J. P. R. David and S. J. Sweeney, *Semicond. Sci. Technol.* **30**, 094010 (2015).

- [14] B. Pursley, M. Luengo-Kovac, G. Vardar, R. S. Goldman and V. Sih, *Appl. Phys. Lett.* **102**, 022420 (2013).
- [15] S. Mazzucato, P. Boonpeng, H. Carrere, D. Lagarde, A. Arnoult, G. Lacoste, T. Zhang, A. Balocchi, T. Amand, X. Marie and C. Fontaine, *Semicond. Sci. Technol.* **28**, 022001 (2013).
- [16] P. B. Dongmo, Y. Zhong, P. Attia, C. Bomberger, R. Cheaito, J. F. Ihlefeld, P. E. Hopkins and J. M. O. Zide, *J. Appl. Phys.* **112**, 093710 (2012).
- [17] L. Nattermann, P. Ludewig, L. Meckbach, B. Ringler, D. Keiper, C. von Haenisch, W. Stolz and K. Volz, *Journal of Crystal Growth* **426**, 54 (2015).
- [18] L. Nattermann, P. Ludewig, N. Knaub, N. W. Rosemann, T. Hepp, E. Sterzer, S. R. Jin, K. Hild, S. Chatterjee, S. J. Sweeney, W. Stolz and K. Volz, *Applied Materials Today* **5**, 209 (2016).
- [19] L. Nattermann, A. Beyer, P. Ludewig, T. Hepp, E. Sterzer and K. Volz, *Journal of Crystal Growth* **463**, 151 (2017).
- [20] L. Nattermann, O. Massmeyer and K. Volz, submitted to *Scientific Reports* (2017).
- [21] K. Oe and H. Okamoto, *Jpn. J. Appl. Phys.* **37**, 1283 (1998).
- [22] K. Oe, *Jpn. J. Appl. Phys.* **41**, 2801 (2002).
- [23] M. Yoshimoto, W. Huang, G. Feng and K. Oe, *Physica Status Solidi (B) Basic Research* **243**, 7 (2006).
- [24] Y. Tominaga, K. Oe and M. Yoshimoto, *Applied Physics Express* **3**, 131915 (2010).
- [25] Y. Gu, Y. G. Zhang, X. Y. Chen, Y. J. Ma, S. P. Xi, B. Du, H. Li, Y. Gu, Y. G. Zhang, X. Y. Chen, Y. J. Ma, S. P. Xi, B. Du and H. Li, **108**, 032102 (2016).
- [26] I. C. Sandall, F. Bastiman, B. White, R. Richards, D. Mendes, J. P. R. David and C. H. Tan, *Applied Physics Letters* **104**, 171109 (2014).
- [27] C. J. Hunter, F. Bastiman, A. R. Mohmad, R. Richards, J. S. Ng, S. J. Sweeney and J. P. R. David, *IEEE Photonics Technology Letters* **24**, 23 (2012).
- [28] J. J. Lee, J. D. Kim and M. Razeghi, *Applied Physics Letters* **70**, 3266 (1997).
- [29] P. Ludewig, L. Nattermann, W. Stolz and K. Volz, *Semiconductor Science and Technology* **30**, 094017 (2015).
- [30] K. Forghani, A. Anand, L. J. Mawst and T. F. Kuech, *J. Cryst. Growth* **380**, 23 (2013).

- [31] C. Kittel, *Introduction to Solid States Physics*, New York, NY, 8 edition, 2013.
- [32] S. Hunklinger, *Festkörperphysik*, DeGruyter, 4 edition, 2014.
- [33] N. Ashcroft and D. Mermin, *Solid State Physics*, Saunders Collage Publishing, 1976.
- [34] L. Vegard, *Zeitschrift für Physik* **5**, 1 (1921).
- [35] S. Tixier, M. Adamcyk, T. Tiedje, S. Francoeur, A. Mascarenhas, P. Wei and F. Schiettekatte, *Appl. Phys. Lett.* **82**, 14 (2003).
- [36] I. Vurgaftman, J. R. Meyer and L. R. Ram-Mohan, *J. Appl. Phys.* **89**, 5815 (2001).
- [37] S. Q. Wang and H. Q. Ye, *Physica Status Solidi (B) Basic Research* **240(1)**, 45 (2003).
- [38] W. Hagen, *Journal of Crystal Growth* **43**, 739 (1978).
- [39] D. Schlenker, T. Miyamoto, Z. Chen, M. Kawaguchi, T. Kondo, E. Gouardes, F. Koyama and K. Iga, *Journal of Crystal Growth* **221**, 42 (2000).
- [40] N. Elayech, H. Fitouri, Y. Essouda, A. Rebey and B. El Jani, *Physica Status Solidi (C) Current Topics in Solid State Physics* **12**, 1 (2015).
- [41] A. T. Dinsdale, *Calphad* **15**, 4 (1991).
- [42] C. Girard, *Excess functions and equilibrium phase diagrams of four ternary metallic systems: Al-Ga-In, Al-Bi-Ga, Bhi-Ga-Zn, Al-Ga-Sb*, PhD thesis, University of Provence, Marseille, (1985).
- [43] X. Lu, D. A. Beaton, R. B. Lewis, T. Tiedje and M. B. Whitwick, *Applied Physics Letters* **92(19)**, 192110 (2008).
- [44] A. Jordan, F. Trumbore, D. Nash and M. Kowalchik, *Journal of Electrochemical Society* **123**, 7 (1976).
- [45] G. B. Stringfellow, *Organometallic Vapor-Phase Epitaxy: Theory and Practice*, Academic Press (Elsevier), 2 edition, (1999).
- [46] K. Alberi, J. Wu, W. Walukiewicz, K. M. Yu, O. D. Dubon, S. P. Watkins, C. X. Wang, X. Liu, Y. J. Cho and J. Furdyna, *Physical Review B - Condensed Matter and Materials Physics* **75**, 045203 (2007).
- [47] K. Alberi, O. D. Dubon, W. Walukiewicz, K. M. Yu, K. Bertulis and A. Krotkus, *Applied Physics Letters* **91**, 051909 (2007).
- [48] W. Shan, W. Walukiewicz, J. Ager, E. Haller, J. Geisz, D. Friedman, J. Olson and S. Kurtz, *Phys. Rev. Lett.* **82**, 1221 (1999).

- [49] C. A. Broderick, M. Usman and E. P. O'Reilly, *Semiconductor Science and Technology* **28**, 125025 (2013).
- [50] A. Janotti, S.-H. Wei and S. Zhang, *Physical Review B* **65**, 115203 (2002).
- [51] M. Usman, C. A. Broderick, A. Lindsay and E. P. O'Reilly, *Physical Review B - Condensed Matter and Materials Physics* **84**, 245202 (2011).
- [52] K. Forghani, Y. Guan, M. Losurdo, G. Luo, D. Morgan, S. E. Babcock, A. S. Brown, L. J. Mawst and T. F. Kuech, *Appl. Phys. Lett.* **105**, 111101 (2014).
- [53] Z. L. Bushell, C. A. Broderick, L. Nattermann, R. M. Joseph, J. L. Keddie, J. M. Rorison, K. Volz and S. J. Sweeney, submitted to *Physical Review Materials* (2017).
- [54] H. Li and Z. M. Wang, *Bismuth-Containing Compounds*, volume 186 of *Springer Series in Materials Science*, Springer New York, New York, NY, 1 edition, (2013).
- [55] S. Francoeur, M.-J. Seong, A. Mascarenhas, S. Tixier, M. Adamcyk and T. Tiedje, *Applied Physics Letters* **82**, 2245 (2003).
- [56] B. Fluegel, S. Francoeur, A. Mascarenhas, S. Tixier, E. Young and T. Tiedje, *Physical Review Letters* **97**, 067205 (2006).
- [57] J. O'Gorman, A. F. J. Levi, T. T. Ek, D. L. Coblenz, R. A. Logan and A. F. J. Levi, *Applied Physics Letters* **60**, 1058 (1992).
- [58] N. K. Dutta, R. J. Nelson, N. K. Dutta and R. J. Nelson, *Applied Physics Letters* **38**, 407 (1981).
- [59] T. Higashi, S. J. Sweeney, A. F. Phillips, A. R. Adams, E. P. O'Reilly, T. Uchida and T. Fujii, *IEEE J. Sel. Top. Quantum Electron.* **5**, 413 (1999).
- [60] M. Silver, E. P. O'Reilly and A. R. Adams, *IEEE J. Quantum Electron.* **33**, 9 (1997).
- [61] S. Sweeney, A. Adams, M. Silver, E. O'Reilly, J. Watling, A. Walker and P. Thijs, *Physica Status Solidi (b)* **211**, 1 (1999).
- [62] M. Usman, C. A. Broderick, A. Lindsay and E. P. O'Reilly, *Phys. Rev. B* **84**, 245202 (2011).
- [63] E. Sterzer, N. Knaub, P. Ludewig, R. Straubinger, A. Beyer and K. Volz, *J. Cryst. Growth* **408**, 71 (2014).
- [64] P. Ludewig, Z. Bushell, L. Nattermann, N. Knaub, W. Stolz and K. Volz, *Journal of Crystal Growth* **396**, 95 (2014).
- [65] K. Forghani, Y. Guan, A. W. Wood, A. Anand, S. E. Babcock, L. J. Mawst and T. F. Kuech, *J. Cryst. Growth* **395**, 38 (2014).

- [66] P. Ludewig, N. Knaub, N. Hossain, S. Reinhard, L. Nattermann, I. P. Marko, S. R. Jin, K. Hild, S. Chatterjee, W. Stolz, S. J. Sweeney and K. Volz, *Applied Physics Letters* **102**, 242115 (2013).
- [67] I. P. Marko, P. Ludewig, Z. L. Bushell, S. R. Jin, K. Hild, Z. Batool, S. Reinhard, L. Nattermann, W. Stolz, K. Volz and S. J. Sweeney, *J. Phys. D. Appl. Phys.* **47**, 345103 (2014).
- [68] I. P. Marko and S. J. Sweeney, *IEEE Journal of Selected Topics in Quantum Electronics* **23**, 6 (2017).
- [69] H. Kim, F. K. Y. Guan, G. Luo, A. Anand, D. Morgan, T. F. Kuech, L. J. Mawst, Z. R. Lingley, B. J. Foran and Y. Sin, *Semicond. Sci. Technol.* **30**, 094011 (2015).
- [70] M. G. Craford, R. W. Shaw, A. H. Herzog and W. O. Groves, *Journal of Applied Physics* **43**, 4075 (1972).
- [71] Z. L. Bushell, P. Ludewig, N. Knaub, Z. Batool, K. Hild, W. Stolz, S. J. Sweeney and K. Volz, *J. Cryst. Growth* **396**, 79 (2014).
- [72] A. Janotti, S.-H. Wei and S. Zhang, *Phys. Rev. B* **65**, 115203 (2002).
- [73] Y. Zhang, A. Mascarenhas and L.-W. Wang, *Phys. Rev. B* **71**, 155201 (2005).
- [74] j. . P. p. . . t. . B. v. . . y. . . Deng, H X and Li, J. and Li, S. S. and Peng, H. and Xia, J.-B. and Wang, L. W. and Wei, S. H., doi = 10.1103/PhysRevB.82.193204.
- [75] S. Nacer, A. Aissat and K. Ferdjani, *Optical and Quantum Electronics* **40**, 9 (2008).
- [76] S. Tixier, M. Adamcyk, E. C. Young, J. H. Schmid and T. Tiedje, *J. Cryst. Growth* **251**, 1 (2003).
- [77] A. R. Mohmad, F. Bastiman, J. S. Ng, S. J. Sweeney and J. P. R. David, *Appl. Phys. Lett.* **98**, 122107 (2011).
- [78] S. Imhof, A. Thraenhardt, A. Chernikov, M. Koch, N. S. Koster, K. Kolata, S. Chatterjee, S. W. Koch, X. Lu, S. R. Johnson, D. A. Beaton, T. Tiedje and O. Rubel, *Appl. Phys. Lett.* **96**, 131115 (2010).
- [79] S. Tixier, S. E. Webster, E. C. Young, T. Tiedje, S. Francoeur, A. Mascarenhas, P. Wei and F. Schiettekatte, *Appl. Phys. Lett.* **86**, 11 (2005).
- [80] J. Yoshida, K. Takashi, O. Wada and K. Oe, *Japanese Journal of Applied Physics* **42**, 371 (2003).
- [81] Y. Y. M. Kondow, K. Uomi, A. Niwa, T. Kitatani, S. Watahiki, *Jpn. J. Appl. Phys.* **35**, 1273 (1996).

- [82] A. Stegmüller, K. Werner, M. Reutzel, A. Beyer, P. Rosenow, U. Hoefer, W. Stolz, K. Volz and R. Tonner, *Chemistry A European Journal* **22**, 42 (2016).
- [83] B. Kunert, W. Stolz, K. Volz and I. Ne, *Journal of Crystal Growth* **310**, 4763 (2008).
- [84] B. Kunert, W. Stolz, K. Volz and I. Ne, *Journal of Crystal Growth* **310**, 1595 (2008).
- [85] B. Kunert, I. Németh, S. Reinhard, K. Volz and W. Stolz, *Thin Solid Films* **517**, 140 (2008).
- [86] H. Doescher, T. Hannappel, B. Kunert, A. Beyer, K. Volz and W. Stolz, *Applied Physics Letter* **93**, 17 (2008).
- [87] A. Beyer, A. Stegmüller, J. O. Oelerich, K. Jandieri, K. Werner, G. Mette, W. Stolz, S. D. Baranovskii, R. Tonner and K. Volz, *Chem. Mater.* **28(10)**, 3265 (2016).
- [88] A. Beyer, J. Ohlmann, S. Liebich, H. Heim, G. Witte, W. Stolz and K. Volz, *Journal of Applied Physics* **111**, 083534 (2012).
- [89] A. Beyer, I. Nemeth, S. Liebich, J. Ohlmann, W. Stolz, K. Volz, A. Beyer and I. Ne, *Journal of Applied Physics* **109**, 083529 (2011).
- [90] A. Beyer, B. Haas, K. I. Gries, K. Werner, M. Luysberg, W. Stolz and K. Volz, *Applied Physics Letters* **103**, 032107 (2013).
- [91] H. P. Hjalmarson, *Physical Review Letters* **44**, 810 (1980).
- [92] A. A. Berg and P. J. Dean, *Proceedings of the IEEE* **60(2)**, 156 (1972).
- [93] T. M. Christian, D. A. Beaton, K. Alberi, B. Fluegel and A. Mascarenhas, *Applied Physics Express* **8**, 061202 (2015).
- [94] T. M. Christian, B. Fluegel, D. A. Beaton, K. Alberi and A. Mascarenhas, *Japanese Journal of Applied Physics* **55**, 108002 (2016).
- [95] M. P. Polak, P. Scharoch and R. Kudrawiec, *Semiconductor Science and Technology* **30**, 094001 (2015).
- [96] D. P. Samajdar, T. D. Das and S. Dhar, *Mater. Sci. Semicond. Process.* **40**, 539 (2015).
- [97] D. P. Samajdar and S. Dhar, *Scientific World Journal* **2014**, 704830 (2014).
- [98] D. P. Samajdar and S. Dhar, *Physica B: Condensed Matter* **484**, 27 (2016).
- [99] D. P. Samajdar and S. Dhar, *Superlattices and Microstructures* **89**, 112 (2016).
- [100] D. P. Samajdar, T. D. Das and S. Dhar, *Computational Materials Science* **111**, 497 (2016).

- [101] J. Belz, A. Beyer, L. Nattermann and K. Volz, *Microsc. Microanal.* **23**, S1 (2017).
- [102] S. Pennycook, *Ultramicroscopy* **30**, 58 (1989).
- [103] Y. Gao, *Journal of Applied Physics* **64**, 3760 (1988).
- [104] C. W. Magee, W. L. Harrington, R. E. Honig, C. W. Magee, W. L. Harrington and R. E. Honig, *Rev. Sci. Instrum.* **49**, 477 (1978).
- [105] H. Liebl, *Journal of Applied Physics* **38**, 5277 (1967).
- [106] K. Thompson, D. Lawrence, D. J. Larson, J. D. Olson, T. F. Kelly and B. Gorman, *Ultramicroscopy* **107**, 131 (2007).
- [107] W. Chen, P. A. Ronsheim, A. W. Wood, K. Forghani, Y. Guan, T. F. Kuech and S. E. Babcock, *Journal of Crystal Growth* **446**, 27 (2016).
- [108] W. M. Sawyer, *Carbon for Electric Lights*, Electric Dynamic Light Company, (1880).
- [109] W. J. Norman Pring, *Journal of Chemical Society* **95**, 1497 (1909).
- [110] R. Hoelbing, *Z. Angew. Chem.* **40**, 655 (1927).
- [111] B. C. Harrison and E. H. Tomkins, *Inorg. Chem.* **1**, 951 (1962).
- [112] H. M. Manasevit, *Appl. Phys. Lett.* **12**, 156 (1968).
- [113] M. Herman, W. Richter and H. Sitter, *Epitaxy*, Springer, 1 edition, (2004).
- [114] M. A. Grayson, *Measuring Mass - From Positive Rays to Proteins*, Chemical Heritage Press Philadelphia, (2002).
- [115] K. Busch, *Spectroscopy* **15**, 11 (2000).
- [116] J. H. Gross, *Massenspektrometrie - Ein Lehrbuch*, Springer Spektrum, (2004).
- [117] K. Hiraoka, *Fundamentals of Mass Spectrometry*, Springer, (2013).
- [118] W. Paul, *Rev. Mod. Phys.* **62**, 531 (1990).
- [119] M. A. Aliman, *Ein Beitrag Zur Breitbandigen Massenspektrometrie mit elektrischen Ionenresonanzzellen*, Bergische Universität Wuppertal, (1998).
- [120] K. Forghani, Y. Guan, A. Wood, S. Babock, L. Mawst and T. F. Kuech, *Chemical Vapor Deposition* **21**, 166 (2015).
- [121] N. Bahlawane, F. Reilmann, L.-C. Salameh and K. Kohse-Hoeingshaus, *Journal of the American Society for Mass Spectrometry* **19(7)**, 947 (2008).
- [122] I. Moussa, H. Fitouri, A. Rebey and B. El Jani, *Thin Solid Films* **516**, 8372 (2008).

-
- [123] P. Ludewig, N. Knaub, W. Stolz and K. Volz, *J. Cryst. Growth* **370**, 186 (2013).
- [124] L. Nattermann, P. Ludewig, E. Sterzer and K. Volz, *Journal of Crystal Growth* **470**, 15 (2017).
- [125] Z. L. Bushell, R. M. Joseph, L. Nattermann, P. Ludewig, K. Volz, J. L. Keddie and S. J. Sweeney, submitted to *Journal of Applied Physics* (2017).
- [126] I. P. Marko, S. R. Jin, Z. Batool, Z. L. Bushell, P. Ludewig, W. Stolz, K. Volz, R. Butkute and V. Pacebutas, *Semicond. Sci. Technol.* **30**, 094008 (2015).
- [127] P. W. Lee, T. R. Omstead, D. R. McKenna and K. F. Jensen, **85**, 165 (1987).
- [128] J. T. Francis, S. W. Benson and T. T. Tsotsis, *The Journal of Physical Chemistry* **95**, 4915 (1991).
- [129] G. Zimmermann, Z. Spika, T. Marschner, W. Stolz, E. O. Goebel, P. Gimmnich, R. Becker, J. Lorberth, A. Greiling and A. Salzmänn, *Journal of Applied Physics* **35**, 2035 (1996).
- [130] G. Zimmermann, H. Protzmann, W. Stolz and E. O. Goebel, *Journal of Crystal Growth* **124**, 136 (1992).
- [131] C. A. Larsen, C. H. Chen, M. Kitamura, G. B. Stringfellow, D. W. Brown and A. J. Robertson, *Applied Physics Letters* **48**, 22 (1986).
- [132] C. W. Hill, R. W. Gedridge, T. J. Groshens, G. B. Stringfellow and L. P. Sadwick, *Journal of Electronic Materials* **25**, 9 (1996).
- [133] C. A. Larsen and G. B. Stringfellow, *Journal of Crystal Growth* **75**, 2 (1986).
- [134] C. H. Chen, C. A. Larsen, G. B. Stringfellow, D. W. Brown and A. J. Robertson, *Journal of Crystal Growth* **77**, 1 (1986).
- [135] M. Mashita, S. Horiguchi, M. Shimazu, K. Kamon, M. Mihara, M. Ishii and E. S. P. B. V., *Journal of Crystal Growth* **77**, 194 (1986).
- [136] K. Deppert and J. Joensen, *Journal of Crystal Growth* **133**, 3 (1993).
- [137] I. Buchan and M. L. Yu, *Surface Science* **280**, 1 (1993).
- [138] M. Yoshida, H. Watanabe and F. Uesugi, *Semiconductor Holes* **132**, 677 (1985).
- [139] N. I. Buchan, C. A. Larsen and G. B. Stringfellow, *Journal of Crystal Growth* **92**, 3 (1988).
- [140] C. A. Larsen, S. H. Li and G. B. Stringfellow, *Journal of Crystal Growth* **94**, 663 (1989).

-
- [141] NIST Mass Spectrometry Data Center, Standart Reference Database Nr 69, 2017.
- [142] G. Zimmermann, *Einfluss neuartiger Ausgangsmaterialien in der MOVPE auf die physikalischen Eigenschaften von III/V Halbleitern*, Cuvillier Verlag Goettingen, Marburg, 1 edition, 1994.
- [143] A. Stegmüller, P. Rosenow and R. Tonner, Physical Chemistry Chemical Physics **16**, 32 (2014).
- [144] A. Stegmüller and R. Tonner, Chemical Vapor Deposition **21**, 7 (2015).
- [145] A. Stegmüller and R. Tonner, Inorganic Chemistry **54**, 13 (2015).
- [146] D. F. Foster, C. Glidewell and D. J. Cole-Hamilton, Journal of Electronic Materials **23**, 2 (1994).